DEVELOPMENT OF AN ULTRA-HIGH EFFICIENCY GAS TURBINE ENGINE (UHEGT) WITH STATOR INTERNAL COMBUSTION: DESIGN, OFF-DESIGN, AND NONLINEAR DYNAMIC OPERATION

A Dissertation

by

SEYED MOSTAFA GHOREYSHI

Submitted to the Office of Graduate and Professional Studies of
Texas A&M University
in partial fulfillment of the requirements for the degree of

DOCTOR OF PHILOSOPHY

Chair of Committee,	Meinhard T. Schobeiri
Committee Members,	J.N. Reddy
	Alan Palazzolo
	Jean-Luc Guermond
Head of Department,	Andreas A. Polycarpou

December 2018

Major Subject: Mechanical Engineering

ABSTRACT

An Ultra-High Efficiency Gas Turbine (UHEGT) technology is developed in this study. In UHEGT, the combustion process is no longer contained in isolation between the compressor and turbine, rather distributed in multiple stages and integrated within the High-Pressure (HP)-turbine stator rows. Fundamental issues of aero-thermodynamic design, combustion, and heat transfer are addressed in this study. The aero-thermodynamic study shows that the UHEGT-concept improves the thermal efficiency of gas turbines by 5-7% above the current most advanced gas turbine engines, such as Alstom GT24. The designed thermodynamic cycle has a 45% thermal efficiency and includes a six-stage turbine with three stages of stator internal combustion. Meanline approach is used to preliminary design the entire flow path in the turbine. Multiple configurations are designed and simulated via Computational Fluid Dynamics (CFD) to achieve the optimum combustion system for UHEGT. Flow patterns, temperature distributions, secondary losses, etc. are among the parameters studied in the results. The final configuration for the combustion system includes two rows of injectors placed before the stator rows in the first three turbine stages. The current injector configuration provides a highly uniform temperature distribution at the rotor inlet, low pressure loss, and low emissions compared to the other cases. Different approaches are numerically studied to lower the stator blade surface temperature distribution in UHEGT from which indexing (clocking) is shown to be very effective.

In the final part of this study, a dynamic simulation is performed on the entire engine using the nonlinear generic code GETRAN developed by Schobeiri. The simulations are in 2D (space-time) and include the complete gas turbine engine. The system performance is studied under variable design and off-design conditions. The results show that most of the system parameters fluctuate with similar patterns to the fuel schedule. However, the amplitudes of the fluctuations are different and there is a time lag in the response profiles relative to the fuel schedules. It is shown that thermal efficiency variations are smaller compared to the other parameters which means the system performs in efficiencies close to the design point throughout the entire cycle.

DEDICATION

I dedicate my dissertation to my parents whom without their support I would never be able to succeed in this path. I also dedicate this dissertation to my wife, Nadia, whose love and companionship gave me the motivation and will to work harder and better to complete this work.

ACKNOWLEDGMENTS

I would like to state my greatest appreciation for my research adviser, Dr. Schobeiri, whom I have learned so much from in the past few years. His knowledge, guidance, and support gave me the power to succeed throughout this research. I would also like to thank my committee members, Drs. Reddy, Palazzolo, and Guermond for their help and guidance. I like to acknowledge the Mechanical Engineering Department and Dale Adams Enterprises Inc. for supporting this project, and the High-Performance Research Computing (HPRC) center at Texas A&M University for providing the commercial softwares.

I would like to thank my friends and co-researchers Dr. Rezasoltani and Dr. Cand. Nikparto whose experience guided me along this path. Also, thanks to all my friends in Texas A&M University who made this experience enjoyable along the way. At the end, I would like to thank my wife and family for their patience and continuous love and support which made all this possible.

NOMENCLATURE

Bh	Blade height (m)
C	Blade chord (m)
C_{ax}	Blade axial chord (m)
C_f	Friction coefficient
C_p	Static pressure coefficient
D	Diameter (m)
D_h	Hydraulic diameter (m)
h	Static enthalpy (J/kg)
h_s	Isentropic enthalpy (J/kg)
H	Total enthalpy (J/kg)
K	Kinetic energy (J)
l_m	Specific load (J/kg)
M	Mach number
$\dot{m}$	Mass flow rate (kg/s)
$\dot{m}_f$	Fuel mass flow rate (kg/s)
N	Rotational velocity (rpm)
P	Static pressure (Pa)
P_{stag}	Stagnation pressure (Pa)
P_{tot}	Total pressure (Pa)
R	Radius

Re	Reynolds number
S	Entropy (J/kg.K)
T	Static temperature (K)
T_c	Coolant temperature (K)
T_{ij}	Shear stress tensor (N/m^2)
T_s	Isentropic temperature (K)
T_{tot}	Total temperature (K)
T_w	Wall temperature (K)
T_∞	Mainstream temperature (K)
U	Blade circumferential velocity (m/s)
V	Velocity (m/s)
V_j	Cooling jet velocity (m/s)
V_m	Meridional velocity (m/s)
V_u	Circumferential velocity (m/s)
W	Relative velocity (m/s)
$\dot{W}$	Power (Watt)
X	Axial location (m)
XL	Length (m)

Greek

α	Flow angle (deg)
β	Blade metal angle (deg)

γ	Heat capacity ratio
η	Efficiency
η_p	Polytropic efficiency
η_s	Isentropic efficiency
η_{th}	Thermal efficiency
κ	Heat capacity ratio
λ	Load coefficient
μ	Meridional velocity ratio
ν	Circumferential velocity ratio
π	Pressure ratio
ρ	Density (kg/m^3)
τ_w	Wall shear stress (N/m^2)
ϕ	Flow coefficient
ϕ_{WE}	Weak extinction equivalence ratio
ψ	Isentropic load coefficient

Abbreviations

BL	Baseline
CAES	Compressed Air Energy Storage
CFD	Computational Fluid Dynamics
CMB	Combustion Chamber
EDM	Eddy Dissipation Model

GT	Gas Turbine
HP	High Pressure
INJ	Injectors
LE	Leading Edge
LP	Low Pressure
M	Million (Mega)
NUI	Non-Uniformity Index
ppmv	parts per million volume
PS	Pressure Surface
R	Rotor
S	Stator
SS	Suction Surface
TIT	Turbine Inlet Temperature
UHEGT	Ultra-High Efficiency Gas Turbine

CONTRIBUTORS AND FUNDING SOURCES

Contributors

This work was supported by a dissertation committee consisting of Professor Schobeiri (adviser) and Professors Reddy and Palazzolo of the Department of Mechanical Engineering and Professor Guermond of the Department of Mathematics.

The compressor data and design were provided by Erie Widyanto of the Department of Mechanical Engineering and were published in 2015 in a thesis listed in the Biographical Sketch.

All other work conducted for the dissertation was completed by the student independently.

Funding Sources

Graduate study was supported by the Department of Mechanical Engineering from Texas A&M University and Dale Adams Enterprises Inc.

TABLE OF CONTENTS

LIST OF FIGURES

LIST OF TABLES

CHAPTER I

INTRODUCTION: GAS TURBINE ENGINE

I.1. Gas Turbine Structure and Components

Gas Turbine (GT) engines are types of Turbomachinery devices that transform the total energy of the working fluid into kinetic energy and vice versa. A gas turbine engine typically has three main components: compressor, combustion chamber, and turbine. In compressor, the mechanical power is transferred to the working fluid (air) to increase its pressure. In combustion chamber, the fuel is added to the working fluid and makes its temperature to increase through combustion process. Finally, the high pressure-high temperature combustion gas goes through turbine where its total energy is transformed to mechanical energy and rotates the shaft [1]. Figure 1 shows a gas turbine and the main corresponding components.

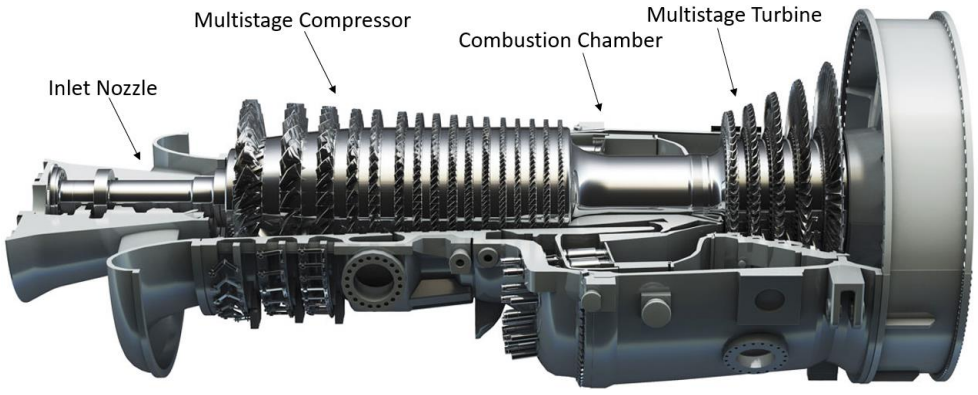

Figure 1. GE-Alstom (former Brown Boveri) heavy duty power generation gas turbine GT13E2 with gross output of 203 MW; Reprinted from GE Power [2].

I.1.1. Turbine

The turbine component in the gas turbine is responsible for extracting the total energy from the working fluid (combustion gas) and converting it into mechanical energy which can be used for power or thrust generation. In an axial turbine, this process happens through consecutive *stages* consisting of *stator* and *rotor* rows. The stator blades, which are stationary and attached to the turbine casing, are responsible for deflecting the high pressure-high temperature combustion gas to an appropriate angle to enter the rotor row. In addition, the deflection process causes the flow to accelerate in the stator channel. The working fluid then enters rotor where its energy is used to rotate the blades and the main shaft. This process is repeated in multiple stages until the gas reaches the exit conditions.

Figure 2. A three-stage high pressure research turbine at TPFL. The blades are cylindrical with tip shroud to reduce the tip leakage losses; Reprinted from Schobeiri [1].

Figure 2 shows a three-stage high pressure research turbine at Turbomachinery Performance and Flow Research Laboratory (TPFL). The rotor blades are cylindrical with tip shroud to reduce the tip leakage losses in this design.

I.2. Gas Turbine Applications

I.2.1 Power Generation

One of the main uses of gas turbines is in power generation plants. Gas turbines have high thermal efficiencies, use air as the working fluid, and have high exhaust temperature. Those characteristics make them very popular for power generation. The high exhaust temperature makes it possible to use the gas turbine in a combined cycle where the exhaust gas is used as a heat source for additional power generation via a steam turbine. The combined cycle can reach astounding net efficiencies of higher than 60%. Figure 3 shows a power generation industrial gas turbine engine, SGT-800 by Siemens.

I.2.2 Aircraft Engine

Gas turbines play a very important role in transportation as they are the main propulsion system for all size aircrafts. The primary function of an aircraft gas turbine is to generate thrust. Typically, aircraft gas turbines are designed as *Turbofans* which contain two (or more) spools (shafts). The HP-spool includes HP-turbine which drives the HP-compressor via the connecting shaft. The LP-spool contains the LP-turbine which drives

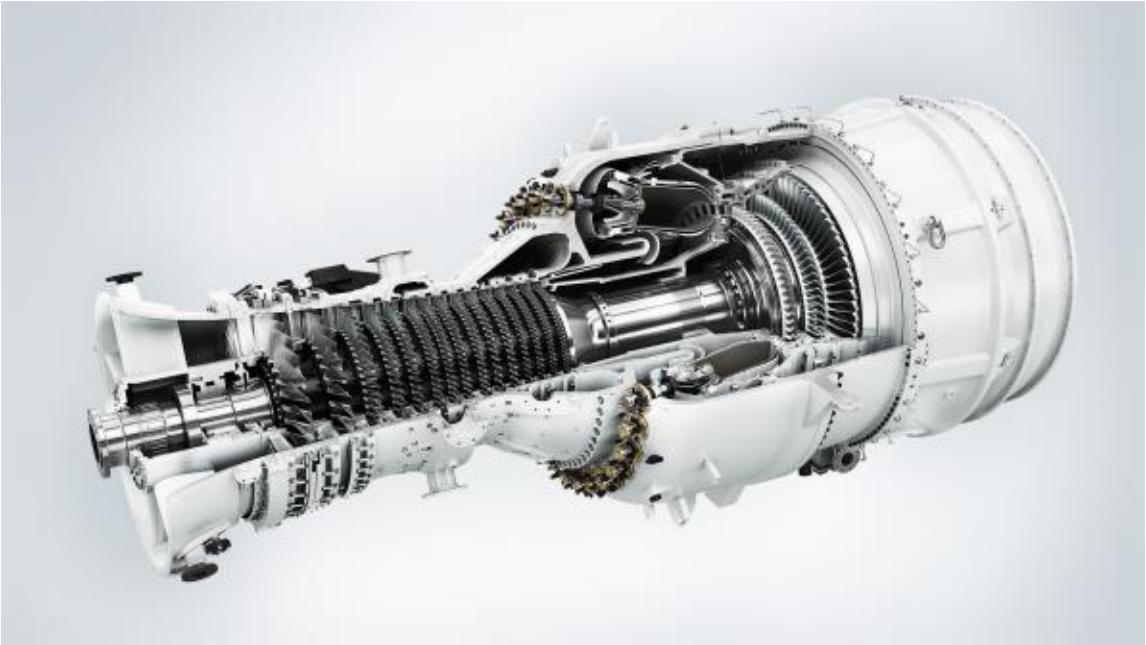

Figure 3. Siemens SGT-800 power generation gas turbine (57.0 MW); Reprinted from Siemens [3].

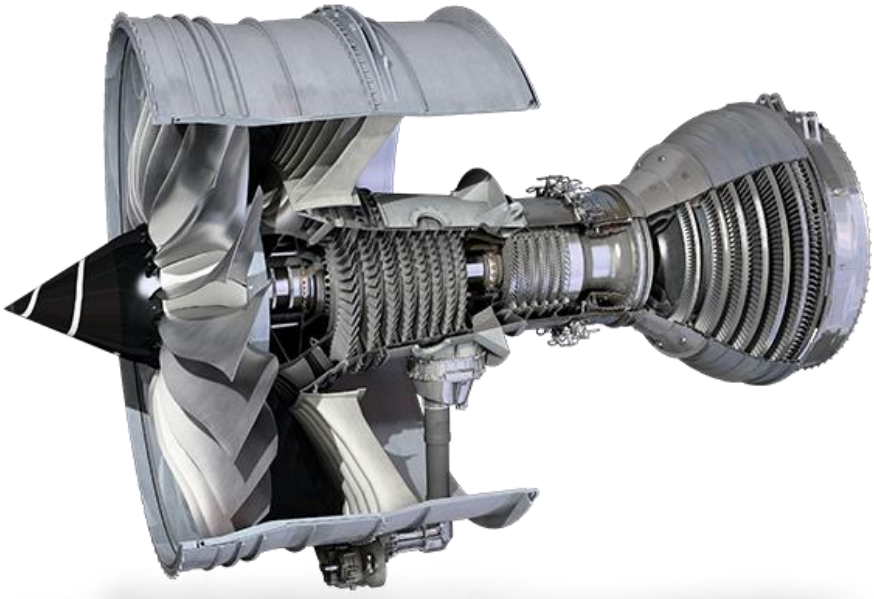

Figure 4. Rolls Royce Trent 1000 aircraft engine. Three-spool, high-bypass ratio gas turbine, designed and optimized for the Boeing 787 Dreamliner; Reprinted from Rolls Royce [4].

the main *fan* which is the main provider of thrust in a high-bypass ratio engine. The bypass ratio is defined as the ratio of air mass flow bypassing the engine core (turbine and combustion chamber) to the air mass flow going through the engine core. Figure 4 shows the Rolls Royce Trent 1000 engine with bypass ratio of 10:1.

I.3. Efficiency Evolution of Gas Turbines

The basic cycle efficiency of the gas turbines prior to 1986 was in the range of 32%-35% [5]. To achieve higher efficiencies, Turbine Inlet Temperature (TIT) has to be substantially increased which requires extensive amount of cooling in the front turbine stages. Studies in [6]-[8] show that a significant efficiency improvement can be achieved by introducing the reheat concept in CAES-turbine design. Figure 5 quantitively shows the efficiency improvement achieved using the reheat concept. The blue curve in this figure represents the efficiency of a relatively advanced GT with conventional thermodynamic cycle. The green curve, on the other hand, represents the efficiency of a generic reheat gas turbine [5]. This concept was adopted by Brown Boveri[1] company in GT24/26 engine, shown in Figure 6. As shown in this figure, GT24/26 has two combustion stages and a reheat turbine stage. The background and evolution of this concept is discussed in further details in the next chapter.

[1] Former Brown Boveri (BBC), then Asea Brown Boveri (ABB), now GE-Alstom.

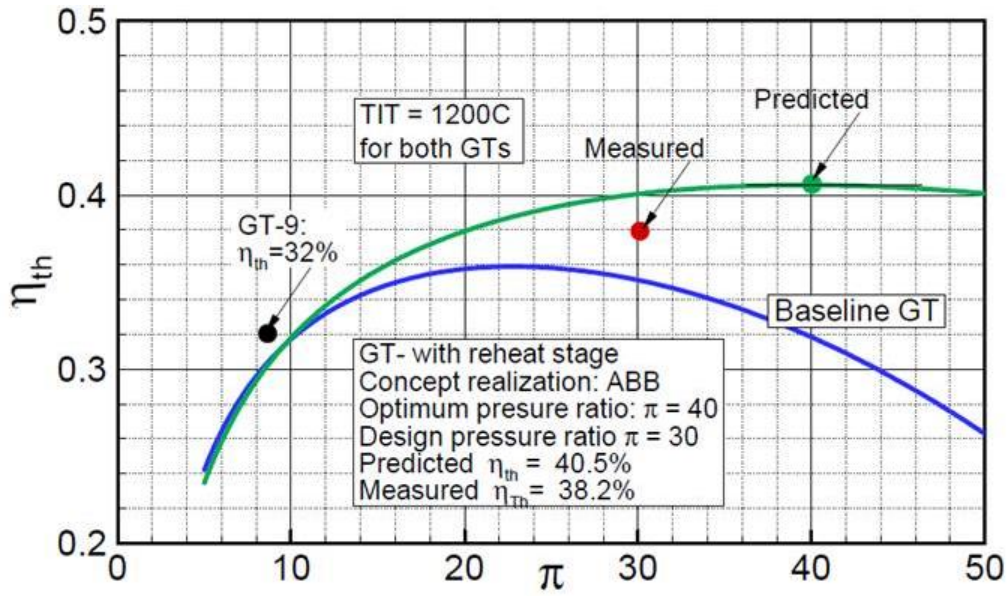

Figure 5. Efficiency comparison between a conventional (blue curve) and a reheat (green curve) gas turbine; Reprinted from Schobeiri [5].

Figure 6. Brown Boveri (GE-Alstom) GT 24/26 with two combustion stages and a reheat turbine stage; Reprinted from GE Power [2].

I.3.1. Alternative Performance Improvement Strategies

Premix Combustion: In 1970's the engine pollution gained attraction and different methods were developed to reduce NOx emission of gas turbines. The lean premix burning concept was introduced which created a step towards low NOx combustion [9]. It was realized that to achieve a low emission combustion process, the mixing process of fuel and air could be separated from the combustion process itself and also combustion could take place under very lean conditions. So, the goal was first to create a lean and homogeneous mixture of fuel and air and then to burn it. Döbbeling et al. [9] from Alstom performed some tests on a premix swirl combustor in conjunction with GASL in Westbury, US. Approximately 10 ppm NOx was measured at the exit with 100% premix oil, which was compared to the 60 ppm NOx in case of 92% premix oil and 8% diffusion oil. This demonstrated the clear superiority of lean premix burning. If fuel and air are not adequately premixed before combustion, it leads to creation of so-called hot-spot regions which will likely cause an increase in NOx emission [10]. In lean premixed combustion, the engine operates in equivalence ratio close to the lean blow-out limit in order to maintain NOx and CO emission at low levels. For instance, as for natural gas, the stoichiometric fuel air ratio is 1:17.2 and the lean blow-out limit is in the range of 0.1-0.4 depending on the performing conditions. Examples of lean blow-out limits are shown in Figure 15 for a number liquid fuel sources. A lean fuel and air mixture may also lead to unstable combustion. So, there should be a tradeoff between low emissions and flame stability [10].

Water Injection: Water or steam injection into the flame was a normal practice to reduce the NOx emissions. An example is one of the former BBC single-combustion chamber gas turbine engines [9]. The injected mass flow of water would be in the same order as the fuel mass flow rate. Although the output power of the gas turbine increased with higher amount of water injection, the efficiency of the cycle dropped. Another disadvantage was that demineralized water and steam were not available in many cases [9].

CHAPTER II[1]

UHEGT: CONCEPT AND BACKGROUND

II.1. Sequential Combustion: Background and Evolution of Technology

Conventional gas turbines have a multistage compressor followed by a combustion chamber and a multistage turbine. To substantially increase the thermal efficiency, in 1986, Schobeiri [6] introduced a multi-stage combustion process into gas turbines in a Brown Boveri[2] report. In this process, the combustion takes place in sequential steps along the turbine stages, which leads to the elimination of the combustion chamber as a single separate unit.

The idea behind the concept above is based on the well-known reheat process in steam turbines. In this process, after the steam exits from the high pressure stages, additional superheated steam is added to the main flow. The reheated steam flow then passes the intermediate and low pressure turbine stages. The addition of the hot steam improves the performance of the system and increases the average temperature of heat addition, making the cycle closer to the ideal Carnot cycle [11].

---

[1] Part of the materials are reprinted with permission from "The Ultrahigh Efficiency Gas Turbine Engine with Stator Internal Combustion," by Meinhard T. Schobeiri and Seyed M. Ghoreyshi, 2016. ASME Journal of Engineering for Gas Turbines and Power Vol. 138, no. 2, Copyright © 2016 by ASME.
[2] Former Brown Boveri (BBC), then Asea Brown Boveri (ABB), now GE-Alstom.

Based on this concept, a change of technology was suggested to increase the gas turbine efficiency without a significant increase in Turbine Inlet Temperature (TIT). This idea was utilized for the first time in order to develop a gas turbine for a compressed air energy storage (CAES) in Huntorf, Germany. Figure 7 and Figure 8 show the schematic of the CAES facility which is described more in details by Schobeiri [12], Schobeiri and Haselbacher [13], and Schobeiri [14]. CAES gas turbine was designed and manufactured by Brown Boveri (BBC) in 1978. The facility has been operating since then as an emergency power generator. Different components are: 1- Compressor gear train, 2- electric motor generator unit, 3- gas turbine, 4- underground compressed air storage.

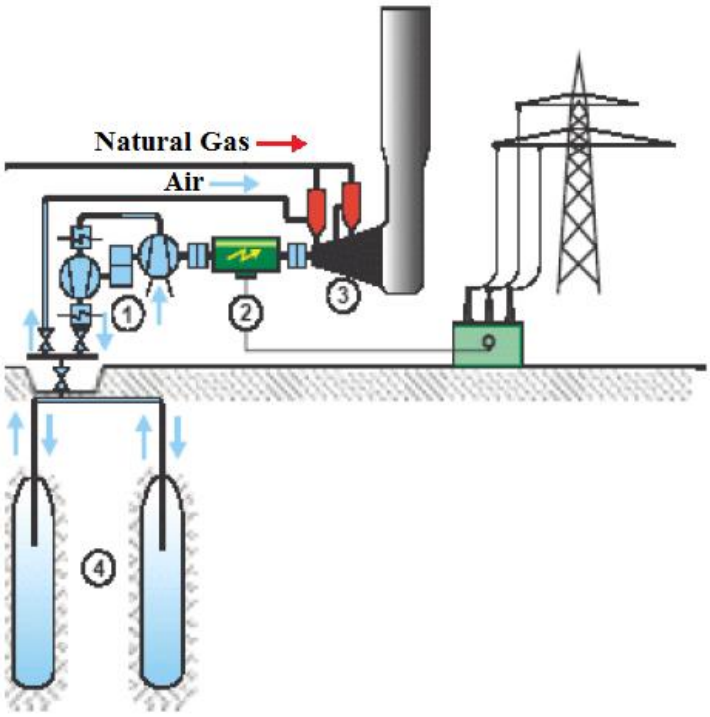

Figure 7. Compressed air energy storage facility, Huntorf, Germany: (1) LP-Gear, HP-Compressor train, (2) electric motor/generator, (3) gas turbine with two combustion chambers and two multi-stage turbines, (4) air storage; Reprinted from Schobeiri [12].

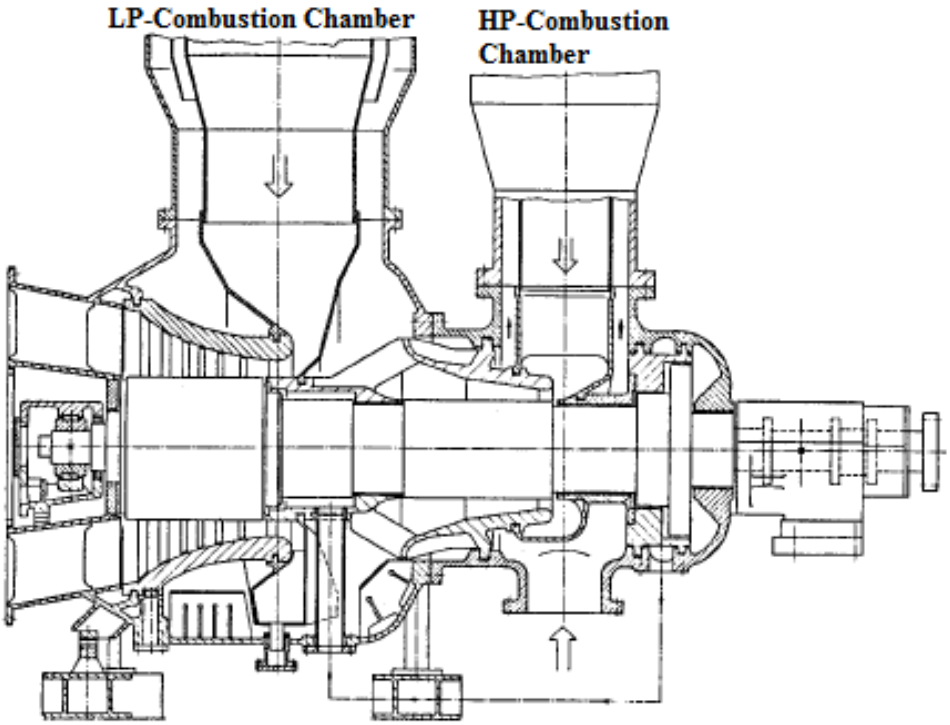

Figure 8. CAES gas turbine engine; Reprinted from Schobeiri [12].

The main component of the CAES facility is the gas turbine shown in Figure 8. It contains a high pressure (HP) combustion chamber followed by a multi-stage HP-turbine and a low pressure (LP) combustion chamber followed by a multi-stage LP turbine. A detailed study of this gas turbine showed a significant improvement in thermal efficiency in the order of 5-7% in comparison with the one with one combustion chamber [12]. Although this standard efficiency improvement method was routinely used in compressed air energy storage facilities, until the late eighties it did not find its way into the power generation and aircraft gas turbine industry. The reason for that was the inherent problem of adding a typical large volume combustion chamber to the engine. It could cause different design integrity and operational problems which made the engine manufacturer

unwilling to implement this technology. So, prior to late eighties, implementing the reheat process by adding a conventional combustion chamber was not a feasible option. But the significant improvement in efficiency motivated Brown Boveri to make a radical change to stay ahead in the increasingly intense global competition. In an intensive effort, a new combustion technology was developed and integrated into a new gas turbine engine with one reheat stage turbine followed by a second combustion and a multi-stage turbine which significantly improved the thermal efficiency [15]-[18].

Although the addition of the second combustion chamber brought a significant efficiency improvement, increasing the number of combustion chambers above two, would result in unforeseeable design integrity problems. In the following section, the new UHEGT technology is introduced which describes how to overcome the problems of implementation of multiple combustion chambers in gas turbines.

II.2. The UHEGT Concept

The concept of the Ultra High Efficiency Gas Turbine (UHEGT) was developed by M.T. Schobeiri, the former Chief of Aero-Thermodynamic Gas Turbine Design Group at Brown Boveri. The new developed technology introduces a gas turbine in which the combustion process is distributed along the turbine stator rows. This allows the elimination of combustion chambers as a separate unit form the turbine leading to high thermal efficiencies that cannot be achieved by conventional gas turbines. Schobeiri [7], [8] proposed a patent which demonstrates that the UHEGT-concept can improve the

thermal efficiency of gas turbines from 5% to 7% above the current highest efficiency gas turbines such as ABB GT24/26 (at full load: 40.5%).

To demonstrate the innovative claim of the UHEGT-concept, a study is conducted comparing three conceptually different power generation gas turbine engines: a conventional gas turbine (single shaft, single combustion chamber), a gas turbine with sequential combustion (GT24/26), and a UHEGT [8]. The evolution of the gas turbine process that represents the efficiency improvement is shown in Figure 9.

In this study, the working fluid is an ideal reacting mixture of methane and air. The compression and each expansion processes is specified with polytropic efficiencies of 90% and 88%, respectively. The energy exchange at each section is calculated based on the static enthalpy difference between inlet and exit. The total net power is computed by adding turbine powers of all stages and subtracting the total compressor power and the power due to the bearing losses. The thermal efficiency is the ratio of the total net power to the fuel energy.

Figure 9a shows a conventional single combustion process in which thermal efficiency is around 32-36% (based on the different turbine inlet temperatures). Substantial efficiency improvement was achieved by introducing a single reheat turbine stage as shown in Figure 9b. By utilizing a higher compression ratio in GT24/26 and a two-stage combustion process, the efficiency of the machine was considerably improved without any significant increase in TIT. The cross-hatched area refers to the baseline process and the simple-hatched area translates to the net work increase. This will lead to

thermal efficiency gain, which in case of the ABB-GT24/26, resulted in 6 to 7% efficiency improvement [8].

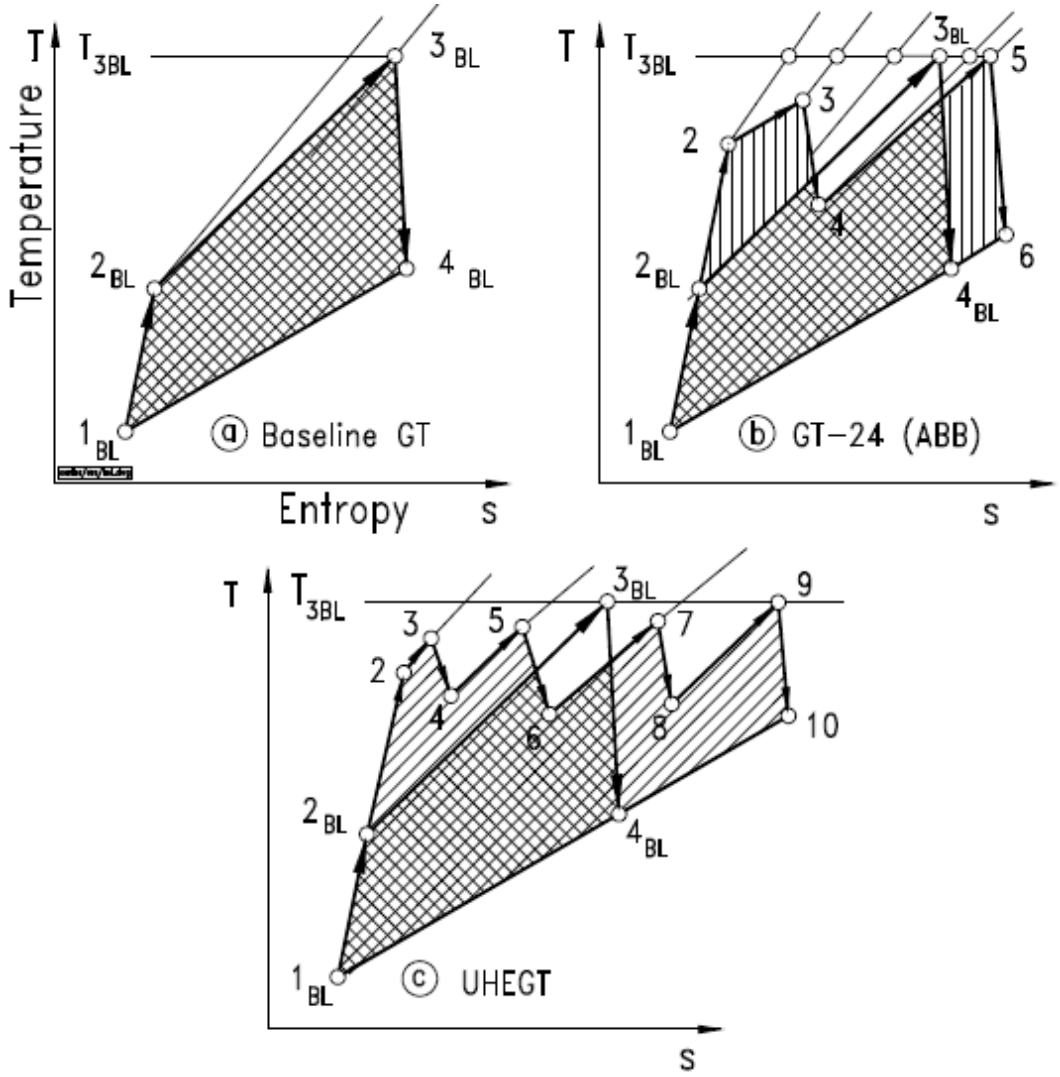

Figure 9. Process comparison for (a) baseline-conventional GT, (b) GT-24, and (c) UHEGT (four stages); detailed processes are: compression 1–2, combustion 2–3, 4–5, 6–7, and 8–9, expansion: 3–4, 5–6, 7–8, and 9–10; Reprinted from Schobeiri [8].

A detailed dynamic engine simulation of the ABB-GT24/26 gas turbine engine showed a thermal efficiency of η_{TH}=40.5%. The corresponding measured efficiency for GT-26 was reported as 38.2%. The difference of 2.3% is attributed to numerous failures associated with compressor blade distress in the form of cracking. The failures occurred at the start of the engine operation [19]. This efficiency improvement was achieved despite the following facts: (a) The compressor pressure ratio is far greater than the optimal conventional one ($\pi_{opt\ GT24} \approx 2 \times \pi_{opt\ BL}$) causing the compressor efficiency to decrease. The latter is because of reduced blade height associated with an increase in secondary flow losses. (b) The introduction of a second combustion chamber inherently causes additional total pressure losses.

A further efficiency improvement is achieved by eliminating the combustion chambers altogether and placing the combustion process inside the stator blade passages. Figure 9c schematically shows the thermodynamic process of this gas turbine engine, where the combustion is placed inside the stator flow passage of a multi-stage turbine. Starting from the compressor exit pressure, Figure 9c, point 2, fuel is added inside the stator flow passage raising the total temperature, to point 3. The expansion in the stator is followed by the expansion through the first turbine rotor flow passage, point 4. The same expansion processes are repeated in the following turbine stator and rotor blade passages (points 5 through 9). The cross-hatched area refers to the baseline process, whereas the simple-hatched area represents the net work gain which leads to thermal efficiency improvement. Aero-thermodynamic calculations show that for a UHEGT with three stator-internal combustions, a thermal efficiency of above 45% can be achieved.

Increasing the number of stator internal combustion to 4, raises the efficiency above 47% [15].

A detailed quantitative calculation of each process is presented in Figure 10. In this figure, the compression ratio is increased while the maximum cycle temperature (TIT) is kept constant. These figures represent a comparison between the thermal efficiencies and specific works of baseline GT, the GT24/26, and a UHEGT with three and four stator-internal combustions, UHEGT-3S and UHEGT-4S, respectively. Maximum temperature for all cycles are the same and equal to TIT=1200 C. As shown in Figure 10a, for UHEGT-3S (with three stator internal combustion stages), a thermal efficiency above 45% is calculated [15]. This exhibits an increase of at least 5% above the efficiency of the most advanced current gas turbine engine, GT24/26. Increasing the number of stator internal combustion to 4, curve labeled with UHEGT-4S, raises the efficiency above 47% which can bring an enormous efficiency increase compared to the existing gas turbine engines. It should be noted that UHEGT-concept requires an optimization of the compressor pressure ratio. As shown in Figure 10a, the optimum pressure ratio for the current UHEGT is around 35 to 40 which is higher than the optimum pressure ratio for a single combustor engine (15-20).

Figure 10b shows the specific work comparison for the gas turbines discussed above. Compared to GT-24, UHEGT-technology has about 20% higher specific work, making this technology very suitable for aircraft engines, stand-alone as well as combined cycle power generation applications. This efficiency increase can be established at a compressor pressure ratio of $\pi_{UHEGT} = 35 - 40$, which can be achieved easily by existing

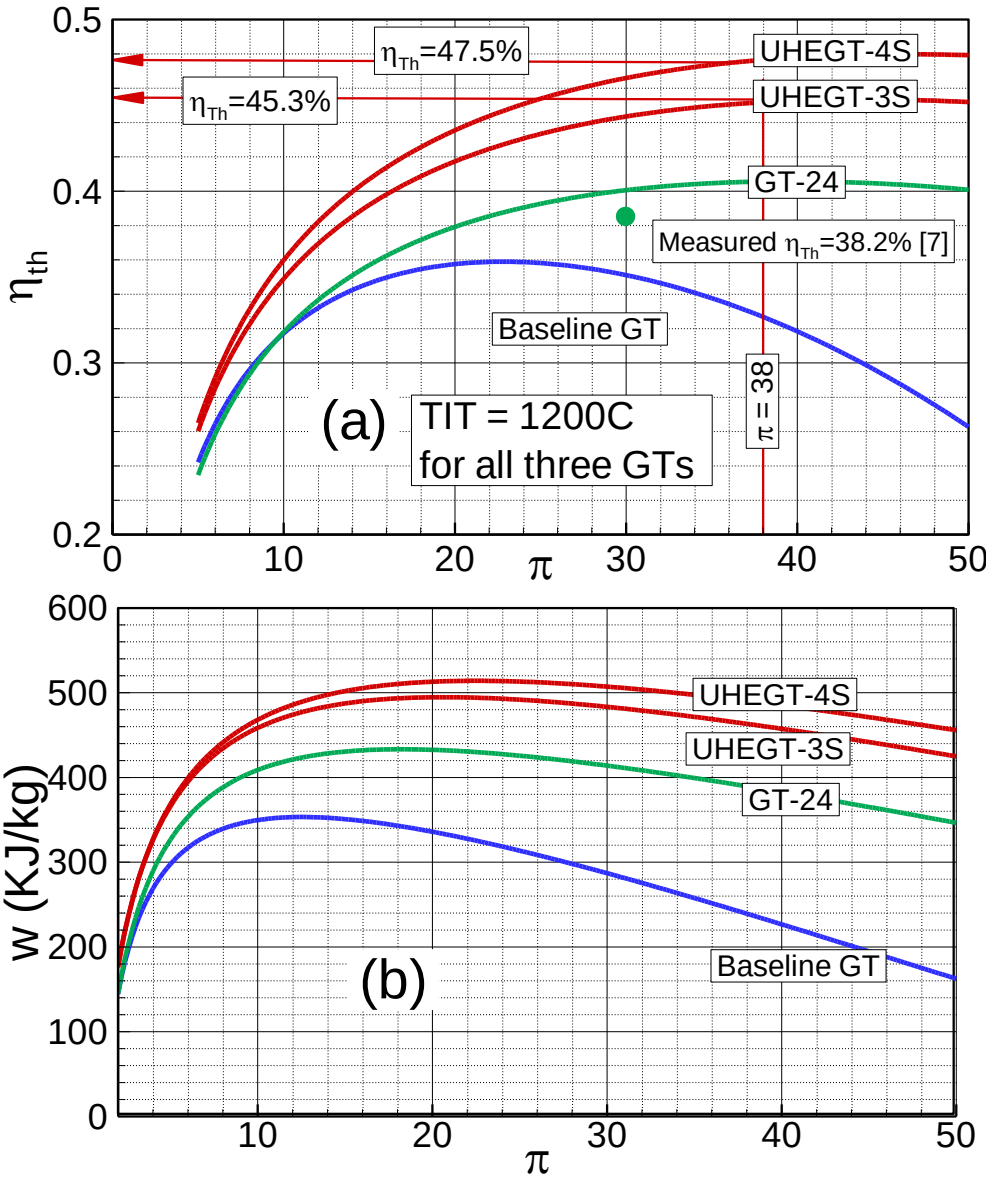

Figure 10. (a) Thermal efficiency and (b) specific work comparison of baseline GT, GT-24, and different UHEGT configurations; Reprinted from Ref. [15].

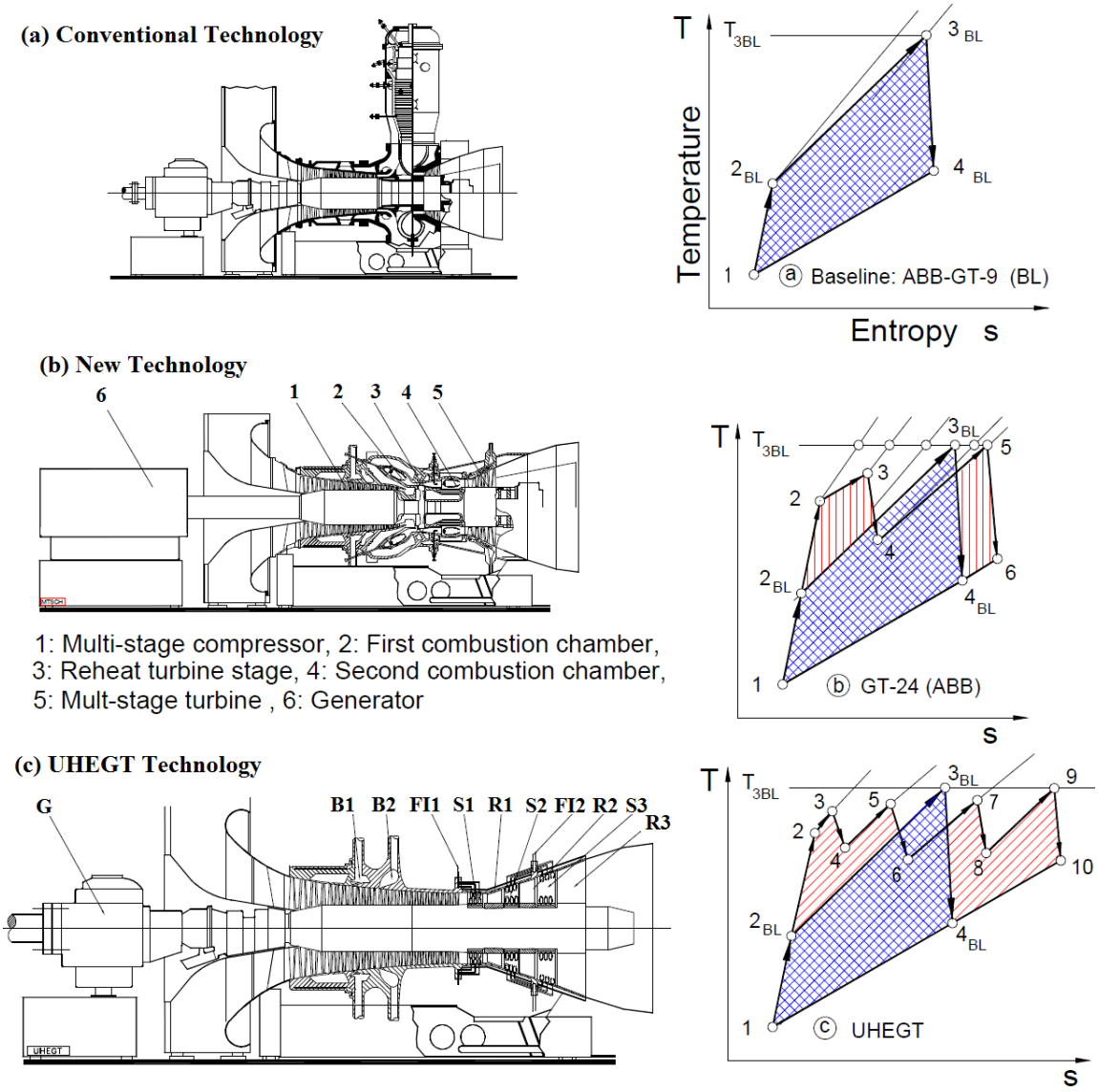

Figure 11. Technology change from conventional GT to more advanced GT24/26 and the most advanced engine with an integrated UHEGT technology: (a) conventional technology, (b) New technology, and (c) UHEGT technology; Reprinted from Ref. [15].

compressor design technology with a conventional polytropic efficiency of around 90% [15]. Figure 11 represents at one glance the evolution associated with the change of technology as discussed. Starting with the conventional design in Figure 11a, through GT24/26 in Figure 11b, and the UHEGT with a multi-stage compressor and internal combustion within the first, second, third, and fourth stators as shown in Figure 11c.

II.2.1. Applications of UHEGT-Technology

The UHEGT-technology is equally applicable to the core of civil and military aircraft engines with single, twin and three spools as well as power generation gas turbine engines. The elimination of the combustion chamber in UHEGT results in a much shorter shaft with a more stable rotor dynamic operation [15]. In aircraft engine applications, in addition to an increased thermal efficiency, the UHEGT design results in higher engine thrust/weight ratio which can lead to considerable fuel savings. With reduced fuel consumption, a consolidated turbine inlet temperature and less CO_2 output, the application of the UHEGT to aircraft and power generation gas turbines significantly contributes to environmental protection. UHEGT configuration also allows the unburned fuel particles to be further burned in the following rotor passages which results in further mixing and makes a complete combustion possible. For supersonic applications, the UHEGT-technology brings additional advantages, namely the elimination of the afterburner and reduction of NO_x as a result of reduced fuel consumption and distributed combustion. Thus, this technology development describes a breakthrough in power and thrust generation gas turbines [15].

II.2.2. Reheat Advantages in Gas Turbines

Asea Brown Boveri (ABB)[1] introduced a new generation of high efficiency gas turbines with two sequential combustion stages in the mid 90's (GT24/GT26), shown in Figure 6. In addition to high efficiency, these gas turbine engines have shown superior flexibility in operation and low emission since their launch [20], [21]. Since the 80's, the advantages of reheat process in gas turbines are discussed in multiple studies by ABB researchers [6], [9], [21], [22]. GT24/GT26 engines use an EV (EnVironmental) burner in the first combustion stage and an SEV (Sequential EnVironmental) burner in the second combustion stage. Combination of the two concepts of low emission EV-burner and sequential combustion in a single shaft engine, GT24/GT26, created a machine with high power density and small footprint. In these engines, a reheat combustor makes a more efficient use of the oxygen by burning twice in lean premix mode. High peak flame temperatures which lead to increase in NOx are avoided in a double stage combustion engine. In addition, the unburned fuel particles from the first combustion stage will be burned in the next combustor. The other reason for the low NOx-emission in a reheat engine, is that second stage combustion occurs at lower O_2 and higher H_2O levels compared to the first one [21]. This allows for the second combustor to operate at a high flame temperature and produce lower NOx compared to a single combustor at the same temperature. With regards to the engine flexibility, the reheat concept allows the combustors to work at a different temperature without a significant effect on the total

[1] Now GE-Alstom

output power. Another advantage to the reheat engine is that the benefits of premix combustion can be used in the entire load range. In these engines, the first combustor operates at constant flame temperature through the entire load range, while the premixed second combustor is used to change loads [21].

II.3. Alternative Combustor Technologies

Cottle and Polanka [23] studied the Ultra-Compact Combustor (UCC) technology. UCC is based on the previously introduced concept of inter-turbine burner (ITB) [24]-[26]. The concept in these type of combustors is to bring the combustion process into the turbine blade channels in order to simulate the theoretical constant temperature work extraction in the ideal (Carnot) cycle. UCC operates by diverting a portion of the compressor exit flow into a cavity around the engine outer diameter. The cavity is used as the primary combustion zone. The burning mixture is brought back into the main axial flow by use of radial guide vanes or similar mechanisms. Although there are some advantages in these type of combustors, they face some challenges such as inward radial migration of the flow in the core turbine passage [23].

In a combustor called “Multi Injection Burner” developed by Brown Boveri [9] and shown in Figure 12, the complete cross section area of the annular combustor is utilized by using a large number of small burners. Subsequently the flame length and residence time is shortened which will lead to lower NOx emissions. The short length of flame causes a short length combustor which leads to lower cooling air consumption and higher air flow to the burners. Also, some ports for quenching air were arranged near to

the swirlers to reduce the high gas temperature immediately after burning. Brown Boveri's GT-8 was equipped with this type of combustor in 1988 along with several other BBC gas turbine engines [9]. Results showed that 70 ppm NOx was generated at the exit which showed that first, combustion was still taking place near stoichiometry conditions and second, the short residence time was not quite enough for bringing down the NOx levels. Alstom also introduced annular premix combustor in GT13E2 (shown in Figure 1) in which multiple singular burners are distributed along the turbine entry circumference. This arrangement has several advantages including an automatic cross ignition along the burners, the possibility to run with some burners turned off, and highly uniform gas temperature at turbine inlet.

EV burner introduced by Alstom[1] and first applied to GT11 in 1993 uses the vortex breakdown of a strongly swirling flow to stabilize the premix flame [27]. As shown in Figure 13, the EV burner consists of two half cone shells with an offset to each other in order to create a tangential slot for air and fuel. The swirl strength of the air flow increases in axial direction in a way that vortex breakdown occurs near the exit of the burner. Upstream of the vortex breakdown, the core flow is strongly accelerated which creates a barrier against flashback. Downstream of the vortex breakdown an inner recirculation zone is created which plays an important part in stabilizing the flame. Modern versions of EV burner have brought down the NOx and CO emissions to very low levels (25 vppm NOx) [9].

[1] Former Brown Boveri (BBC), now GE-Alstom.

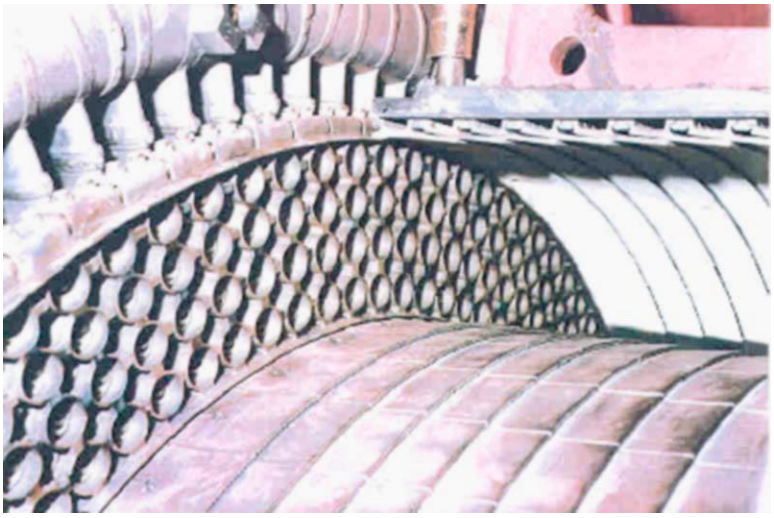

Figure 12. Brown Boveri's Multi Injection Burner in the GT8 annular combustor; Reprinted from Ref. [9].

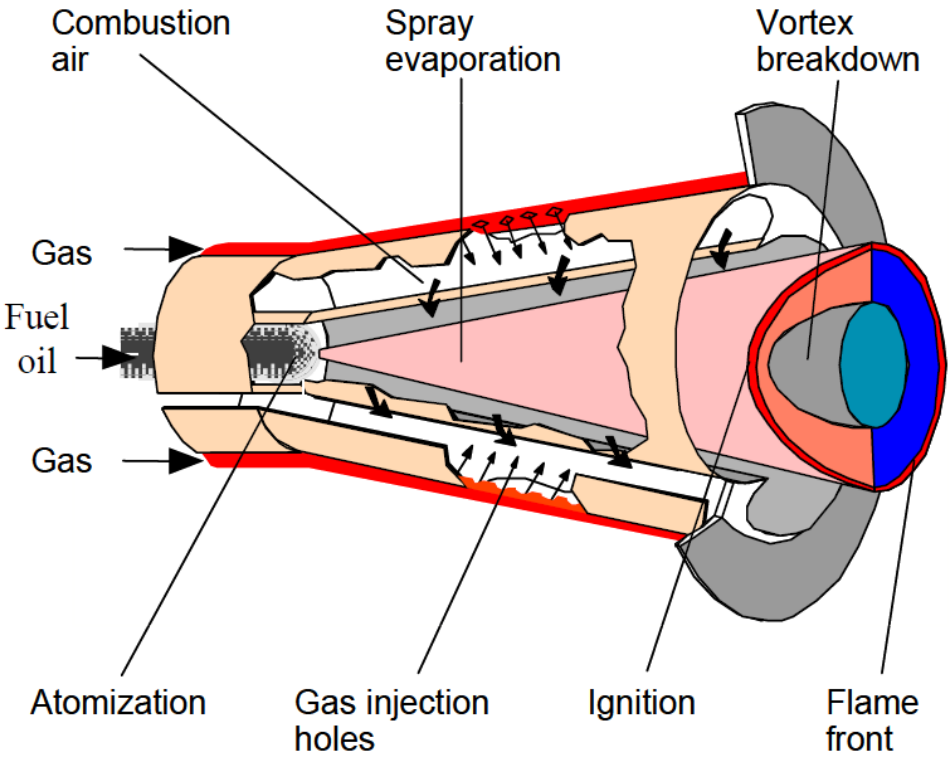

Figure 13. EV burner by Alstom; Reprinted from Döbbeling et al. [9].

Following the introduction of sequential combustion into Alstom gas turbines in 1990, a second EV burner called SEV burner was utilized after the first expansion process. In the SEV burner, carrier air which is extracted from compressor is used to enhance premixing and as an ignition controller [9].

One of the recently introduced concepts in gas turbine combustion is the Shockless Explosion Combustion (SEC). SEC, suggested by Bobusch et al. [28], intends to enable the approximate constant volume combustion (aCVC) in the gas turbine engine. In aCVC, combustion process takes place in constant volume instead of constant pressure which can theoretically lead to thermal efficiency improvement. Reichel et al. [29] performed an experimental investigation of an SEC system. SEC is based on a periodic combustion process which intends to create a lasting pressure wave inside a combustion tube. Combustion of the fuel-air mixture takes place in phase with the pressure wave raising the pressure at the tube inlet. After that, when the pressure at the tube inlet gets below the plenum pressure (suction wave), the tube is filled with the compressor air. After filling the tube with a small portion of pure air, fuel is injected into the tube to create a nearly homogeneous combustible mixture. The pure air packet is used to separate the fresh fuel-air mixture from the hot gases of the previous combustion cycle in order to prevent premature combustion. The entire packet of fresh fuel-air mixture undergoes a spatially quasi-homogeneous autoignition process due to the high temperature of the compressor air. In this process, the combustion takes place in a constant volume process with an increase in pressure and temperature. Because of the homogeneity of the ignition process,

no shock waves occur and the losses associated with a detonation wave are not present [29].

CHAPTER III

RESEARCH OBJECTIVES

III.1. General Outline

This study aims to design and simulate a complete UHEGT engine. This system includes a multistage compressor and a multistage combustion unit combined with a multistage turbine. To achieve the goals of this study, major phases are outlined as follows:

1- Design and simulation of a combustion system that is compatible with UHEGT requirements.
2- Cycle, flow path, and solid design for the UHEGT along with implementation of the combustion units.
3- Simulation and analysis of the turbine stages with stator internal combustion via CFD.
4- Simulation of the entire system performance at design, off-design and dynamic operation with GETRAN.

Each of these phases will be discussed in details in the following sections.

III.2. Major Study Phases

III.2.1. Phase I: Combustion System Requirements and Design Process

The main question in developing the UHEGT technology is: How to distribute the combustion process along multiple gas turbine stages in a practical way? The key to

answer this question lies in the design of combustors that can be implemented in the engine stator rows along multiple stages without creating structural problems. The appropriate fuel injectors would have some characteristics similar to the currently used fuel injectors in industry along with new features that makes them fit for our specific design. The main requirements for a combustion system for UHEGT are summarized as follows and will be discussed in further details in the next chapter:

1- Small volume occupation: one of the major goals of UHEGT is to combine the combustion process into the stator rows of the turbine stages. So, a UHEGT combustion unit must occupy as minimum volume as possible to make this integration possible.

2- Enable sequential combustion: the most important requirement for a UHEGT combustor is to provide the conditions for sequential combustion. The combustion units need to be designed in a way that they could be integrated into the turbine stator rows in multiple stages. This integration removes the combustion chamber as a separate unit and makes it possible for the reheat process to take place along the turbine stages.

3- Provide a stable combustion: combustion stability is one of the main features of any practical combustor. The unit needs to maintain the flame in high air speeds and a wide enough range of fuel/air ratios during the engine's full or part load performance.

4- Uniform temperature distribution at the rotor inlet: one of the most important factors determining the engine performance is the temperature uniformity at the

rotor entrance. A UHEGT combustion unit needs to provide a temperature distribution at the rotor inlet which is as uniform as possible.

5- Utilize inherent secondary flows in the channel: there are different patterns of secondary flows existent in the turbine channel flow path. A UHEGT combustion unit must be able to utilize these vortices in order to enhance the mixing between fuel and air particles.

6- Induce additional vortices: proper mixing between fuel and air particles is a very important factor in enabling a stable combustion. In order to achieve that goal, UHEGT fuel injectors must be able to induce additional vortices in the flow path. These vortices along with the inherent existent vortices in the flow channel, will help providing a stable combustion process in UHEGT.

7- Low pressure loss: combustor pressure loss is the main contributor to the total loss in a gas turbine engine. UHEGT has multiple combustion stages. Therefore, it is very important that the combustors are designed in way to minimize the pressure loss. This will help to achieve the highest possible efficiency from the engine.

8- Low pollutant emission: to comply with environmental standards, UHEGT combustors will have to achieve minimum levels of air pollutants (such as NOx and CO) emission. As discussed before, enabling a reheat system, bringing down flame peak temperature, bringing down TIT, and enabling proper mixing between fuel and air particles are some of the factors that can be utilized to achieve this goal.

9- Keep the high temperature away from the blade surfaces, shaft and casing: it is preferred in the integrated UHEGT combustion process, that the hot zone is kept away from the blade surfaces, shaft and casing as much as possible. This makes it easier for these areas to be cooled and also protects them against possible damage.

These parameters will be discussed in further details in section IV.1. Each of the factors discussed above need to be measured accurately and compared to modern day conventional gas turbine combustors in order to assess how well they satisfy the requirements. To achieve this goal, different types of 3D injector models will be designed. These models will then be implemented in a single stage turbine row that performs in conditions similar to UHEGT (the single stage turbine is designed based on the same principles as the complete UHEGT which will be discussed later). This unit is taken to grid generation and will be simulated with CFD. The CFD simulations will take place in real-time and include rotor motion and complete combustion modeling. The results of the CFD simulations will provide all of the necessary factors such as temperature distribution at rotor inlet, pressure loss, output emissions, and others. Based on the CFD results each design will be evaluated. Different types of combustion units will be simulated by this method and the results are compared to each other. Moreover, different modifications are applied to each model based on the strong and weak features that they demonstrate in the outcome. At the end of this phase of the project, a preliminary design for the fuel injectors has been obtained. This design satisfies the requirements of UHEGT, but it is also subject to further modifications as the complete system is simulated in the following phases.

III.2.2. Phase II: Turbine Cycle and Flow Path Design

Cycle design is the first step in designing the multistage turbine for UHEGT. The UHEGT cycle is based on the reheat principle which means subsequent combustion and expansion processes take place in the system. The turbine cycle determines all the major flow parameters (such as pressure, temperature, fuel/air ratio, etc) at each section of the machine. This cycle will be optimized by varying different parameters such as compressor pressure ratio, turbine inlet temperature, turbine stages pressure ratios, and others. The main objective of the optimization process is to achieve the cycle with the highest efficiency and power output which fits within the manufacturing and performance limits of UHEGT. Details of the cycle design process will be discussed in the next chapter. Based on the designed cycle, all of the turbine stage parameters are calculated. These parameters include mean diameter, blade heights, blade angles, stage load and flow coefficients, degree of reaction and others. By determining all of these parameters, the flow path through the turbine stages is determined.

After the flow path along the turbines stages is determined, the data is taken for solid design. The first step in this process is blade profiling. All of the stator and rotor blades are profiled based on the calculated inlet and outlet metal angles. Free vortex flow rule is applied to the blades for radial equilibrium and standard base profiles and chord to spacing ratios are used which are going to be further discussed in the next chapter. After the solid design and assembly is complete, it will be taken to mesh generation and CFD simulation.

III.2.3. Phase III: UHEGT Simulation and Analysis

At this point, UHEGT includes multiple turbine stages from which the first three or four of them have stator internal combustion. The following turbine stages will be used for further expansion to the atmospheric pressure. In order to make the CFD simulation feasible, only the high pressure turbine stages that include stator internal combustion will be modeled. The rest of the machine is similar to a conventional gas turbine engine, so it is not necessary to simulate that portion. Each combustion unit, stator row, and rotor row needs be meshed separately. After that, all of the units will be imported to the CFD simulation software (ANSYS CFX). A real-time unsteady simulation which includes rotor motions and full combustion modeling will be performed on the system. Velocity patterns, temperature distribution, pressure loss, pollutant emissions, and other parameters will be studied as a result of this multi-stage CFD simulation.

Based on the simulation results, the turbine blades and combustion units will be modified. These modifications include changing the shape, size, location, and arrangement of the combustors, changing fuel distribution patterns, modifying the flow path by changing the blade angles, number of the blades, etc. The temperature distribution over blade surfaces will be studied in this phase as well and appropriate strategies will be developed to control the blade surface temperature distribution.

III.2.4. Phase IV: Dynamic Simulation of the Engine

In this section, the entire UHEGT engine will be simulated using a time-dependent unsteady code (GETRAN) developed by Schobeiri and described in NASA reports [30]-

[32] and Schobeiri's text book [1]. As we know, a full four-dimensional space-time simulation of the gas turbine engine as a whole is not feasible at the current computational capacities. However, GETRAN enables us to perform a two-dimensional space-time simulation for the entire gas turbine engine in variable design and off-design conditions. These simulations help us to understand the engine response in dynamic operation in different conditions such as start-up, shut down, load change, variable fuel schedules, etc.

CHAPTER IV

DESIGN AND SIMULATION OF A SINGLE STAGE SAMPLE TURBINE WITH STATOR INTERNAL COMBUSTION

In this chapter, different configurations for the UHEGT combustion unit are designed and implemented in a single stage test turbine which performs at similar conditions as the first stage of a multistage UHEGT. The configurations are simulated via Computational Fluid Dynamics (CFD) and the results are investigated to develop the optimum combustion system for UHEGT.

IV.1. UHEGT Combustion System: Important Design Parameters

IV.1.1. Controlled Fuel and Air Mixing by Vortex Generation

In conventional combustion chambers, shown in Figure 14, majority of the compressed air (primary air) goes through a swirler vane and enters the relatively large combustion zone via a diffuser. The sudden expansion at the combustor inlet generates a primary vortex that facilitates the fuel and air mixing. Going through the mixing zone, secondary air is added and mixed with the combustion gas to accomplish a stable combustion [15].

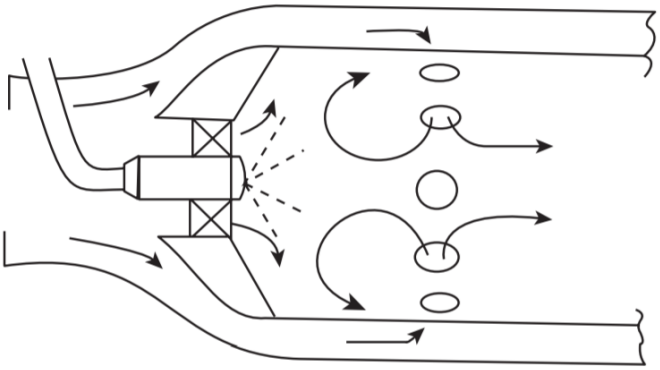

Figure 14. Conventional combustion chamber: Typical primary-zone configuration with inlet swirler; Reprinted from Lefebvre [33].

The mixture and dilution zones occupy a large portion of the combustor. Thornburg et al. [34] employed a fueled-cavity type flame holder in a turbine vane with an angled injection of air and fuel from the outer casing. His case and many similar cases were critically investigated by Schobeiri and Ghoreyshi [15], [16] using Navier-Stokes simulations; none of them delivered results that can be applied to gas turbine engines.

Inherent Vortices in Turbine: One of the essential features for properly mixing the fuel with the combustion air is the existence of vortices that are inherently present in a turbine. The flow through a turbine stage is highly turbulent and inherently unsteady due to the stator rotor interactions. Comprehensive studies by Schobeiri and his co-researchers among others [35]-[39] in the past twenty years show the significance of the effect of unsteady wakes, turbulence and inlet flow conditions on the turbine blade aerodynamics and heat transfer. At the hub and tip regions, the adjacent blades cause a system of vortices (horseshoe and passage vortices) that induce secondary flow. Furthermore, for unshrouded rotor blades, the pressure differences at the blade tip generate the tip clearance vortices. It

should also be noted that the type of flow field with lean flames is only marginally influenced by the flame compared to the case without reaction [40]-[42]. In other words, the existence of the flame in the flow domain, does not fundamentally change the flow patterns.

Additional Vortex Generation: As mentioned before, swirl flow associated with vortex breakdown is one of the most effective ways to induce flow recirculation. Vortex breakdown can be defined as a change in the structure of a vortex initiated by variation of tangential to axial velocity ratio [43], [44]. It causes flow recirculation in the core region of the combustor which moves the combustion products upstream to better mix with the incoming air and fuel [33]. Vortex breakdown, its physics, stability, and its application in combustor design are reported in the papers by Keller et al. [45], Schobeiri [35] and Keller et al. [46], as well as its other characteristics in [47], [48]. Gupta et al. [49] thoroughly reviewed swirl flows, their characteristics, and their applications in flame stabilization in their book 'Swirl Flows'. Lucca-Negro and O'Doherty [44] reviewed studies undertaken on vortex breakdown in the second half of 20th century. Anacleto et al. [50] performed an experimental investigation on swirl flow and flame structure in a lean premixed combustor. They investigated the effects of different parameters such as swirl number (as defined by Beer and Chigier [51]) on flame stability and pollutant emission in a model combustion chamber. Duwig et al. [52] numerically and experimentally studied flow dynamics and flame structure in a swirling partially premixed operation on a simplified model combustor. Galley et al. [53] performed a similar experimental study on a model combustion chamber. Wurm et al. [54], [55] investigated the impact of swirl flow on

combustor liner cooling performance. They performed their experiments on a model test section in which the interaction between swirl flow and coolant flow is studied. Beard et al. [56] performed an experimental and numerical study on the effects of combustor swirl on a high pressure turbine efficiency. Their results show that there can be about 1% efficiency drop due to combustor swirl, but it could be recovered by appropriate design. Agbonzikilo et al. [10] studied fuel injection into a radial swirler of a Dry Low Emission (DLE) gas turbine combustor using experimental and numerical simulations. They concluded that fuel injection into the suction side of the radial swirler slot will enhance the mixing of fuel and air due to lower pressure and secondary flows near the suction side.

IV.1.2. Flame Stability

One of the major requirements for a gas turbine combustor is to maintain the combustion process over a wide range of operating conditions. The good stability performance of a combustor can be described in two ways: either by the range of fuel/air ratio that provides a stable combustion or the maximum air velocity that the system can tolerate without flame extinction [33]. In other words, if the combustor can handle a larger range of fuel/air ratio or higher speed of combustion air without losing the flame, it has a better stability performance.

Among different approaches to stabilize the flame, bluff-body stabilization is often used as an effective method in variable combustion systems. A Bluff-body flame holder can be defined as a geometrical obstacle placed in the path of the reactive mixture; introducing turbulence, secondary flows, and low speed recirculation zones into the domain [33], [57].

They enhance flame stability and are especially practical in flowing combustible mixtures. Some of their applications include afterburners of ramjet and turbojet systems and supplementary firing in industrial boilers and heat recovery steam generators [57]. Many researches have studied the effects of different parameters on flame stability in a bluff-body stabilized combustion. Lefebvre and his coworkers [58], [59] have provided equations for predicting stability limits in terms of bluff-body dimension, blockage ratio, pressure, temperature, velocity and other parameters. Figure 15 a-d shows the effects of different parameters on flame stability based on the experimental studies by Lefebvre and his coworkers [60]-[62]. The vertical axes on these figures represent the weak extinction limit which is defined as the minimum equivalence ratio required to enable a stable combustion. Thus, a lower weak extinction limit means a higher stability range for the flame. Equivalence ratio, φ, is defined as the mixture fuel/air ratio divided by the stoichiometric fuel/air ratio for each type of fuel. Different independent affecting parameters are presented on the horizontal axes as well. As shown in Figure 15 and based on Lefebvre's conclusion [33], following parameters can improve the stability performance of a combustion system:

1. Higher gas pressure
2. Higher gas temperature
3. Lower Mach number
4. Lower turbulence intensity
5. Equivalence ratio close to unity
6. Higher flameholder size and lower blockage

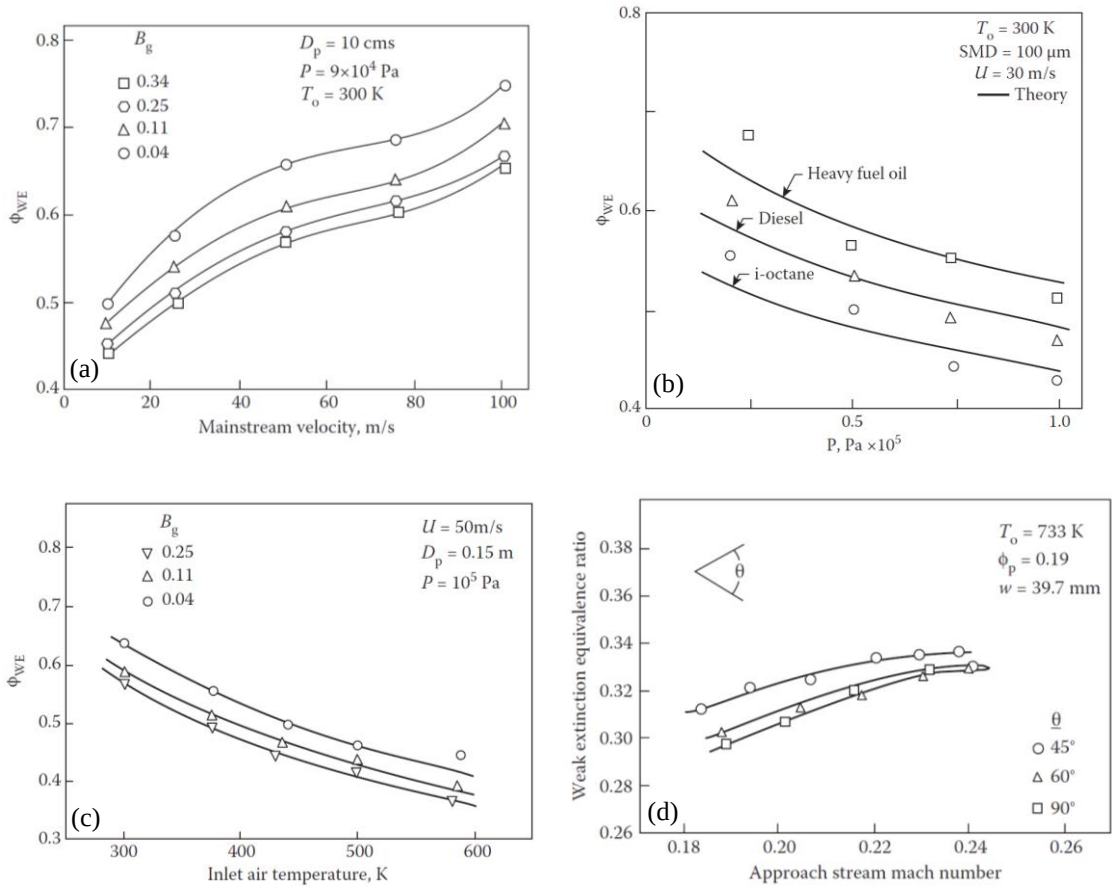

Figure 15. Effects of different parameters on weak extinction limit in a bluff-body stabilized flame using liquid fuel sources: (a) Effect of mainstream velocity, (b) effect of air pressure, (c) effect of inlet flow temperature, (d) effect of approach stream Mach number. Φ_{WE} is weak extinction equivalence ratio, B_G and θ are the flame holder blockage and angle, respectively; Reprinted from Refs. [60]-[62].

The issue of stability becomes less critical in industrial gas turbines as the pressure and temperature values are higher in these systems. Moreover, using gaseous fuels increases the stability performance as fuel drop size, atomization, and two phase flows will not be an issue anymore [33].

IV.1.3. Temperature Distribution at Rotor Inlet

The effects of non-uniform temperature distribution after combustion chamber on the engine performance have been investigated by many authors [63]-[68]. One of the effects of temperature non-uniformity at the turbine inlet is the reduction in efficiency and power production of the rotor row. That is a result of non-uniform distribution of high-enthalpy flow over the rotor blades which prevents full extraction of power from the combustion gas by the blades [15]. Furthermore, turbine inlet temperature distortions or so-called hot-streaks can cause flow unsteadiness and adversely affect the engine performance [66]. Increase in the blade thermal load, overheating, and thermal fatigue are other consequences of non-uniform temperature distribution at the rotor inlet [65], [69]-[73]. There have also been studies in blade stress analysis which take the effects of blade temperature distribution into account (Jafari et al. [74], [75]). Moreover, a uniform temperature distribution can reduce hot spots and bring down the NO_x emissions. It is also worth mentioning that temperature non-uniformities will not have a sever adverse effect on the stator row. That is because the guide vanes are stationary and no power extraction takes place in the stator. Therefore, the design should mainly focus on achieving a uniform temperature distribution at the rotor inlet.

IV.2. Single Stage Turbine Design

Table 1 shows different parameters for the single stage test turbine used in this chapter for all the numerical investigations. The stage is designed to have a swirl-free flow at the inlet and exit planes.

Table 1. Single-stage turbine parameters

Parameter	Value
Inlet total pressure	$P_{in} = 35\ bar$
Inlet total temperature	$T_{in} = 887.2$ K
Turbine inlet temperature	$TIT \approx 1250$ K
Total mass flow	$\dot{m} = 76.3\ kg/s$
Fuel mass flow	$\dot{m}_f = 0.61\ kg/s$
Mean diameter	$D_m = 500\ mm$
Blade number	$N = 36$
Blade height	$H = 50\ mm$
Blade chord	$C = 76\ mm$
Degree of reaction	$R = 0.5$
Stagger angle	$\gamma = 45°$
Blade inlet metal angle	$\beta_1 = 90°$
Blade exit metal angle	$\beta_2 = 19.7°$

Figure 16 shows the static pressure coefficient distribution for the stator blade which is defined as,

$$C_P = \frac{P - P_{stag}}{1/2\rho V^2} \tag{4.1}$$

The blade profile shown in this figure remains constant from hub to tip for both stator and rotor rows.

IV.3. Injector Design and Geometry

Different configurations are designed for UHEGT combustion system at this stage. These configurations integrate the combustion unit with the stator row of the single-stage turbine described before. The main requirements for UHEGT combustion units are described in section III.2.1. The designs are mostly based on the concept of bluff-body flame holders as explained in section IV.1.2. The introduced UHEGT combustion units or *Fuel Injectors*

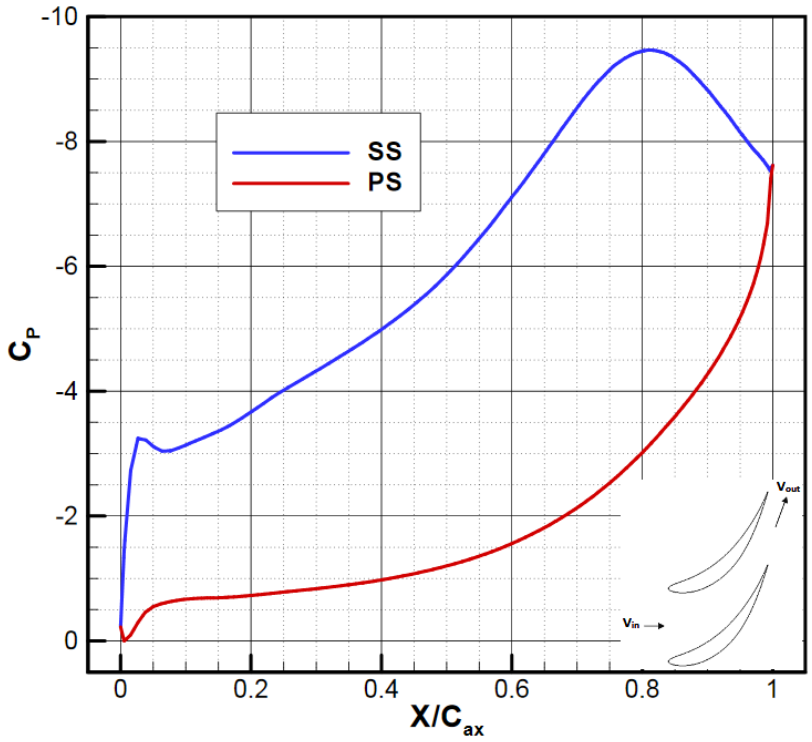

Figure 16. Pressure coefficient distribution along suction and pressure surfaces for the single-stage turbine stator blade.

takes advantage of the inherent secondary flow vortices inside the turbine blade channel which will be enhanced by vortex filaments generated by a number of integrated vortex generator fuel nozzles. Three of the main injector configurations are discussed in details in the following sections.

IV.3.1. Injector Configuration 1

In this configuration, gaseous fuel is injected from cylindrical tubes extended from hub to shroud, shown in Figure 17.

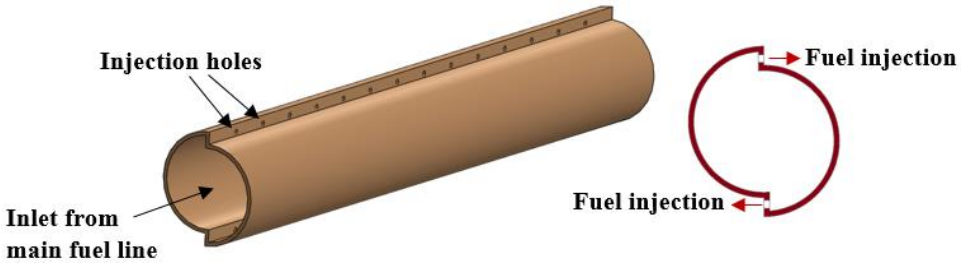

Figure 17. Injector configuration 1: cylindrical fuel injectors extended from hub to shroud.

Fuel enters the tube from the main fuel line located on the casing and it is injected into the domain through small injection holes on the top and bottom. In the current design, the sizes of the injection holes are the same, but they can also vary in size to allow different fuel-air ratios at different radial locations. Figure 18 shows the numerical domain for this geometry. Periodic boundary conditions are utilized in order to reduce the size of computational domain by simulating only one blade from each row. In this configuration, flow over cylinders creates Von Karman vortices along with Coanda effect. The interact-

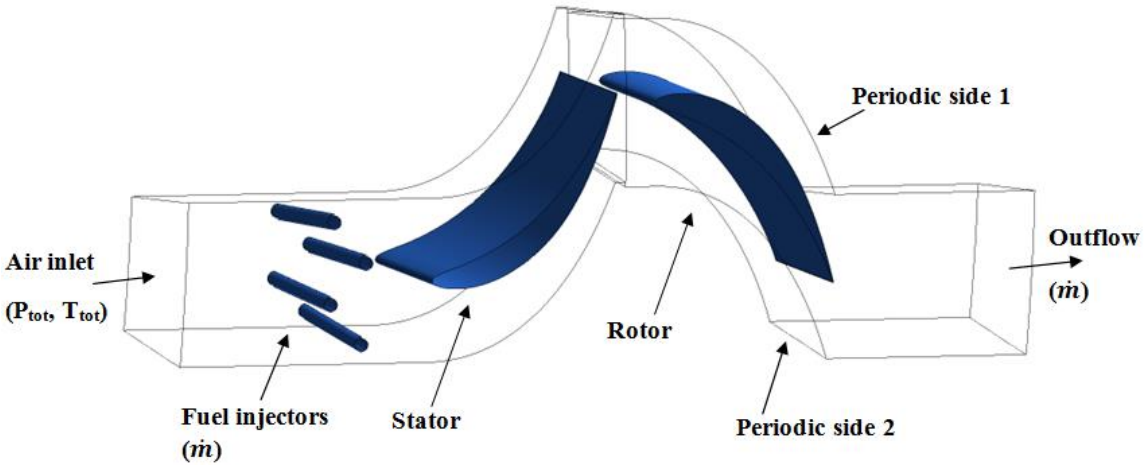

Figure 18. Injector configuration 1: computational domain.

ion of Von Karman vortices and the Coanda effect causes the fuel particle to stay longer in vortical motion to facilitate better mixing with the compressed air and enhance flame stability.

Figure 19 shows a sample single-stage turbine with current configuration. As shown in this figure and Figure 18, two rows of fuel injectors are located before the stator row. These injector rows are staggered compared to each other in order to bring down the flow blockage and pressure loss while enhancing the mixing between fuel and air particles and temperature uniformity.

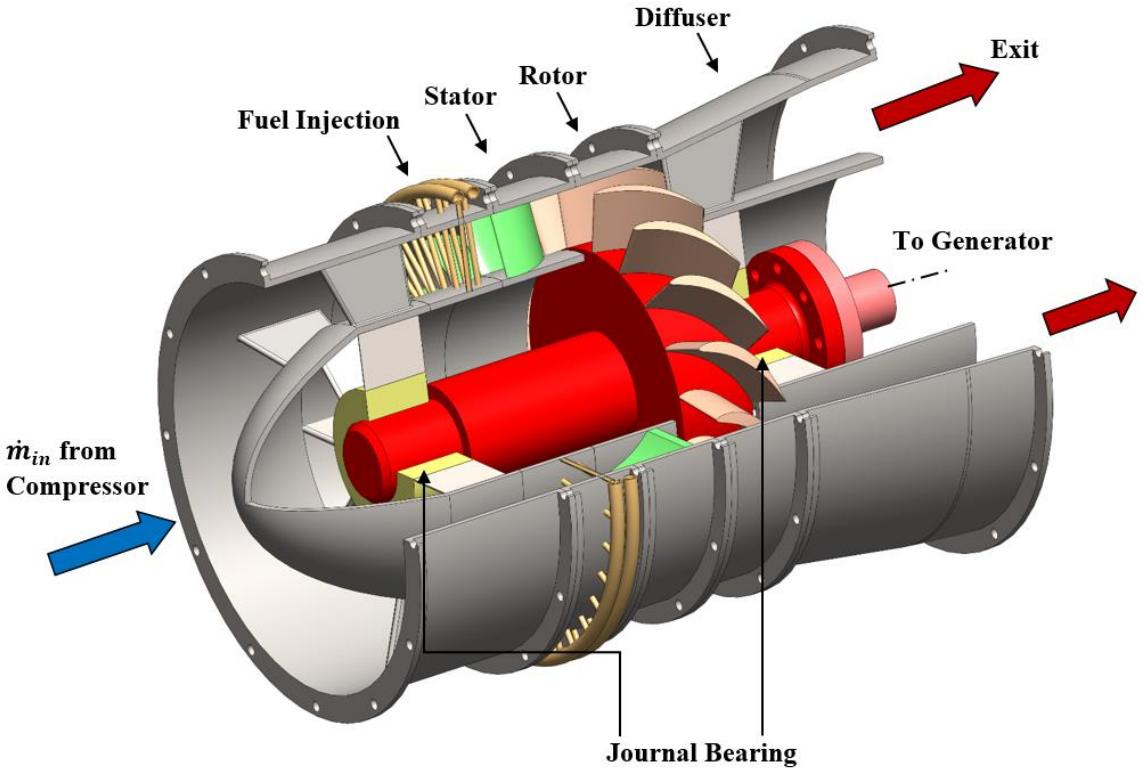

Figure 19. Single-stage sample turbine with injector configuration 1.

IV.3.2. Injector Configuration 2

In this configuration a new type of stator blade is utilized to enable the combustion process inside the blade. The corresponding blade is designed by Schobeiri and his co-workers [76] in order to reduce the incidence losses associated with strong off-design operations. This design presents an appropriate space for implementation of injectors inside the blade. As shown in Figure 20, the blade is hollowed for the purpose of creating the space for combustion. The leading edge of the blade is opened in order to take in the incoming air into the blade. The cross section increases in this area to produce a diffuser effect. Two half cylinders facing each other are placed inside the hollow blade. The fuel

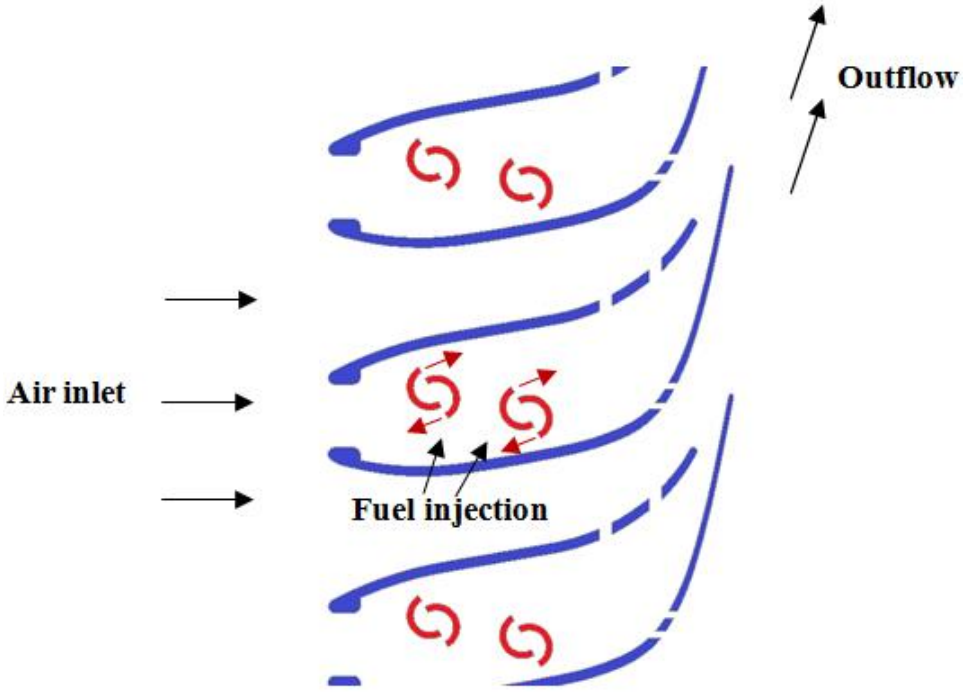

Figure 20. Injector configuration 2: cylindrical fuel injectors implemented inside the stator blades.

is injected into the half cylinder body and exits from the cutting surface into the flow domain. Multiple slots are opened on suction and pressure surfaces as well as the blade trailing edge. The hot gas mixture exits from those slots and flows toward the rotor.

IV.3.3. Injector Configuration 3

In this configuration, axial swirlers are designed for vortex generation as shown in Figure 21. The vane profiles are based on a Bezier curve with inlet and exit angle of 90 and 45 degrees, respectively. In the single layer vortex generator shown in Figure 21a, the vanes are scaled from hub to tip to maintain a constant chord to spacing ratio. Figure 21b shows a multilayer vortex generator which can be used to achieve different swirl numbers at different radial locations. The fuel is injected in the center of the vortex generator through a gaseous fuel injector as shown in Figure 21c.

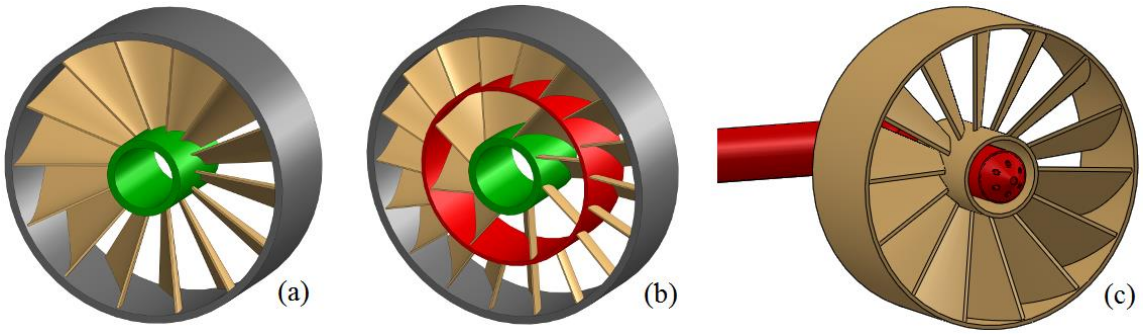

Figure 21. Injector configuration 3: (a) single layer and (b) multilayer vortex generators; (c) gaseous fuel injector in the center of the swirler.

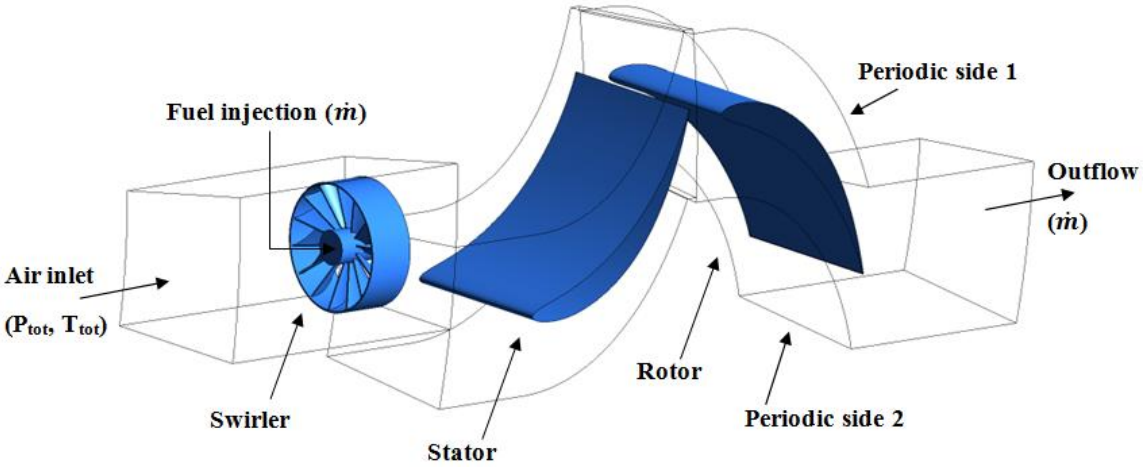

Figure 22. Injector configuration 3: computational domain.

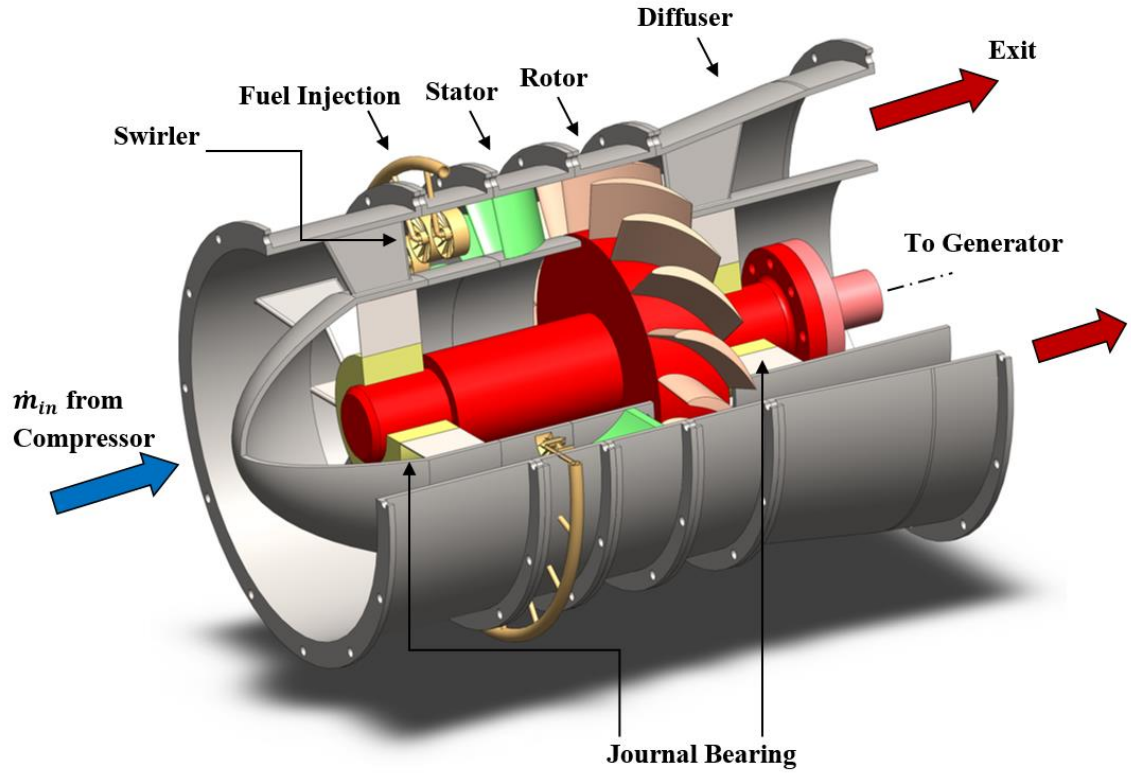

Figure 23. Single-stage sample turbine with injector configuration 3.

Figure 22 shows the numerical domain for this configuration. In this design swirlers are placed right before the stator blades injecting fuel and air into the blade channels. The swirler is positioned in the middle of two adjacent blades, thus minimizing direct interaction between the flame and stator blades. Figure 23 shows a sample single-stage turbine with the current configuration.

IV.4. Mesh Generation

The grids are generated using the commercial software ANSYS ICEM CFD 17.1. Each stator, rotor, or injector component is treated as a separate unit in the grid generation process. For the stator and rotor units, fully structured hexahedral grids are generated as shown in Figure 24a. They incorporate boundary layer (BL) grids near the blade and hub and shroud surfaces. BL grids near the blade leading and trailing edges are shown in Figure 24b and Figure 24c, respectively. Based on the utilized turbulence model (SST) and the mainstream Reynolds number (*RE=2.8E6*), the corresponding y+ value of the first boundary layer node is kept in the order of 1 over all of the blade surfaces. Inside the boundary layers, between 16 to 22 nodes are distributed with a growth factor of 1.1 to 1.2. For the injector components, a tetrahedral grid with hexa core is generated as shown in Figure 24d. In this type of grid, fine tetrahedral elements are generated near the injector surfaces and domain boundaries, and they are combined with a hexahedral grid in the main domain. Meshing strategy and parameters are based on many previous studies [77]-[87].

A grid study is performed on the single stage turbine with injector configuration type 1 to evaluate grid independency of the simulation results. The grid is refined until the

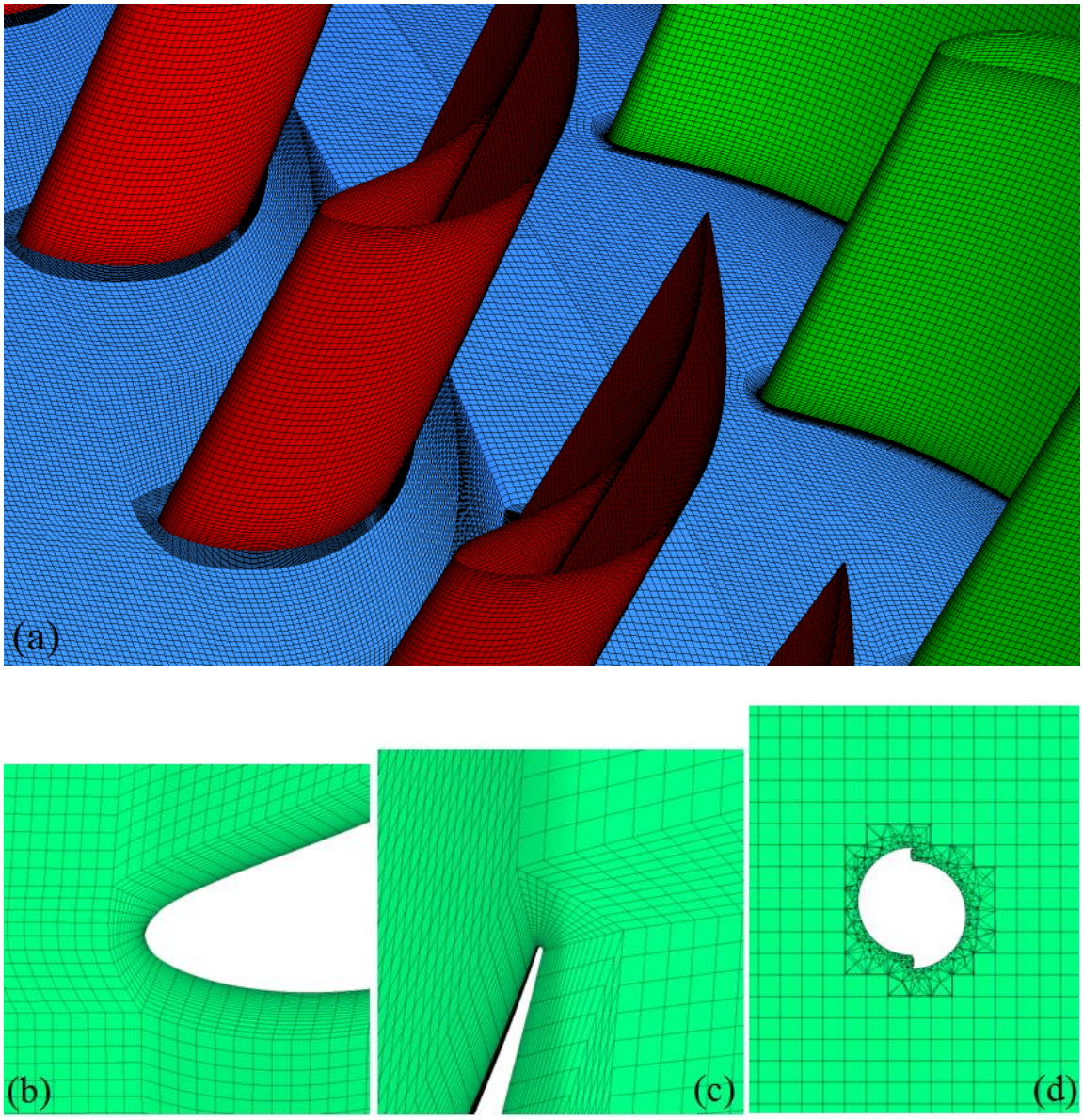

Figure 24. Computational grid: (a) structured hexahedral grid over the blade components, (b) boundary layer grid near the blade leading edge, (c) boundary layer grid near the blade trailing edge, (d) tetrahedral elements near the injector surface combined with hexahedral grid in the main domain.

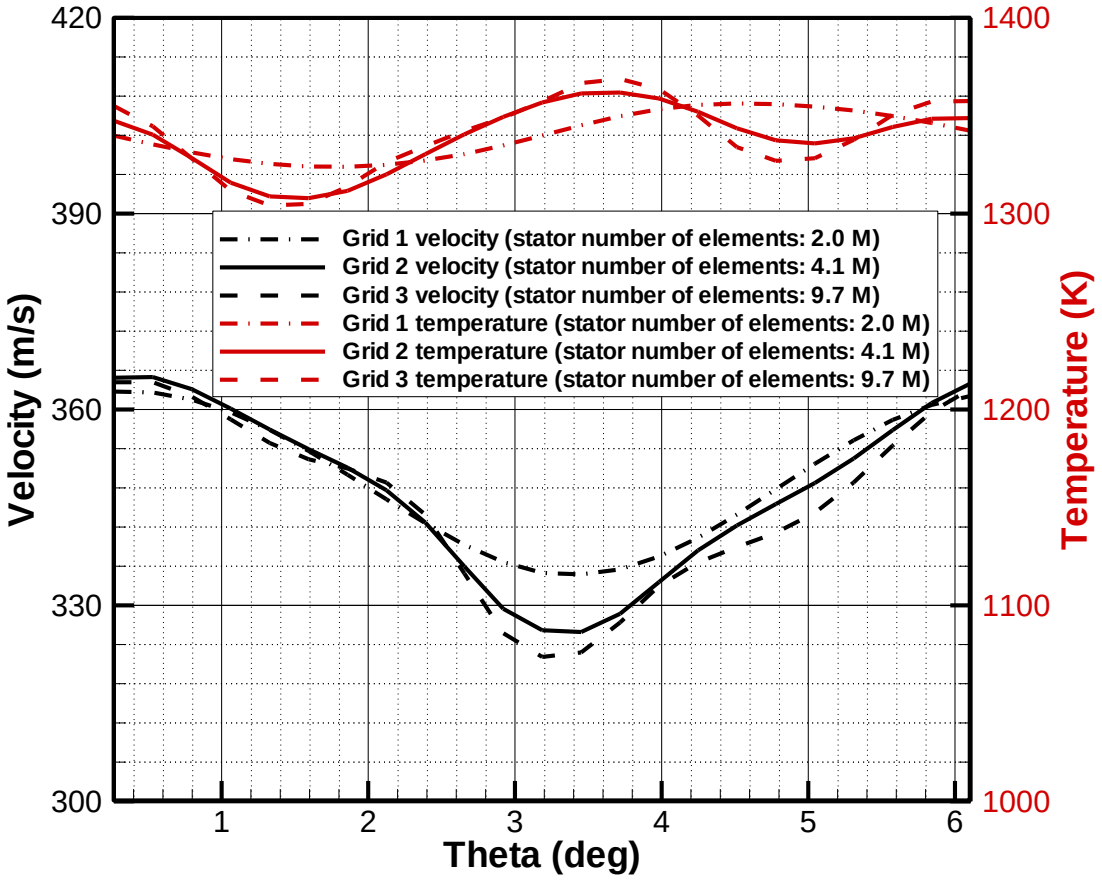

Figure 25. Grid independence study results: velocity and temperature distribution on the midspan line at the exit of stator in configuration 1 for three different grid sizes.

velocity and temperature distributions at rotor inlet are almost independent from the grid size. Figure 25 shows the velocity and temperature distributions on the mid-span line at the rotor inlet for three different grid sizes. The corresponding number of elements for the stator component in each grid is shown in the figure. According to the results, grid size 2 can properly capture the *Mountains* and *Valleys* in velocity and temperature profiles. Moreover, the maximum difference between the results of grids 2 and 3 is less than 0.5% which is acceptable for the purposes of the current simulations. Therefore, considering

accuracy and the cost of calculation, grid size 2 has been selected for all simulations in this study. Total number of elements for a single stage simulation (including inlet extension, injectors, stator, and rotor) in configuration 1 is 12.2 M.

IV.5. Numerical Method and Boundary Conditions

ANSYS CFX 17.1 is used for the CFD simulations. As mentioned before, periodic boundary conditions are used to reduce the size of the computational domain. Rotational periodic boundary condition around the turbine axis of rotation simulates a complete row of blades for each component. In order to establish the unsteady simulation, a steady solution with frozen rotor interface between the stator and rotor components is used as the initial guess. In frozen rotor, the frame of reference is changed but the relative orientation of the components across the interface is fixed [88]. The interfaces are changed to Transient Rotor Stator as the unsteady solution is started. In this approach, the transient relative motion between the sliding components on each side of the connection is simulated. It accounts for all interaction effects between the components that are in relative motion with regards to each other, i.e. stators and rotors. The interface position is updated at each timestep, as the relative position of the grids on each side of the interface changes [88]. The interface between the stationary components such as injectors and stator is a general connection with no change in relative frame positions. For the boundary conditions, total pressure and total temperature are specified at the inlet along with the mass flow rate at the exit. Hub, shroud, blade, and injector surfaces are assumed as no slip adiabatic walls.

The fuel, methane (CH_4), is injected in each injector as an ideal gas with the mass flow rates mentioned before. The solution is performed for an ideal gas reacting mixture of air and methane. The combustion is simulated based on the Eddy Dissipation Model (EDM). This turbulence-chemistry interaction model is based on the work of Magnussen and Hjertager [89]. The Eddy Dissipation model tracks each individual chemical species with its own transport equation and is very suitable for fast combustion modeling. This model is flexible in that new materials, such as additional fuels, can be added to the simulation without complications [88].

For the turbulence simulation, the shear stress transport (SST) k-ω model is utilized along with automatic wall function. This model is based on the turbulent viscosity proposed by Menter [90] which adds a cross diffusion term in the ω-equation. In many cases, SST model shows a better performance compared to the standard k-ε model [91]. For the energy equation, the total energy model is utilized which accounts for the kinetic energy effects in the equation. These effects are significant in the current flow conditions which represent a compressible flow with high Mach number. For numerical discretization of the momentum and energy equations, the CFX advection scheme of High Resolution is used along with an automatic timescale. The high resolution scheme uses a blend factor to combine the first and second order advection schemes. The blend factor values vary throughout the domain based on the local solution field [88]. Each solution cycle is defined by the third stage rotor blade passing through 1 pitch and it is divided into 20 timesteps. The convergence criteria require the global root mean square residuals for momentum and energy equations to reach values below 10^{-5}. The unsteady solution initiates upon the

results of the steady solution and it runs for multiple cycles before the final results are exported.

IV.6. Results and Discussion

In this section the results of the main three injector configurations are studied and compared to each other to select the optimum configuration for UHEGT. The single stage turbine (previously described in this chapter) exhibits the main test platform for all CFD investigations presented bellow in conjunction with the geometry optimization of various injectors.

IV.6.1. Injector Configuration 1

Figure 26 and Figure 27 show the computed mid-span velocity contours in the stationary frame and velocity vectors in the relative frame, respectively. As shown in Figure 27, fluid particles follow the metal angle with little deviation. It should be noted that the velocity vectors are shown in the relative frame for each component which is stationary for stator and rotating with the shaft rotational speed for rotor. That change in the frame of reference is why the vectors' direction suddenly change from stator to rotor.

Figure 28 shows the velocity vectors around the fuel injectors in which the Von Karman vortices and Coanda effect are observable. Fuel particles move forward and backward among these vortices, which helps them to further mix with air particles.

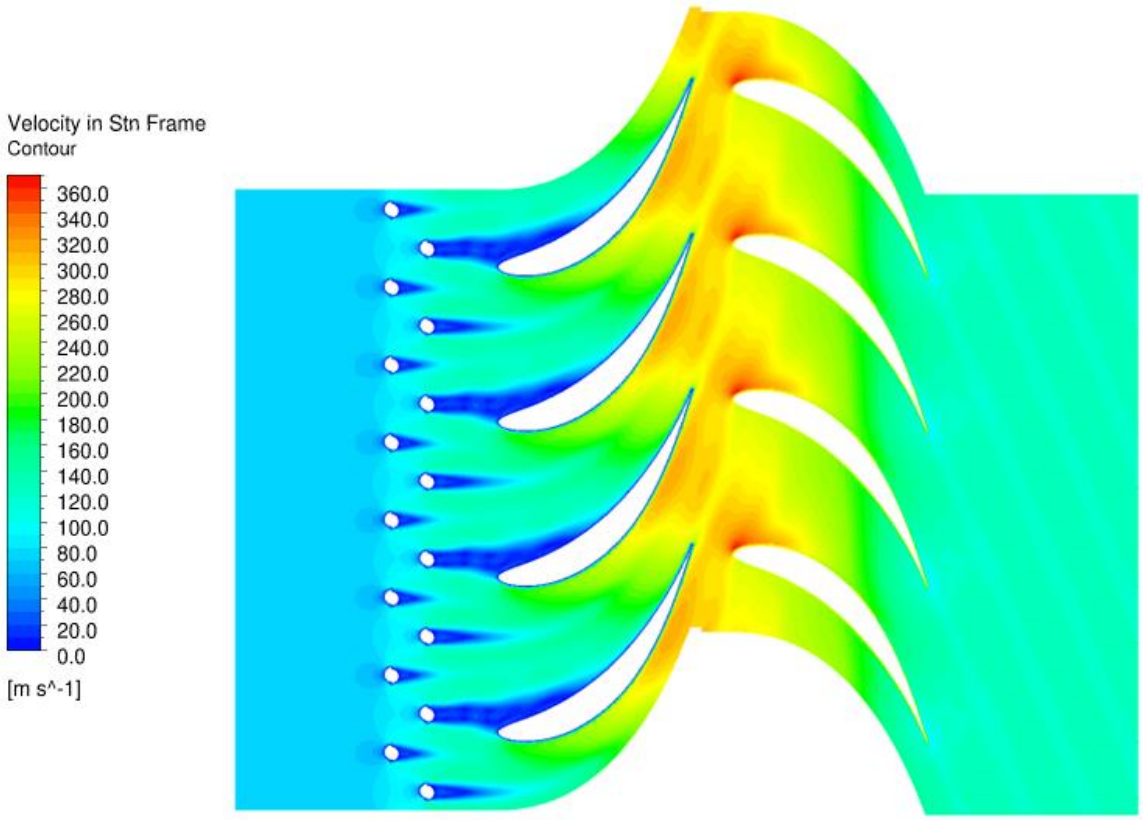

Figure 26. Injector configuration 1: Mid-span velocity distribution in stationary frame.

The amount of torque on each blade is 156.7 N.m and the total power is 6.1 MW. Figure 29 shows the resulted mid-span temperature distribution. As shown in this figure, most of the combustion process takes place before the stator and the temperature distribution at rotor is very uniform. Figure 30 and Figure 31 show the temperature distribution before and after stator and rotor blades and the temperature distribution at rotor inlet, respectively. As seen in these figures, the temperature distribution at the rotor inlet is relatively uniform. The Non-Uniformity Index defined as $(T_{max}-T_{min})/T_{ave}$ is equal to 9.2% at this cross section. The temperature gradient in radial direction shows that the temperature is slightly higher near the hub compared to the shroud. That is because of the

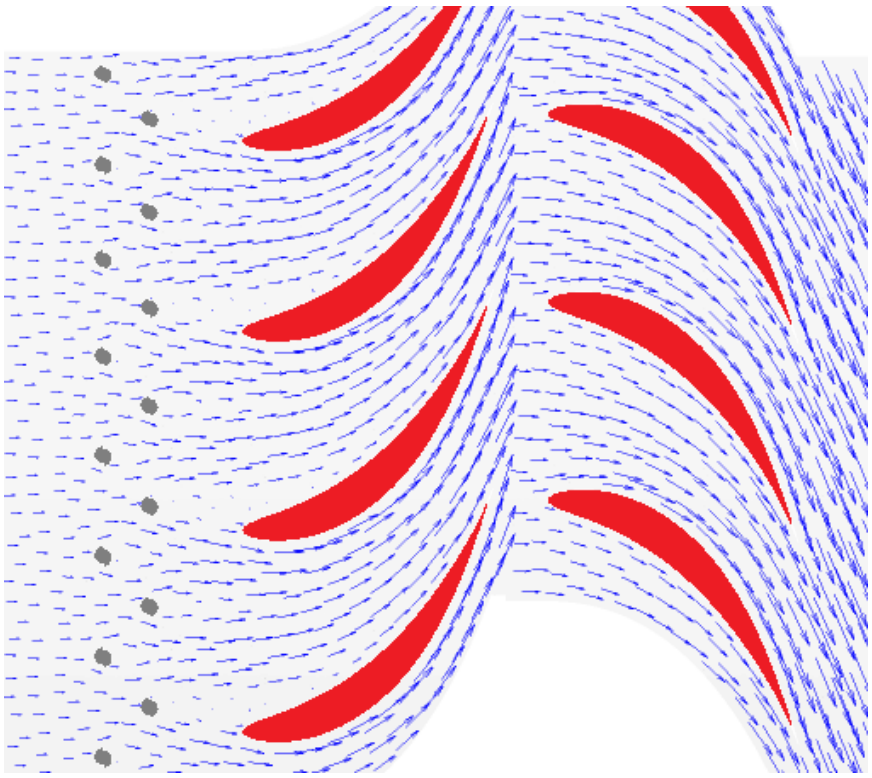

Figure 27. Injector configuration 1: Mid-span velocity vectors in relative frame.

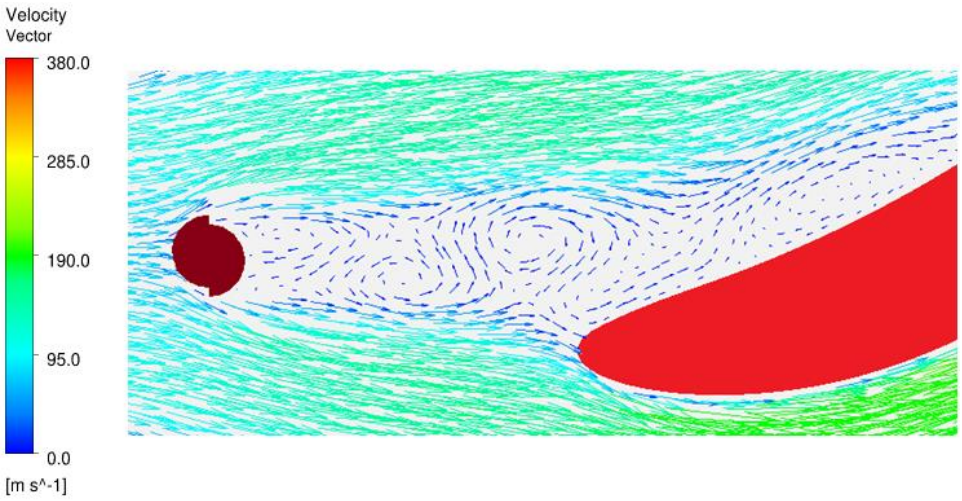

Figure 28. Injector configuration 1: Fuel injector, velocity vectors and Von-Karman vortices.

higher fuel concentration close to the hub due to the lower cross section area. It is noticeable that in rotor, as result of rotation and due to buoyancy effects, the higher density (lower temperature) fluid moves towards the shroud and vice versa. The buoyancy force is caused by centrifugal acceleration in rotor. The effect of this phenomenon can be clearly seen in the temperature contours after the rotor and it is approved by previous studies [69]. Moreover, adding a distance between the injection holes and the endwalls can help to protect them from the high flame temperature.

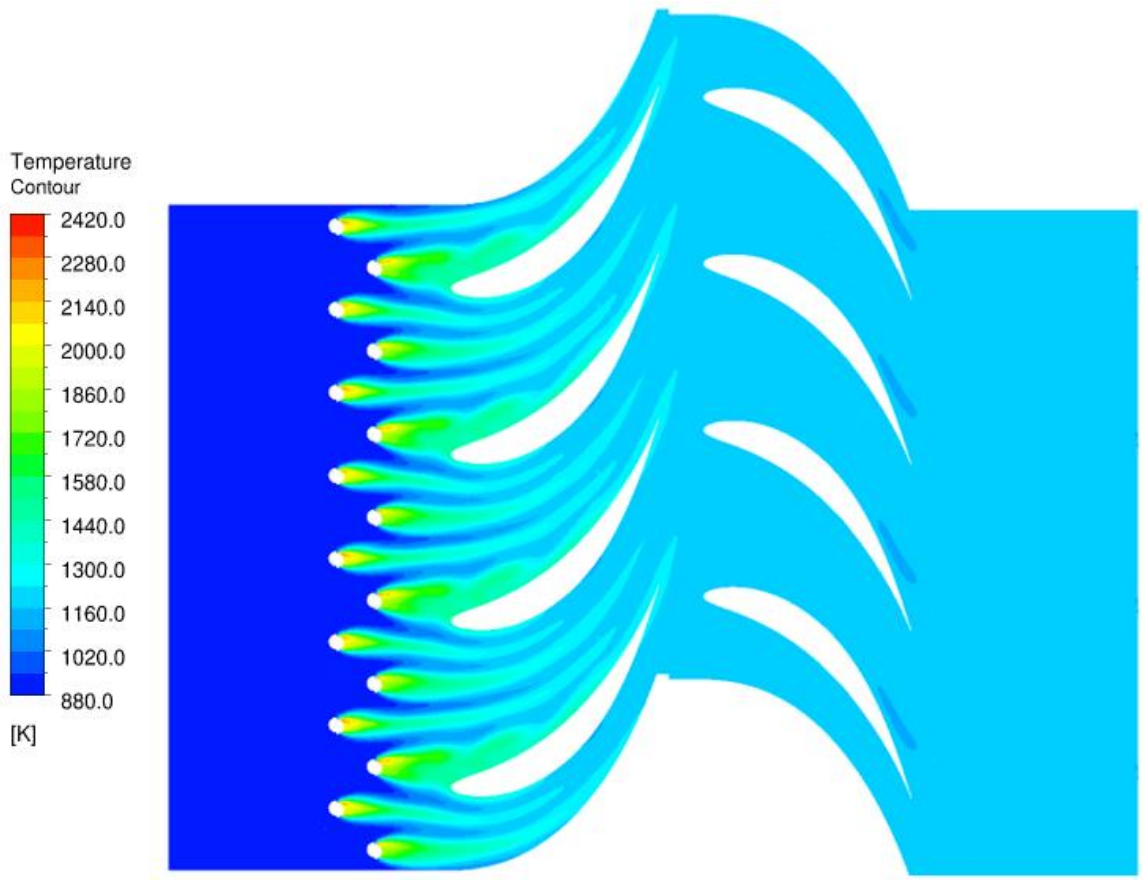

Figure 29. Injector configuration 1: Mid-span temperature distribution.

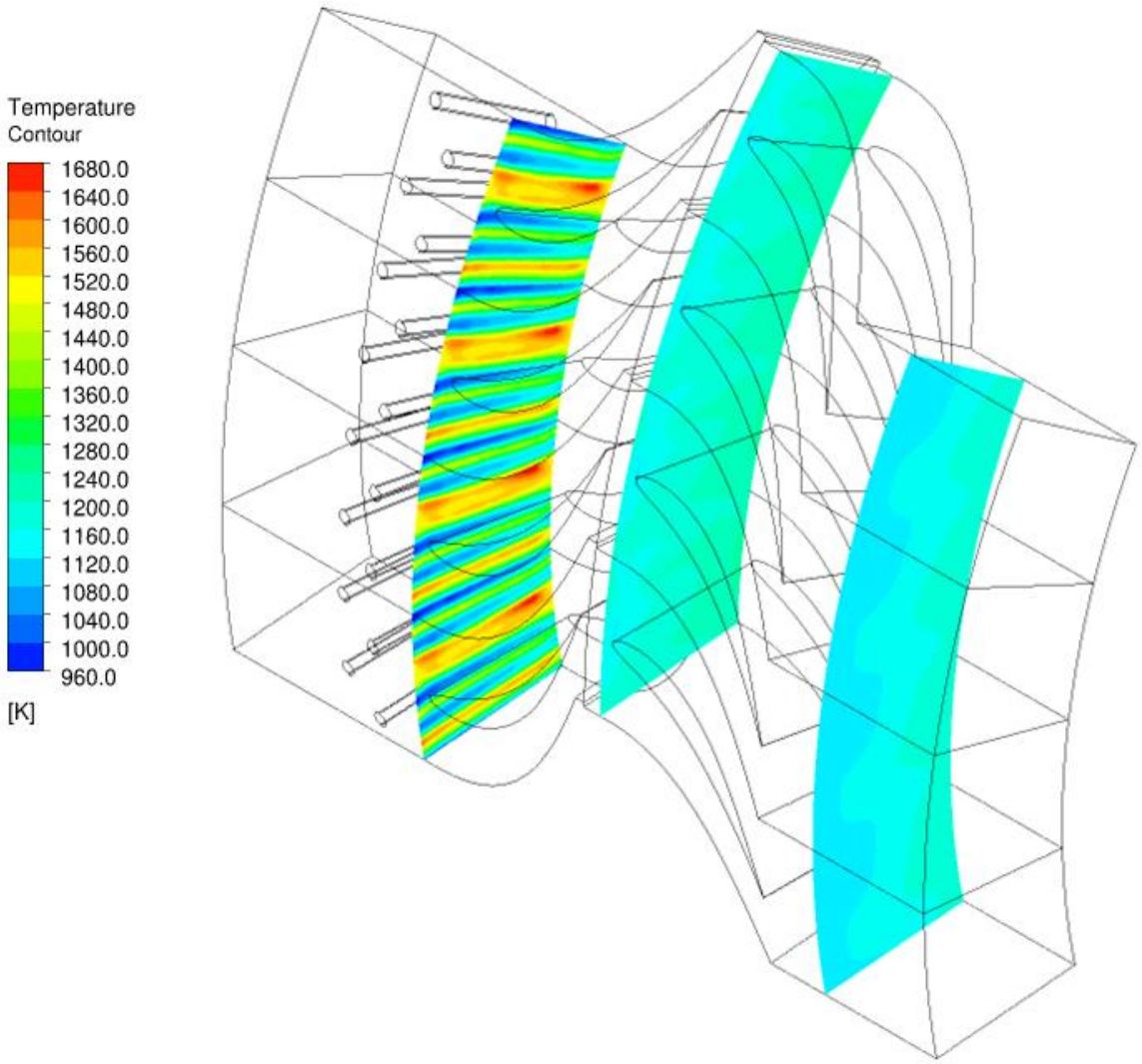

Figure 30. Injector configuration 1: Temperature distribution before and after stator and rotor.

Figure 32 shows the meridional temperature distribution. The temperature is averaged in circumferential direction and it is presented from hub to shroud and from inlet to outlet. As shown in this figure, maximum temperature is reached before the stator leading edge which means that most of the fuel is burned quickly after the injection.

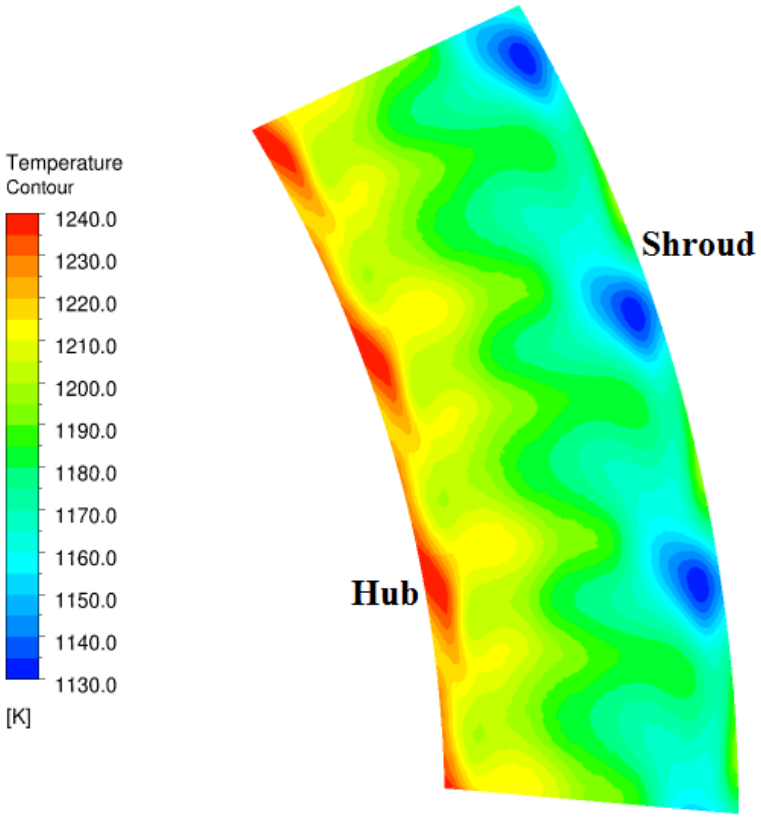

Figure 31. Injector configuration 1: Temperature distribution at the rotor inlet (Non-uniformity=9.2%).

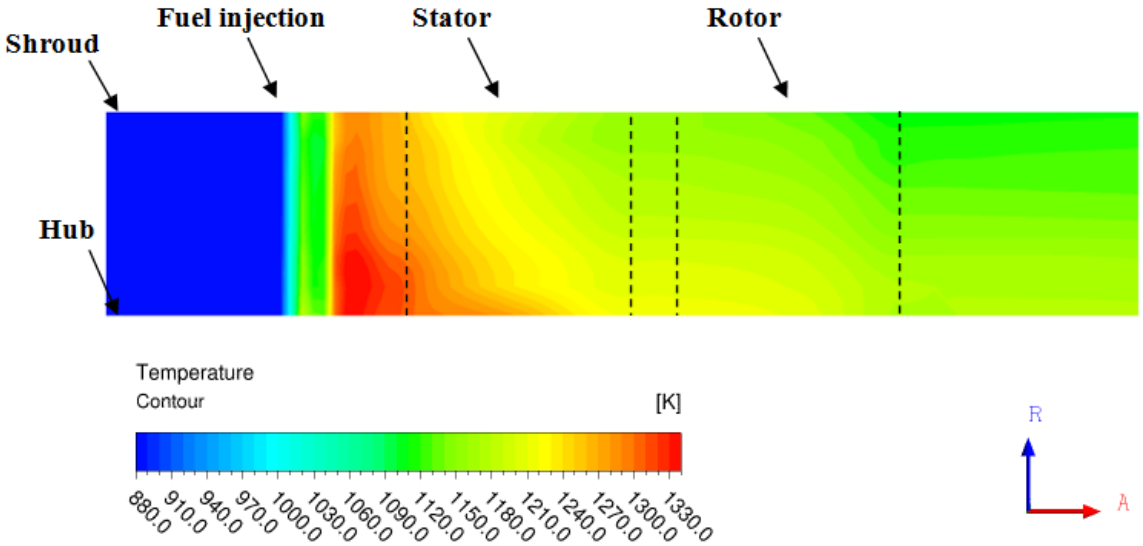

Figure 32. Injector configuration 1: Meridional temperature distribution.

Moreover, there is a temperature gradient in radial direction which shows a higher temperature near the hub. This is because of the lower cross section area close to the hub which causes higher fuel concentration, as mentioned before.

In order to overcome the temperature gradient in radial direction and improve temperature distribution at the rotor inlet, a modification is performed in the fuel injection pattern. In this method, fuel injection is linearly increased from hub to shroud to provide an injection pattern proportional to the corresponding radial location. This modification is applied via boundary conditions in the CFD simulation by defining variable inlet velocities on the fuel injection holes. In reality, this modification can be applied using variable sizes for the injection holes. Figure 33 and Figure 34 show the corresponding temperature distribution at the rotor inlet and meridional temperature distribution, respectively. As seen in Figure 33, the temperature distribution in radial direction is considerably improved by this modification. The Non-uniformity is reduced to 5.1% which is far below conventional combustion chambers which could have more than 40% non-uniformity at the rotor inlet [70], [71]. Figure 34 reveals that the temperature gradient in radial direction is almost eliminated and a consistent temperature distribution is observed from hub to shroud. It should be noted that the mid-span velocity and temperature distributions maintain a similar pattern before and after this modification.

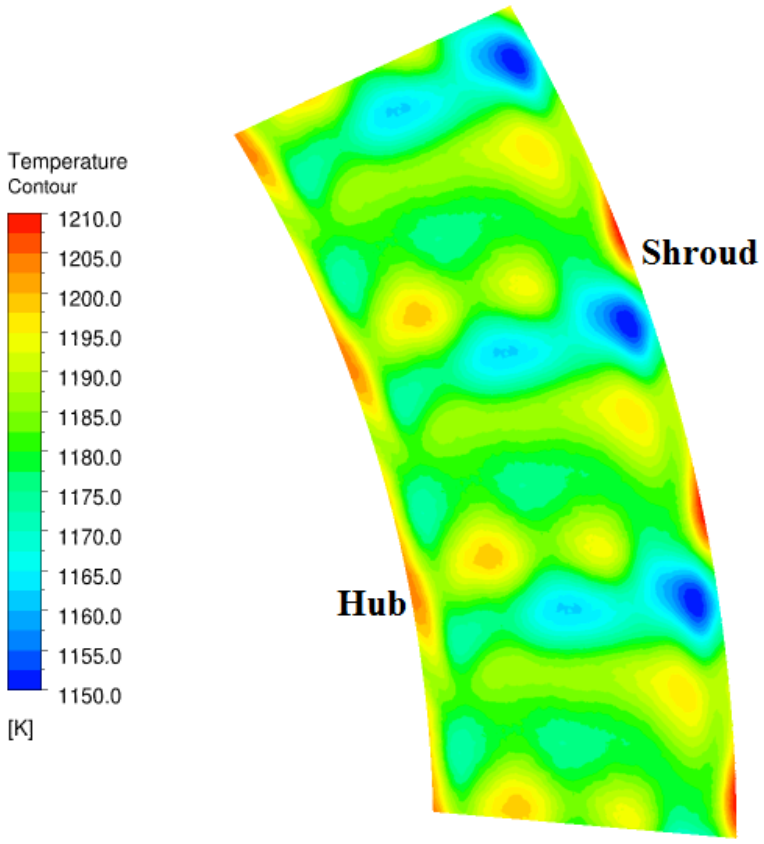

Figure 33. Modified injector configuration 1: Temperature distribution at the rotor inlet (Non-uniformity=5.1%).

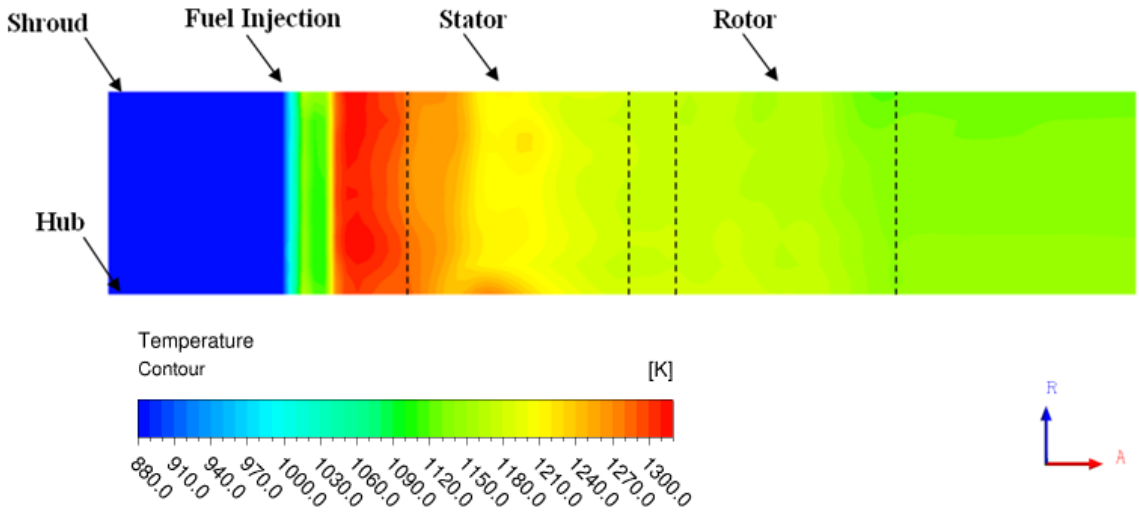

Figure 34. Modified injector configuration 1: Meridional temperature distribution.

Figure 35 and Figure 36 show the average temperature and average fuel mass fraction changes with regards to streamwise location from inlet to exit. As shown in Figure 35, temperature rises very fast after the fuel injection and reaches its maximum right before the stator leading edge. The temperature decreases along the stator due to increase in kinetic energy and it falls in rotor because of power extraction. Figure 36 shows the pattern of fuel burning which indicates most of the fuel particles are burned before the stator leading edge. It should be noted that since the combustion process is completed right after the fuel injection, the injectors could be moved further close to the stator leading edge to

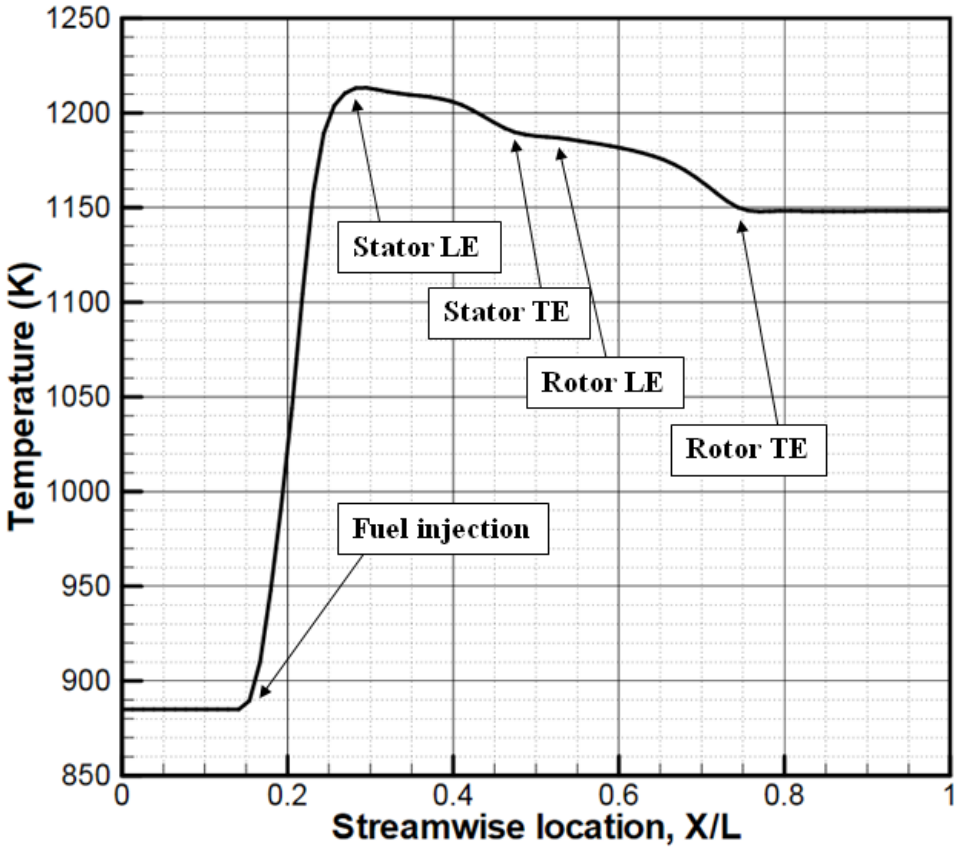

Figure 35. Injector configuration 1: Average temperature profile.

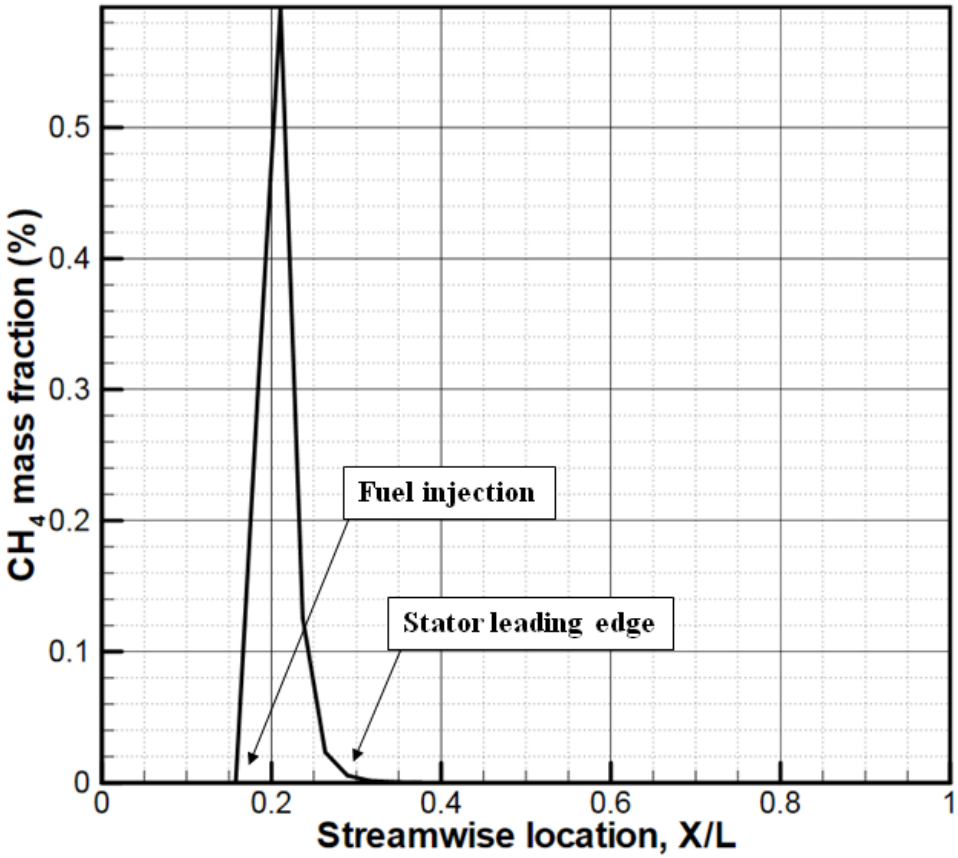

Figure 36. Injector configuration 1: Average fuel mass fraction profile.

make the engine more compact. However, the blade material temperature limits need to be taken into careful consideration.

Total pressure loss due to secondary flows and friction in the injector segment for this configuration is slightly higher than 1% which is quite suitable for a single-stage combustion unit. Moreover, NO_x emission at the stage outlet is 0.5 ppm which is totally acceptable based on the regulated standard emissions [92]. According to the results, this configuration provides a very suitable design option for UHEGT.

IV.6.2. Injector Configuration 2

An infinite blade height (2D) simulation is performed on the second configuration including the stator blade and fuel injectors to provide a general pattern of velocity and temperature distributions. Figure 37 and Figure 38 show the velocity vectors and temperature distribution inside the blade and around the injectors. As shown in Figure 37, the flow expands at the blade inlet due to an increase in cross section. This reduces the air velocity and makes it more appropriate for combustion [33]. Secondary flows are generated as the flow passes the injectors which helps the mixing between the combustion gas particles.

Figure 39 shows the temperature contours in the domain. As shown in this figure, the temperature distribution after the stator is not uniform. The high non-uniformity at stator outlet can adversely affect the turbine performance. In order to improve the temperature distribution at this area, two external injectors are added to the combination which is shown in Figure 40. This modification helps to achieve a more uniform temperature distribution at the exit.

This Figure 40 configuration provides a very compact space for combustion unit/stator combination and it can lead to small engine sizes. But, it needs to be noted that placing the injectors inside the blade creates a very high flame temperature near the blade internal surface, and also takes out the option for blade internal cooling. Therefore, at this point configuration 2 is not considered an optimum design option for UHEGT.

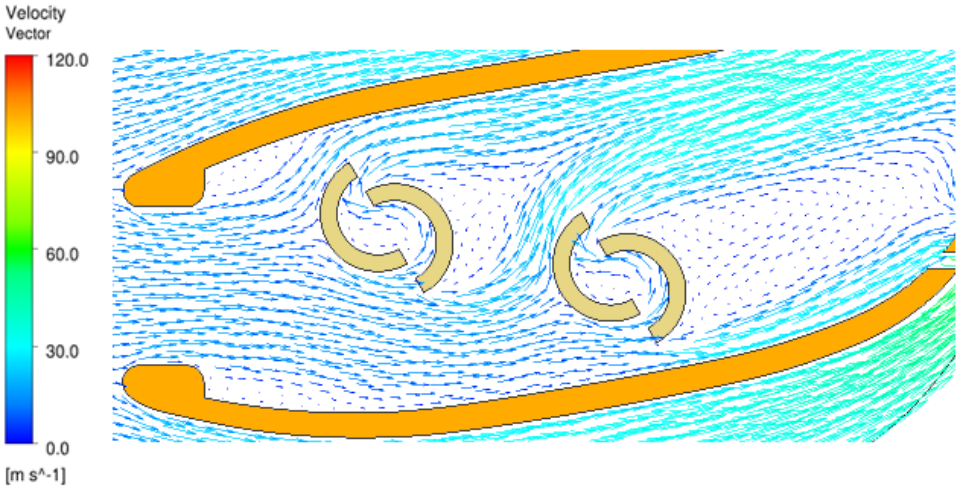

Figure 37. Injector configuration 2, blade inlet and fuel injectors: Velocity vectors.

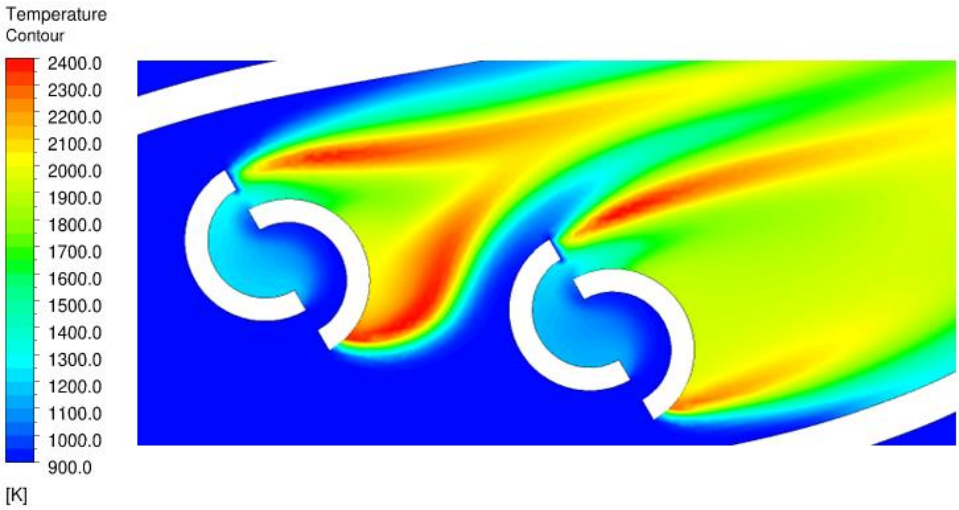

Figure 38. Injector configuration 2, fuel injectors: Temperature contours show the fuel ejection from the cutting surface into the flow field.

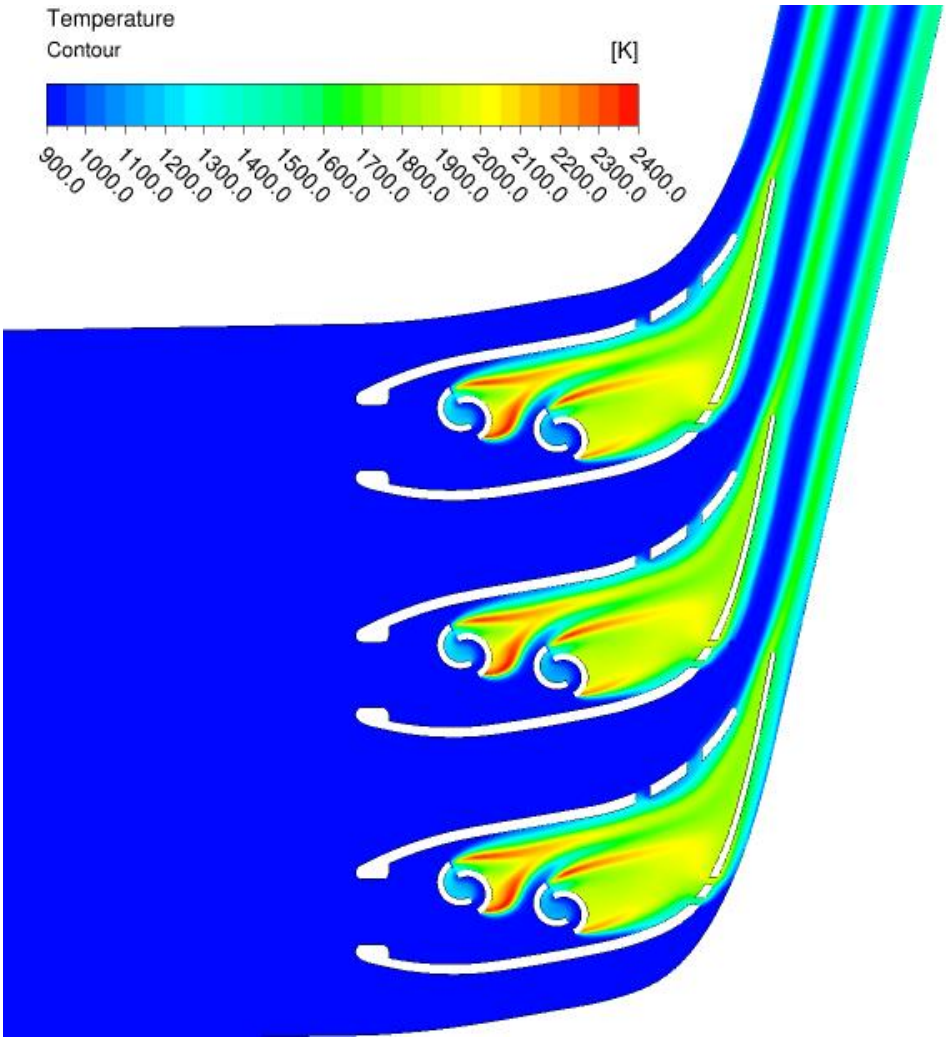

Figure 39. Injector configuration 2: Mid-span temperature distribution.

IV.6.3. Injector Configuration 3

Figure 41 shows a swirling flow approaching the stator blades. The recirculation zone in the core in which fluid particles travel upstream due to vortex breakdown can be clearly seen in this figure [15].

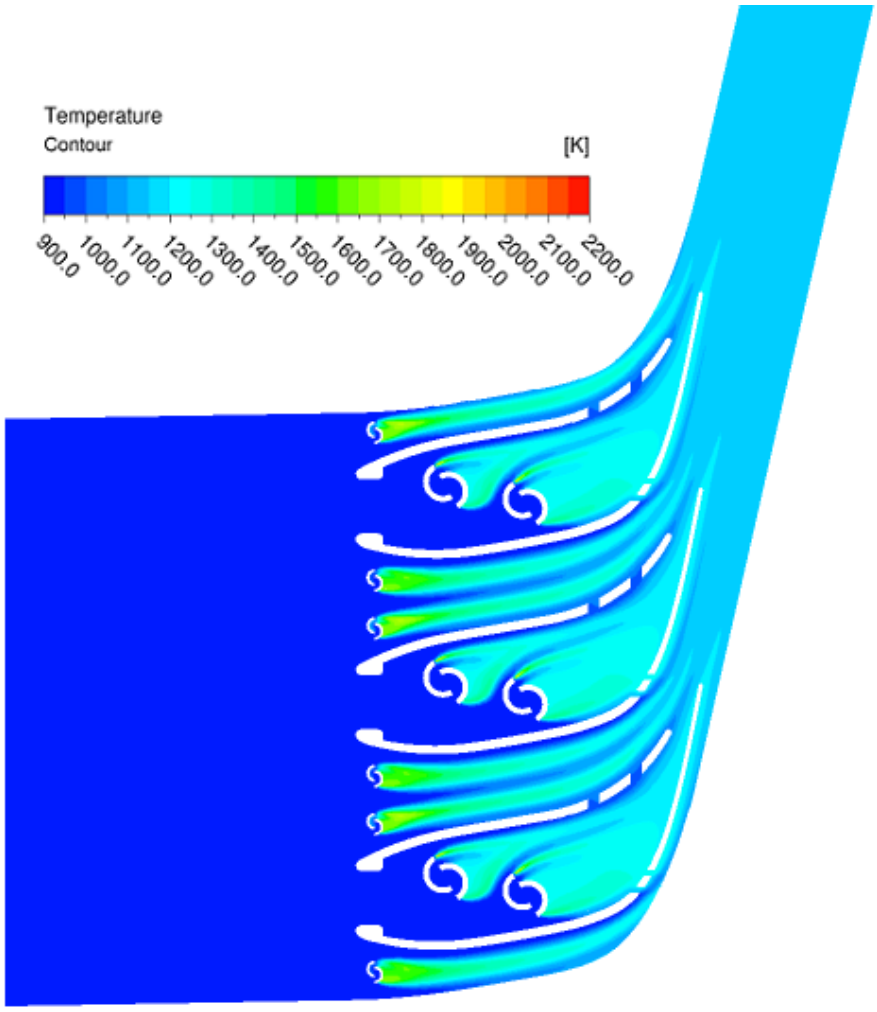

Figure 40. Modified injector configuration 2: Mid-span temperature distribution.

Figure 42 and Figure 43 show the derived mid-span velocity contours in the stationary frame and velocity vectors in the relative frame for injector configuration 3. As shown in Figure 43, fluid particles follow the blade metal angle with little deviation. A portion of the air goes through the swirler and attains a rotational velocity component. The rotating air is mixed with the fuel injected in the center of the swirler and burns to a high temperature. The rest of the air which does not pass through the swirler keeps its axial

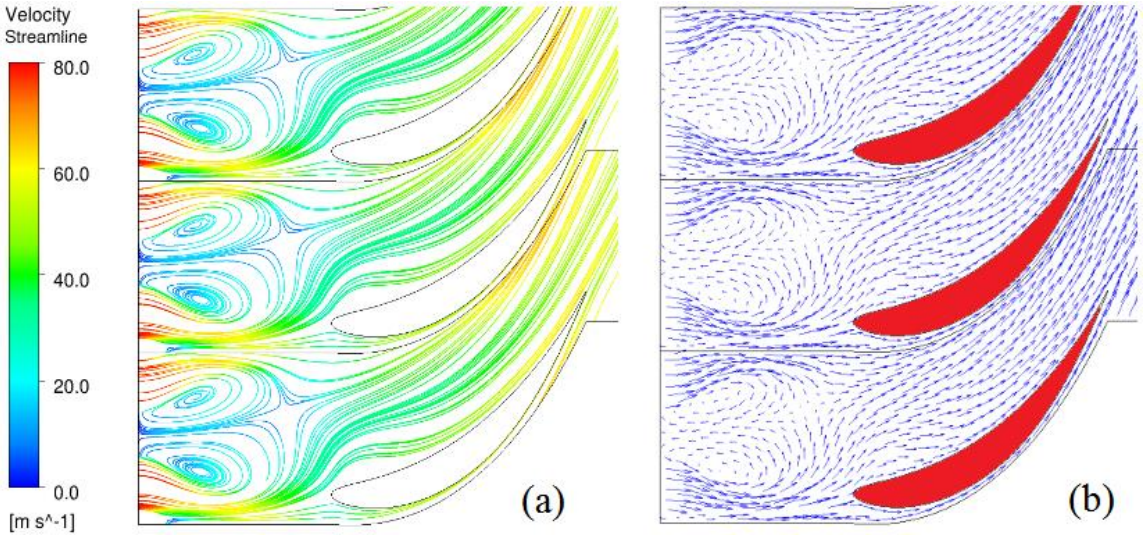

Figure 41. Vortex breakdown in a swirling flow approaching stator blades. Midspan velocity streamlines (a), and velocity vectors (b), from Ref. [15].

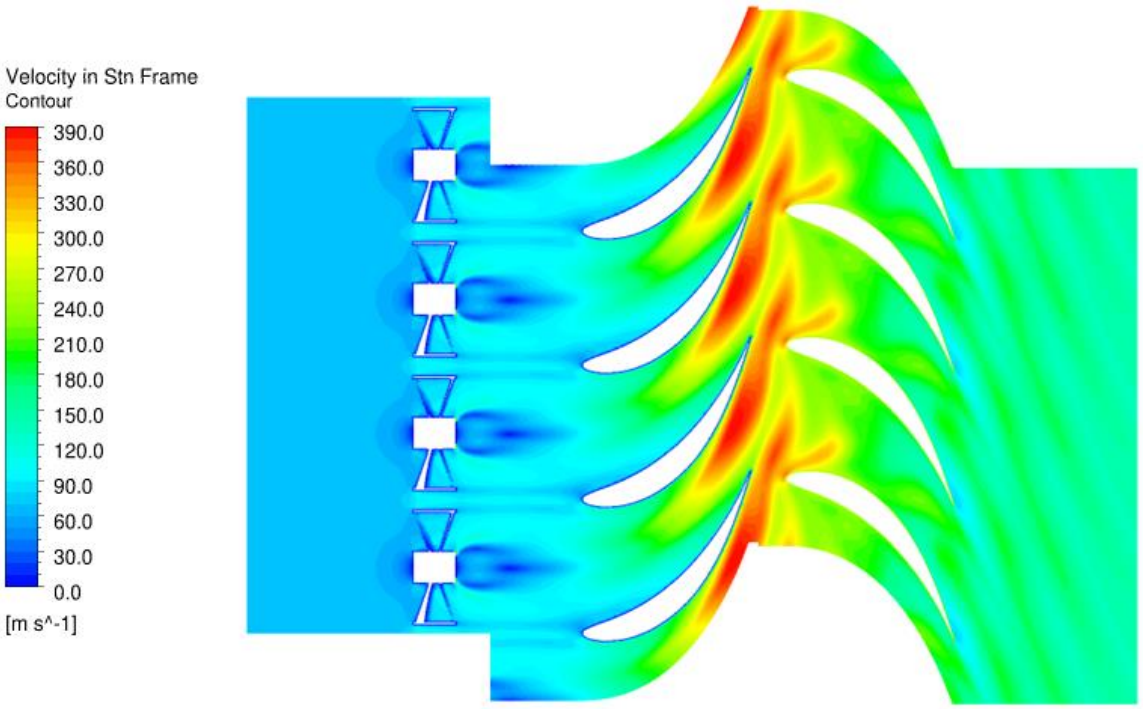

Figure 42. Injector configuration 3: Mid-span velocity distribution in stationary frame.

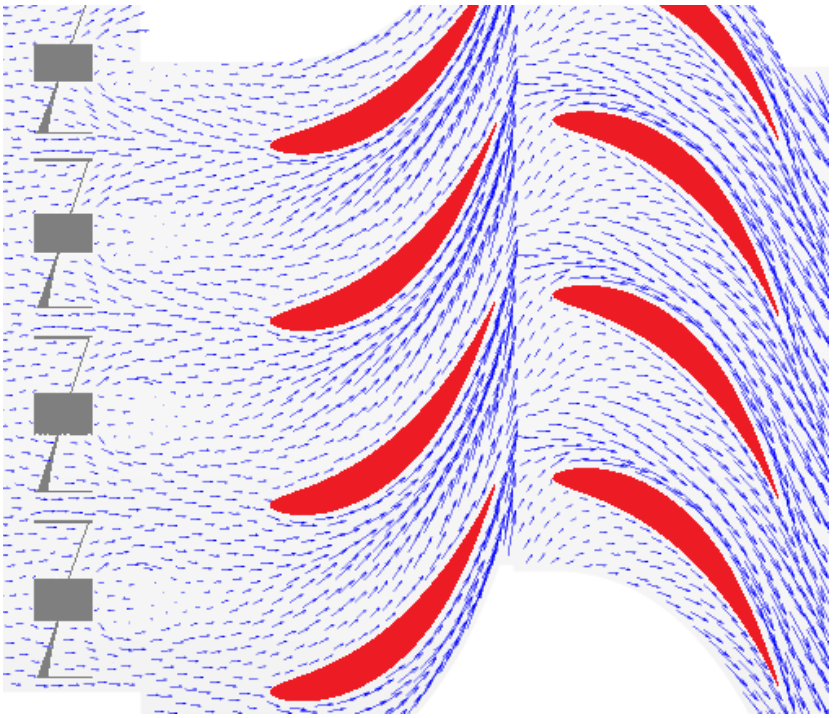

Figure 43. Injector configuration 3: Mid-span velocity vectors in relative frame.

velocity direction and surrounds the flame.

The amount of torque on each blade is 142.9 N.m and the total power is 5.2 MW. Figure 44 shows the temperature distribution at span=0.6. As shown in this figure, temperature rises along the stator and the early stages of rotor blade due to fuel burning. Figure 45 and Figure 46 show the temperature distribution before and after stator and rotor blades and the temperature distribution at rotor inlet, respectively. As shown in these figures, at the rotor inlet there is a cold flow near the endwalls and a hot core in the middle. Lower temperature near hub and shroud can be a positive factor because it protects the endwalls from the hot flame radiation [66]. But despite swirling flow, in this case the hot

core does not mix completely with the surrounding flow. Therefore the temperature distribution at rotor inlet is not quite uniform which can adversely affect the turbine performance. The non-uniform temperature distribution in this case results in 14.7% lower power generation compared to configuration 1. That is because the high enthalpy combustion gases are not distributed properly around the rotor blades. The reason behind the low mixing between the hot core and the surrounding flow can be the high pressure and density of the fluid. In the simulated models with very low inlet pressure (1.5 bar), more mixing was observed. The low amount of mixing causes the temperature in the core to rise very high. This generates a very hot flow near the blade surfaces which is not favorable with regards to blade material and manufacturing.

Figure 47 shows the meridional temperature distribution. As shown in this figure, maximum temperature is reached at the early stages of rotor blade which means the combustion process is taking place up to that area. Also it is seen that the hot core is not expanded and mixed with the surrounding flow as explained before. The other phenomenon is that the hot fluid in center does not follow the centerline. This is most likely due to the swirling flow and it causes the maximum temperature to occur at about span=0.6.

Figure 48 and Figure 49 show the average temperature and average fuel mass fraction changes with regards to streamwise location from inlet to exit, respectively. As shown in Figure 48, temperature rises at a high rate after the fuel injection. The rate of temperature rise decreases as it approaches the stator blade. That is because of the increase of kinetic energy in stator. After the stator trailing edge the temperature increases with a

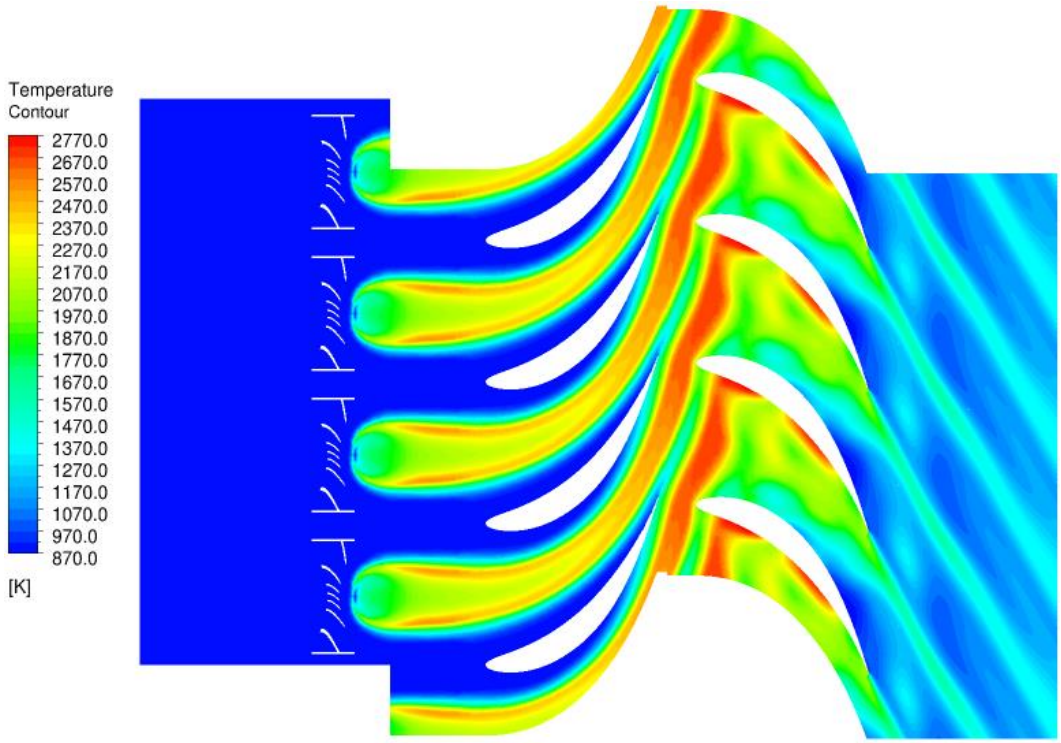

Figure 44. Injector configuration 3: Temperature distribution at span=0.6.

high rate up to the rotor leading edge. In the early stages of the rotor blade, temperature is still rising which indicates that the fuel particles are still burning in this area. After temperature reaches its maximum and all the fuel is burned, temperature starts to decrease along the remaining parts of rotor blade. That is because of power extraction in rotor. Figure 49 shows the pattern in which the fuel is burned along the stator and rotor blades.

Total pressure loss due to secondary flows and friction in the injector segment for this configuration is around 1% which is considered a good value for a single-stage combustion unit. With regards to pollutant emissions, NO_x concentration at the stage outlet is around 120 ppm which is slightly higher than the regulated 100 ppm NO_x emission for industrial engines under 50 MW [92].

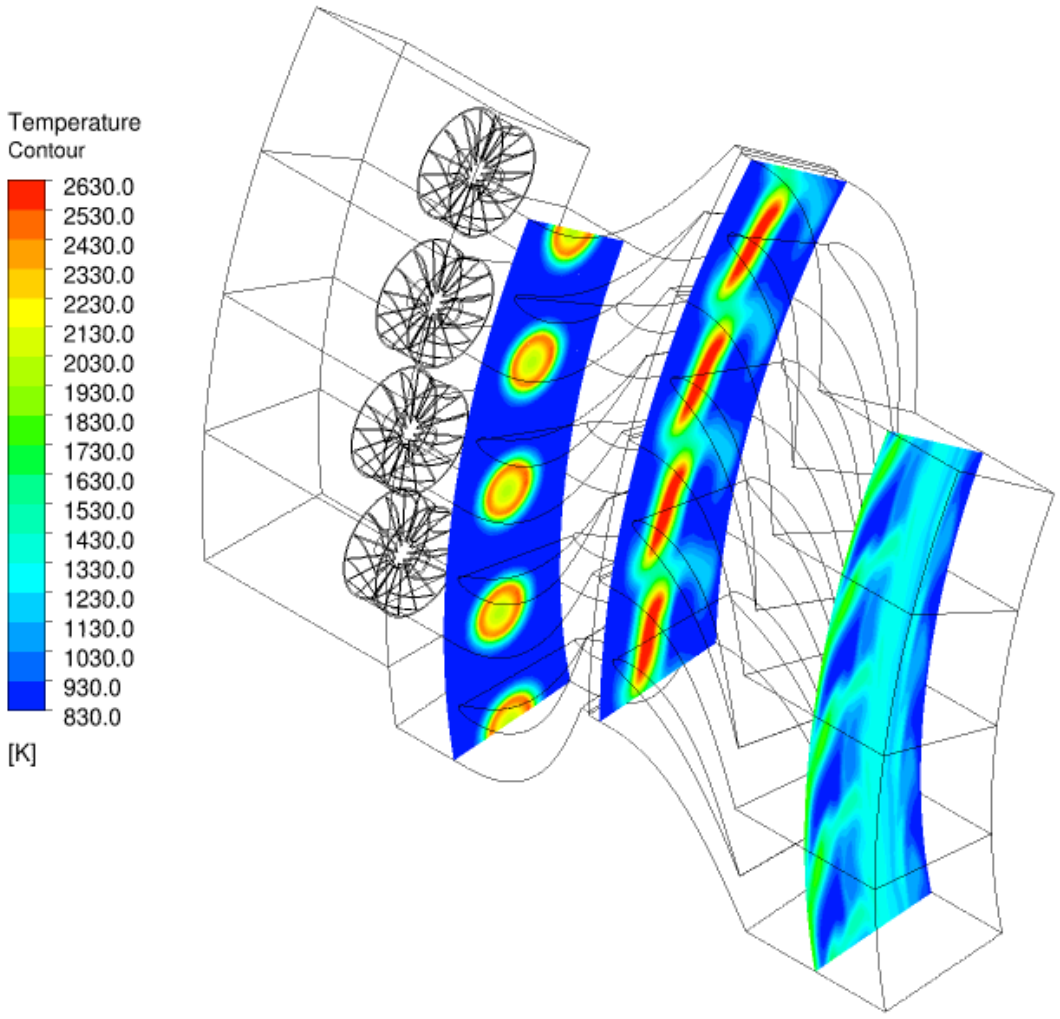

Figure 45. Injector configuration 3: Temperature distribution before and after stator and rotor.

IV.6.4. Further Discussion on Different Injector Configurations

In order to achieve the optimum design for UHEGT, numerous configurations have been designed and investigated numerically. These configurations utilize vortex generation to enhance the mixing between air and fuel particles. They present a combination of combustion unit, stator and rotor components for the first stage of a high

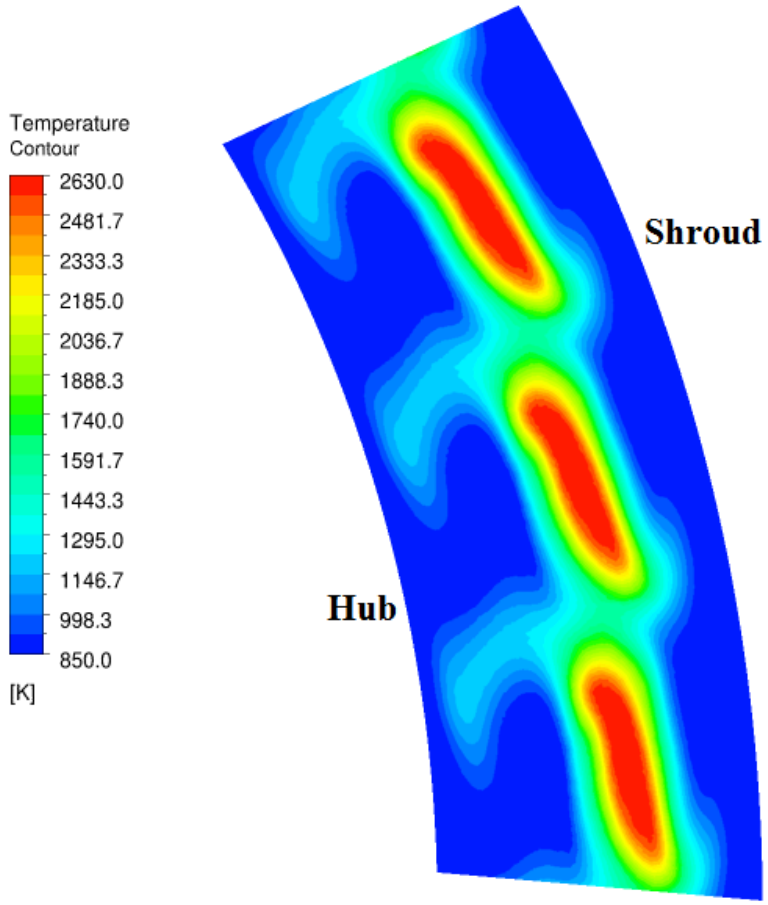

Figure 46. Injector configuration 3: Temperature distribution at the rotor inlet.

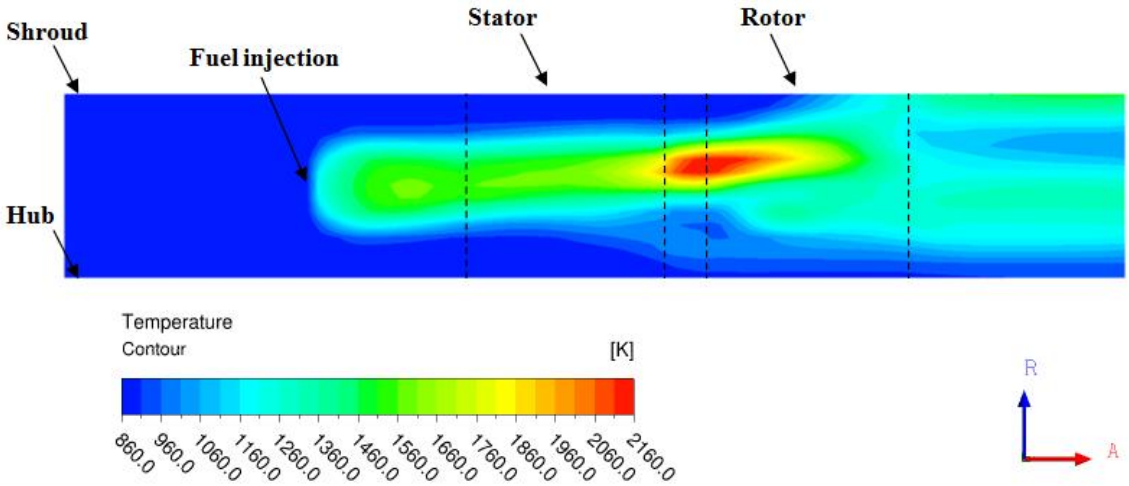

Figure 47. Injector configuration 3: Meridional temperature distribution.

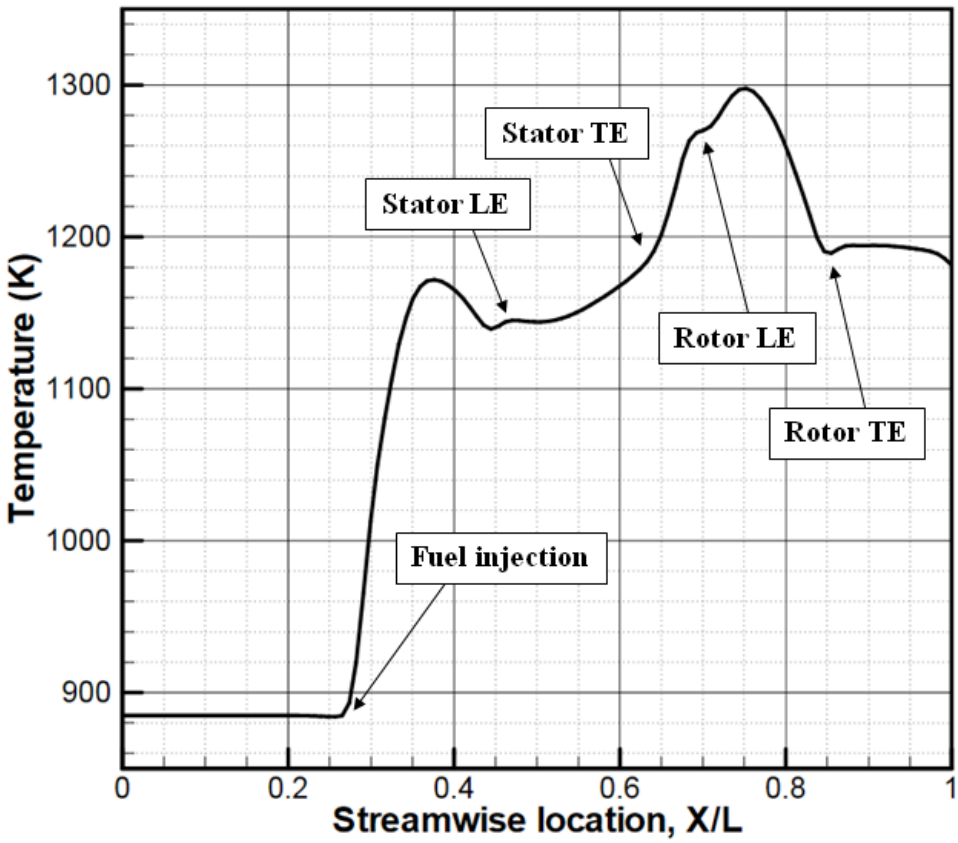

Figure 48. Injector configuration 3: Average temperature profile.

pressure UHEGT. Transient numerical simulations which include both combustion process and rotor motion are performed on each configuration. Velocity, pressure, and temperature distributions, fuel mass fraction, power generation, pressure losses, and pollutant emissions are investigated in the domains. Three of these configurations are presented in this study.

In the first configuration, fuel is injected into the domain through cylindrical tubes extended from hub to shroud. Flow over cylindrical tubes creates Von Karman vortices which help the mixing between fuel and air particles. This configuration provides a very

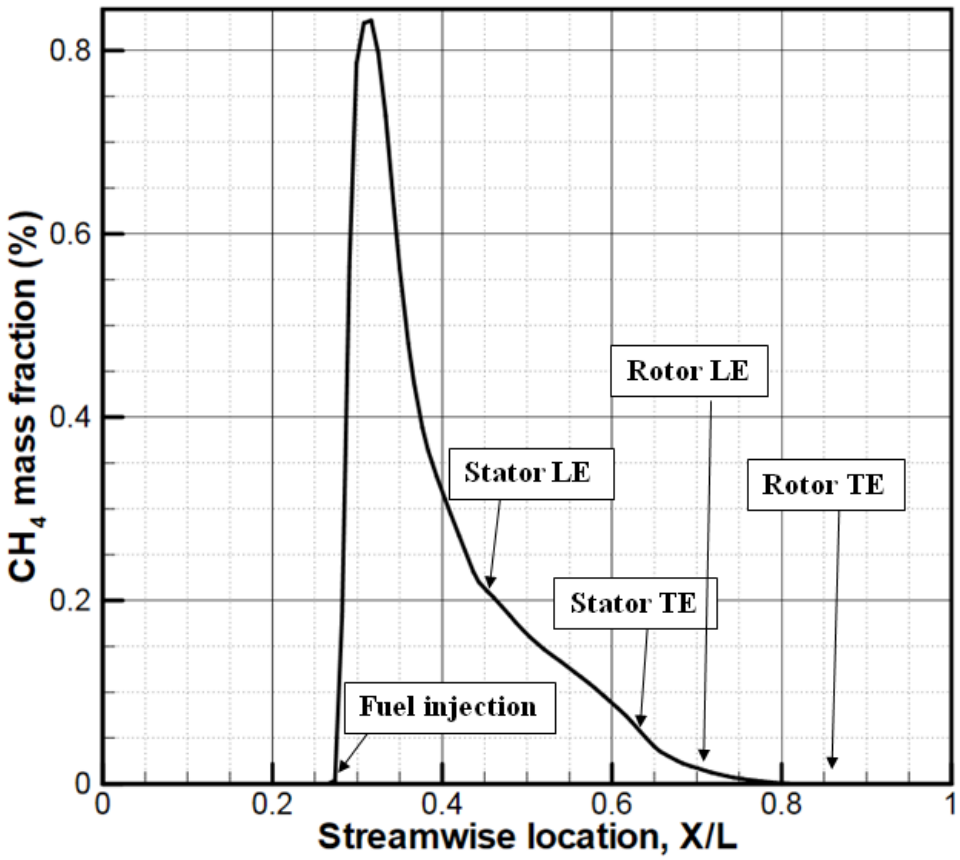

Figure 49. Injector configuration 3: Average fuel mass fraction profile.

uniform combustion process, a good mixing between air and fuel, and a highly uniform temperature distribution at the rotor inlet. Temperature distribution at the rotor inlet is considerably improved using linearly increasing fuel injection from hub to shroud. As a result, this configuration generates more than 17% higher power compared to configuration 3 which is quite noticeable. It was also observed that due to rotation and buoyancy effects, the lower temperature (higher density) fluid particles move toward the shroud in rotor and vice versa. This configuration has a low pressure loss and very low pollutant emission and provides a very suitable design option for UHEGT.

Configuration 2 presents a total new design for the blade and injectors. It enables the combustion process to take place inside the stator blades which leads to a very compact engine. Cylindrical fuel injectors are placed inside the stator blades and multiple slots are opened on suction and pressure surfaces and the trailing edge. The hot flow exits those slots and flows toward the rotor. Temperature distribution at rotor inlet was improved by adding external injectors. It needs to be noted that in this design, temperature near the blade internal surface may get too high and the blade cannot be cooled internally.

In the third configuration, axial swirlers are placed before the stator row for the purpose of vortex generation. This configuration provides a hot core in the center of the domain and low temperature flow near the endwalls. Although the cold flow near hub and shroud can be helpful by protecting them from the hot flame radiation, the hot core is highly concentrated in the center of the domain. So the temperature distribution at rotor inlet is not quite uniform which have negative effects on the engine performance and reduces the amount of power generated by rotor. Moreover, since all the fuel is injected in the center, it takes some time for fuel particles to mix with air and burn. Therefore it was observed that the burning process continues up to the early stages of the rotor blades. The non-uniform temperature distribution causes the temperature in the core and near the blade surfaces to rise very high which is not a favorable design parameter. Another observed phenomenon is that the hot core does not follow the centerline of the domain and it is deviated towards the shroud, which is most likely due to the swirling flow. This configuration has a slightly higher than standard NO_x emission and low pressure loss.

Table 2 presents a comparison between the advantages and disadvantages of different UHEGT configurations.

Table 2. Comparison of different UHEGT injector configurations

	Advantages	**Disadvantages**
Config 1	Highly uniform temperature distribution at rotor inlet, uniform combustion, low pressure loss, low pollutant emission	--
Config 2	Compact engine size	Non-uniform temperature distribution at rotor inlet (if used without external injectors), high temperature near the blade internal surface, no possibility for blade internal cooling
Config 3	Low pressure loss, low temperature near the endwalls	Non-uniform temperature distribution at rotor inlet, high temperature in the core and near the blade surfaces, high pollutant emission

As shown in this table and by looking at temperature distributions at different locations, fuel burning patterns, power generation, pressure loss, and pollutant emission, modified configuration 1 in which the fuel is injected into the domain through cylindrical tubes is considered the optimum design for UHEGT among current options. Additional modifications such as moving the injectors closer to the blades and adding a distance between the injection holes and the endwalls can further improve the characteristics of this configuration.

CHAPTER V

DESIGN AND SIMULATION OF THE MULTISTAGE UHEGT

In this chapter, a complete UHEGT engine with a multistage compressor, a multistage turbine, and multiple stages of stator internal combustion integrated within the HP-turbine stages is developed. The turbine is designed as a single spool turboshaft power generation system and could also be modified for aero-industry in future. The HP-turbine stages with stator internal combustion and rotor motion are simulated and analyzed via Computational Fluid Dynamics (CFD).

V.1. Turbine Stage Design

The high pressure and temperature gas in a gas turbine is guided through the stator blades where it gains the proper angle and velocity; then it passes through the rotor in which it transfers mechanical energy to the shaft. Figure 50 shows a sample axial turbine stage with corresponding velocity diagrams [1].

The turbine stages are designed based on a 1D/2D approach also known as meanline calculation. In [1], it was shown that the compressor and turbine stages of axial, radial or mixed geometry can be described in a unique manner by a few dimensionless parameters only, which are:

$$\mu = \frac{V_{m2}}{V_{m3}}\ , \nu = \frac{R_2}{R_3} = \frac{U_2}{U_3}\ , \phi = \frac{V_{m3}}{U_3}\ , \lambda = \frac{l_m}{U_3^2}\ , reaction = \frac{\Delta h_r}{\Delta h_s + \Delta h_r} \qquad (5.1)$$

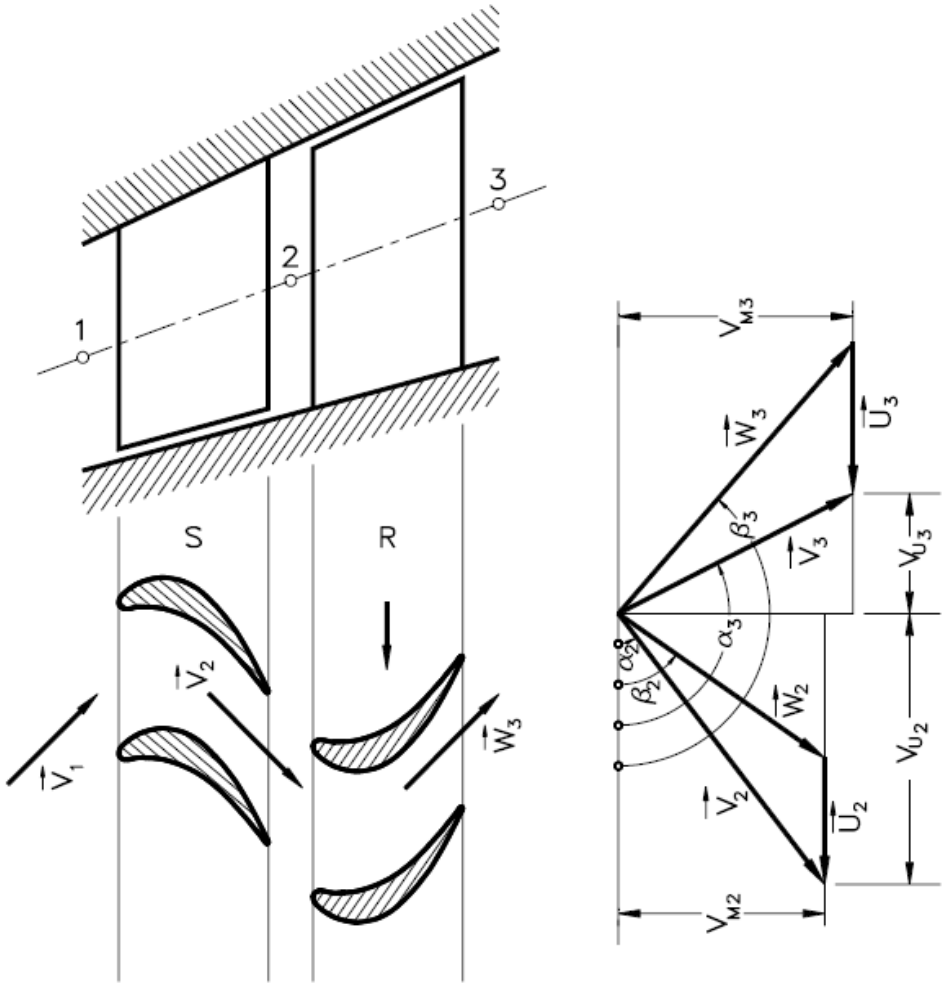

Figure 50. A sample axial turbine stage (left) with corresponding velocity diagrams (right); (V and W show the absolute and relative velocities, respectively); Reprinted from Ref. [1].

In which μ is the meridional velocity ratio, ν is the circumferential velocity ratio, ϕ is the flow coefficient, λ is the load coefficient, *reaction* is the degree of reaction, V_m is the meridional (axial) velocity, U is the blade circumferential velocity, and l_m is the specific

load of the stage. Introducing the above dimensionless parameters into the equations of continuity, moment of momentum, and degree of reaction, the stage is fully defined by the following set of equations [1],

$$cotg\alpha_2 - cotg\beta_2 = \frac{\nu}{\mu\phi} \tag{5.2.a}$$

$$cotg\alpha_3 - cotg\beta_3 = \frac{1}{\phi} \tag{5.2.b}$$

$$reaction = 1 + \frac{\phi^2}{2\lambda}[1 + cotg^2\alpha_3 - \mu^2(1 + cotg^2\alpha_2)] \tag{5.2.c}$$

$$\lambda = \phi(\mu\nu cotg\alpha_2 - cotg\beta_3) - 1 \tag{5.2.d}$$

In which, α and β show the flow's absolute and relative angles at stator and rotor, respectively (Figure 50). The above equations include 9 unknown parameters from which 5 of them should be assumed and the other 4 will be calculated by solving the Eq. 5.2a-d. All the mixture properties such as enthalpy, entropy, γ, Cp, etc at different pressures, temperatures, and fuel/air ratios are calculated using a FORTRAN gas table developed by Schobeiri [1]. At the inlet of each stage, the inlet conditions (i.e. pressure and temperature) are known from the previous stage. Based on the stage desired pressure ratio and a preliminary assumed isentropic efficiency, the exit pressure and temperature of the stage are calculated. The final isentropic efficiency is found after implementation of all individual losses [1]. In order to come up with the appropriate values for 5 of the unknown parameters in Eq. 5.2a-d, the stage geometry (i.e. mean diameter and blade height), rotational speed, and α_2 values are specified. Moreover, μ and ν are calculated assuming average blade height and velocity at the middle section of the stage. The remaining

unknown parameters (α_3, β_2, β_3 and r) are calculated by solving the equation set of 5.2a-d. In this process, we tried to distribute the stage load coefficients, λ, properly over different stages. To achieve this goal, the initial assumptions are modified in a trial and error process until the desired values are acquired. Finally, in order to maintain radial equilibrium from hub to shroud, the free vortex flow equation is applied as described in [1]. In this process, after calculation of all the stage parameters at the mean diameter, the free vortex law is applied at hub and shroud sections to calculate the corresponding blade angles. All of the stage design and calculation processes are performed in an in-house FORTRAN code developed for this study (Appendix A).

V.2. Cycle Design

As the system is designed to use natural gas as the main source of fuel, the thermodynamic cycle is based on the methane air mixture. A 3-stage combustion process is considered for the current design. It provides enough room for reheat while not making the system too complicated. The process starts at near atmospheric pressure and temperature. Based on the previous and current calculations, and as shown in Figure 10a, the optimum compressor pressure ratio for a 3-stage combustion UHEGT is around 40:1. So, the compressor is set up as one unit with the pressure ratio of 40:1 and an estimated isentropic efficiency of 90%. The next design factor is the turbine inlet temperature. In the Brayton cycle (which describes the process in conventional gas turbines), increasing the TIT leads to an increase in the cycle efficiency. But on the other hand, a higher TIT requires a higher amount of cooling air and a more complicated cooling system which can

lead to a total efficiency loss. Another disadvantage of high TIT is an increase in the pollutant emissions as a results of the higher flame temperatures [21]. It will also make the manufacturing process more difficult as the system requires more advanced and expensive materials. In UHEGT, high thermal efficiencies can be achieved without a dramatic increase in TIT. TIT=1500 K is considered as the maximum temperature limit in the current cycle design. This temperature limit allows us to achieve the main objectives of the design which are high thermal efficiency, high output power, and low emissions, without the downsides of a super high TIT system. It should be noted that the highly advanced Mitsubishi GT G-series with TIT close to 1800 K has less than five percentage point thermal efficiency compared to UHEGT [93].

The next deciding factor in cycle design for UHEGT is the distribution of pressure ratios on different turbine stages. An optimization program is developed in FORTRAN to calculate what combination of the pressure ratios produces the best performance for the system. The results show that the maximum cycle efficiency is achieved when the first two turbine stages have a pressure ratio of between 1.4-2 each; with the rest of the pressure applied on the following stages. It is also shown that higher pressure ratio in the first two stages results in higher output power. As both high efficiency and output power are important factors in the design, a compromise between the two criteria results in an optimum outcome. Other than that, we tried to maintain a reasonable balance between the fuel flow rates injected in each combustion stage. Therefore, we avoided injecting too much (more than 50%) or too low (less than 10%) of the total fuel mass flow in any of the three combustion stages. Considering all of the parameters above, Figure 51 shows the

final thermodynamic cycle for the current UHEGT design. In this figure, the corresponding pressure ratios for the compressor and each turbine stage are specified. Each combustion stage is shown by the symbol MF and its corresponding fuel mass flow

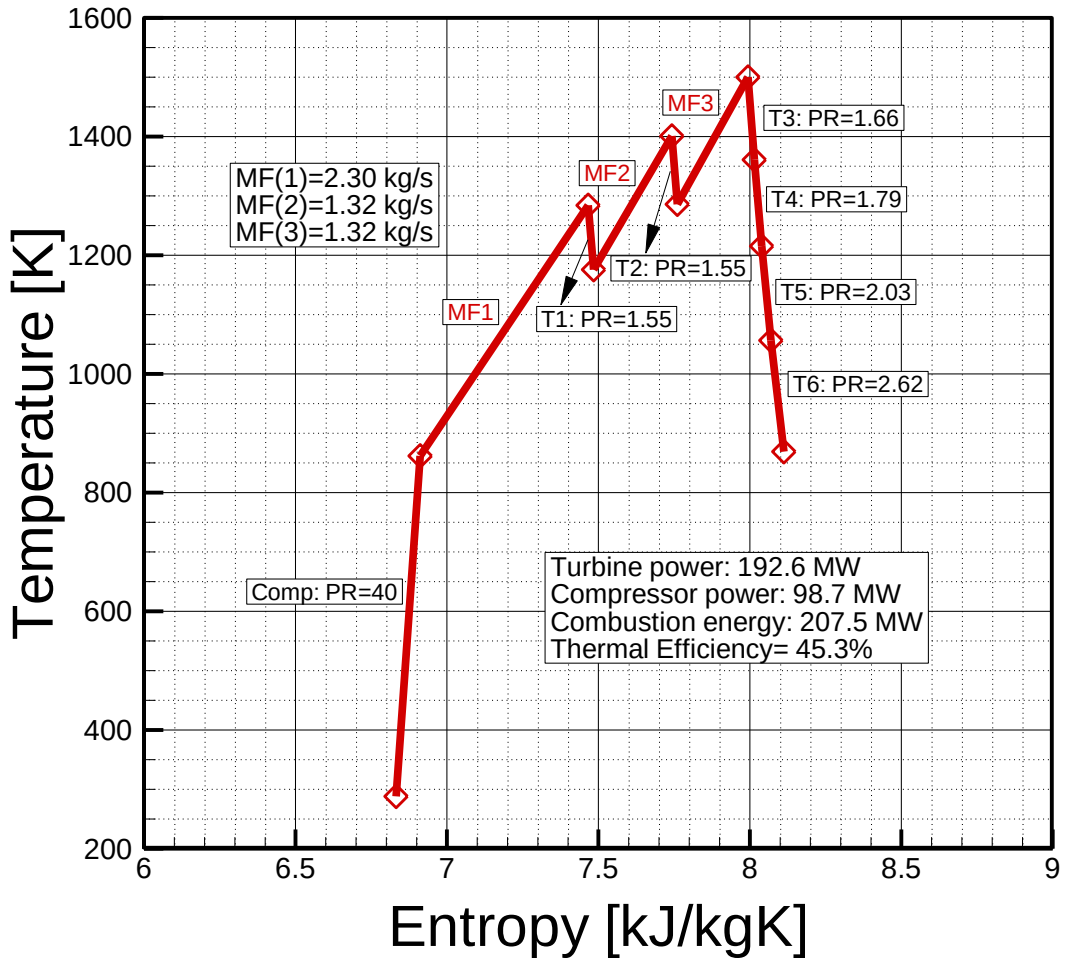

Figure 51. UHEGT thermodynamic cycle: Pressure ratio for compressor and each turbine stage, fuel mass flow rate for each combustion stage, corresponding total power for each component, and the cycle thermal efficiency are shown.

rate. On the bottom side of this figure, the turbine output power, compressor input power, and the total fuel energy are shown. The cycle thermal efficiency is calculated as,

$$\eta_{th} = \frac{W_{turb} - W_{comp}}{Q_{fuel}} \tag{5.3}$$

The incoming air at atmospheric pressure and temperature (1 atm, 300 K) and mass flow rate of 150 kg/s passes through the compressor with the pressure ratio of 40:1. The high pressure air is injected with 2.3 kg/s of fuel flow in the first combustion stage. The high pressure and temperature gas then expands in the first turbine stage with the pressure ratio of 1.55:1. After that, the gas passes through the second combustor and the same combustion-expansion process takes place again. After the final combustion stage, the gas reaches its highest temperature (1500 K). At this point, it has expanded through the first two turbine stages and is at the pressure of 15.5 bar. The high pressure hot gas then expands through the last turbine set which consists of four turbine stages. At the exit point, the mixture is at atmospheric pressure and a relatively high temperature (869.1 K). The exit gas could be used in a following power cycle (combined system) to considerably increase efficiency. After the cycle design is finalized, all of the stage parameters are calculated as explained in the previous section. Table 3 shows the turbine stage parameters at mean section for the current design. The rotational speed is N=6000 rpm and the hub diameter is D_{hub}=0.5 m for all stages. The geometry of the turbine is discussed in the next section.

Table 3. Turbine stage parameters at the mean section for UHEGT

	stage 1	stage 2	stage 3	stage 4	stage 5	stage 6
Power (MW)	23.7	26.0	32.5	33.1	35.9	41.4
Pressure ratio	1.55	1.55	1.66	1.79	2.03	2.62
V_{in} (m/s)	88.1	126.2	144.3	137.5	138.4	142.9
V_{out} (m/s)	102.9	120.2	137.5	138.4	142.9	191.4
M_{out}	0.23	0.20	0.25	0.25	0.27	0.34
Reaction	0.64	0.47	0.45	0.48	0.50	0.38
λ	1.40	1.45	1.66	1.51	1.37	1.29
φ	0.31	0.35	0.39	0.37	0.35	0.42
Bh_1 (mm)	50.0	60.0	87.2	132.5	198.4	310.0
Bh_3 (mm)	60.0	87.2	132.5	198.4	310.0	450.0
α_2 (deg)	15.0	16.0	16.0	16.0	16.0	16.0
α_3 (deg)	137.4	120.5	128.1	125.9	123.2	99.6
β_2 (deg)	75.4	53.1	44.6	50.2	55.5	48.2
β_3 (deg)	167.0	163.8	163.5	163.8	164.2	158.6
Chord (mm) (stator/rotor)	80.0	100.0	120.0	140.0	160.0	180.0
Blade number (stator/rotor)	60	48	40	32	30	28

V.3. Turbine Geometry and Blade Profiling

After all of the stage parameters are determined, blades need to be aerodynamically profiled. In order to do that, the geometrical parameters including blade metal angles, blade heights, and mean diameters are imported into a separate FORTRAN code. Based on the equations explained previously, radial equilibrium is applied at the hub and shroud sections to modify the blade angles. The blade chords are specified based on the conventional values as a linearly increasing number through the six stages. The chord to spacing ratios of about 1.4 and 1.2 are applied to the high pressure (HP) and low pressure (LP) turbine stages, respectively. The blade number for each stage is then calculated based on the chord to spacing ratio. Bezier camberlines, detailed in [1], are generated for all of

the stator and rotor blades at hub, mean, and tip sections. After that, standard base profiles are superimposed on each camberline to generate suction and pressure surfaces. The maximum thickness increases 20% from tip to hub in each blade in order to overcome the higher torque near the hub.

The profiles at hub, mean and tip sections are imported into SolidWorks. The 3D model of each blade is generated and all components are assembled together. Figure 52 shows the cross section of the six-stage turbine with three stages of stator internal combustion. The numerical domain generated for the CFD simulation is shown in Figure 53. This domain represents the first three stages of the system which includes 3 injector rows, 3 stators, 3 rotors, and an inlet extension. Periodic boundary conditions are used in each component in order to bring down the size of the computational domain to include only one blade and its corresponding injectors at each row. The design of the injectors is based on the single stage simulations which will be discussed in the next section.

The mesh generation process, numerical method and boundary conditions are similar to the single stage turbine described in the previous chapter. The total number of elements for the computational domain of the 3-stage assembly is more than 25 m. For further details, please refer to the sections IV.4 and IV.5.

V.4. Results and Discussion

Figure 54 shows the blade loading (static pressure coefficient distribution, $C_P = \frac{P-P_{stag}}{\frac{1}{2}\rho V^2}$) over the first stator's suction and pressure surfaces. This diagram shows a high amount of pressure difference between the suction and pressure surfaces which means a

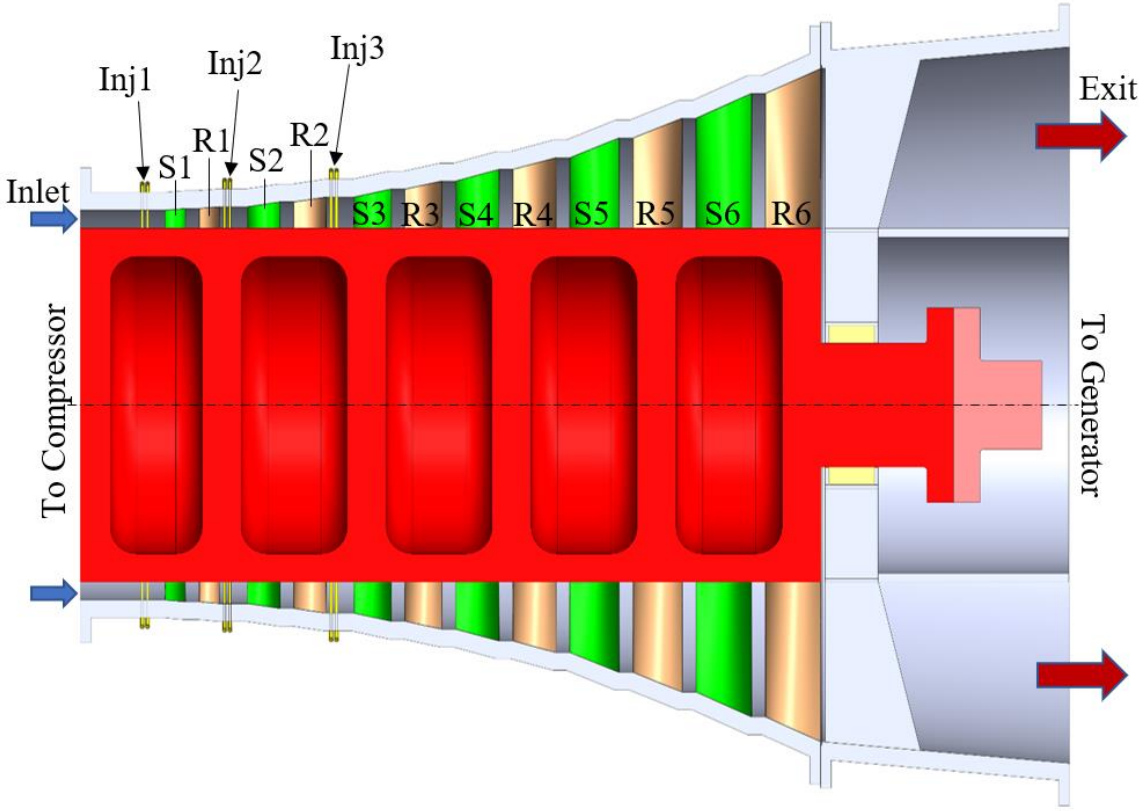

Figure 52. Six-stage UHEGT turbine with three stages of stator internal combustion.

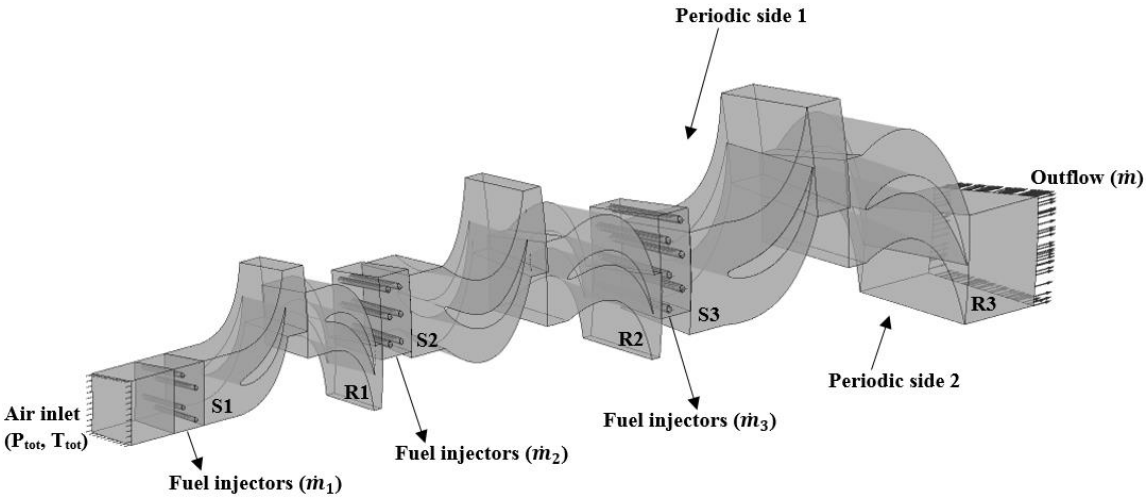

Figure 53. Computational domain for the 3-stage assembly: the domain has 10 total components which include 3 injector rows, 3 stators, 3 rotors, and an inlet extension.

proper load is applied on the blade. As seen in this figure, the stagnation point is not located exactly on the LE and it is slightly moved towards the pressure side. That is due to incidence angle between the inlet flow and the blade metal angle which will be discussed more in the following.

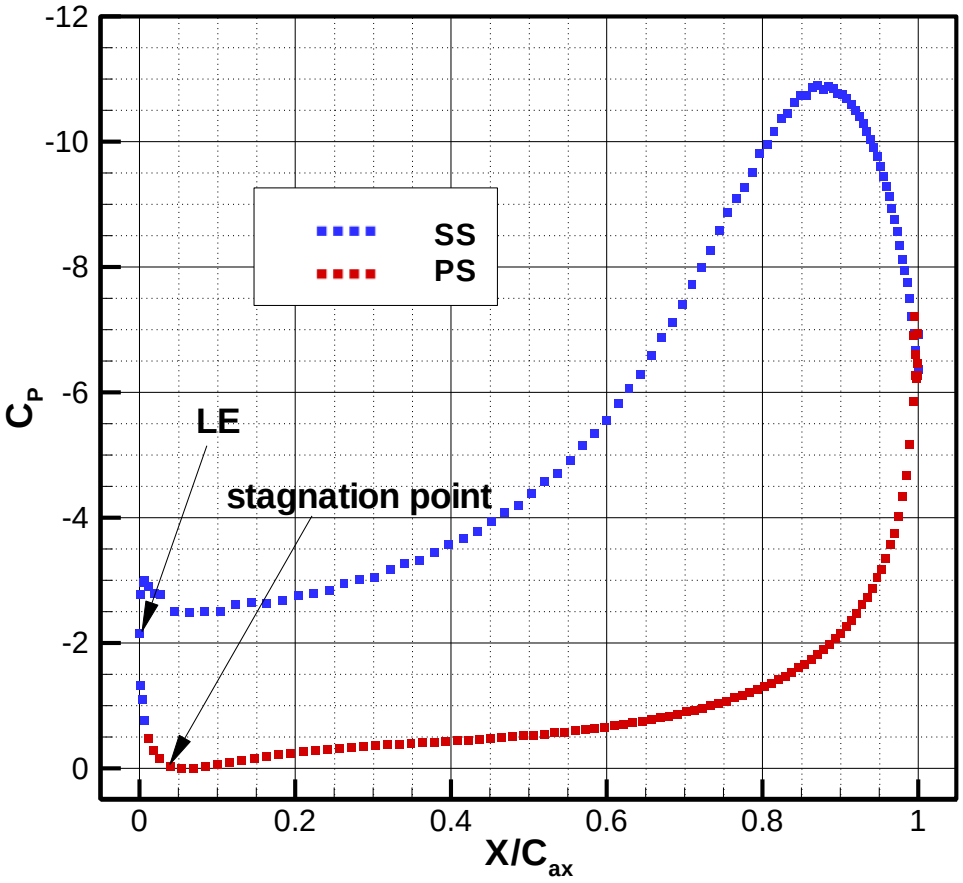

Figure 54. Midspan blade loading on the first stator: pressure coefficient distribution on suction and pressure surfaces.

Figure 55 shows the midspan streamlines in the relative frame of reference over the three stages. As shown in this figure, streamlines follow the blade metal angles very

closely and the incidence angles are minimized. To achieve the current flow pattern, multiple steps of modification are applied to the blades. In the original case, the deviation angle at the exit of each stator and rotor row caused a huge incidence angle at the inlet of the next component. This caused the flow to not follow the next component's inlet metal angle which created big flow separations and reduced the generated power by up to 75%. The effects of exit deviation angle seemed to be more intense due to the high rotational speed and high exit metal angles. These factors make the small deviation angle (below 6 degrees) to amplify in the following component and create large incidence angles (up to 45 degrees). In order to fix this problem, the stagger angles of each stator and rotor components are slightly modified (each blade was rotated 5-6 degrees). This change in the stagger angle makes up for the deviation angle at the exit of each component, reducing the incidence angle at the following component. As shown in Figure 55, by applying this modification the incidence angle in all components are minimized and the separations are dramatically reduced.

Figure 56 shows the midspan Mach number distribution in the relative frame over the three stages. Different parameters are noticeable in this figure. First is the local maximum Mach numbers which occurs at the throats. The Mach numbers are kept under 1 to prevent sonic flow which could lead to shock and increasing losses. The next parameter to notice is the approach stream Mach number. As shown in Figure 56, the average approach stream Mach number over the first injectors is about 0.1. Based on the experiments run by Baxter and Lefebvre [62], this Mach number allows for an appropriate margin of flame stability in a bluff body stabilized combustion. The first combustion stage

is the most critical one with regards to the flame stability since it has the lowest temperature among the three combustion stages. As the gas moves on along the turbine stages and reaches the second and third injectors, the average approach stream Mach number increases to about 0.2. Although the higher Mach number provides a lower stability margin, but with the incoming temperatures of above 1200 K at the second and third injectors, the combustion process will most likely be stable (according to similar studies [60]).

The next noticeable parameter in Figure 56 is the clocking of the injectors and turbine stator blades. Wakes from the upstream injectors impinge on the following injectors and stator blades. In conventional gas turbines, clocking (indexing) is considered a way of influencing the flow by changing the circumferential position of rotor-rotor rows and stator-stator rows relative to each other [94]. It has been shown that clocking can affect the turbine efficiency by up to 1% [95]. This efficiency variation is called *clocking effect*. In UHEGT, clocking concept could be extended to define adjusting of the circumferential location of the injector rows with regards to each other and the following stator blades. Therefore, it is considerable from two aspects: the first is how the two adjacent injector rows are clocked relative to each other; and the second is how the injectors are clocked relative to the following stator rows. In the current design, the two injector rows in each stage are aligned in a way that the wakes from the first row do not impinge on the injectors in the second row. This prevents the wakes from being combined with each other which could contribute to increasing losses. It would cause stronger wakes approaching the stator blades generating stronger secondary flows and separations. The second aspect is the

clocking of the injector rows with the following stator blades. Many studies have been performed on the interactions between the wakes produced by blades or rods on the following sets of blades [94]-[96]. They study the stage performance and efficiency and how they could be improved by clocking the blades. This topic will be a subject of study in section V.5.

Last but not the least, is the amplification of the injector wakes that approach the stator blades' pressure surfaces. This phenomenon can be seen in all of the three stages in Figure 56, but it is mostly visible in the third stage. As seen in the picture, the injector wakes that are approaching the stator blades' pressure surfaces in the third stage, become larger as they get closer to the surface. This is due to the high pressure in the wake core being combined with the high pressure near the pressure surface. This phenomenon amplifies the pressure in the wake core and results in stronger wakes near the blades' pressure sides.

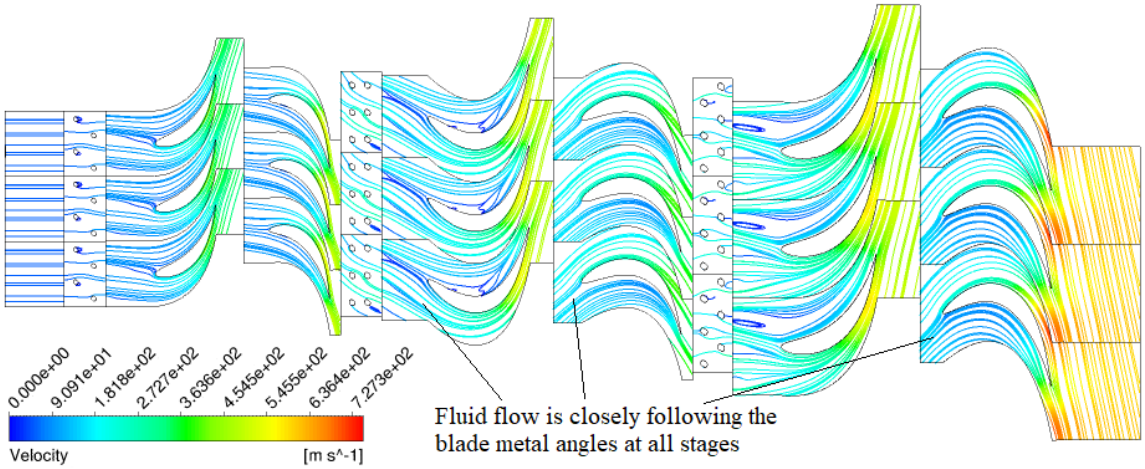

Figure 55. Midspan streamlines in relative frame for the three-stage assembly.

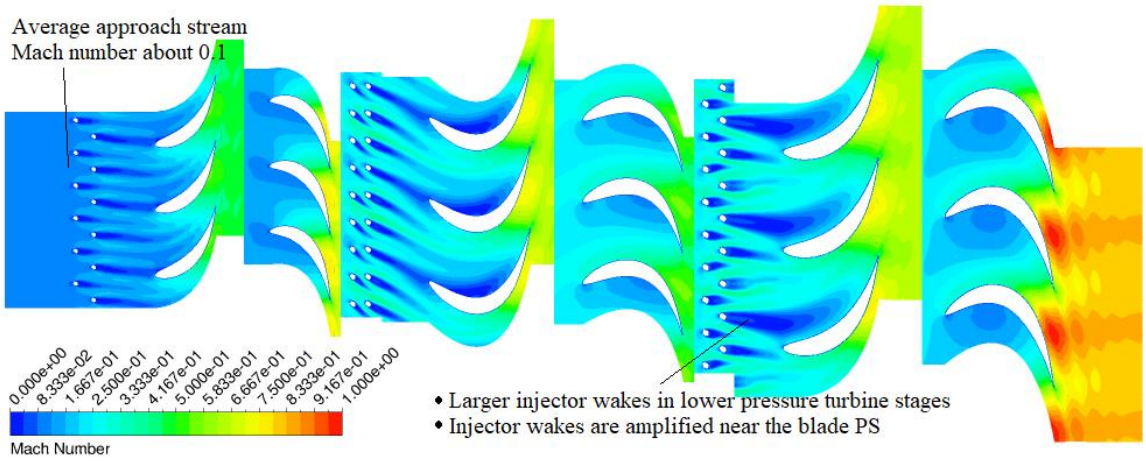

Figure 56. Midspan Mach number in relative frame for the three-stage assembly.

Figure 57, Figure 58, and Figure 59 show the midspan static temperature distributions in the three stages. It is seen that the combustion takes place in a short space after the fuel is injected and the hot gas is mixed with the main stream as it moves along the channel. A relatively uniform temperature distribution is achieved by the end of each stator row. That creates a uniform temperature distribution near the rotor blades which improves engine efficiency and performance.

As seen in Figure 57 to Figure 59, the temperature near the stator blade LE's could go up to 1800 K. The high temperature in some areas on the stator blade surfaces could be managed in three ways: (1) indexing the fuel injectors in order to minimize the direct interaction of injector wakes with the stator blade surfaces. For example, in the first stage, this could be done by indexing the one injector which generates a wake hitting the stator LE; (2) use of thermal-barrier coating in some areas on the stator blades. Such coatings are introduced and investigated in many studies such as Padture et al. [97] and Clarke et

al. [98]; (3) design and implementation of a cooling system for the stator blades. Showerhead film cooling may be applied to the stator leading edge area. Different approaches in reducing stator blade surface temperature will be further studied in the next section.

The main factor that affects the rotor performance is the temperature non-uniformity at the rotor inlet. Figure 60a-c shows the temperature distributions at the inlet of each rotor stage. The Non-Uniformity Index (NUI) defined as $(T_{max}-T_{min})/T_{ave}$ is shown for each section. In the calculation of NUI, the thin areas with low temperature near hub and shroud surfaces are excluded. That is because those thin layers are generated intentionally through design to protect the endwalls from the high flame temperature. Based on the results, as the gas moves through the turbine stages, the non-uniformity index may slightly rise. That is due to two reasons: (1) the inlet gas temperatures at the second and third injectors are not fully uniform due to the combustion and incoming non-uniformity from the previous stage. That adds up to the non-uniformity caused by the new injectors which will lead to higher non-uniformity at the next rotor inlet; (2) as the combustion gases pass through rotor, higher density (lower temperature) fluid moves towards the shroud and vice versa. That causes more temperature non-uniformity at the inlet of the next injector which transfers to the rotor inlet. Considering all of the above, the temperature non-uniformity at the inlet of each rotor is quite acceptable. In conventional combustion chambers, the turbine inlet temperature non-uniformity can be up to 40% ([70], [71]) which shows that the current design is performing very well in comparison. Figure 60d shows the temperature distribution at the exit of the third stage.

As seen in this figure, the lower temperature fluid which has higher density has moved towards the shroud and the higher temperature fluid has moved towards the hub. As explained before, this is due to the centrifugal effect as the flow passes through the rotor components.

Table 4 compares the power generated by each turbine stage based on 2D and 3D calculations. The numbers in the first column show the expected values from the 1D/2D design process which are calculated based on the expected enthalpy drop in each stage. The numbers in the second column show the resulted power values from the CFD calcula-

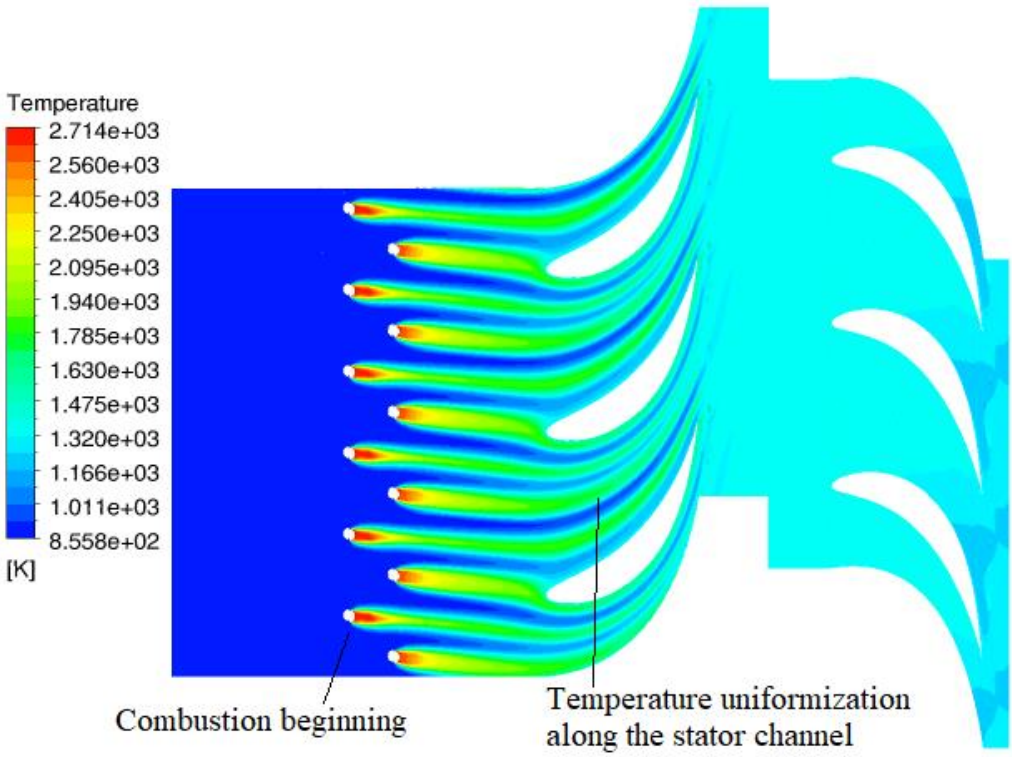

Figure 57. Midspan static temperature distribution in stage 1.

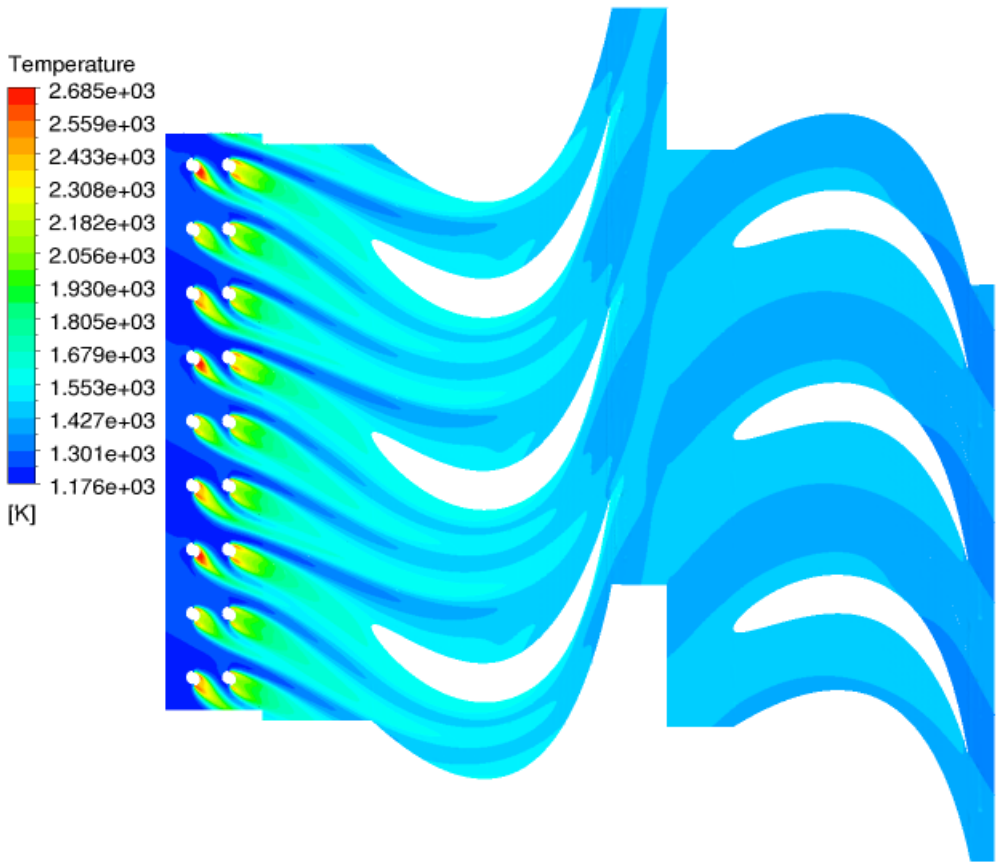

Figure 58. Midspan static temperature distribution in stage 2.

tion. In CFD, the power is calculated based on the torque applied to each blade and the shaft rotational speed ($\dot{W} = T.\omega$). As shown in this table, the power values differ by less than 10% between the two calculation methods. This difference is in the acceptable range and shows a good agreement between the two methods. The difference in the power values is due to the intrinsic differences between 2D and 3D simulations in modeling parameters such as flow patterns, flow angles, average velocity, temperature values, secondary flows, etc. Moreover, the isentropic efficiencies of the blades were estimated in the 1D/2D design

process (not calculated based on the loss models). This is also partially responsible for the difference between the 2D and CFD power values.

Table 5 shows the total pressure loss for each of the three injectors. As seen in this table, the first stage which has 4 injectors per blade has the lowest amount of pressure loss. As the number of injectors increases in the second and third injector units (6 per blade), their pressure losses go up. Another reason for higher pressure losses over the second and third injectors, is larger wakes and vortices as it was observed in Figure 56. The wakes in

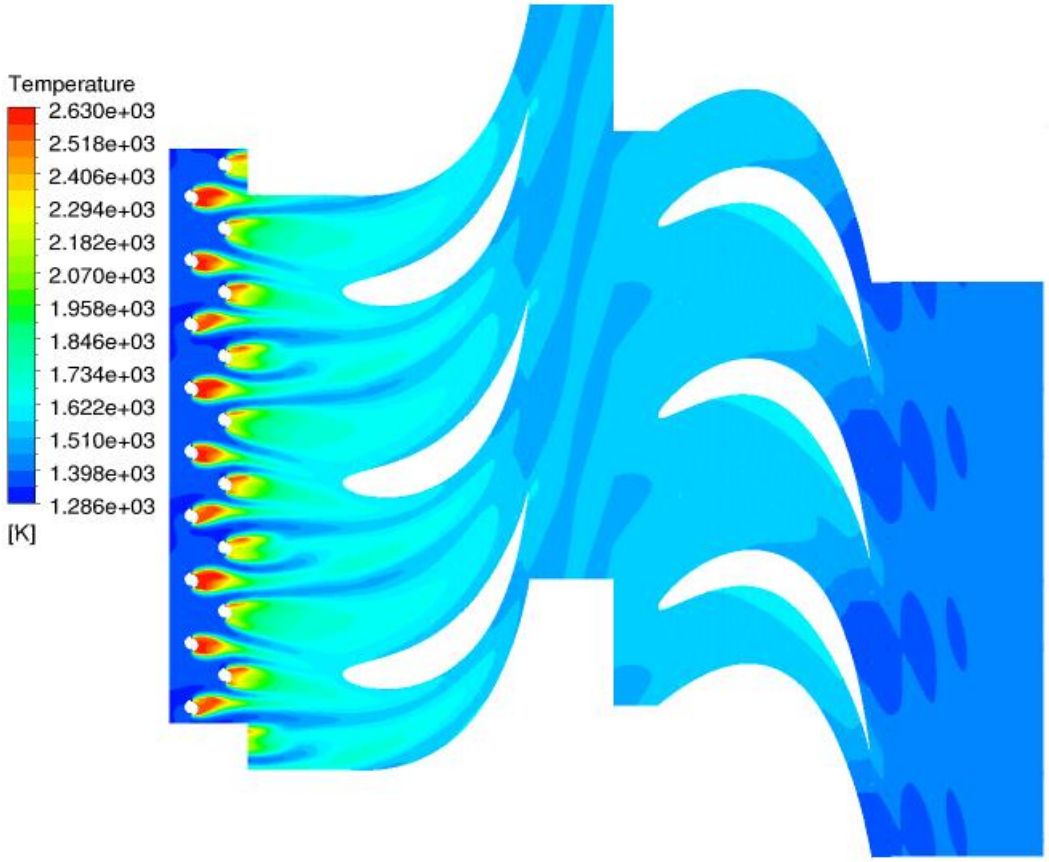

Figure 59. Midspan static temperature distribution in stage 3.

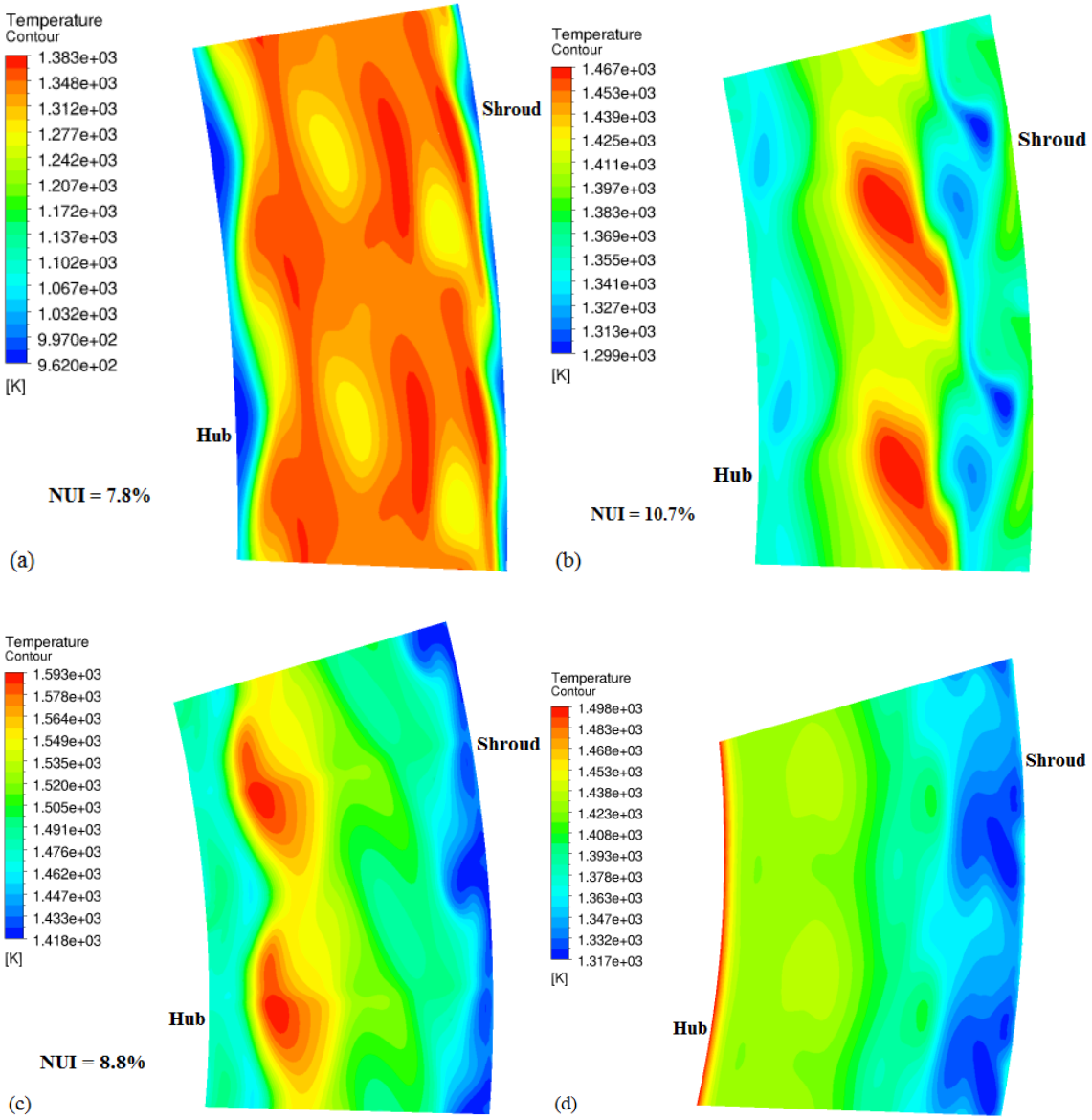

Figure 60. Temperature distribution at different axial locations: (a) stage 1 rotor inlet, (b) stage 2 rotor inlet, (c) stage 3 rotor inlet, (d) stage 3 exit.

Table 4. Comparison between turbine stage power productions calculated by 2D and CFD simulations

	2D design power (MW)	CFD calculated power (MW)	Difference (%)
Stage 1	23.7	21.5	-9.3
Stage 2	26.0	23.6	-9.2
Stage 3	32.5	34.9	+7.4

Table 5. Total pressure loss values in the injector rows

	Total pressure loss (%)
Injector row 1	0.8
Injector row 2	1.9
Injector row 3	2.5

those regions are larger because of lower mainstream pressure. The total pressure loss in all of the three injector components is about 5% which is an acceptable value in comparison with conventional combustion chambers.

Figure 61 shows the average fuel mass fraction in terms of the axial (streamwise) location. As shown in this figure, the fuel particles burn immediately after they are injected into the domain. So the fuel mass fraction goes to near 0% before the flow has reached the stator LE. This provides a proper space for the hot gas to mix with the mainstream flow along the stator channel. When the combustion gas reaches the rotor, the mixture has reached a relatively uniform temperature distribution which provides a proper working environment for rotor. NOx emission at the system exit is 107 ppmv. Considering the high load of the system and multiple steps of fuel injection, and based on the regulated standard emissions (mentioned in [92]), and also in comparison with other studies (Kroniger et al. [99]), the NOx emission of the current system is completely in the acceptable range.

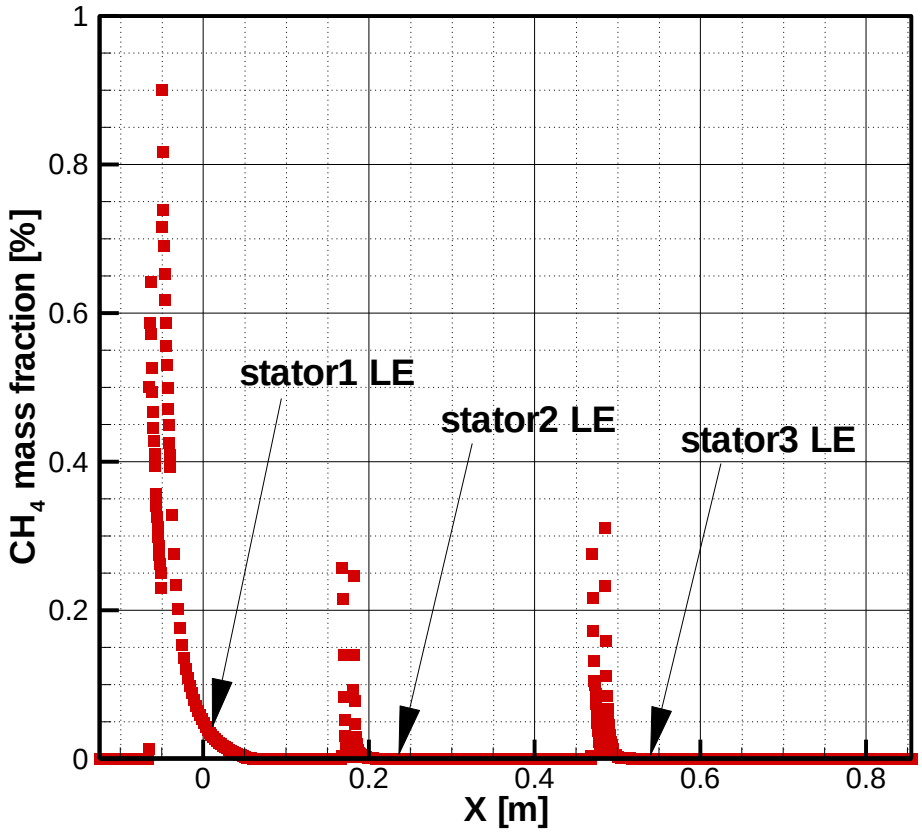

Figure 61. Average fuel mass fraction changes with axial location.

Further modifications such as reducing temperature non-uniformities could lead to lower emissions in future.

V.5. Reducing the Stator Blade Surface Temperature

V.5.1. Introduction and Methodology

One of the issues that we have faced in the design process of UHEGT, is the high temperature on the blade surfaces, especially in stator. Bringing the combustion process into the stator channel makes the blades exposed to the hot combustion gases and

vulnerable to being overheated. To resolve this issue, besides use of thermal-barrier coating and other new materials and manufacturing technologies [97], blade surface temperature needs to be reduced. Two different cooling approaches for stator blades are studied in this section: one is indexing the fuel injectors relative to each other and the stator blades, the other is using film cooling. Both approaches will be discussed in the following paragraphs.

UHEGT uses the inherent vortices in stator channel along with induced vortices by the specifically designed injectors to enhance mixing between air and fuel particles and increase flame stability [15]-[17]. The wakes produced by the injectors carry on the hot combustion gases along the stator channel. These wakes interact with the stator blade surfaces and cause them to exceed their material limits at certain areas. To control the temperature distribution on the blade surfaces, indexing (clocking) method could be used. In this method, the location of the injectors relative to each other and to the stator blades will be adjusted in a way that results in lower temperature distribution over the blade surface. The concept of indexing between the stator and rotor blades of consecutive turbine stages has been studied before by different scholars [94]-[96]. Indexing in conventional gas turbines is considered a way of influencing the flow by changing the circumferential position of rotor-rotor rows and stator-stator rows relative to each other. It is shown that clocking can affect the turbine efficiency by up to 1% which is called *clocking effect*. But, indexing in the current context (between the fuel injectors and stator blades) is a new concept which will be studied in this section.

Another approach to controlling the blade surface temperature is Film Cooling. Film cooling has been used as a common method in recent years to overcome the constantly increasing cycle temperatures in gas turbines and their negative effects on the blade material. The source of the cooling fluid is usually the compressor output air which has high enough pressure to be injected through the cooling holes and low enough temperature to protect the blade material from overheating. Many scholars have studied different film cooling methods and different ways to optimize them. Studies by Schobeiri and coworkers [100], [101], Nirmalan and Hylton [102], Heidmann and co-workers [103], [104], Abuaf and co-workers [105], Jafari et al. [106], Khodabandeh et al. [107], and Volino and co-workers [108]-[110] are only a few examples of the many studies taken place by different scholars on film cooling methods, hole shape design, blowing ratio effects, and combination of unsteady wakes with film cooling. In the current study, one set of film cooling holes on the leading edge and three sets of film cooling holes on each suction and pressure surface of the stator blade will be used to analyze the effects of film cooling in UHEGT.

The first stage of the six-stage UHEGT turbine described previously in this chapter and shown in Figure 52 is used for simulations and analysis in the current section. Four different configurations are studied in this section via Computational Fluid Dynamics (CFD). The first configuration represents the basic scenario which is used as a reference case to evaluate the other configurations. The second and third configurations use indexing approach in order to bring down the stator blade surface temperature. The fourth configuration uses film cooling approach to reduce the surface temperature. Different

performance parameters such as blade surface temperature, rotor inlet temperature distribution, total pressure loss, and total power generation are compared between different configurations to evaluate them. Finally, the pros and cons of each approach are discussed and the best method for controlling the blade surface temperature in UHEGT is designated.

Figure 62 shows the numerical domain used for CFD simulation in the first scenario presented by configuration 1. In this configuration, four injectors are uniformly distributed in front of each stator blade in the circumferential direction. The circumferential location of the injectors relative to the stator blade has not been taken into consideration in this case. In configuration 2, which is designed based on the results of configuration 1, one of the injectors that is located right in front the stator LE is removed. The remaining three injectors are circumferentially distributed between the two adjacent blades while keeping a certain circumferential distance between the injectors and the blade LE (about 0.5 degrees on each side). In configuration 3, four injectors are distributed between the two adjacent blades while still keeping a certain circumferential distance between the injectors and the blade LE. The corresponding positioning of the injectors will be further discussed in the RESULTS AND DISCUSSION section with additional details and figures.

Configuration 4 uses a different approach in reducing the blade surface temperature and that is film cooling. As shown in Figure 63, one set of film cooling is applied to the blade leading edge along with three sets of cooling holes on each suction

and pressure surfaces. 1.5% of the total compressor air output is diverted into the hollow stator blade and injected through the cooling holes (D_{hole}=1 mm). An ejection angle of 35

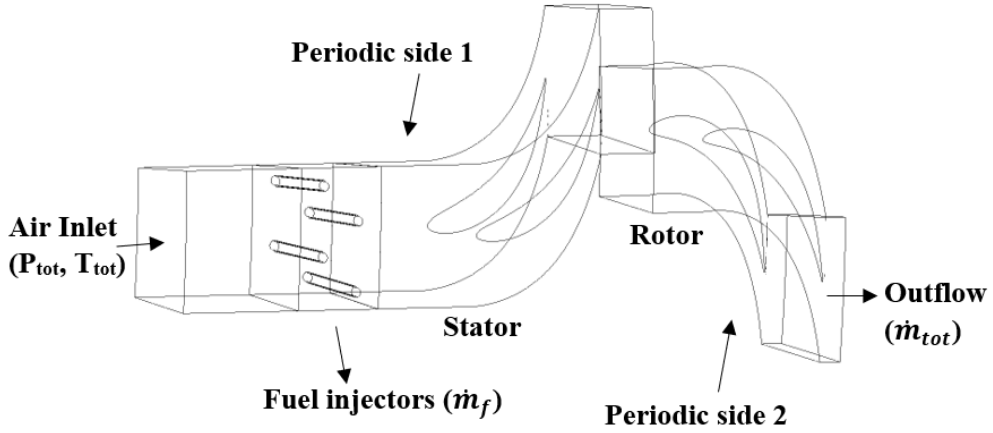

Figure 62. Numerical domain for CFD simulation in configuration 1. The injectors' circumferential locations will be adjusted in configurations 2 and 3.

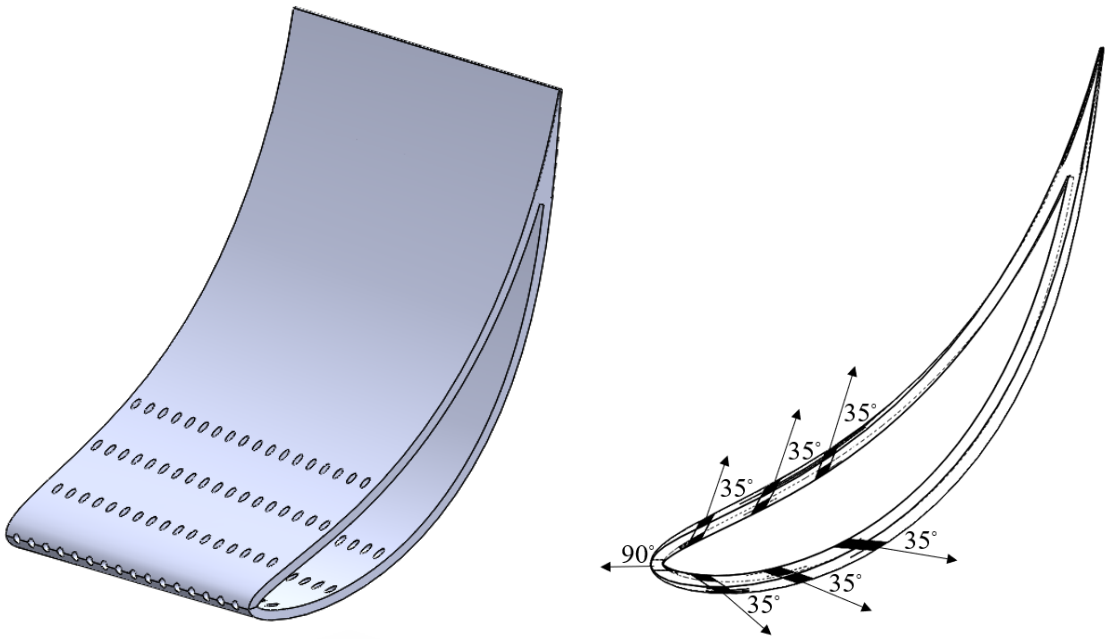

Figure 63. Stator blade with film cooling holes in configuration 4: 3D view (left) and side view (right).

degrees is applied to the cooling holes on the suction and pressure surfaces at each location. This will help to prevent the cooling jets from lift off or separation from the surface [100]. The blowing ratio ($M = \frac{\rho_j V_j}{\rho_\infty V_\infty}$) for the cooling jets is about 1. This blowing ratio has been chosen because it provides enough power for the jet to penetrate the main flow while preventing it from separating from the blade surface. Moreover, the mixing losses are minimum at this blowing ratio [100], [101].

V.5.2 Results and Discussion

Figure 64 shows the midspan Mach number distribution and velocity vectors in configuration 1. As shown in this figure, the flow is closely following the blade metal angle and the incidence angle is minimized in stator and rotor. The maximum Mach number in the rotor throat does not exceed 0.85 which represents a subsonic flow along the entire passage. Moreover, the approaching flow Mach number is about 0.1 which provides a suitable environment to achieve a stable combustion process [60], [62]. The Mach number distribution and velocity vectors in configurations 2 to 4 are similar to configuration 1 with slight differences. Therefore, the figures have not been presented independently to avoid repetition. Moreover, it should be mentioned that the stage power calculated by the CFD simulation in configuration 1 (23.0 MW) only slightly differs from the results of meanline calculation (22.1 MW). Similar agreement is observed in other parameters such as velocity, pressure, temperature, etc. This further validates the results of both simulations, considering the two methods use completely different approaches and tools to solve the problem.

Figure 65 shows the midspan temperature distribution in the four configurations. As shown in the figure on top left, the temperature is uniformized along the stator channel and a uniform temperature distribution is achieved over the rotor. But, due to a direct interaction between one of the injectors' wakes and the stator blade, the temperature on the blade surface is increased to a high level (above 1600 K). This would negatively affect the overall performance of the system by requiring the stator blade to be cooled down due to material limitations. In order to avoid the direct interaction between the stator blade and the injectors wakes, the injectors are indexed relative to the stator blade in the second and third configurations. In the second configuration which is shown in Figure 65 top right, the one injector that was located in front of the stator LE in the previous configuration is removed. In this scenario, three injectors are distributed in the circumferential space between the two adjacent stator blades and a certain circumferential distance is kept between the injectors and the LE's of the blades. The results show that a cool layer of flow is preserved near the stator blade surface in this case. The temperature in this layer is nearly the same as the compressor exit temperature which can completely protect the blade from the high flame temperature. On the other hand, it is seen that the temperature distribution over the rotor in this configuration is not as uniform as configuration 1, which can adversely affect the system performance. In configuration 3, shown in Figure 65 bottom left, four injectors are distributed in the circumferential space between the two adjacent blades while keeping a certain circumferential distance from the LE's of the blades. Adding one injector between the two blades could potentially increase the temperature uniformity over the rotor blades. As seen in the figure, the cool layers of air

near the stator blade surfaces are still preserved in this case, but the temperature distribution over the rotor is not significantly improved compared to configuration 2. This shows that adding the number of injectors between the two blades, cannot necessarily increase the temperature uniformity in the rotor channel. Configuration 4 takes a different approach to bringing down the blade surface temperature and that is to use film cooling. In this configuration, the injectors are located at the same positions as configuration 1. But 1.5 percent of the incoming compressor air is diverted into the film cooling holes distributed on the stator LE, SS, and PS. Figure 65 bottom right, represents the midspan

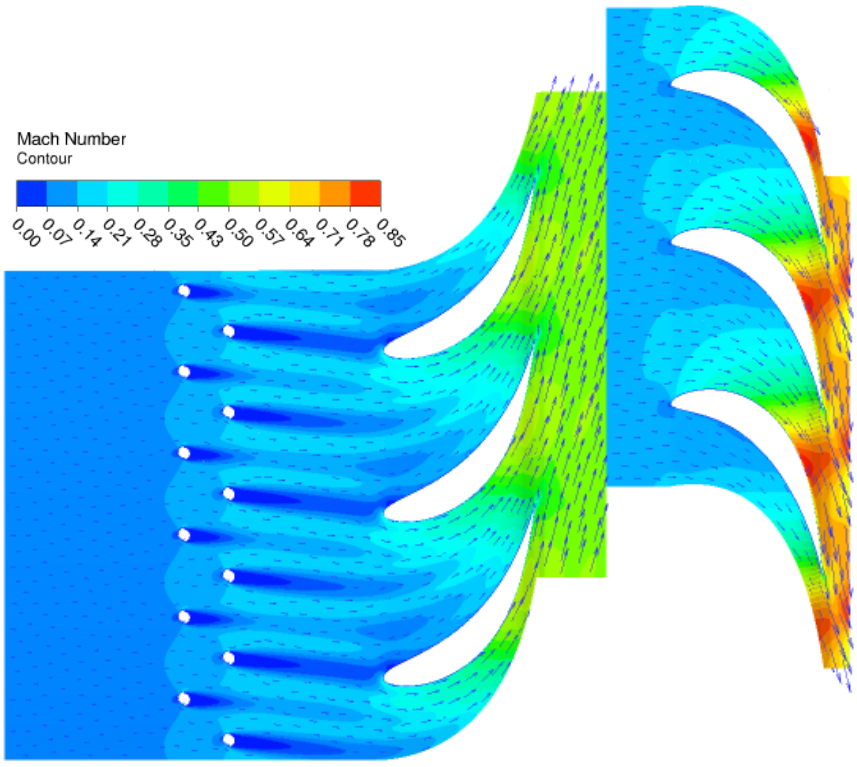

Figure 64. Midspan Mach number distribution and velocity vectors for configuration 1. The distribution is similar for the other configurations as well.

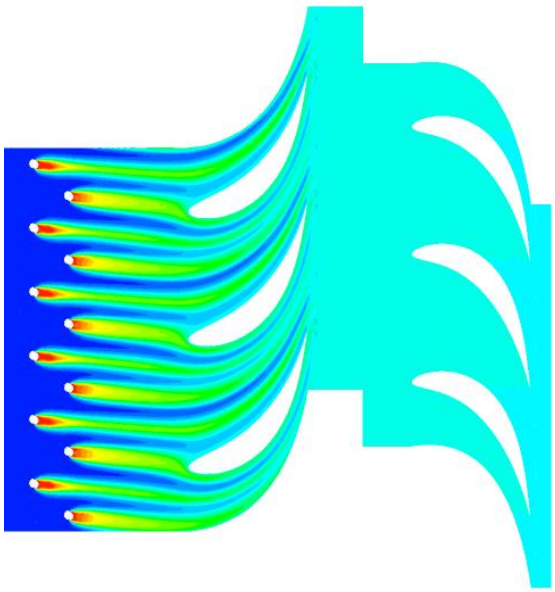

Config. 1: Midspan temperature distribution

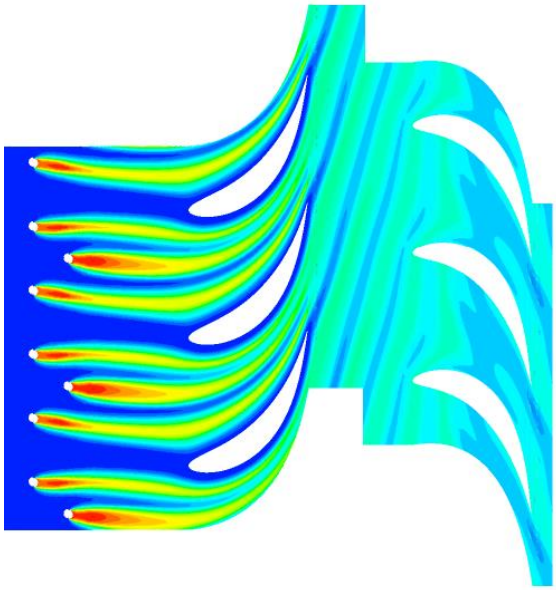

Config. 2: Midspan temperature distribution

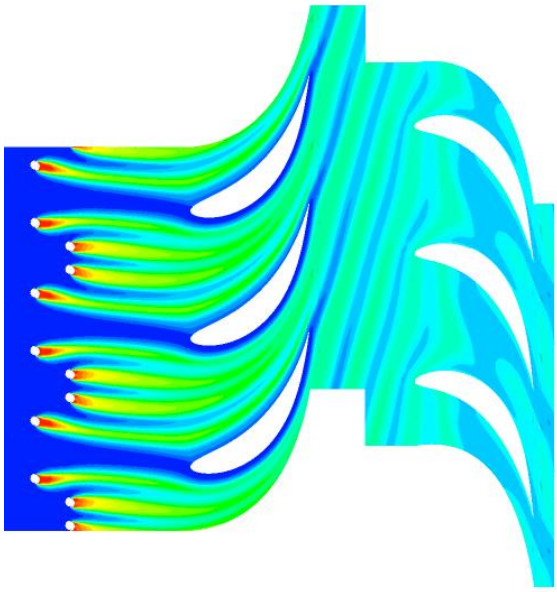

Config. 3: Midspan temperature distribution

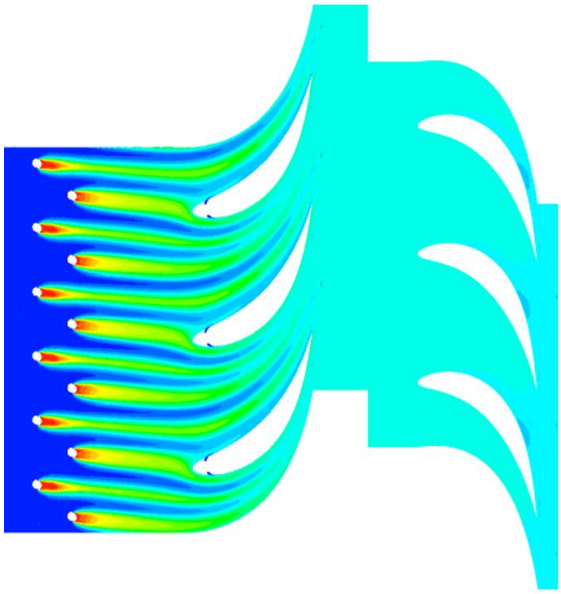

Config. 4: Midspan temperature distribution

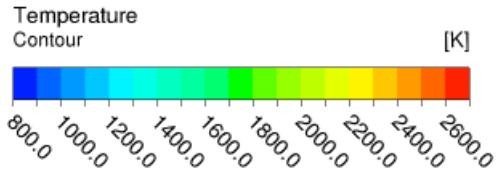

Figure 65. Midspan temperature distribution for the four configurations.

temperature distribution for this case. The results show a similar pattern for this configuration and configuration 1 at this scale. But a closer look at the blade surface temperature distribution in the next figure will reveal how much difference the film cooling holes are actually making in bringing down the blade surface temperature.

Figure 66 shows the blade surface temperature on stator PS and SS for all different configurations. As shown in this figure, for configuration 1, temperature would go up to 1600 K on the suction side. This temperature is relatively high and requires the blade to be cooled down due to material limitations. In configurations 2 and 3, as shown in the picture, indexing the injectors and the stator blade has led to a significant reduction in the blade surface temperature. The temperature on these surfaces is nearly as low as the compressor air temperature which is ideal for the blade surfaces and completely protects them from the high temperature of the combustion gas. This demonstrates the high effectiveness of the indexing method in order to control the temperature distribution on the blade surfaces. The results for the film cooled blade in configuration 4 are shown in the last part of Figure 66. As shown in this picture, the cooling fluid has successfully brought down the blade surface temperature in all locations. In the areas near the film cooling holes the temperature is dropped significantly, while in the farther areas the temperature drop is relatively lower. Figure 67 shows the film cooling effectiveness ($\eta = \frac{T_\infty - T_w}{T_\infty - T_c}$) contours on stator blade pressure and suction surfaces in configuration 4. As shown in this figure, film cooling effectiveness has its maximum value at about 1 at the exit of each cooling hole. By getting further away from the cooling holes, the values are reduced. The minimum film cooling effectiveness is about 0.1 which takes place on the suction

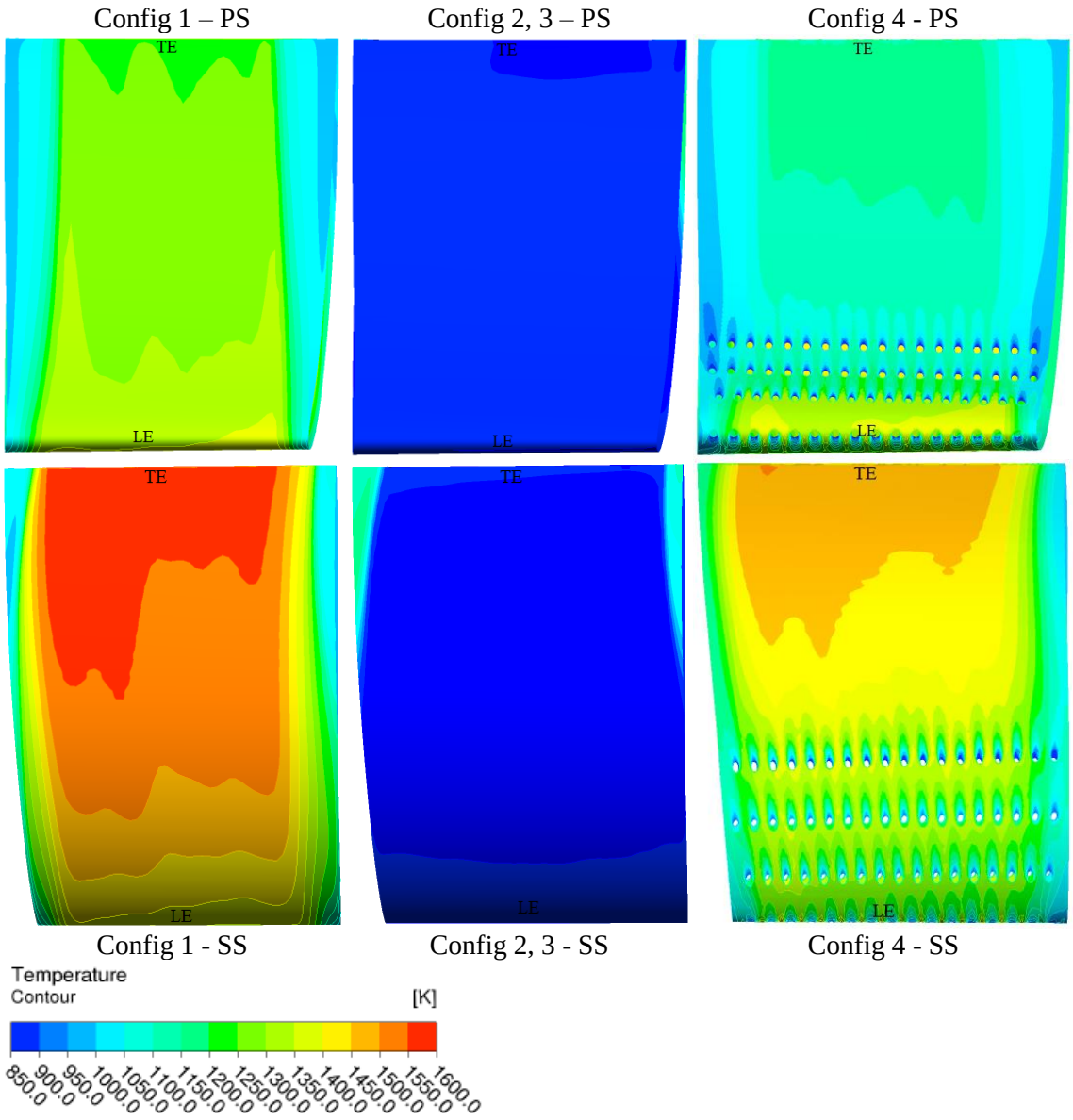

Figure 66. Stator blade surface temperature distribution for all configurations: Configuration 1 represents the basic case with uniformly distributed injectors in the circumferential direction; Configurations 2 and 3 represent the case with the indexed injectors; Configuration 4 represents the film cooled stator blade.

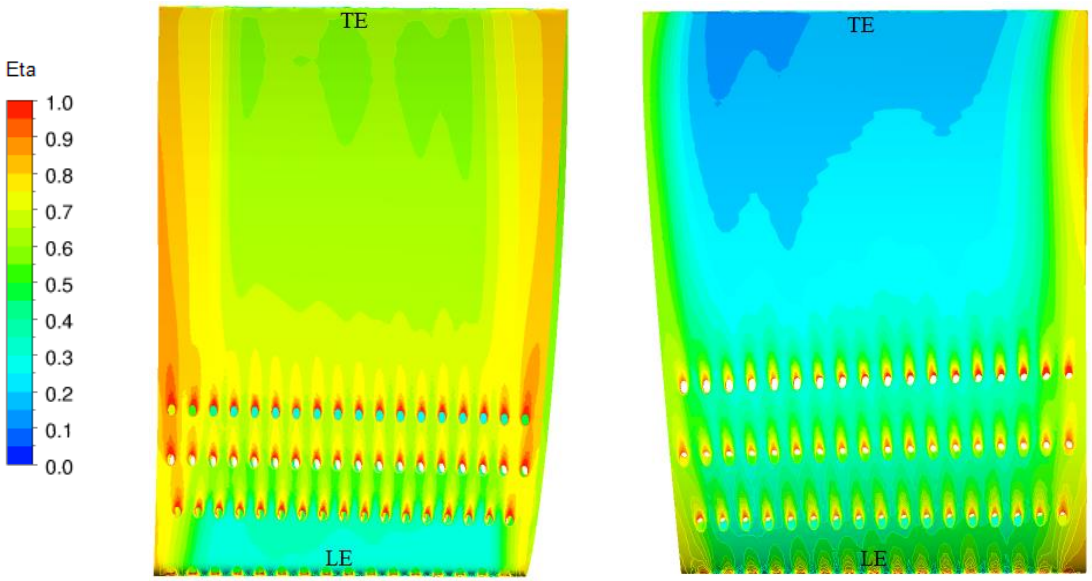

Figure 67. Film cooling effectiveness contours on stator blade, configuration 4: PS (left), SS (right).

surface near the TE. The maximum surface temperature is reduced by about 100 degrees in this area.

By comparing the results of configurations 2 and 3 with configuration 4, all shown in Figure 66, it is clear that although film cooling method is effective in bringing down the blade surface temperature, it is not as highly effective as the indexing method. Using indexing in configurations 2 and 3, the blade surface temperature has been completely brought down to near compressor air temperature which is regularly used for cooling. But in configuration 4 which uses film cooling, the temperature drop is not as strong as the previous two configurations. This further proves the high effectiveness of the indexing method in lowering the stator blade surface temperature.

Now it is time to take a look at the temperature distribution at the rotor inlet resulted from different configurations which is shown in Figure 68. As shown in this figure, the temperature at this section is highly uniform in configuration 1, relatively uniform in configuration 4, and less uniform in configurations 2 and 3. The Non-Uniformity Index (NUI, defined as $(T_{max}-T_{min})/T_{ave}$) is 4.1, 26.2, 27.2, and 6.3 percent for configurations 1 to 4, respectively. This shows that although configurations 2 and 3 are very successful in lowering the blade surface temperature, they produce a relatively non-uniform temperature distribution at the rotor inlet compared to the other cases. The higher temperature non-uniformity at rotor inlet could potentially affect the system performance adversely by reducing rotor power production and causing thermal fatigue. This will be further discussed in the following paragraphs. Moreover, due to centrifugal (buoyancy) effect on the flow in rotor, higher density (lower temperature) flow moves towards the shroud and vice versa [111]-[113].

Table 6 shows a comparison between different performance parameters resulted from different configurations. The average stator surface temperatures are shown in the second column. The results show that indexing the injectors with the stator blade in configurations 2 and 3 significantly brings down the blade surface temperature. In configuration 2, the average blade surface temperature is about the compressor output air temperature which is commonly used for cooling. This temperature is ideal for the blade metal and completely protects it from the hot gases in the main channel. Moreover, using film cooling in configuration 4, the average surface temperature is reduced by about 107 degrees which is noticeable and shows the effectiveness of the utilized film cooling meth-

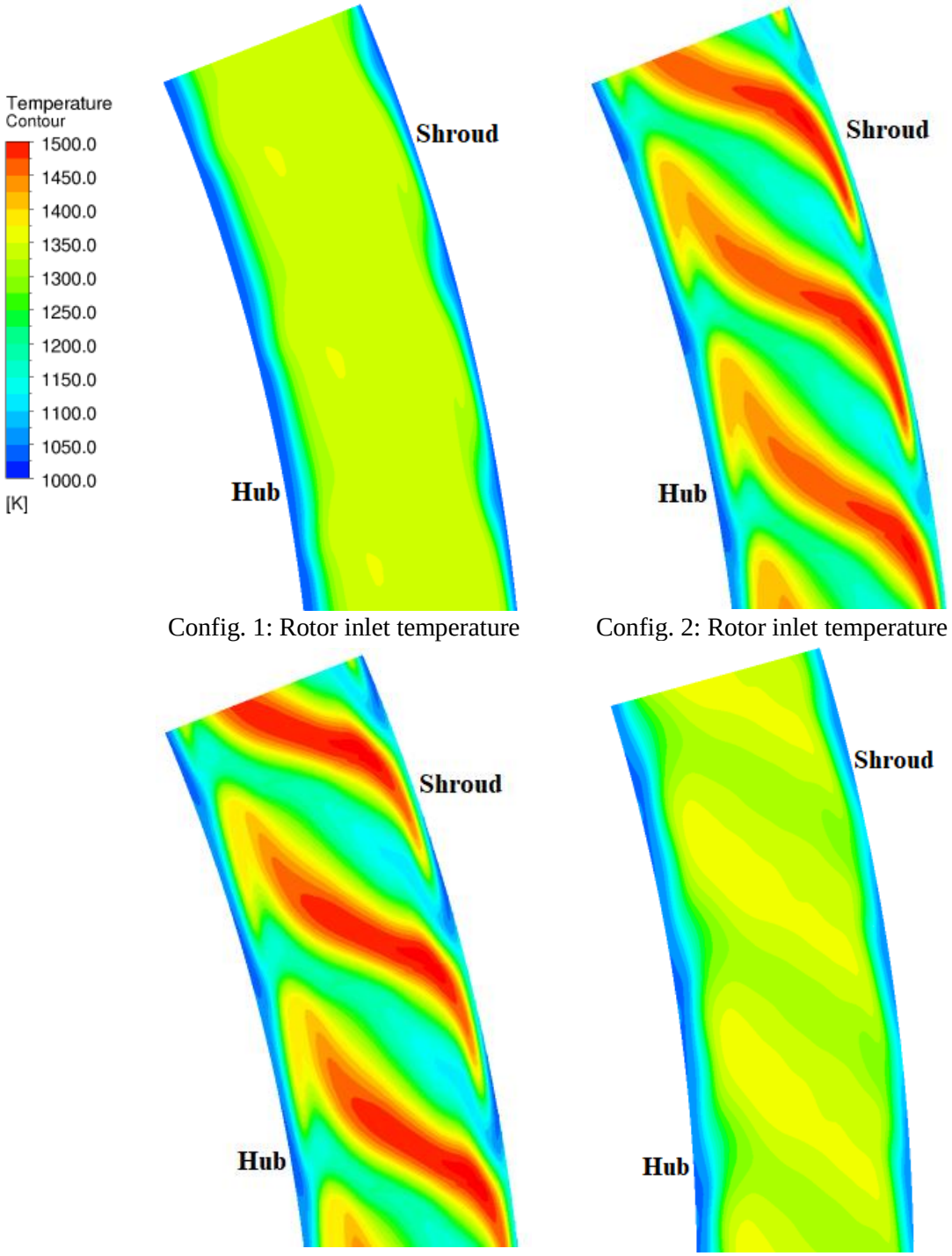

Config. 1: Rotor inlet temperature

Config. 2: Rotor inlet temperature

Config. 3: Rotor inlet temperature

Config. 4: Rotor inlet temperature

Figure 68. Rotor inlet temperature distribution for the four configurations.

Table 6. Comparison of the performance parameters between different configurations

	Average stator surface temp. (K)	Rotor inlet temp. NUI (%)	Rotor power generation (MW)	Total pressure loss over injectors (%)
Config 1	1341.0	4.1	23.0	0.68
Config 2	855.2	26.2	22.5	0.57
Config 3	887.0	27.2	22.8	0.73
Config 4	1233.7	6.3	22.8	0.69

od. In the third and fourth columns of the table, rotor inlet temperature non-uniformity index and rotor power production values can be observed. Based on the results, the non-uniformity index is much higher in configurations 2 and 3. This higher NUI means more hotspots which could negatively affect the rotor blade material [66], [69]. However, NUI at the current levels for configurations 2 and 3 is still lower than many industrial engines which could have nonuniformities as high as 40% and more ([70], [71]). Moreover, as seen in the fourth column, the higher NUI in configurations 2 and 3 does not lower the power generated by rotor. The injectors total pressure loss values are also compared in the last column of the table. Based on the results, configuration 2, which uses the least number of injectors per blade (3), produces the least amount of total pressure loss. That would be even more considerable when the injectors are used in the second and third turbine stages in UHEGT where the pressure loss caused by injectors tends to be higher [17]. Also, it is seen that configuration 3 has a slightly higher pressure loss compared to configuration 1. That is because of the injectors in the second row of configuration 3 are located close to each other.

Overall, based on the results, configuration 2 produces the best temperature distribution over the stator blade surface, generates the least amount of total pressure loss

over the injectors, uses the lowest number of injectors per blade, generates almost the same amount of power as other configurations, and it is the easiest configuration to manufacture. No further cooling would be required while using this configuration. Therefore, configuration 2 can be considered as the best option in reducing the stator blade surface temperature among the cases studied in this research. However, it should be noted that higher NUI in configuration 2 compared to other configurations leads to more hotspots in rotor which could negatively affect the rotor blade material and blade life [66], [69]. Therefore, if this configuration is used, rotor surface temperature should be studied closely, and appropriate cooling strategy should be employed. The second-best option would be configuration 4 which uses film cooling and effectively reduces the average surface temperature by more than 100 degrees. This configuration produces a highly uniform temperature distribution at the rotor inlet as well.

Finally, it should be mentioned that for the second and third turbine stages with stator internal combustion, a similar approach could be used to optimize the temperature distribution. Based on the results presented in section V.4, the temperature distribution in each stage is mainly dependent on the arrangement of the burners in the same stage. That means most hotspots are damped and the temperature distribution is more uniform at the exit of each stage due to the interactions with rotor. Therefore, the fuel injectors need to be indexed based on the flow patterns and temperature distribution in each stage. Moreover, use of film cooling is recommended for the rotor blades.

CHAPTER VI

ENGINE SIMULATION IN DESIGN, OFF-DESIGN AND DYNAMIC OPERATION

VI.1. Introduction

A gas turbine engine goes through variable performance conditions throughout its life which include design and off-design conditions such as start-up, shutdown, load change, change of altitude, etc. Operating in the dynamic state requires changing the fuel mass flow regularly or randomly. To simulate the engine as a whole through these variable conditions, we cannot use four-dimensional space-time CFD simulations because they are too heavy and cannot run the entire engine model at once in the current computational capacities. The best alternative in this situation is a 2D space-time simulation. This type of simulation enables us to study the entire engine at the same time through variable time-dependent conditions. For this purpose, the computer code GETRAN developed by Schobeiri and described in NASA reports [30]-[32], Schobeiri's text books [1], [5] and articles [114], [115] is used. GETRAN is a generic modular non-linear code in FORTRAN which is developed to simulate the dynamic behavior of single- and multi-spool high pressure core engines, turbofan engines, and power generation gas turbines. The theoretical background including engine structure, governing equations, and certain

component geometries for the current simulation will be discussed in the following sections.

VI.2. Theoretical Background

VI.2.1. The Engine Structure

3D Model: Figure 69 shows the cross section of the complete UHEGT model with a six-stage turbine and three stages of stator internal combustion. This engine was designed and analyzed via CFD in the previous chapter. As shown in Figure 69, the assembly consists of three main components: compressor on the left, connection piece in the middle, and turbine on the right. The compressor is created by and taken from Widyanto [116]. Different components such as inlet nozzle, exit diffuser, shaft, casing, blades, injectors, journal bearings, etc. can be seen in this figure. Figure 70 shows the 3D model of the rotor and casing.

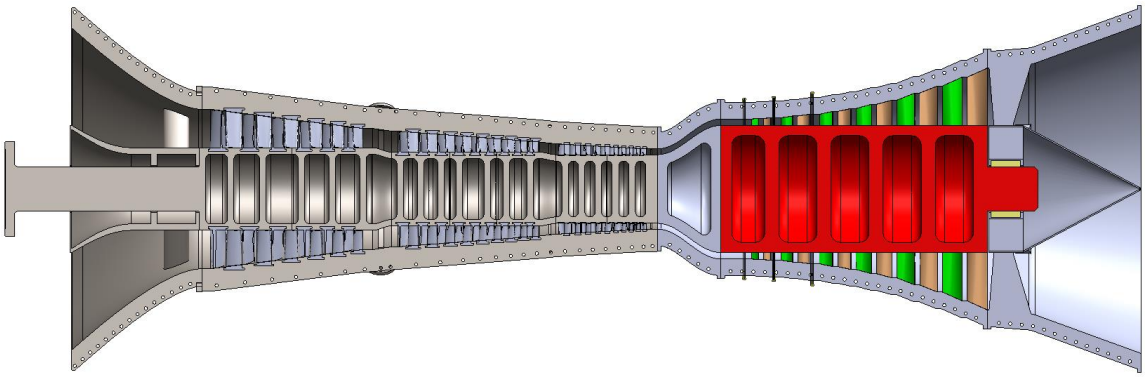

Figure 69. UHEGT, cross section of the complete assembly. The assembly consists of three main components: Compressor on the left, connection piece in the middle, and turbine on the right.

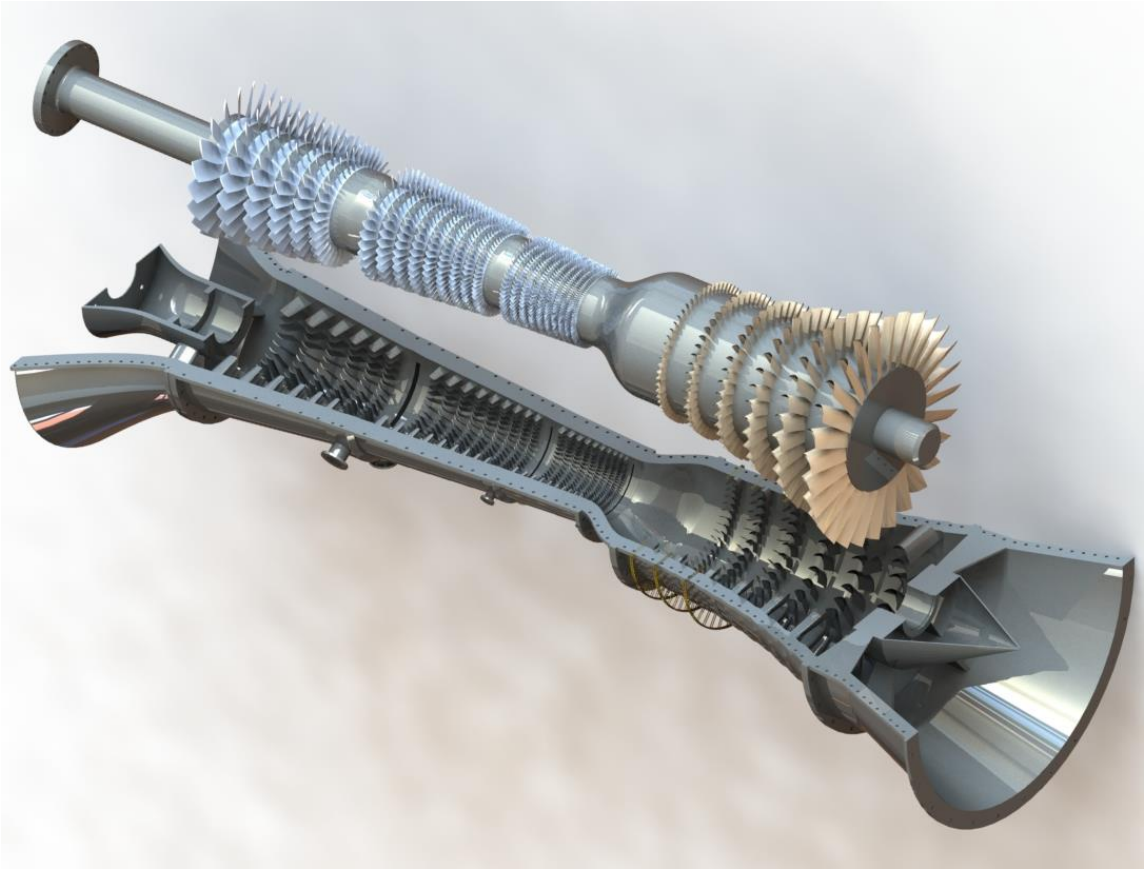

Figure 70. UHEGT, 3D model of the rotor and casing.

GETRAN Simulation Schematic: Figure 71 shows the simulation schematic for this engine which will be used for the simulation via GETRAN. As shown in this figure, the system is a single-spool single-shaft engine with four sets of compressor rows, three combustors which represent the injector rows, four sets of turbines which have six stages overall, three controllers, fourteen plena, an inlet nozzle, an exit diffuser, a generator, fuel and bypass valves, and multiple pipes. GETRAN is a fully modular code which can take any number and combination of components in the system. These components are coupled to one another via plena. Each component sends and receives information (i.e. mass flow,

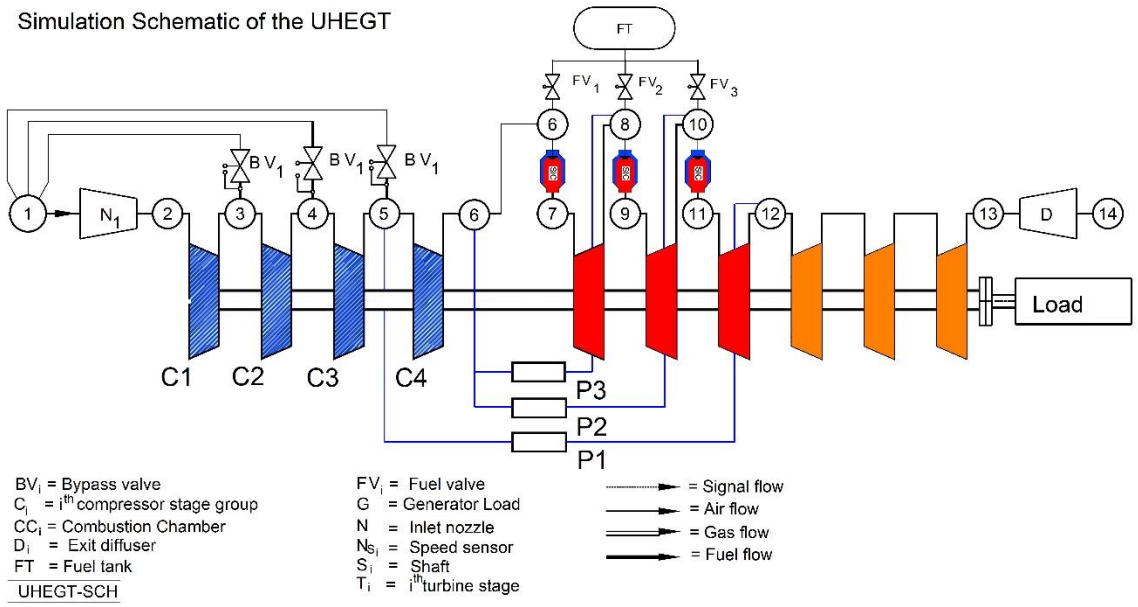

Figure 71. Simulation schematic of UHEGT (by Schobeiri).

total pressure, total temperature, etc.) to and from the corresponding plena. The plenum acts as a mixing hub for all the incoming data and it exports the information to the receiving components. Each component is represented by a set of Partial Differential Equations (PDEs) in its corresponding module. The PDEs include the continuity, momentum, and energy equations in each corresponding thermo-fluid region plus conduction PDE in the metal areas in between. The governing equations are discussed in the next section.

VI.2.2. Governing Equations

Conservation of Mass: For an unsteady flow, the conservation of mass is described as [1],

$$\frac{\partial \rho}{\partial t} = -\nabla \cdot (\rho \boldsymbol{V}) \tag{6.1}$$

With V as velocity and ρ as density. This equation in 2D space-time is translated as,

$$\frac{\partial \rho}{\partial t} = -\frac{\partial}{\partial x}\left(\frac{\dot{m}}{s}\right) \tag{6.2}$$

In which x is the axial location, $\dot{m}$ is the mass flow rate, and $S=S(x)$ is the cross-sectional area. To develop a numerical solution for this PDE, the flow field is uniformly divided into discrete zones with prescribed length ΔX [1]. Figure 72 shows a discretized flow path with changing cross section $S=S(x)$. Based on the discretized flow path, the conservation of mass is approximated as,

$$\frac{\partial \rho_k}{\partial t} = -\frac{1}{\Delta X}\left(\frac{\dot{m}_{i+1}}{S_{i+1}} - \frac{\dot{m}_i}{S_i}\right) \tag{6.3}$$

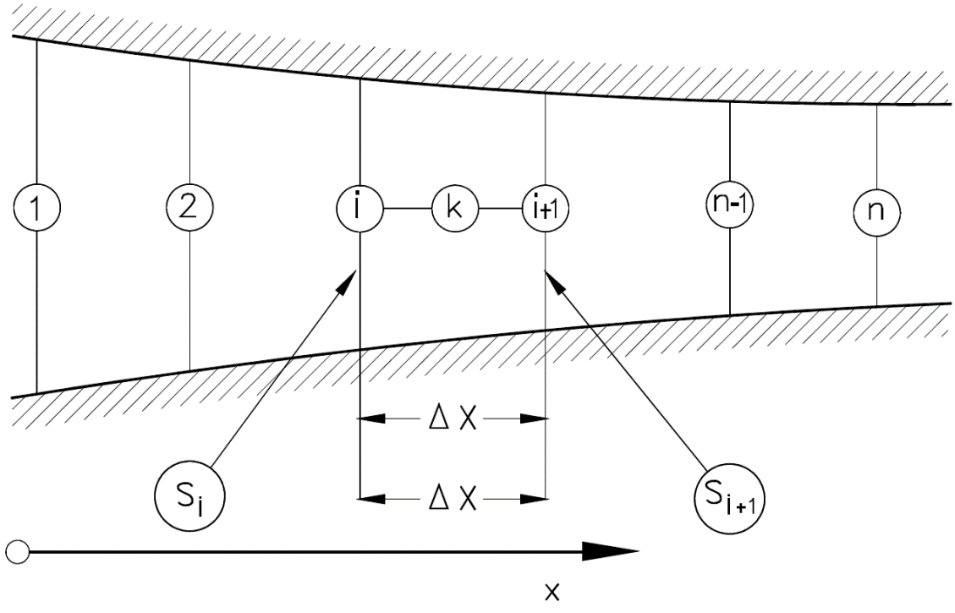

Figure 72. Discretized flow path with changing cross section $S=S(x)$; Reprinted from Schobeiri [1].

In which the index k refers to the axial position at $\Delta X/2$.

Equation of Motion: The equation of momentum in the index notation is described as,

$$\frac{\partial(\rho V_i)}{\partial t} = -\frac{\partial}{\partial x_j}\left(\rho V_i V_j\right) - \frac{\partial p}{\partial x_i} + \frac{\partial T_{ij}}{\partial x_j} \tag{6.4}$$

In which the divergence of shear stress tensor $\nabla \cdot T = e_i \partial T_{ij}/\partial x_j$ represents the shear force acting on the surface of the element. In a one-dimensional flow, the only non-zero term is related to the wall shear stress τ_w that can be expressed in terms of friction coefficient c_f as,

$$\tau_w = c_f \frac{\rho}{2} V^2 \tag{6.5}$$

Considering that the shear stress is zero outside of the boundary layer, and by replacing Δy by the characteristic length hydraulic diameter D_h, after inserting all variables and simplification, the momentum equation for a discretized domain will be approximated as [1],

$$\begin{aligned}\frac{\partial \dot{m}_k}{\partial t} = &-\frac{1}{\Delta \mathrm{x}}\left(\dot{m}_{i+1}V_{i+1} - \dot{m}_i V_i + p_{i+1}S_{i+1} - p_i S_i\right) \\ &+ \left(\frac{\dot{m}_k V_k + P_k S_k}{S_k}\right)\left(\frac{S_{i+1} - S_i}{\Delta x}\right) - c_f \frac{\dot{m}_k^2}{2 D_{h_k} \rho_k S_k}\end{aligned} \tag{6.6}$$

The Energy Equation: The energy equation can be expressed in terms of total enthalpy H in index notation as,

$$\frac{\partial H}{\partial t} = -kV_i \frac{\partial H}{\partial x_i}$$

$$-\frac{\kappa - 1}{\rho}\left((H + K)\frac{\partial(\rho V_i)}{\partial x_i} + \frac{V_i \cdot \partial(\rho V_i)}{\partial t}\right) \tag{6.7}$$

$$-\frac{\kappa}{\rho}\left(\frac{\partial \dot{q}_i}{\partial x_i} - \frac{\partial\left(V_j T_{ij}\right)}{\partial x_i}\right)$$

In which K is the kinetic energy, k is the fluid conductivity, and κ is the heat capacity ratio. In a one-dimensional flow, the work by shear stress compared to the enthalpy is negligible. Thus, after simplification, the energy equation in terms of total enthalpy for a discretized flow path can be approximated as [1],

$$\frac{\partial H}{\partial t} = -\kappa_k \frac{\dot{m}_k}{\rho_k S_k}\left(\frac{H_{i+1} - H_i}{\Delta x}\right)$$

$$-\left(\frac{\kappa - 1}{\rho}\right)_k \left[\left(\frac{H_k + K_k}{\Delta x}\right)\left(\frac{\dot{m}_{i+1}}{S_{i+1}} - \frac{\dot{m}_i}{S_i}\right) + \frac{\dot{m}_k}{\rho_k S_k^2}\frac{\partial \dot{m}_{i+1}}{\partial t}\right] \tag{6.8}$$

$$-\frac{\kappa_k}{\rho_k}\left(\frac{\Delta \dot{Q} + \Delta L}{\Delta V}\right)$$

VI.2.3. Numerical Approach

The above equations on all components create a system of coupled PDEs that need to be solved using a numerical approach. An implicit method described below will be used for this purpose. The system of PDEs can be represented by a system of Ordinary Differential Equations (ODEs) as,

$$\frac{dX}{dt} = G(X, t) \tag{6.9}$$

In which X is the state vector. Knowing the X vector at time t, it can be approximated at time t+dt by,

$$X_{t+\Delta t} = X_t + \frac{1}{2}\Delta t(G_{t+\Delta t} + G_t) \tag{6.10}$$

which can be rewritten in terms of a nonlinear function $F(X_{t+\Delta t})$ as,

$$X_{t+\Delta t} - X_t - \frac{1}{2}\Delta t(G_{t+\Delta t} + G_t) = F(X_{t+\Delta t}) \tag{6.11}$$

This equation can be used to determine X_{t+dt} based on X_t. The iteration process will continue until the vector converges or the maximum number of iteration is achieved. In case the vector is not converged by the maximum number of iterations, the time interval Δt will be halved and the process is repeated [1].

VI.2.4. Engine Components and Simulation Schematics

As mentioned before, the current model includes four sets of compressor rows, three combustors which represent the injector rows, four sets of turbines which have six stages overall, three controllers, fourteen plena, an inlet nozzle, an exit diffuser, a generator, fuel and bypass valves, and multiple pipes. *Engine Schematics* or modular representations are vital for the proper description and simulation of the engine components. The schematics are important in that they portray the spatial location of each component in the system and the corresponding inlet and outlet flows. Figure 73 shows some of the system components and their modular representations. Detailed analysis method for common components such as inlet nozzle, exit diffuser, pipes, valves, etc. can be found in [30] and [1]. The models for these components are developed based on the

user defined geometries and matched with the combination of other major components (i.e. compressor, turbine, combustion chamber, etc.).

Compressor: For the compressor, a global compressor is used where performance is obtained from polynomial maps. In the current model, there are four sets of global compressors where the coefficients are specified and taken from Schobeiri [31]. Values for pressure, temperature, and cross section area are specified at the inlet and exit of each

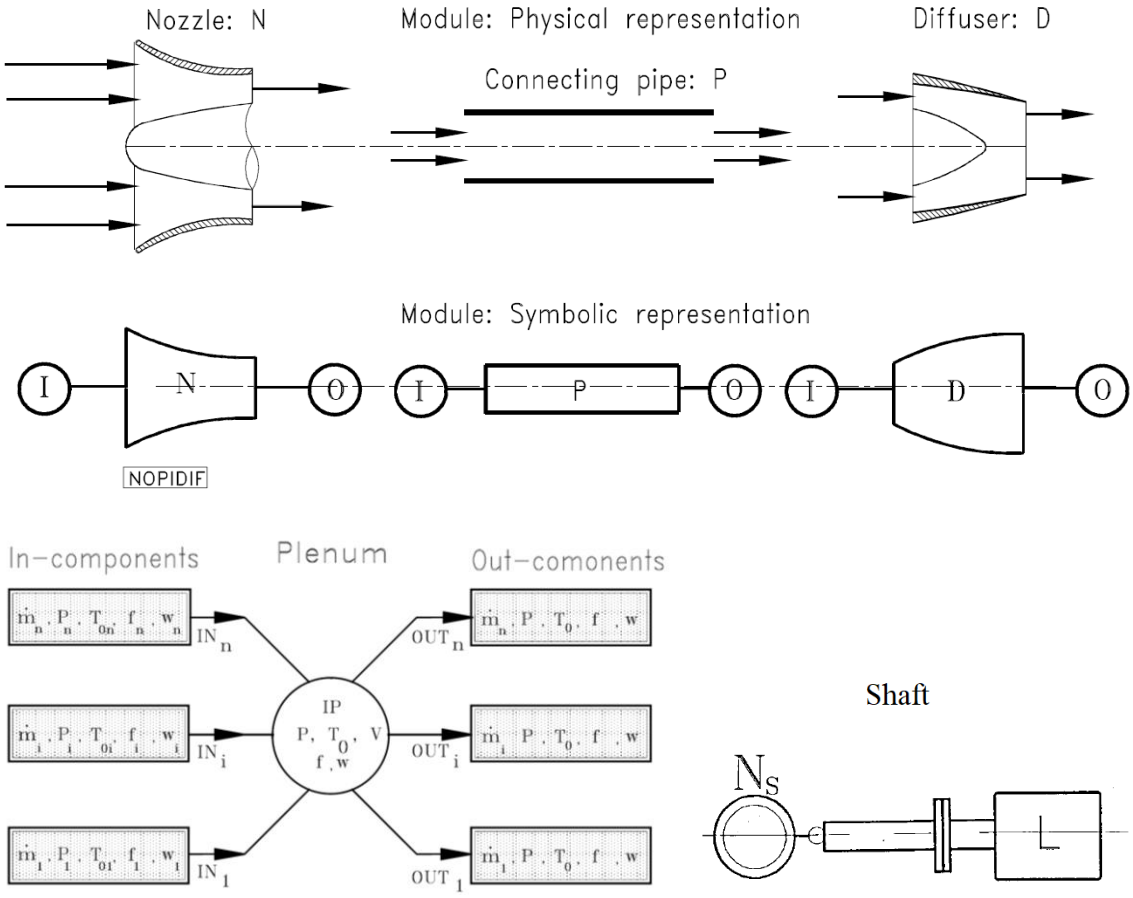

Figure 73. System components and their modular representation; Reprinted from Schobeiri [1].

compressor set. These values are based on the compressor designed by Widyanto [116]. Further details regarding the compressor simulation model and performance maps can be found in [1] and [30].

Turbine: There are four sets of turbines in the current design: the first three stages which are preceded with injector rows create turbine sets 1 to 3, and the last three stages with conventional gas expansion create turbine set 4. For the turbine, a row-by-row calculation method is used, in which the turbine performance is directly computed based on each stator and rotor row's geometry. In this method, the geometrical parameters such as mean diameter, blade height, and inlet and exit angles for each stator and rotor row are specified in the input file. Figure 74 shows the schematic representation of consecutive adiabatic turbine stages in row-by-row calculation. As shown in this figure, each stage is decomposed into two rows that are connected with each other via the middle plenum. More details regarding the row-by-row calculation process for turbine can be found in [1].

Injector Rows: In order to model the injector rows in UHEGT, a tubular combustion chamber, shown in Figure 75, is modified. For this purpose, the combustion chamber is scaled down in both axial and radial directions. Two independent scale factors are used in axial and radial directions for each combustion stage. The resulted combustion volume at each stage will be equal to the combustion volume at the corresponding injector row. Figure 76 shows a schematic representation of the injector components in UHEGT used in the current simulations. The combustion volume is calculated based on the length, width, and height of the injector component as shown in the figure. Based on the structure

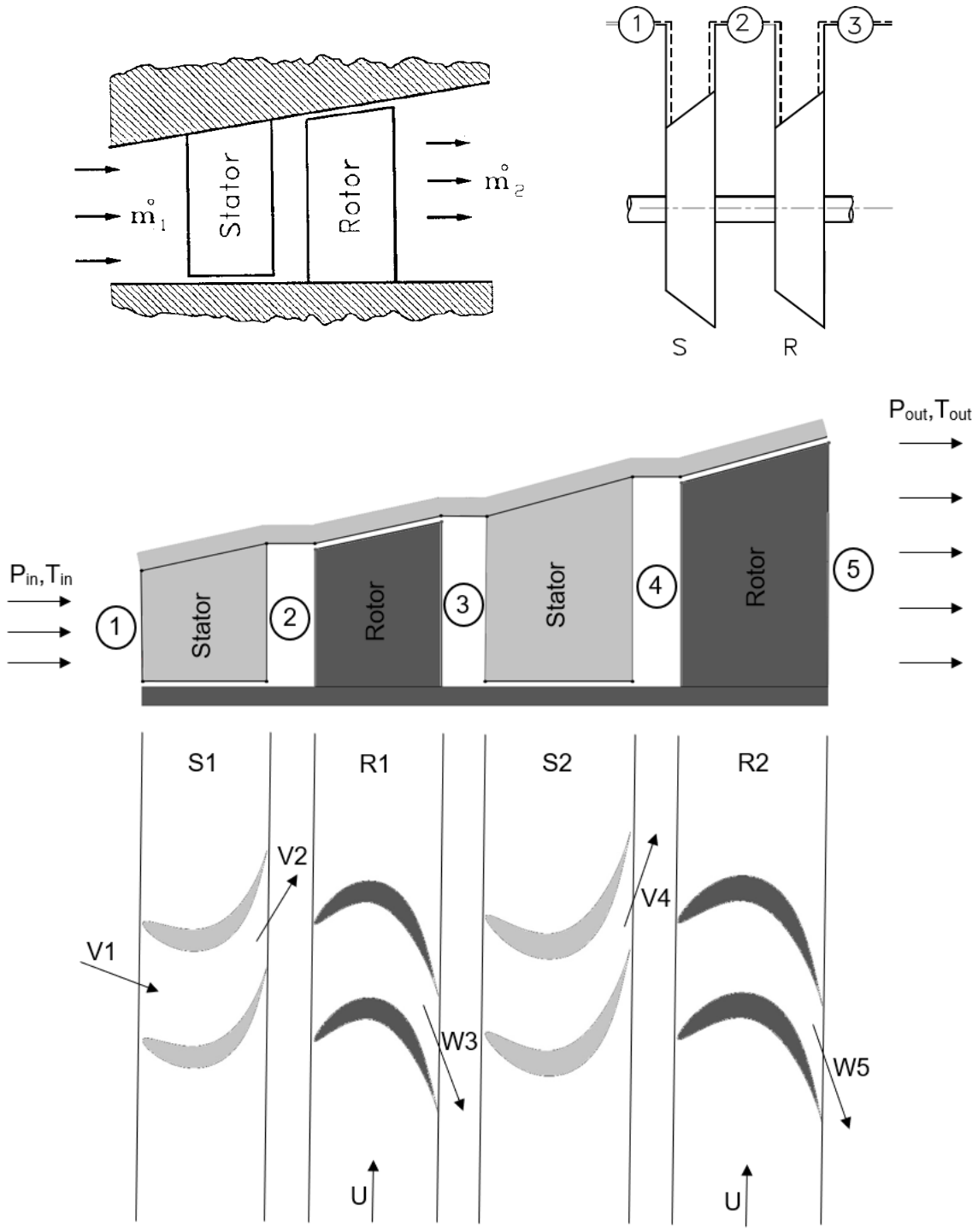

Figure 74. Representation of an adiabatic turbine component in the row-by-row calculation. Each stage is decomposed into two rows that are connected via the middle plenum.

of the current rows of injectors in UHEGT, the combustor model is created to simply represent the combustion volume without much focus on the geometrical details inside the combustion unit. The main goal in this process is to simulate the temperature increase in the combustible flow as it passes over the injector rows. Figure 77 schematically represents the fuel schedule applied through fuel valve to the injector component.

In the injector components, the temperature in the primary combustion zone is

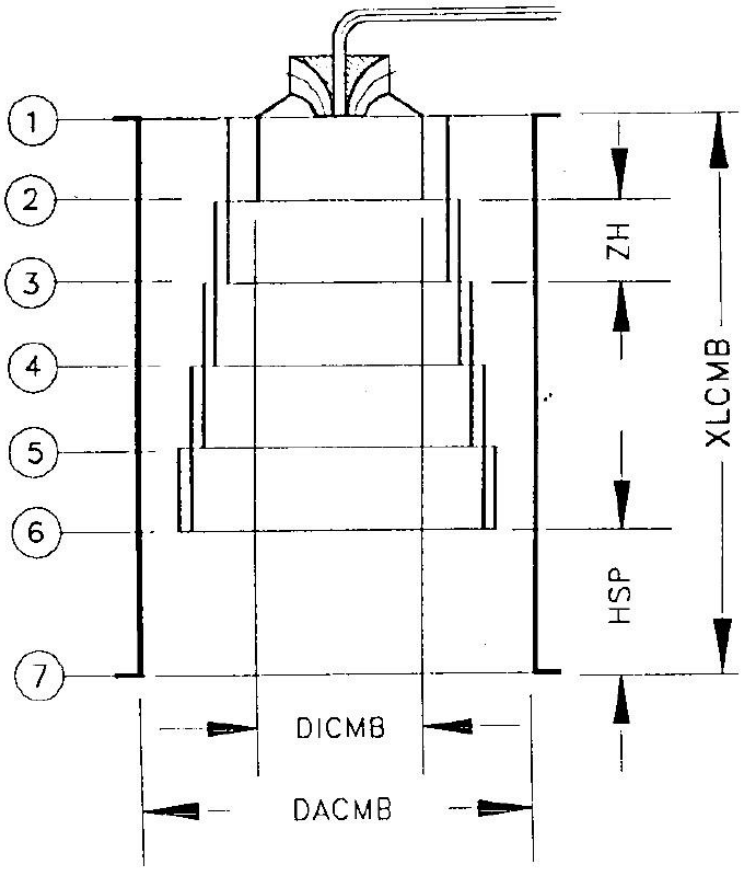

Figure 75. Tubular combustion chamber; Reprinted from Schobeiri [31].

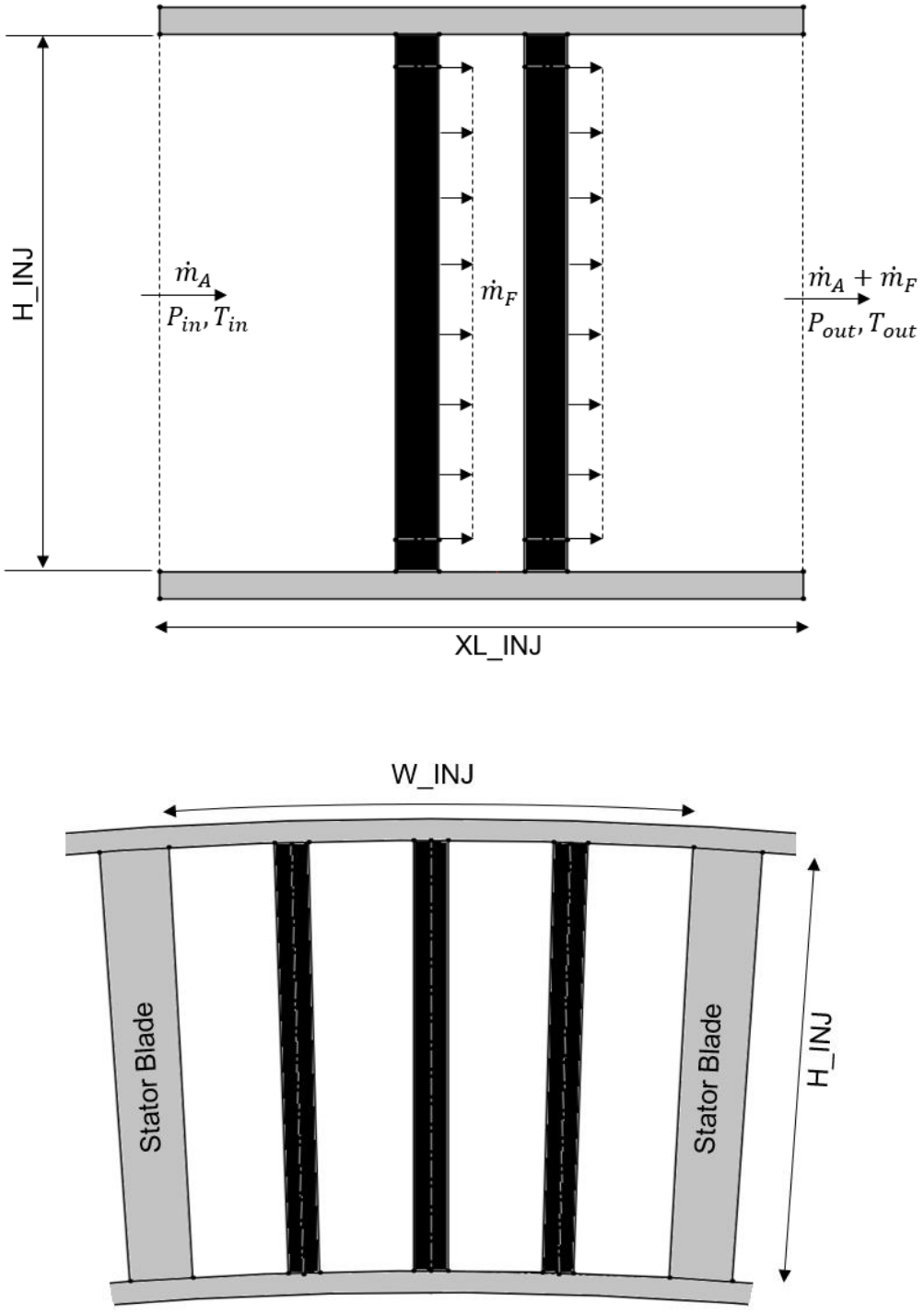

Figure 76. UHEGT injector component: Front view (top) and left view (bottom).

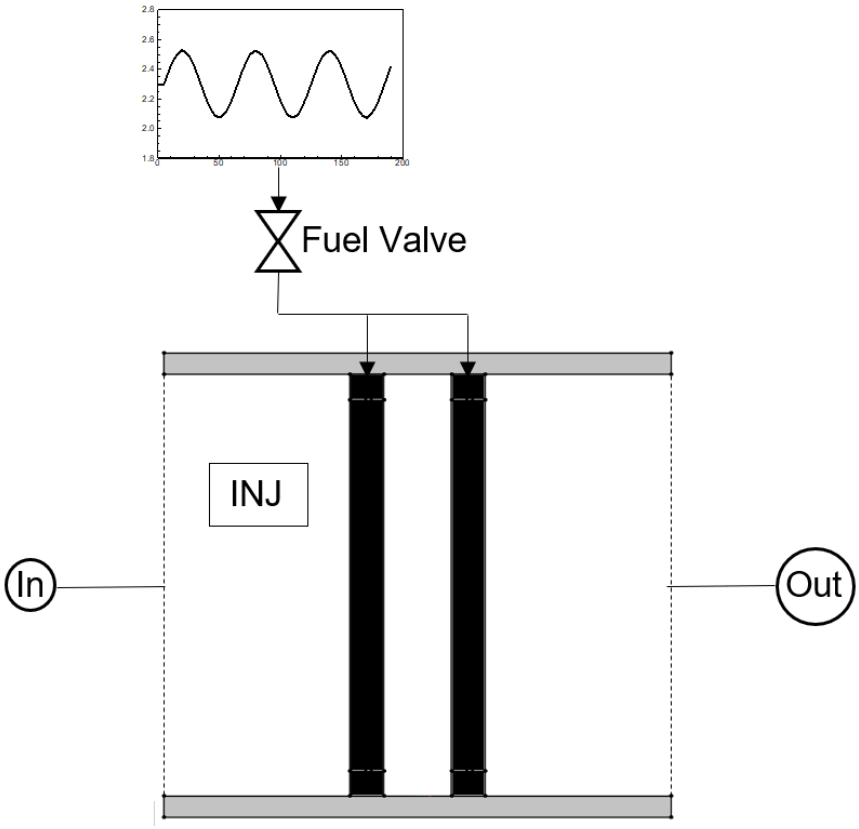

Figure 77. Schedule applied through fuel valve to the injector component.

determined by [1],

$$\frac{\partial T_{o_{i+1}}}{\partial t} = \frac{1}{V\rho_{i+1}c_{p_{i+1}}}\left(\sum_{k=1}^{K}\dot{m}_{ik}\left[\kappa_{i+1}\left(c_{p_i}T_{o_i}\right)_k - c_{p_{i+1}}T_{o_{i+1}}\right]\right)$$

$$+\frac{1}{V\rho_{i+1}c_{p_{i+1}}}\left[(1-\kappa_{i+1})\dot{m}_{i+1}c_{p_{i+1}}T_{o_{i+1}} - \kappa_{i+1}\dot{Q}_G\right] \qquad (6.12)$$

$$-\left(\frac{1-\kappa_{i+1}}{c_{p_{i+1}}}\right)\left(\frac{\dot{m}}{\rho^2 S^2}\right)_{i+1}\frac{\partial \dot{m}_{i+1}}{\partial t}$$

The mixing components in this equation are specified with index *k* changing from 1 to the number of species in the combustion process, *K*.

VI.3. Results and Discussion

In this section, different fuel schedules are applied to the engine and its unsteady response is studied in each case. The variations are selected in a way to represent the cases that the engine goes through in actual performance conditions. All the simulations start at the steady performance of the engine at the design point.

VI.3.1. Sinusoidal Fuel Schedule

In this scenario, a sinusoidal fuel schedule is applied to all injectors as shown in Figure 78. The sinusoidal schedule represents regular changes in the fuel flow rate that may take place in power plants or aircrafts. The schedule ranges from 90% to 110% in 60 s periods over a total time period of 200 s. The *Amplitude* value for each profile is shown

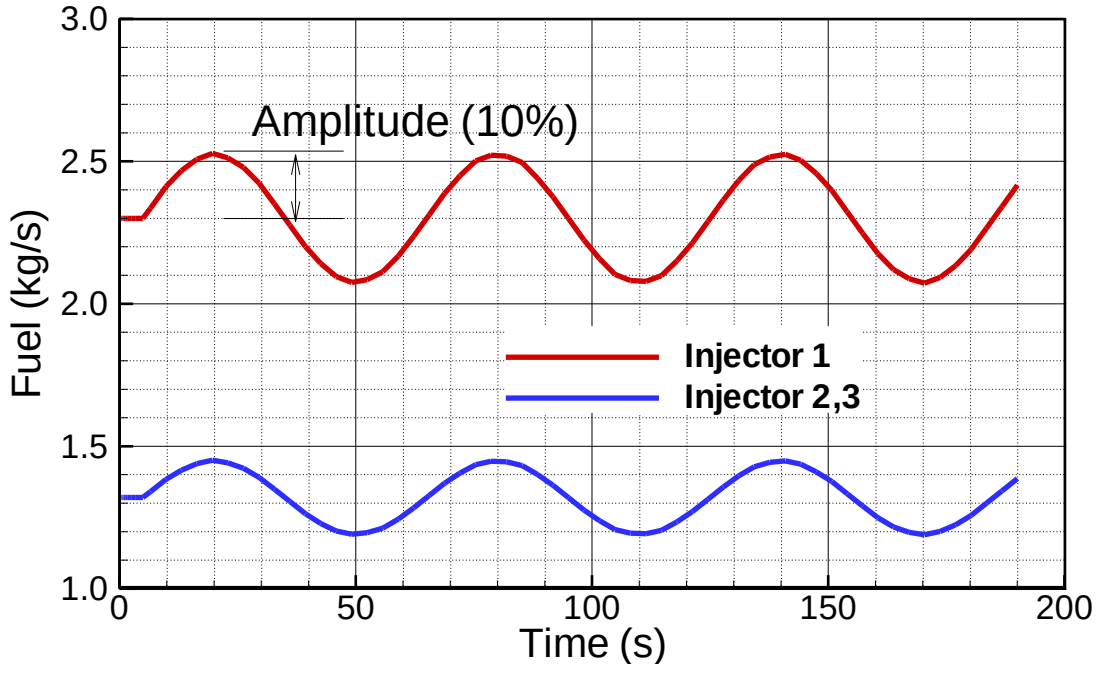

Figure 78. Sinusoidal fuel schedule.

in the plot as well.

Figure 79 and Figure 80 show the compressor and turbine mass flow rates. As shown in these figures, the compressor and turbine mass flow rates fluctuate with the similar pattern as the fuel schedule. However, there are a few important parameters that need to be discussed. The first thing to notice is that at the beginning (the first fluctuation cycle), the response is not quite similar to the second and third fluctuation cycles. That is because of the *Transient* response that exists in the system as it starts on the new fuel schedule. This transient response is usually damped away quickly and what remains is the steady fluctuations due to the driving profile (fuel schedule). The next important parameter is the time lag between the mass flow rate responses and the fuel schedule. These delays represent the reaction time of the engine and the control system. In other words, they describe how long it takes each component to adjust itself to the changes in fuel schedule. The next factor to notice is the amplitude values for different profiles. As shown in Figure 79 and Figure 80, the amplitudes of the compressor and turbine mass flow rates are about 3%. These values are less than half of the fuel schedule amplitude (10%) which shows that the turbine and compressor flow rates do not oscillate as intensely as the fuel.

Figure 81 and Figure 82 show the inlet and exit temperature distributions for each turbine set. As shown in these figures, the temperature profiles fluctuate with amplitudes of about 5-6%. The fluctuation amplitudes are slightly increased in the later turbine stages which is due to the fuel injection in the second and third injector rows.

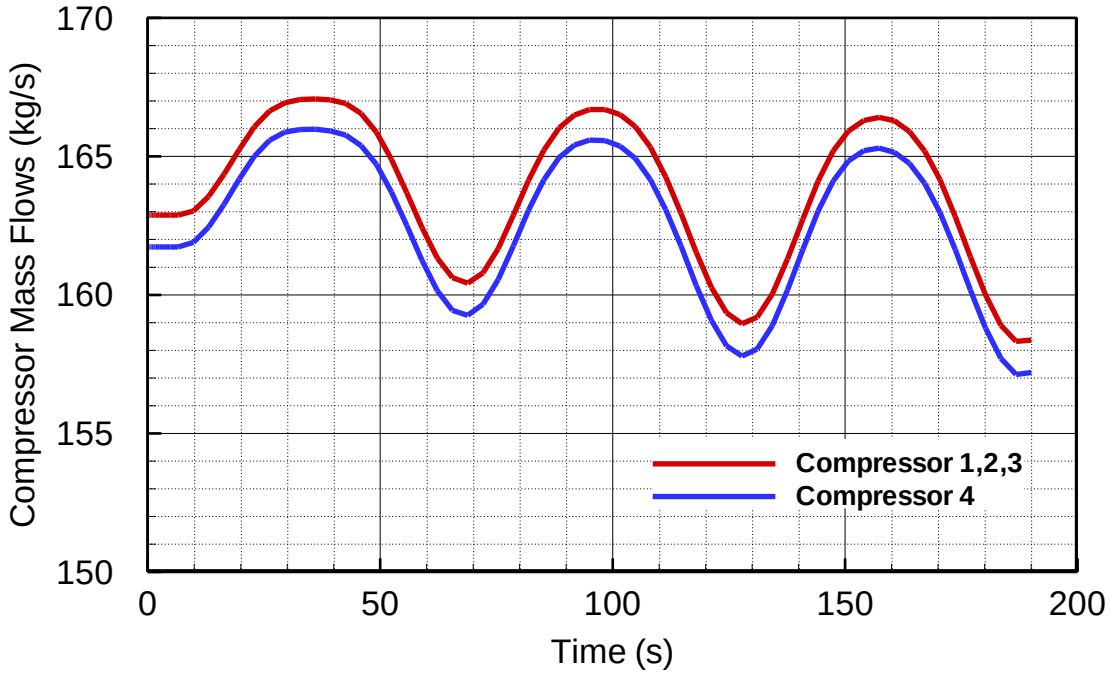

Figure 79. Sinusoidal schedule: Compressor sets' mass flow rates.

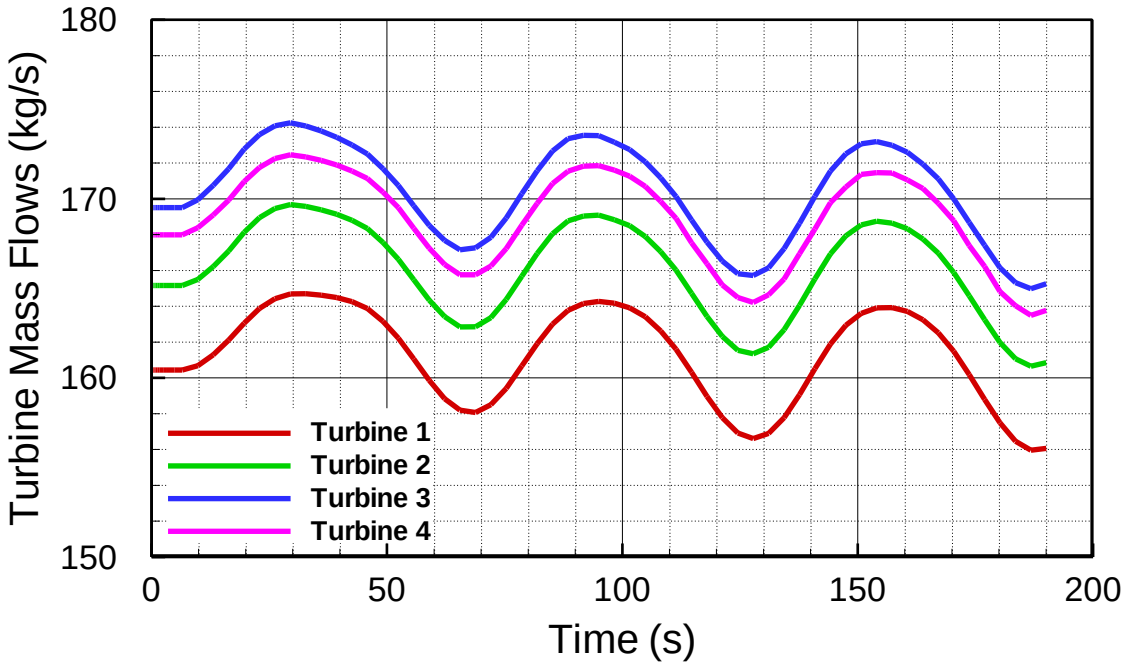

Figure 80. Sinusoidal schedule: Turbine sets' mass flow rates.

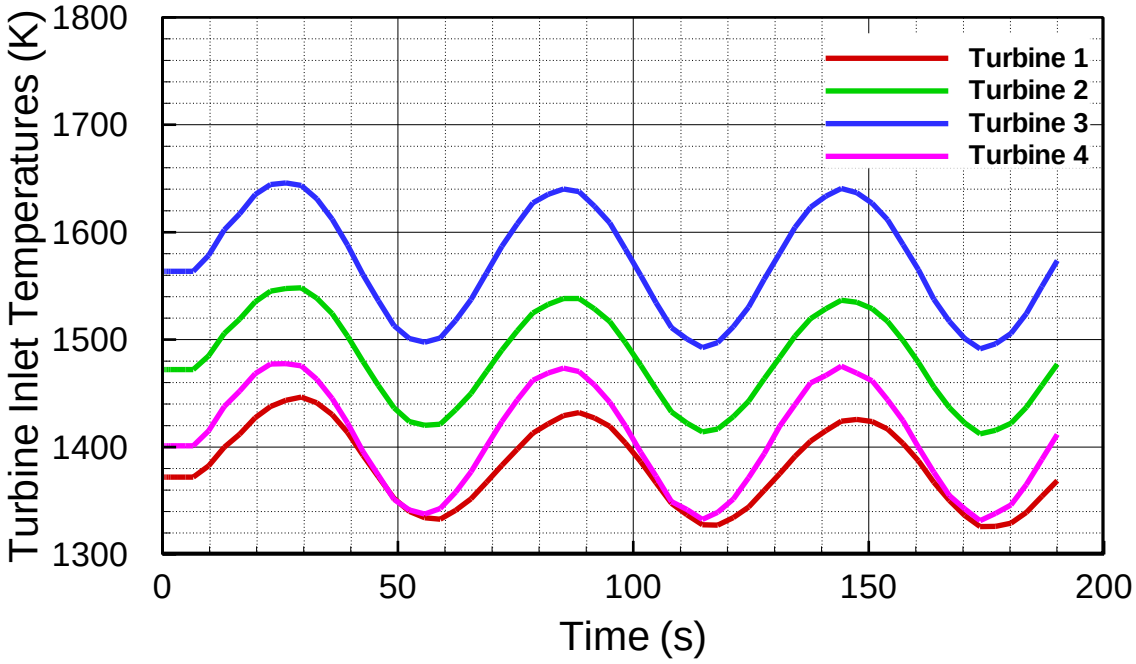

Figure 81. Sinusoidal schedule: Turbine inlet temperatures.

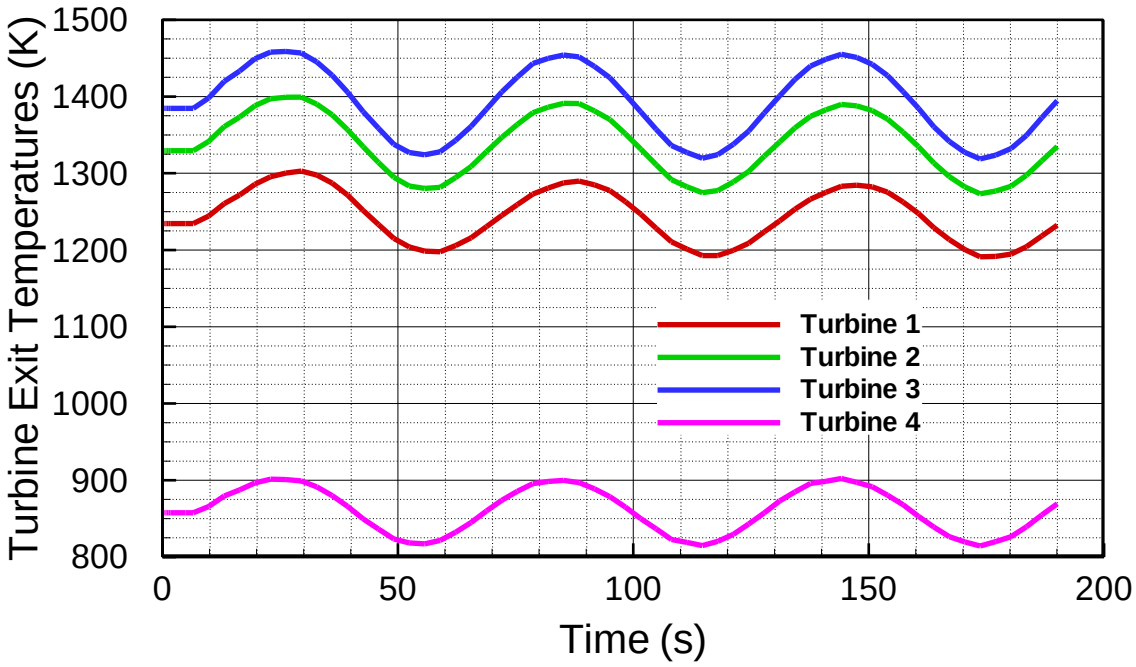

Figure 82. Sinusoidal schedule: Turbine exit temperatures.

Figure 83 and Figure 84 show the compressor and turbine sets' power distributions, respectively. As shown in the figures, power values for these components fluctuate with an approximately 7-10% amplitude which is close to the fuel flow fluctuation amplitude. It should also be noted that Turbine 4 which consists of three turbine stages produces a much higher amount of power compared to the other turbine sets with one stage each.

Figure 85 shows the total power distributions for turbine, compressor, and generator. The generator power (net power) is calculated by subtracting compressor power from turbine power and reducing mechanical and winding losses. As seen in this figure, the fluctuation amplitudes for turbine, compressor, and generator total powers are approximately 7%, 8%, and 10%, respectively.

Figure 86 shows the engine thermal efficiency which is calculated by dividing the generator power by the total fuel energy. As shown in this figure, the efficiency fluctuates between 44% and 46%. That means the range of fluctuations in efficiency is relatively lower than the other parameters. In other words, the system's efficiency does not drop noticeably, and it performs near the design point efficiency (45%) throughout the entire cycle.

Figure 87 shows the non-dimensional shaft rotational speed. The amplitude is 3.9% which is relatively low compared to the fuel schedule. The total moment of inertia about the axis of rotation for all rotating components including shaft, rotor blades, generator, etc. is shown in the figure. The moment of inertia determines the shaft response and the intensity of the fluctuations in rotational speed.

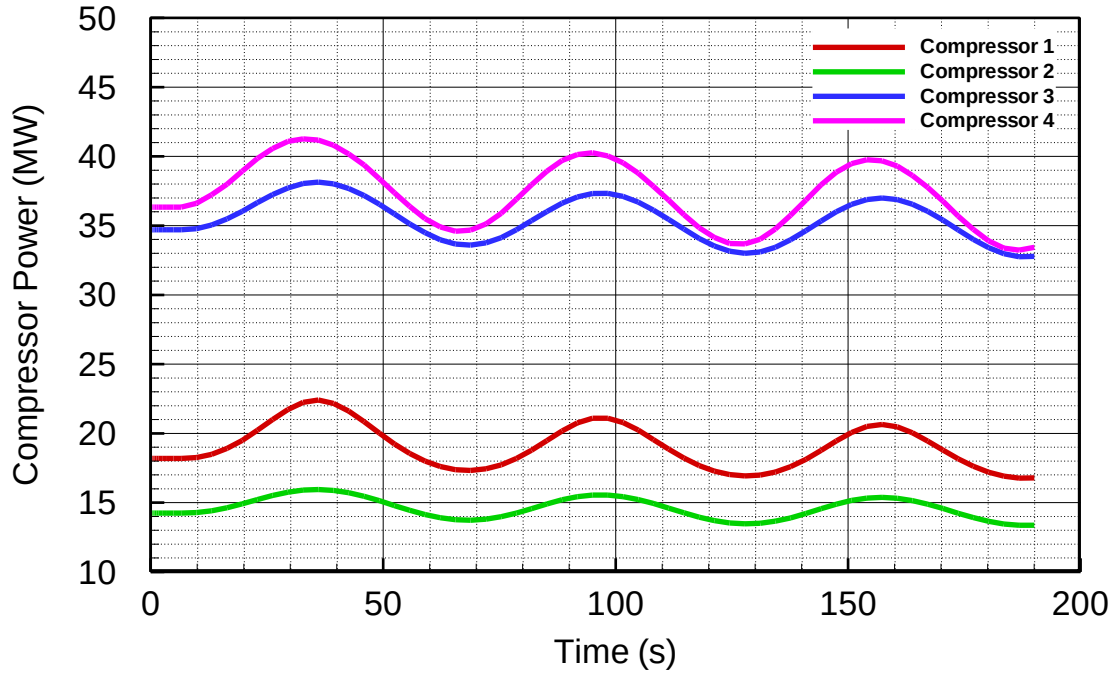

Figure 83. Sinusoidal schedule: Compressor sets' power consumptions.

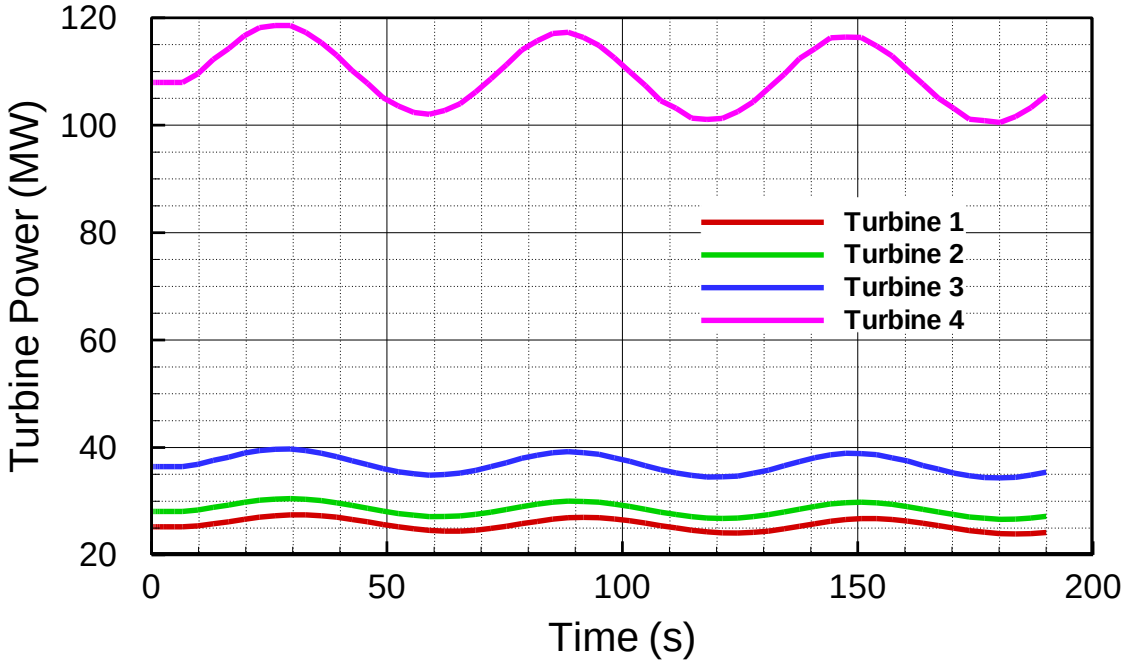

Figure 84. Sinusoidal schedule: Turbine sets' power generations.

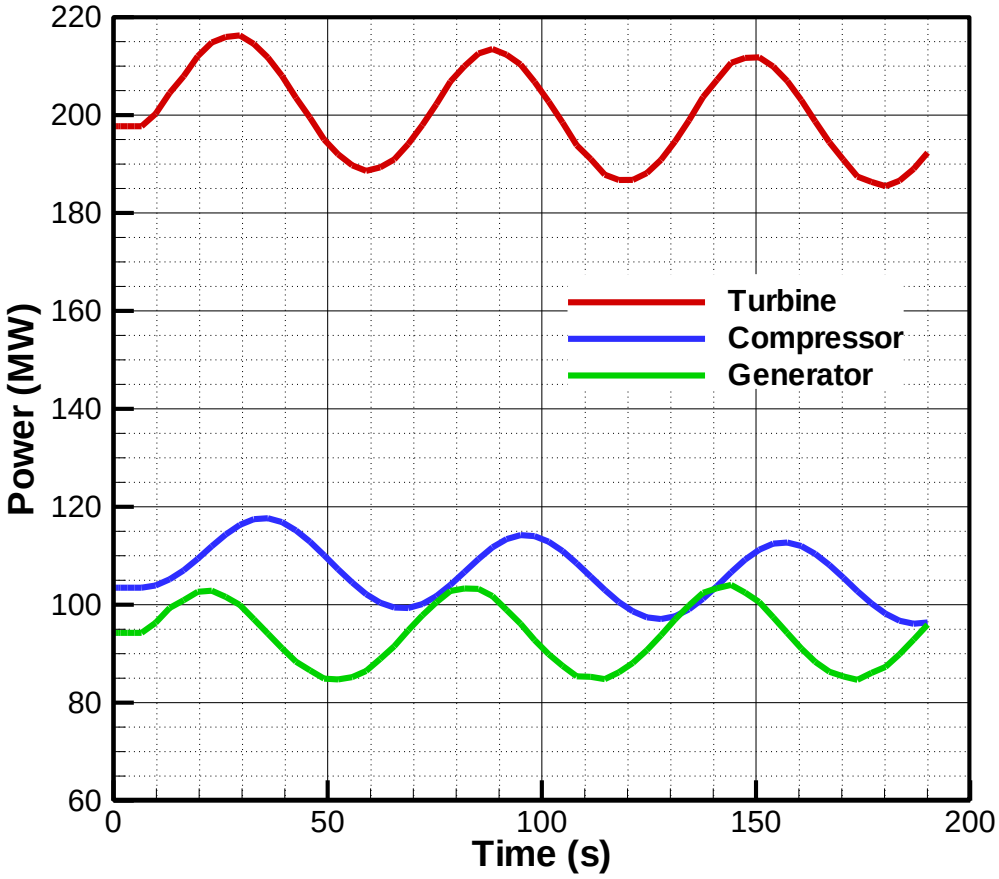

Figure 85. Sinusoidal schedule: Total power for each component.

Finally, Figure 88 and Figure 89 show the pressure and temperature distribution in all 14 plena, respectively. As seen in the first figure, the pressure values in plena 1 to 5 do not fluctuate at all. That shows fuel schedule does not affect the pressure values in the compressor significantly. Starting at plenum 6, which is the inlet of the first injector row, pressure in the following plena fluctuate with an amplitude of about 4%. Regarding the temperature, as shown in Figure 89, except the inlet plena 1 and 2, all other plena temperatures fluctuate under the influence of the fuel schedule. However, the amplitudes of the compressor temperature fluctuations are lower than the injector and turbine. As the

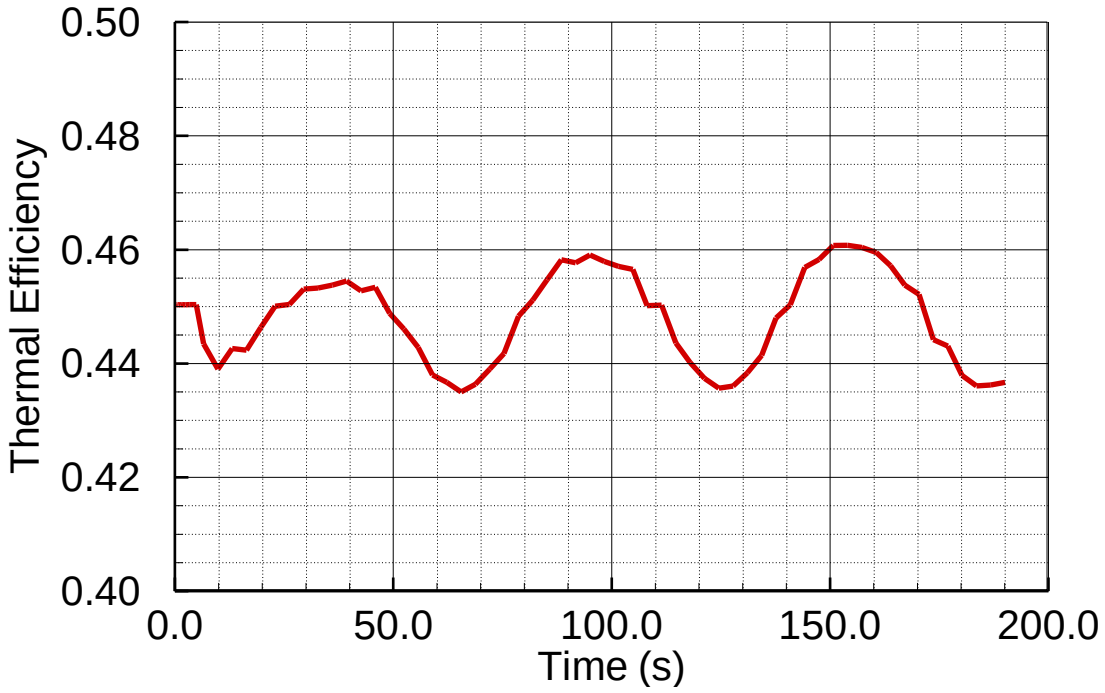

Figure 86. Sinusoidal schedule: Engine thermal efficiency.

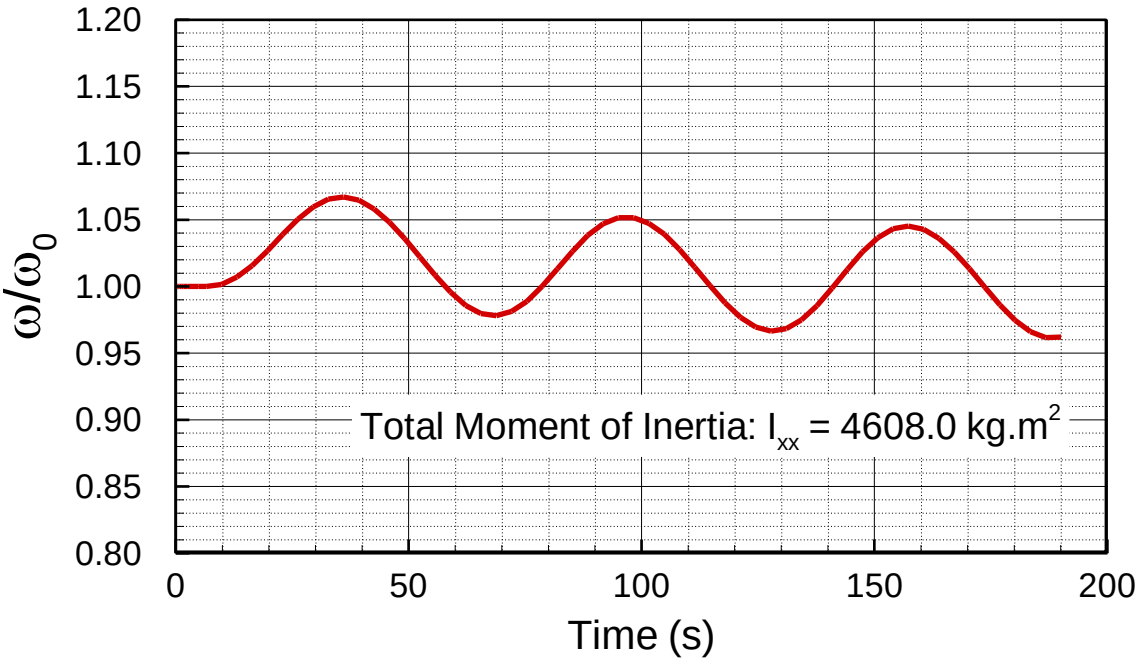

Figure 87. Sinusoidal schedule: Non-dimensional shaft rotational speed.

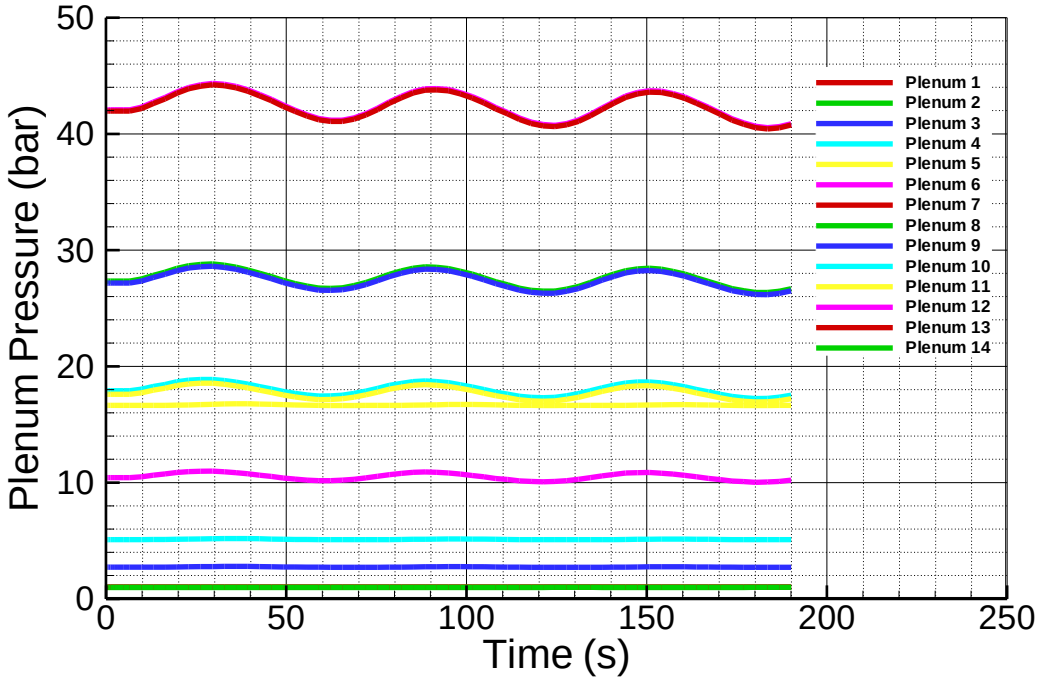

Figure 88. Sinusoidal schedule: Plena pressure.

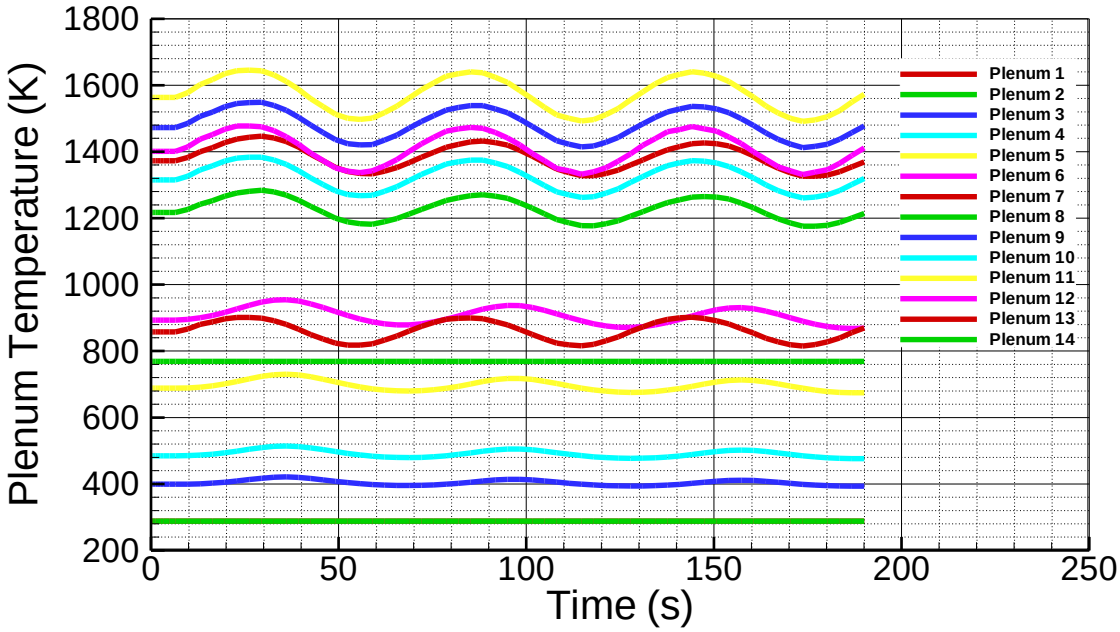

Figure 89. Sinusoidal schedule: Plena temperature.

flow moves towards the later stages, the intensity of the fluctuations increases due to injection of more fuel.

VI.3.2. Gaussian Fuel Schedule

In the second scenario, a Gaussian fuel schedule is applied to the injectors as shown in Figure 90. This schedule represents the random load changes in the power plants and aircrafts which have been shown to follow a Gaussian (normal) distribution pattern [1]. The schedule ranges from 100% to 110% in 50 s periods over a total time period of 200 s. As shown in the figure, the amplitude in this case is measured from the top point to the minimum part of the profile which is the flat section at 100%. The same amplitude measurement technique is used in all the following diagrams in this section.

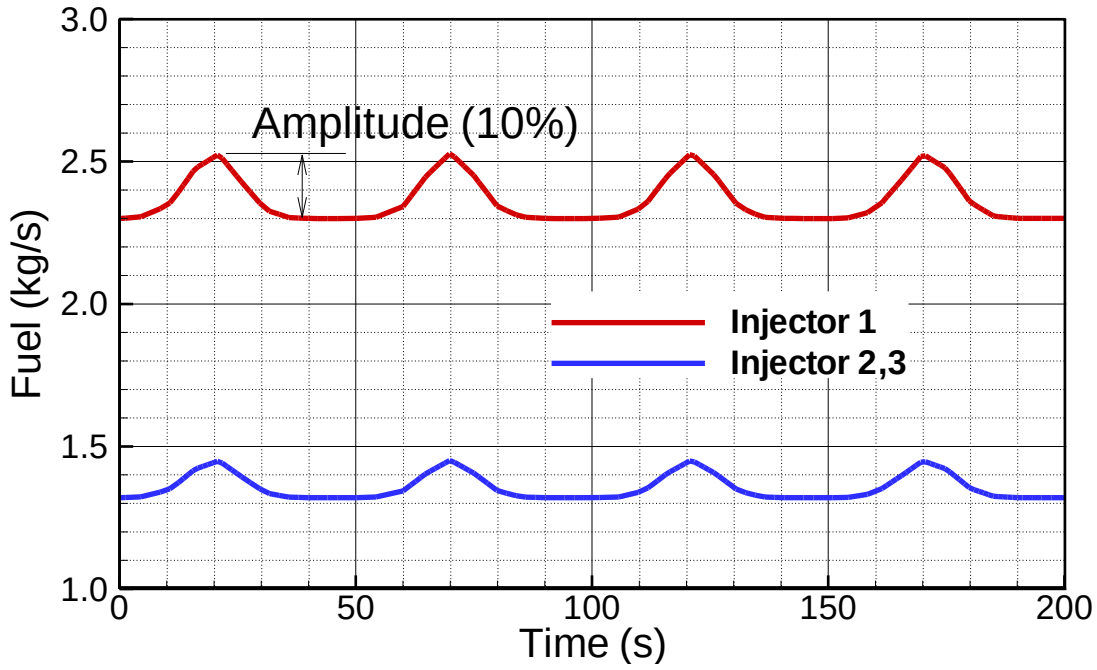

Figure 90. Gaussian fuel schedule.

Figure 91 and Figure 92 show the compressor and turbine mass flow rates. As shown in these figures, the mass flow rates fluctuate with amplitudes of about 3%. Also, the flat parts in the fuel schedule are not reproduced in the mass flow rates.

Figure 93 and Figure 94 show the inlet and exit temperature distributions for each turbine set. As shown in these figures, temperature values fluctuate with amplitudes of about 5-6% which are relatively higher than the mass flow rate fluctuation amplitudes. It is interesting to notice that in contrast to the mass flow rates, the rising sections in the temperature profiles are shorter than the descending sections. That means while the fuel schedule is flat, the temperatures continue to drop.

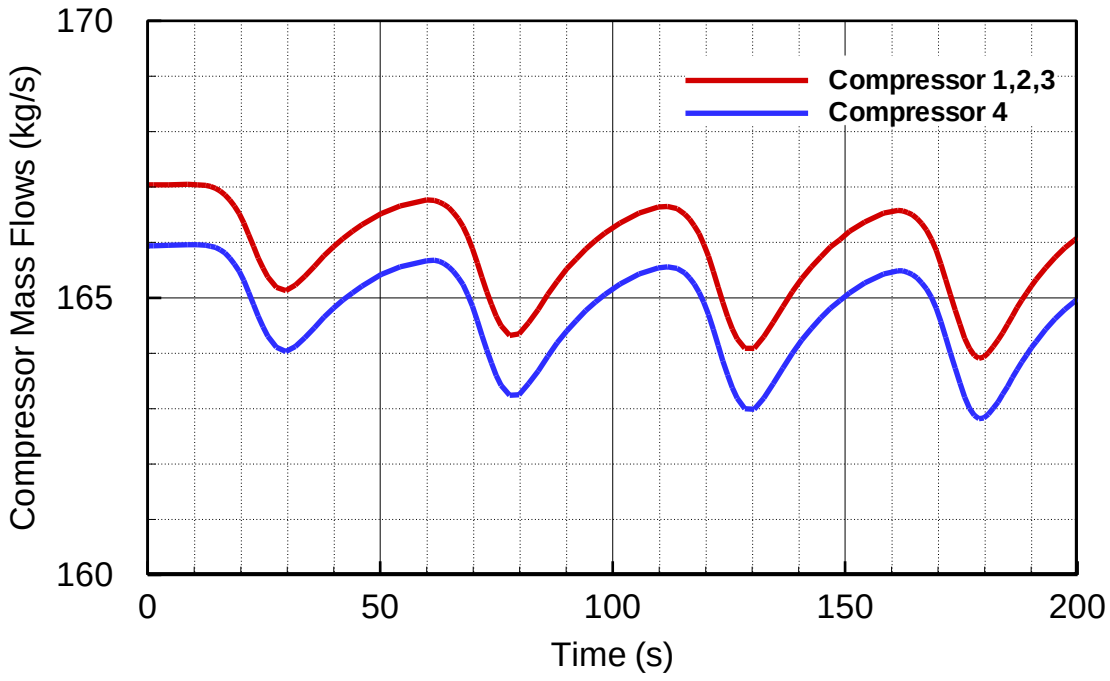

Figure 91. Gaussian schedule: Compressor sets' mass flow rates.

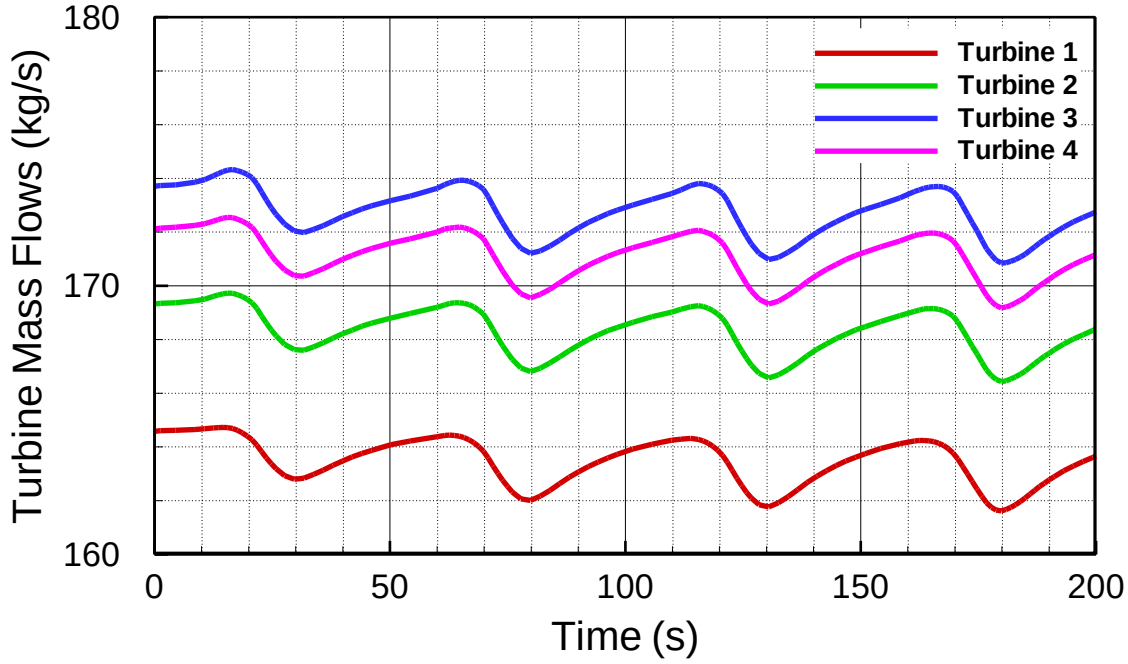

Figure 92. Gaussian schedule: Turbine sets' mass flow rates.

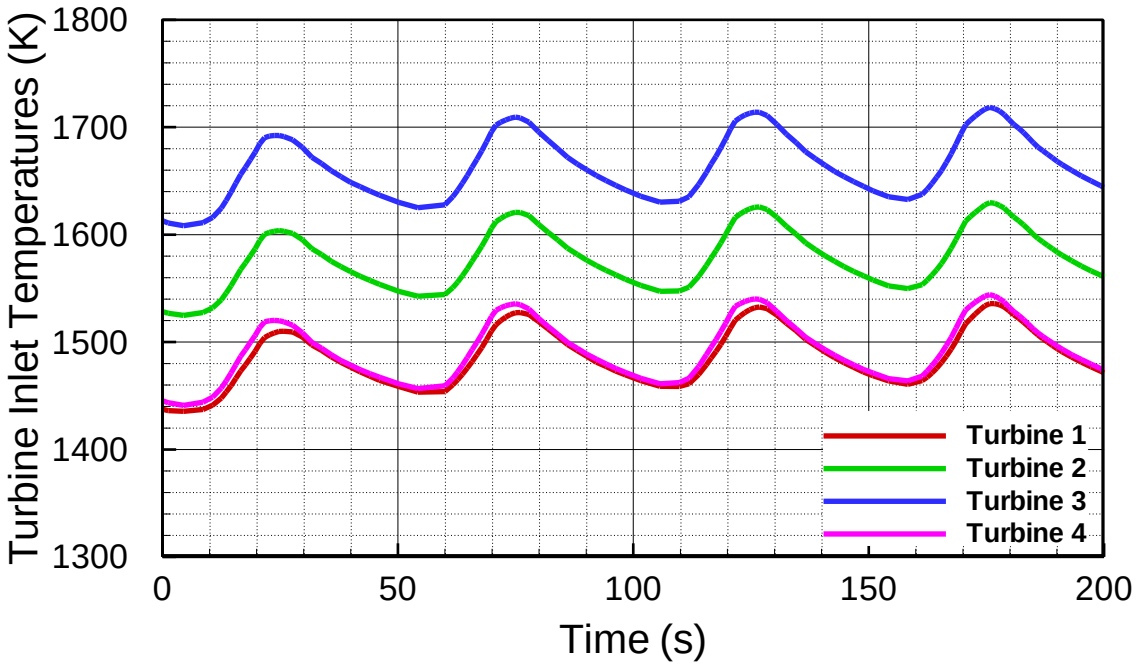

Figure 93. Gaussian schedule: Turbine inlet temperatures.

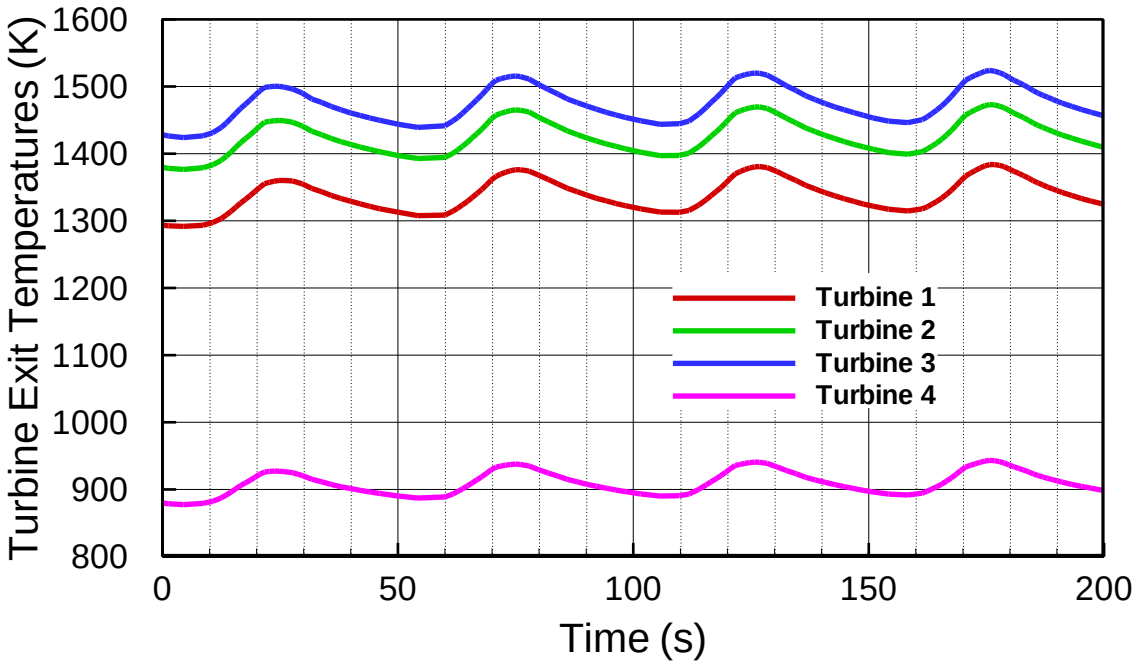

Figure 94. Gaussian schedule: Turbine exit temperatures.

Figure 95 and Figure 96 show the compressor and turbine sets' power distributions, respectively. Moreover, Figure 97 shows the total power for turbine, compressor, and generator. As seen in this figure, the fluctuation amplitudes for turbine, compressor, and generator are approximately 5%, 5%, and 8%, respectively. It is also noticeable that the generator power profile looks very similar to the fuel schedule.

Figure 98 shows the engine thermal efficiency. It is seen that in the beginning of the cycle, efficiency drops about 2% compared to the design point efficiency (45%). After that it oscillates between 42% and 43%. The reason for this decline is that the engine is performing on a higher average fuel flow compared to the design point. The net increase in the average fuel causes the cycle to move from the design point and reduces efficiency.

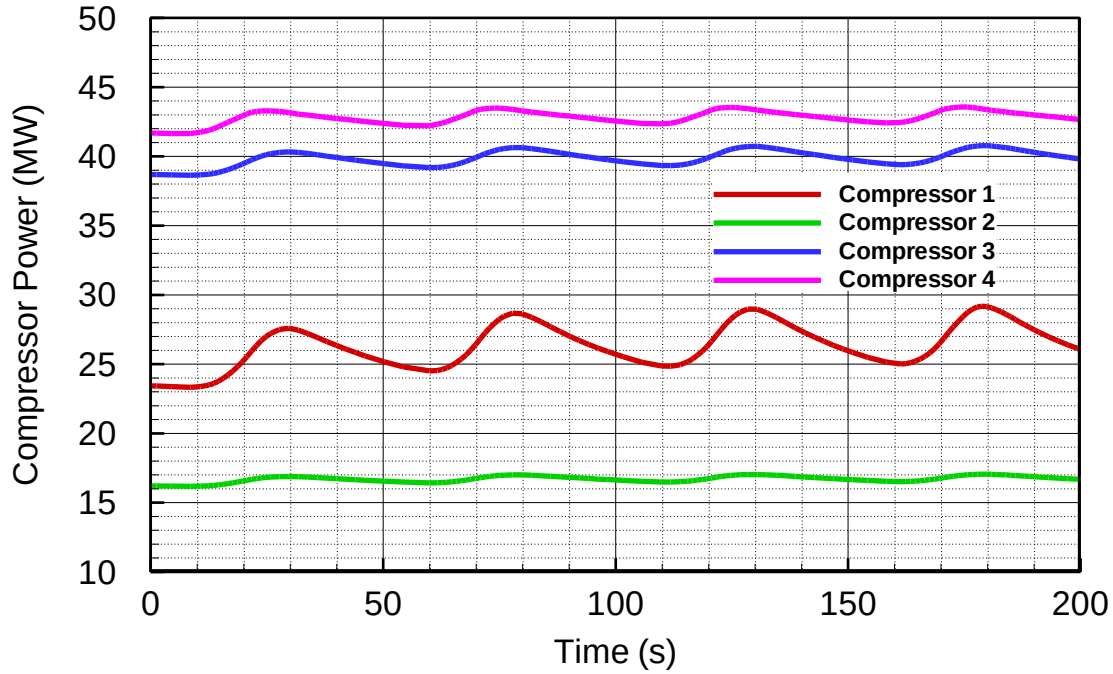

Figure 95. Gaussian schedule: Compressor sets' power consumptions.

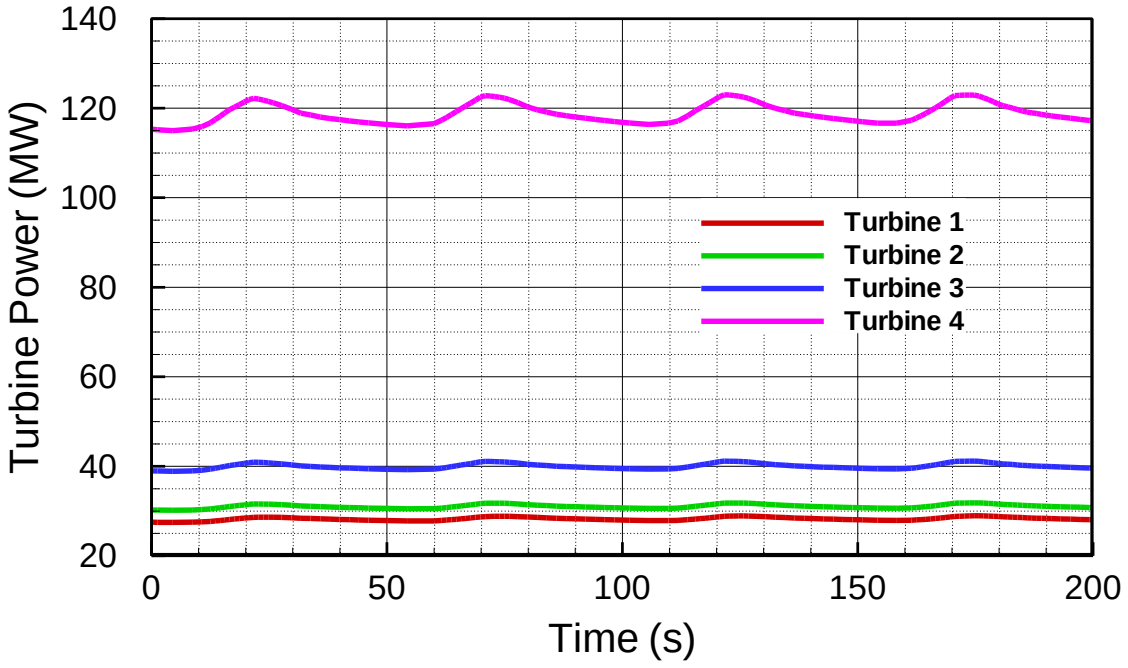

Figure 96. Gaussian schedule: Turbine sets' power generations.

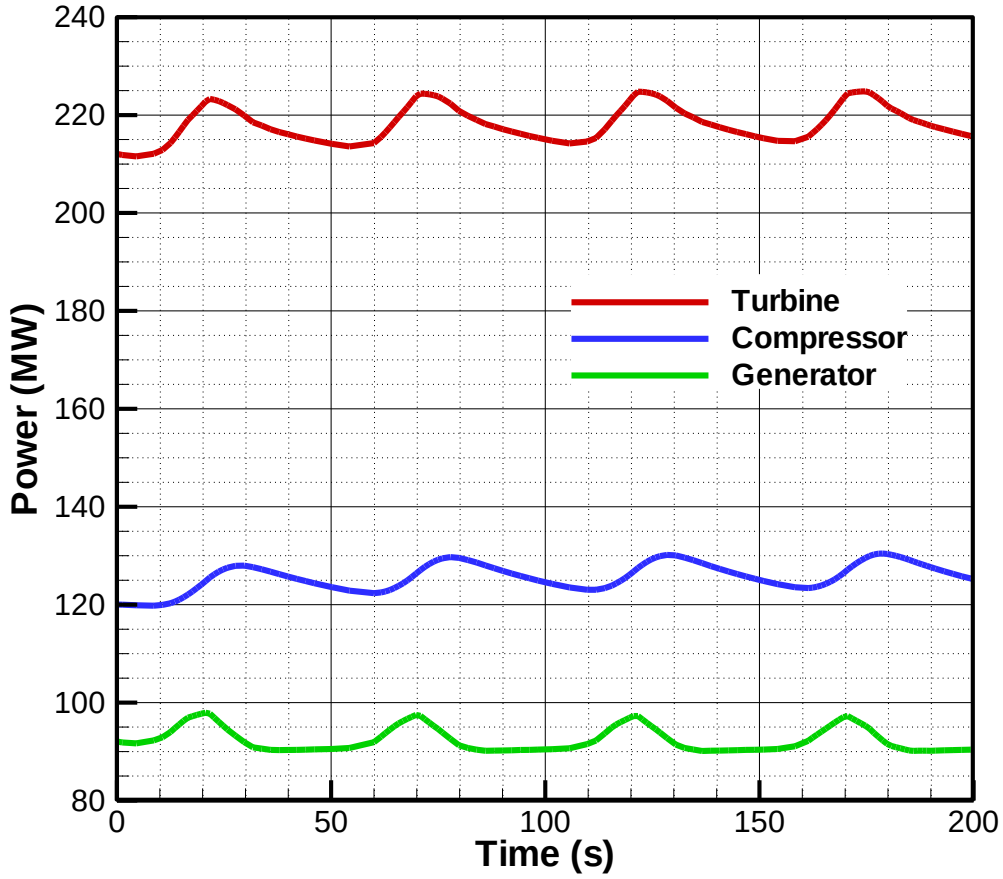

Figure 97. Gaussian schedule: Total power for each component.

Figure 99 shows the non-dimensional shaft rotational speed. The amplitude is 2.0% which is relatively lower than the other parameters. An overall increase in the average shaft rotational speed is observed which is due to the increase in the average amount of fuel.

Finally, Figure 100 and Figure 101 show the pressure and temperature distribution in all 14 plena, respectively. As seen in the first figure, the pressure values do not fluctuate strongly, and fluctuation amplitudes are below 2%. However, the fluctuations in the temp-

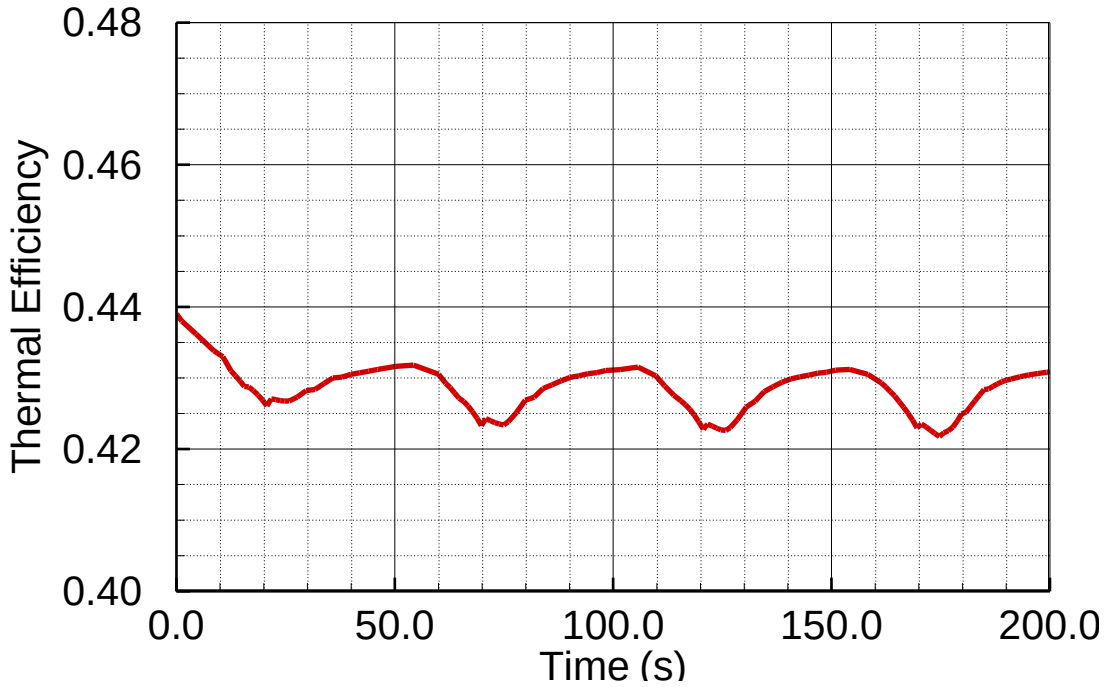

Figure 98. Gaussian schedule: Engine thermal efficiency.

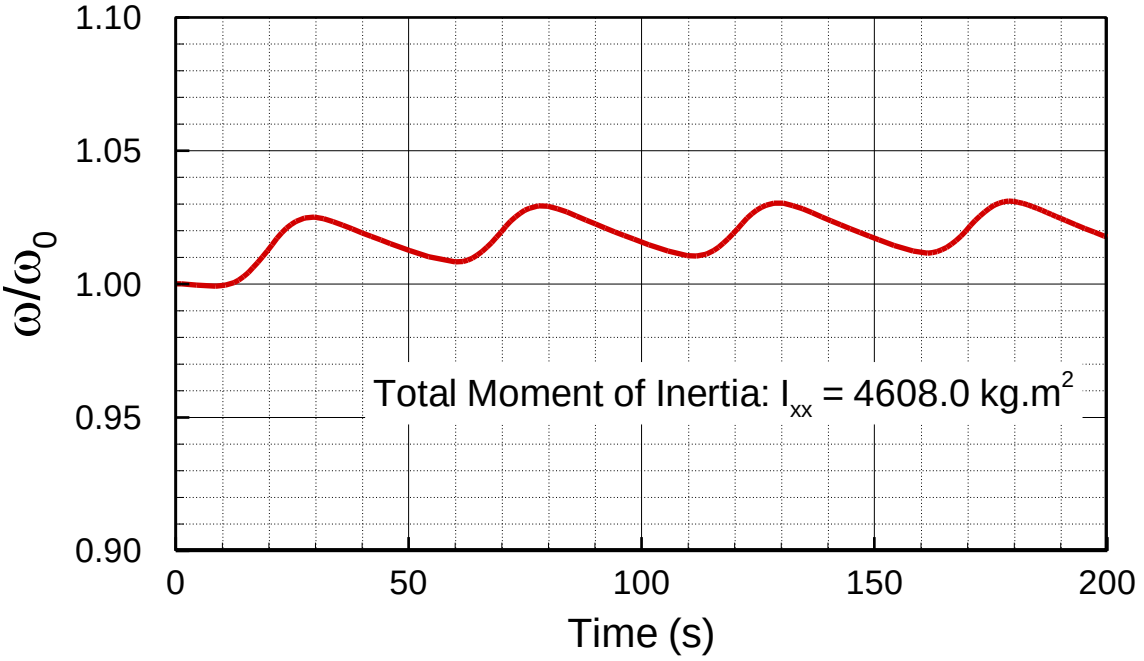

Figure 99. Gaussian schedule: Non-dimensional shaft rotational speed.

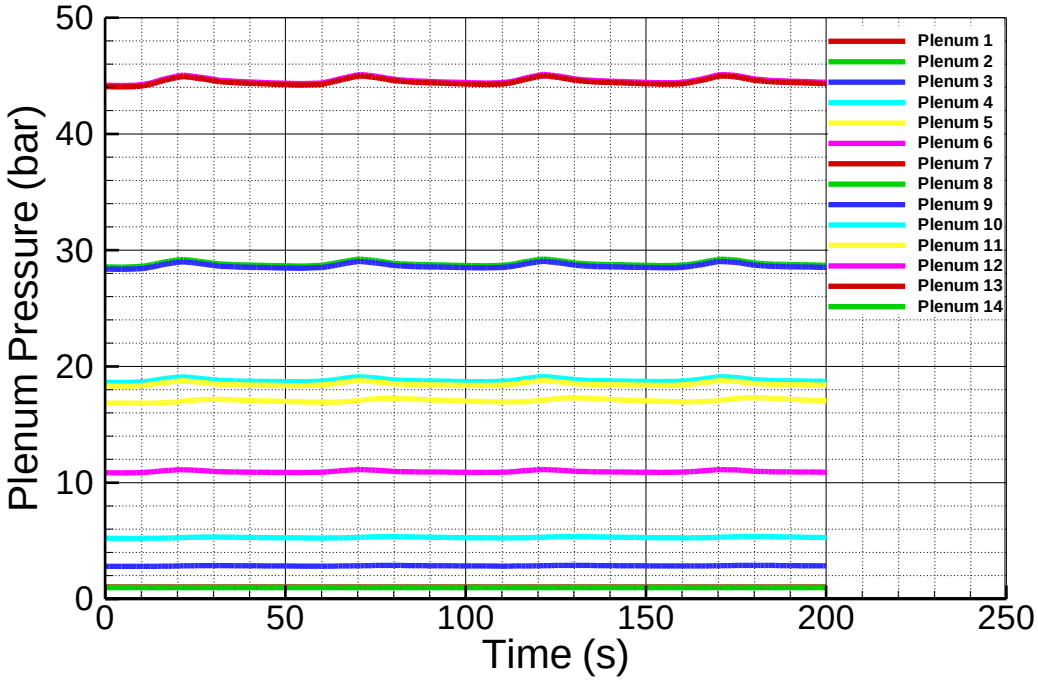

Figure 100. Gaussian schedule: Plena pressure.

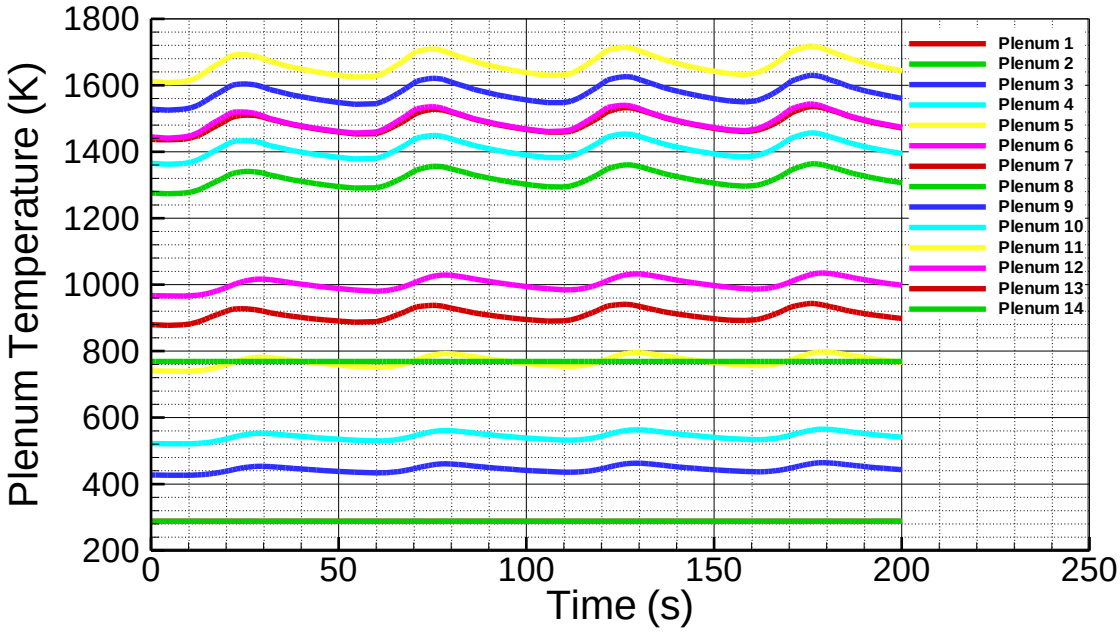

Figure 101. Gaussian schedule: Plena temperature.

erature values are stronger as seen in Figure 101. Moreover, due to the increase in the average fuel flow in the system, average temperature values for most plena are increased.

VI.3.3. Step Function Fuel Schedule

In this simulation, the fuel flow rate is increased by 5% in all injectors through a step function as shown in Figure 102 and Figure 103. The step function represents sudden changes taking place during the engine performance time. The current simulation runs for a total of 400 seconds and the responses in all components are studied.

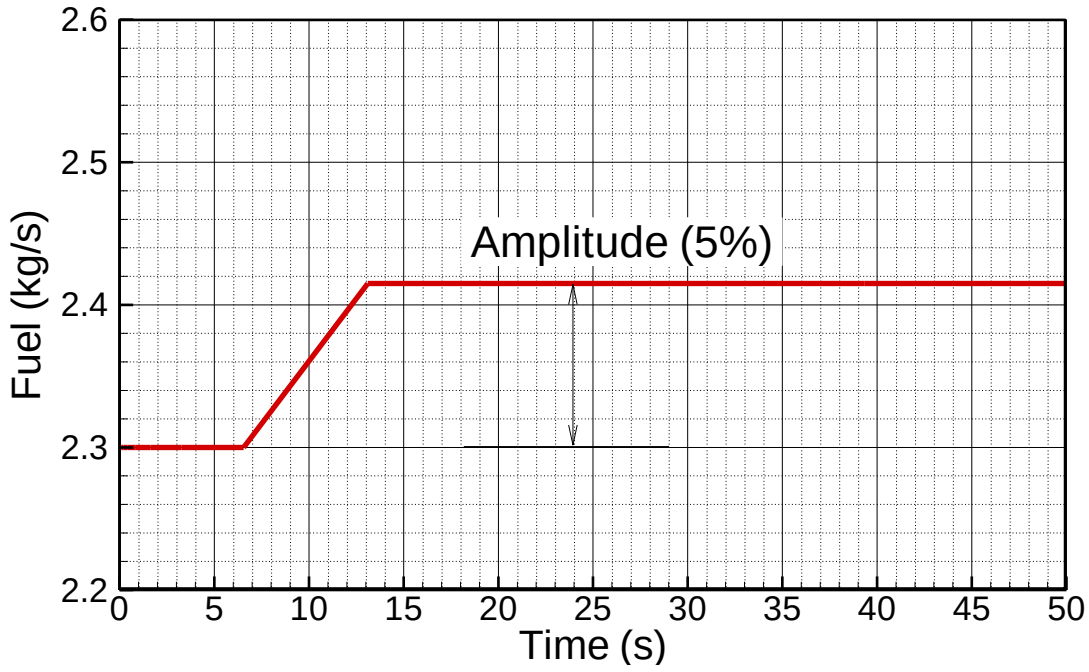

Figure 102. Step function fuel schedule: Injector 1.

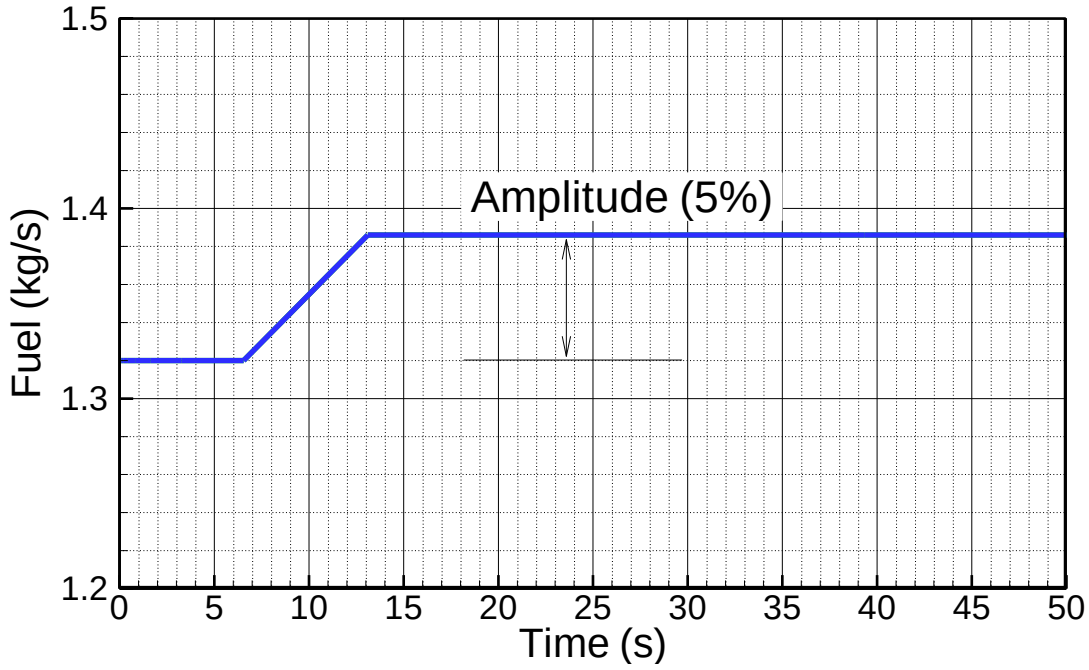

Figure 103. Step function fuel schedule: Injectors 2 and 3.

Figure 104 and Figure 105 show the compressor and turbine mass flow rates. As seen in these figures, the increase in fuel at first causes the mass flow rates to go higher than the steady response (overshoot), reach a maximum point and eventually come down to the steady state value. The mass flow rates in these components increase by about 1% due to the increase in fuel flow.

Figure 106 and Figure 107 show the inlet and exit temperature distributions for each turbine set. As shown in these figures, the steady amplitudes of the temperatures are above 10% which is more than double the fuel amplitude.

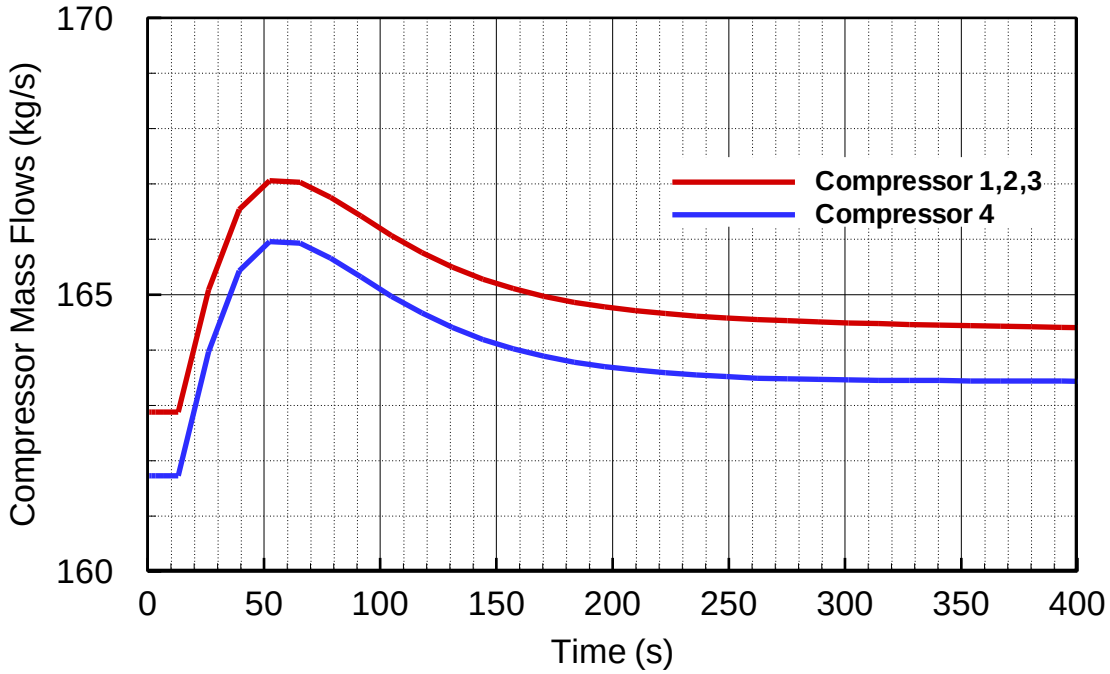

Figure 104. Step function schedule: Compressor sets' mass flow rates.

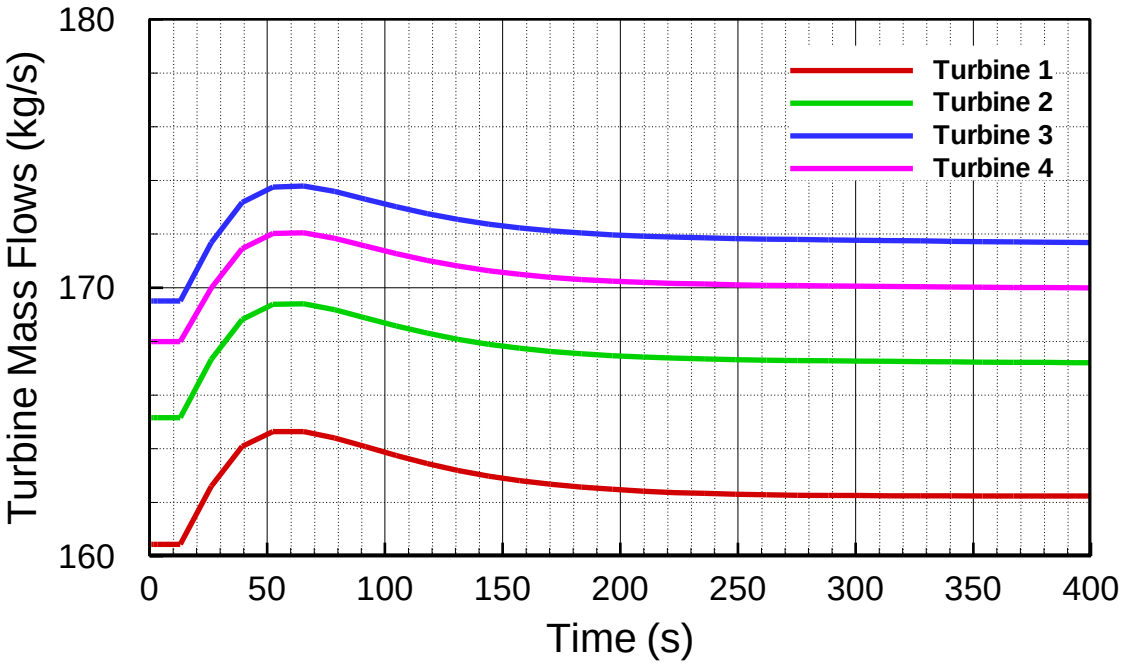

Figure 105. Step function schedule: Turbine sets' mass flow rates.

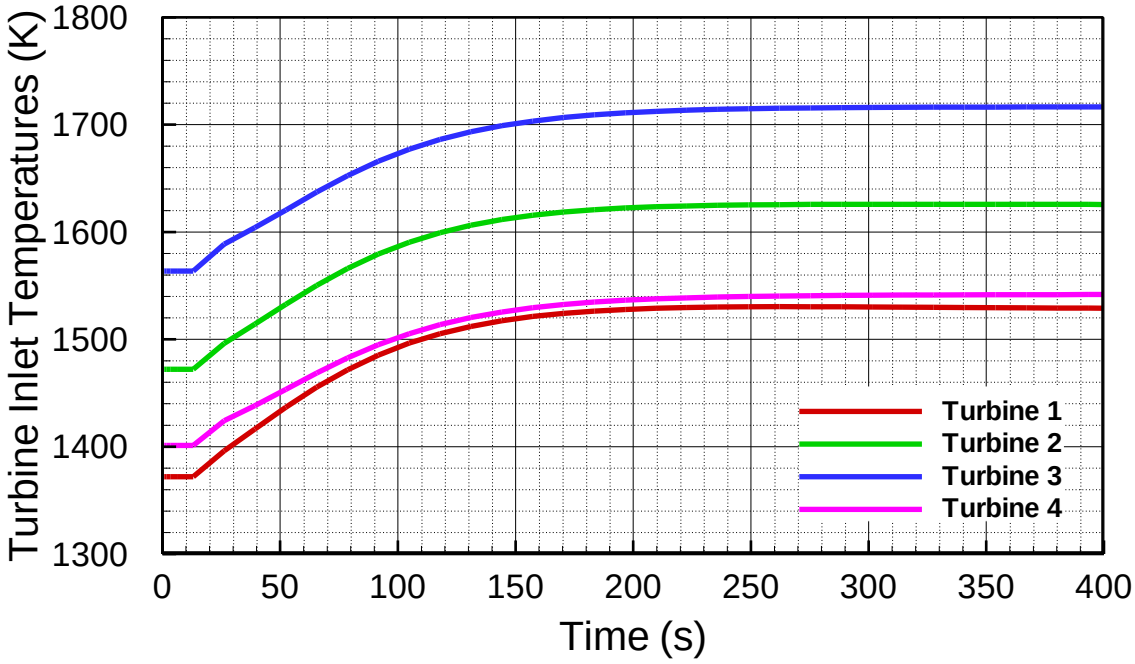

Figure 106. Step function schedule: Turbine inlet temperatures.

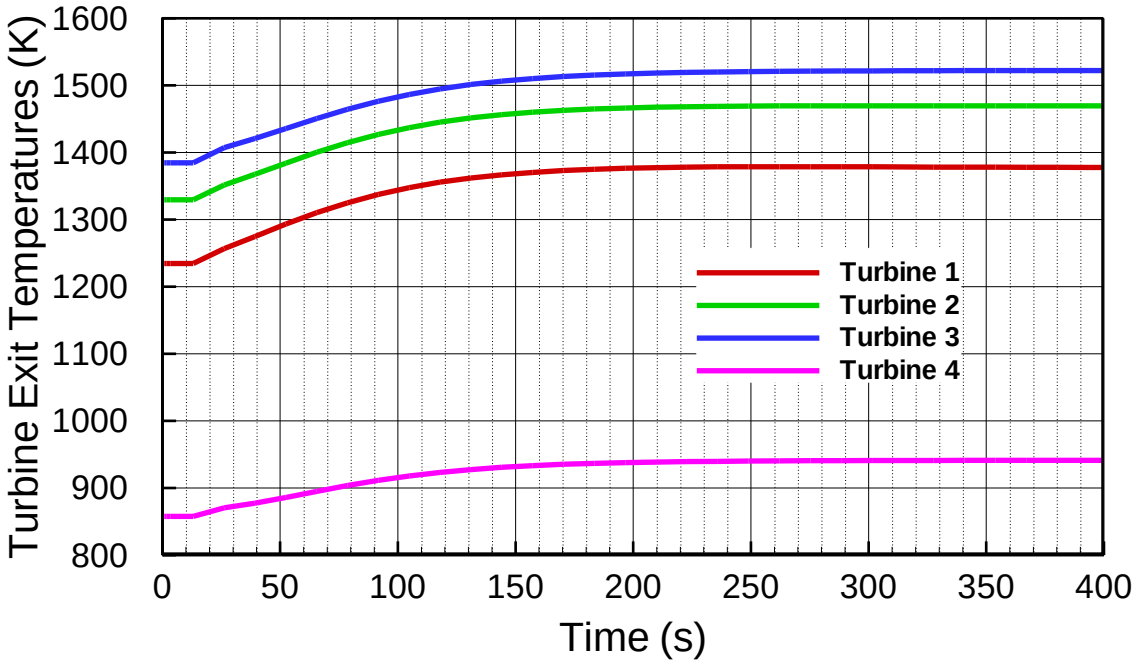

Figure 107. Step function schedule: Turbine exit temperatures.

Figure 108 to Figure 110 show the power distributions for each compressor and turbine set. As shown in the figures, power values for all turbines and compressors increase due to the increase in fuel. Figure 111 shows the total power for turbine, compressor, and generator. Although the powers of turbine and compressor increase with increase of fuel, these changes cancel each other out and the net power remains almost constant. That means the increase in fuel has not resulted in the proportional increase in the net power which implies a drop in efficiency.

Figure 112 shows the engine thermal efficiency. As it was discussed before, the efficiency is dropped by about 2%. This decline is due to the increase in amount of fuel that changes the thermodynamic cycle from the design conditions.

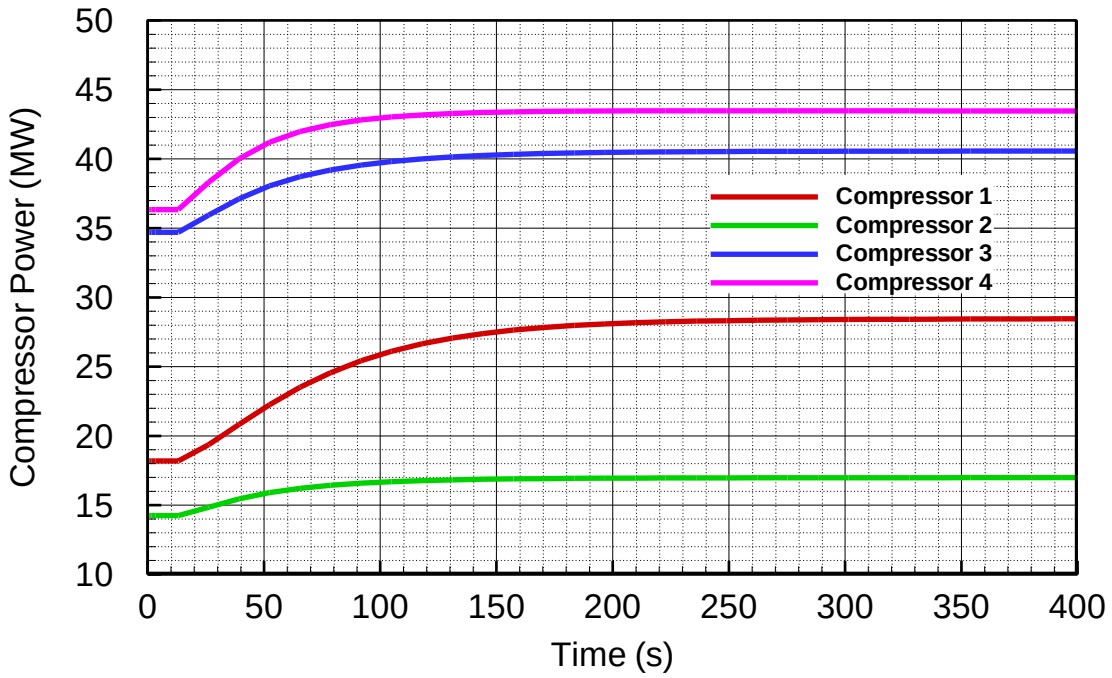

Figure 108. Step function schedule: Compressor sets' power consumptions.

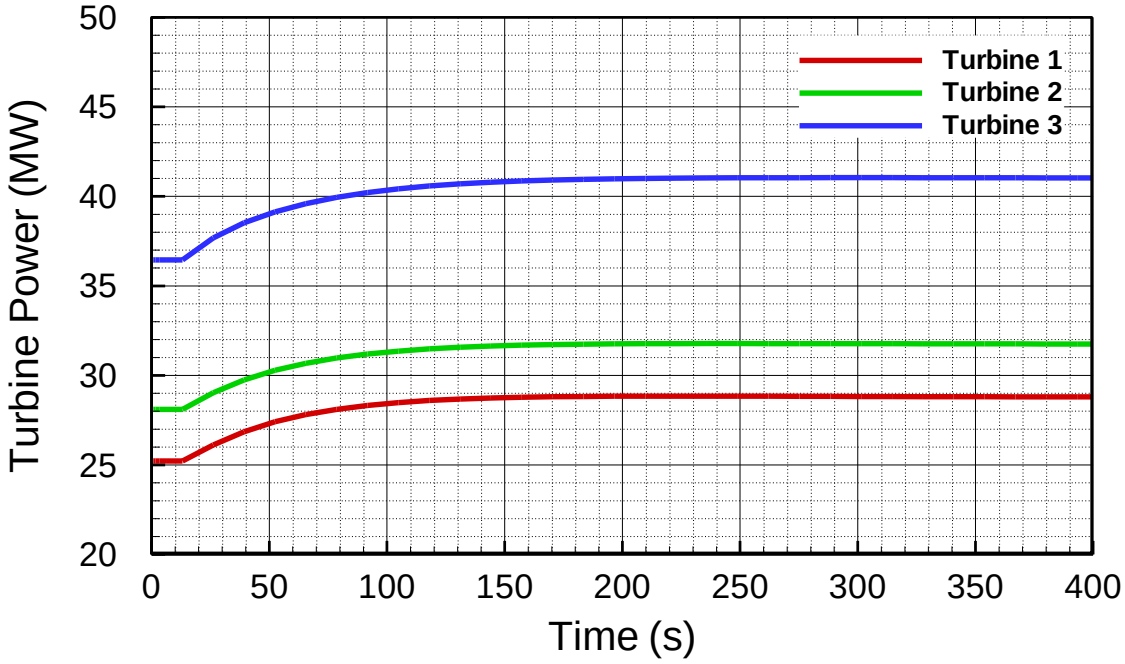

Figure 109. Step function schedule, turbine sets' power generations: Turbines 1 to 3.

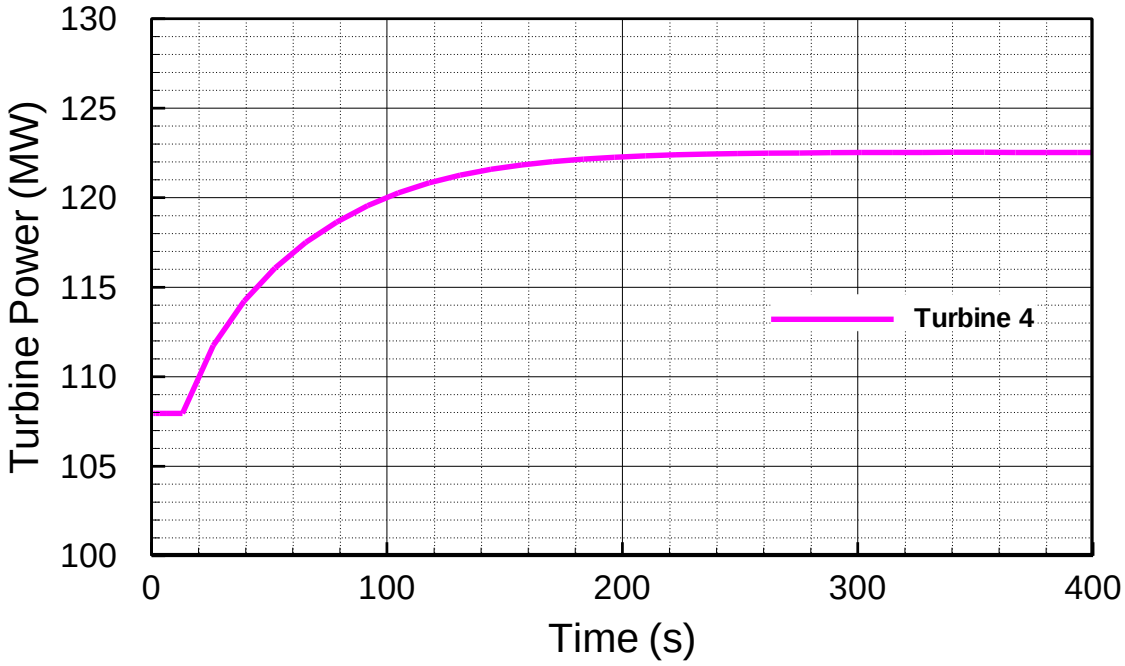

Figure 110. Step function schedule, turbine sets' power generations: Turbine 4.

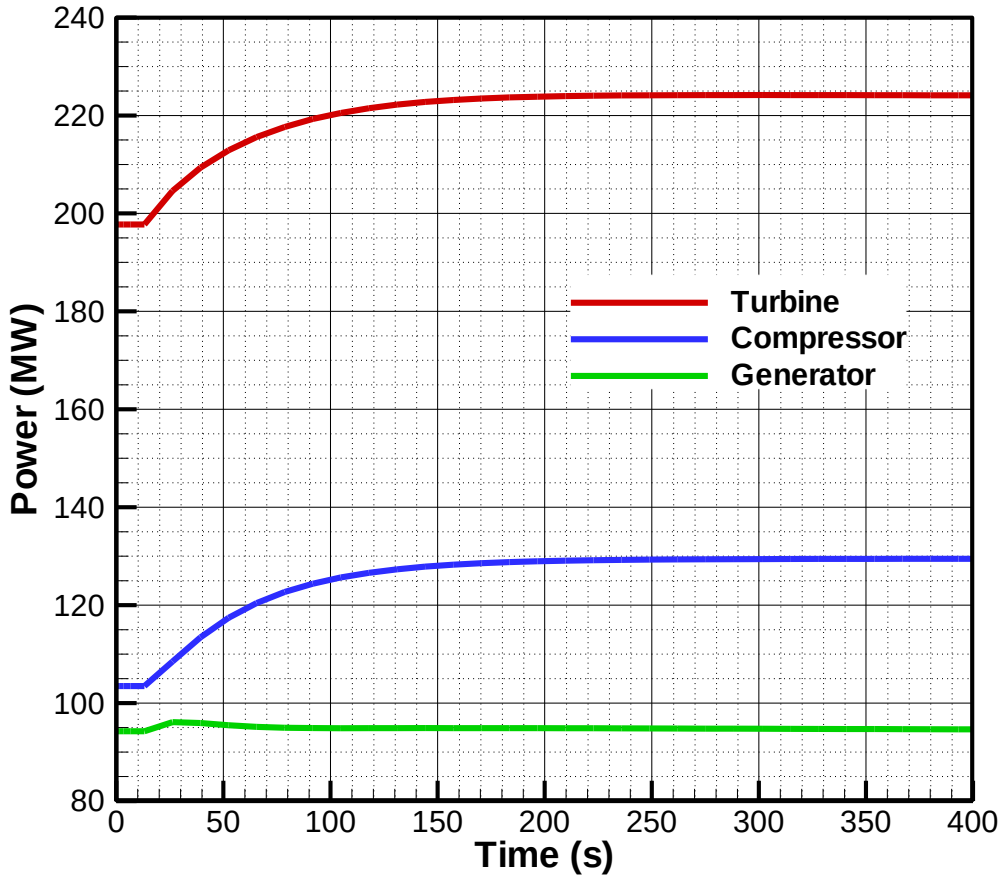

Figure 111. Step function schedule: Total power for each component.

Figure 113 shows the non-dimensional shaft rotational speed. The rotational speed increases by 11% as a result of the increased fuel flow.

Finally, Figure 114 and Figure 115 show the pressure and temperature distribution in all 14 plena, respectively. As seen in the first figure, the pressure values increase by 5-10% in different stages. On the other hand, temperature values in compressors are increased by about 5% contrary to turbines and injectors in which temperatures are increased by about 10%.

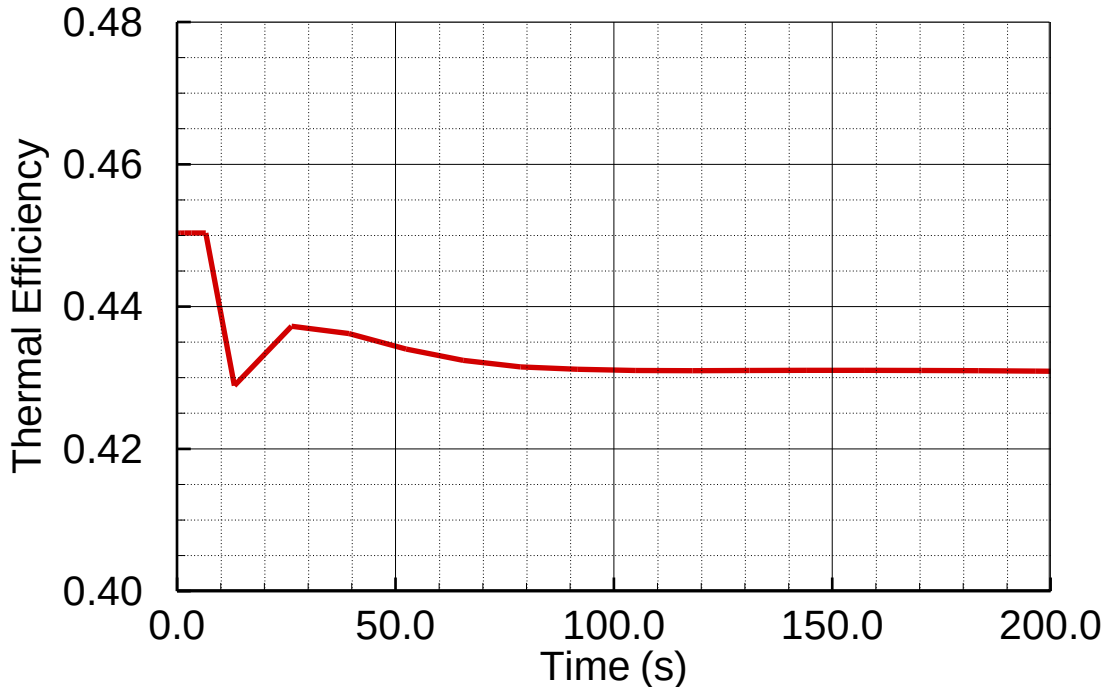

Figure 112. Step function schedule: Engine thermal efficiency.

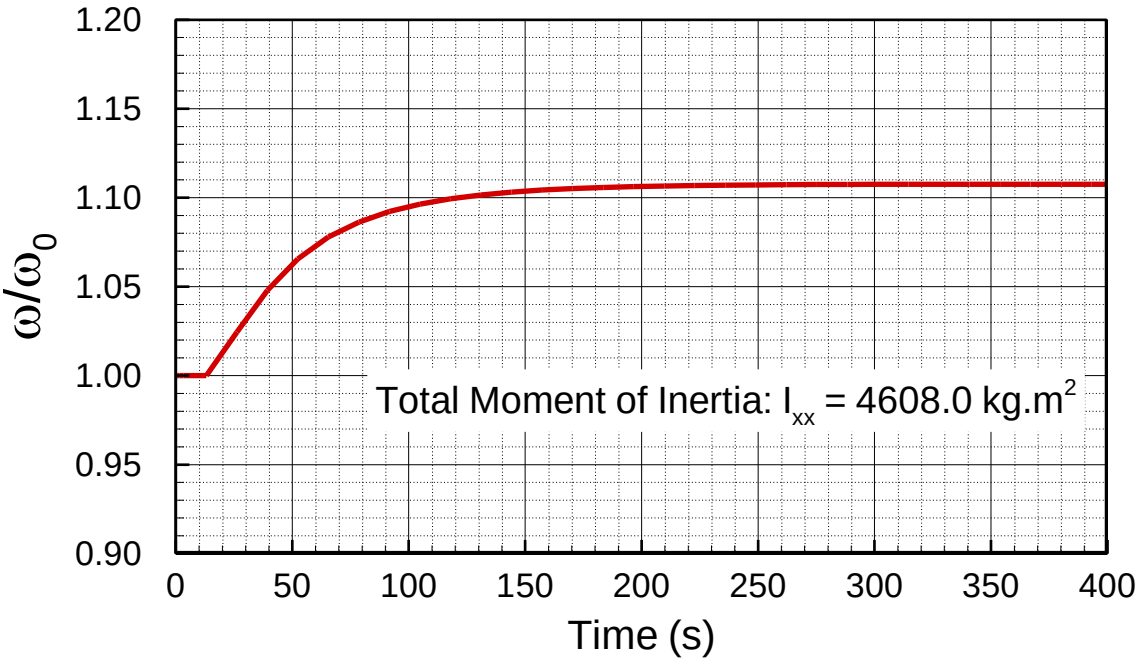

Figure 113. Step function schedule: Non-dimensional shaft rotational speed.

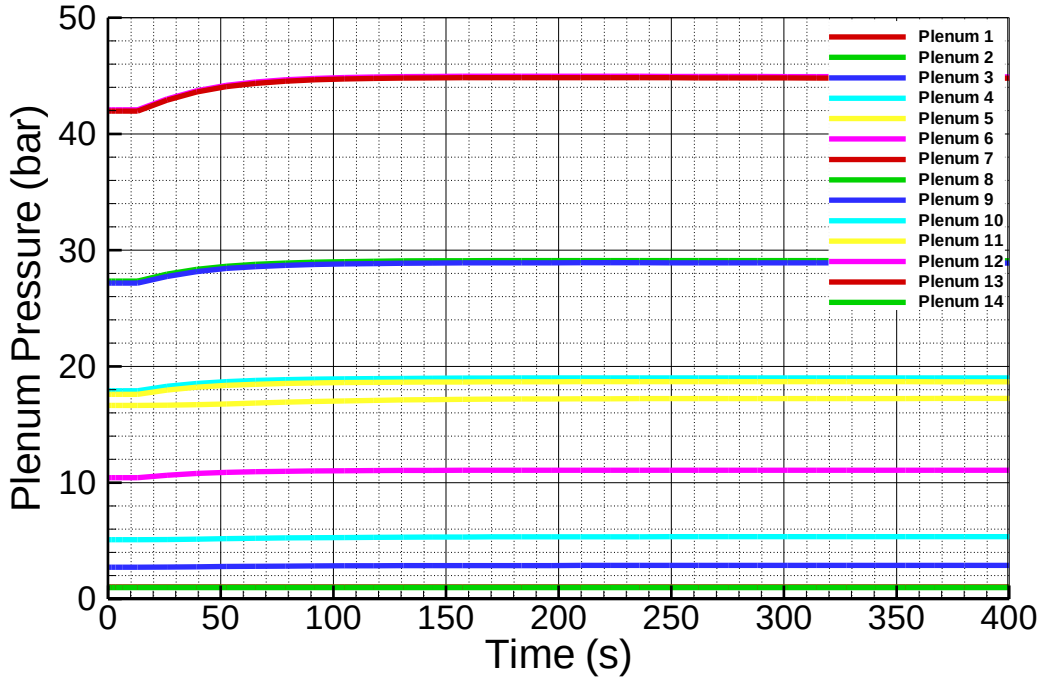

Figure 114. Step function schedule: Plena pressure.

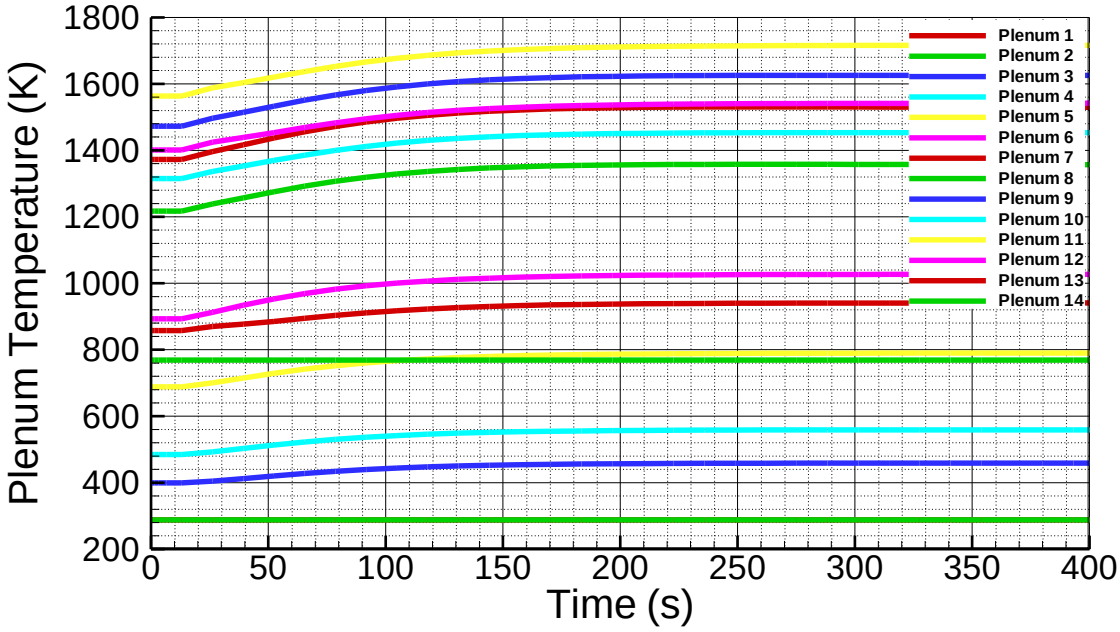

Figure 115. Step function schedule: Plena temperature.

CHAPTER VII

CONCLUSION

The Ultra-High Efficiency Gas Turbine Engine (UHEGT) is introduced, designed, and simulated in this study. UHEGT is based on the concept of sequential combustion (reheat) in the gas turbine engine. In UHEGT, the combustion process is no longer contained in isolation between the compressor and turbine, rather distributed and integrated within stator rows of the HP-turbine stages. As shown in this study, this technology substantially increases the thermal efficiency of the engine. Additionally, it significantly increases the engine power output, reduces pollutant emissions, and reduces the engine size and weight.

In the first part of this research, a comprehensive aerothermodynamic study is conducted which shows that the UHEGT technology increases the engine efficiency by 5-7% compared to current most advanced gas turbine engines such as Alstom's GT 24/26. Moreover, the total output power is significantly increased due to an increase in the total amount of fuel combined with higher thermal efficiency. Based on all the important parameters including thermal efficiency, total power, fuel flow rate in each combustion stage, Turbine Inlet Temperature (TIT), etc., the complete thermodynamic cycle for the system is developed. The final system has a six-stage turbine with three stages of stator internal combustion and a compressor with pressure ratio of 40:1. The thermodynamic

efficiency of more than 45% is achieved in this cycle. Based on the thermodynamic cycle, 1D/2D (meanline) approach is used to design the entire flow path for the turbine.

In the next section, different injector configurations are designed and studied to develop the optimum combustion system for UHEGT. The important parameters for a suitable combustion unit for UHEGT are: enabling sequential combustion, utilizing inherent secondary flows and induced vortices to provide a stable combustion environment, provide uniform temperature distribution at the rotor inlet, etc. The studies are performed on a single-stage turbine via Computational Fluid Dynamics (CFD) and the simulations are unsteady and include multispecies combustion process along with rotor motion. The flow field is analyzed based on different parameters such as velocity patterns, Mach number, pressure, and temperature distribution, losses and emissions, etc. The final configuration for the combustion system includes two rows of injectors placed before the stator rows in the first three turbine stages. The injectors are hollow tubes extended from hub to shroud with slots on top and bottom for fuel injection. Three or four injectors per stator blade are included in each combustion stage. This configuration provides a highly uniform temperature distribution at the rotor inlet, low pressure loss, low emissions, small weight and volume, and ease of manufacturing compared to the other cases. Von Karman vortices and the Coanda effect help to enhance the mixing between fuel and air particles and increase combustion stability.

In the next section, a complete CFD model is developed to simulate multiple stages of the UHEGT turbine with stator internal combustion. Flow patterns, secondary flow losses, temperature distribution, and pollutant emissions are studied in the results in order

to investigate the interactions between consecutive combustion and turbine stages. The flow paths are modified based on the CFD results in order to reduce separation and pressure losses while enabling maximum mixing of fuel and air and reducing temperature non-uniformities. The results show that:

1. There is a deviation angle at the exit of each stator or rotor component. This deviation transforms to a large incidence angle in the following component. The stagger angle for each component is slightly modified in order to make up for the deviation.

2. The injector wakes become larger as they move towards the blades' pressure sides which is due to the higher resistance against the flow in that area.

3. Injector wakes are larger in the lower pressure turbine stages. This causes the injector pressure loss to increase in the second and third stages.

4. Combustion takes place mostly before the gas reaches the stator leading edge. The hot gases are mixed with the mainstream flow along the stator channel.

5. Highly uniform temperature distribution is achieved at the inlet of each rotor stage (non-uniformity is below 10%).

6. There is a good agreement between the meanline and CFD calculations for different parameters.

Since the combustion process is brought into the turbine stages in UHEGT, the stator blades are exposed to high temperature gases and are prone to be overheated. That is one of the main phenomena observed in the simulation results discussed before. The next part of this research is dedicated to investigation of different methods to reduce the stator blade surface temperature. Two different approaches in this regard are numerically

studied: the first is based on indexing (clocking) fuel injectors relative to each other and the stator blades and the second is based on using film cooling. Four different configurations are designed and simulated via CFD to evaluate the effectiveness of the two approaches. Based on the results, the configuration with indexing approach provides the best option in lowering the stator blade surface temperature. This configuration brings down the average stator blade surface temperature to near the compressor air temperature which is ideal for the blade material. The blade surface is completely protected against the hot combustion gases in this configuration. However, this configuration produces a higher temperature non-uniformity compared to the other configurations. The higher non-uniformity could negatively affect the rotor blade material, but it does not noticeably reduce the amount of power generated by the rotor. Moreover, this configuration uses the lowest number of injectors per blade, produces the least amount of total pressure loss, and is the easiest configuration to manufacture. Therefore, the indexing in this configuration is the best option in reducing the stator blade surface temperature among the cases studied in this research. Film cooling approach can be considered the second-best option in controlling the blade surface temperature. This approach successfully brings down the average stator blade surface temperature by more than 100 degrees and produces a highly uniform temperature distribution at the rotor inlet. For the second and third turbine stages with stator internal combustion, a similar indexing approach could be used to optimize the temperature distribution. The fuel injectors need to be indexed based on the flow patterns and temperature distribution in each stage. Moreover, use of film cooling is recommended for the rotor blades.

In the last part of this research, a dynamic simulation is performed on the entire engine using the nonlinear generic code GETRAN developed by Schobeiri [1], [30]. The simulations are in 2D (space-time) and include majority of the engine components, i.e. compressor, turbine, injectors, diffuser, control system, pipes, etc. The time-dependent simulations are performed in variable design and off-design conditions that engine goes through during its performance. Three main conditions are simulated via fuel schedules applied through fuel valves which include sinusoidal, Gaussian, and step function. The results show that fluctuations in the fuel flow rate lead to fluctuations with similar patterns in the majority of the system parameters such as compressor and turbine mass flow rates, temperatures, pressures, power, shaft speed, etc. However, the fluctuation profiles in different parameters are different in amplitude and typically have a time lag compared to the fuel schedules. The time lag represents the reaction time of the engine and the control system to adjust itself to the changes in fuel flow. Regarding the intensity of the fluctuations, usually mass flow rates of turbine and compressor and shaft rotational speed fluctuate with lower amplitudes compared to the fuel schedule. The intensity of fluctuation in those parameters are directly affected by the rotating shaft moment of inertia. On the other hand, the fluctuation amplitudes in temperatures, and compressor and turbine powers usually tend to be higher. It is also seen that generator (or net) power has a very similar fluctuation pattern to the fuel schedule, both in shape of the profile and intensity of the fluctuation. Regarding the thermal efficiency, it is seen that the range of the changes is relatively lower than the other parameters. That means the system performs near the design point efficiency throughout the entire cycle. However, an increase in the total average fuel in the system

causes the average thermal efficiency to drop slightly. That is due to the thermodynamic cycle being moved from the design point conditions. It is also seen that the first fluctuation cycle in the each response profile is slightly different than the following cycles. That is due to the transient response in the beginning of the oscillation which will be damped quickly.

REFERENCES

[1] Schobeiri, M. T. *Turbomachinery Flow Physics and Dynamic Performance.* 2nd and enhanced ed., Springer (2012).

[2] GE Power, URL https://www.gepower.com.

[3] Siemens, URL https://www.siemens.com.

[4] Rolls-Royce, URL https://www.rolls-royce.com.

[5] Schobeiri, M. T. *Gas Turbine Design, Components and System Design Integration*. Springer (2018).

[6] Schobeiri, M. T. “Prozessoptimierung fur die Kombianlagen.” BBC–Internal Classified Report No. BBC-TN-86-112. 1986.

[7] Schobeiri, M. T. “The Ultra-High Efficiency Gas Turbine Engine with Stator Internal Combustion, UHEGT.” US Patent pending, No. 1389-TEES-99. 1999.

[8] Schobeiri, Meinhard T. "Ultra-High Efficiency Gas Turbine (UHEGT) with Stator Internal Combustion." US patent application. No. US 14/595,417. 2014.

[9] DÃķbbeling, Klaus, Hellat, Jaan and Koch, Hans. "25 years of bbc/abb/alstom lean premix combustion technologies." *ASME Journal of Engineering for Gas Turbines and Power* Vol. 129, no. 1 (2007): pp. 2-12. DOI 10.1115/1.2181183.

[10] Agbonzikilo, F. E., Owen, I., Stewart, J., Sadasivuni, S. K., Riley, M., and Sanderson, V. “Experimental and Numerical Investigation of Fuel–Air Mixing in a Radial Swirler Slot of a Dry Low Emission Gas Turbine Combustor.” *ASME J. Eng. Gas Turbines Power* Vol. 138, no. 6 (2016): pp. 061502.

[11] Moran, M. J., Shapiro, H. N., Boettner, D. D., Bailey, M. B. *Fundamentals of Engineering Thermodynamics.* 7th Edition, John Wiley & Sons (2011).

[12] Schobeiri, M. T. “Dynamisches Verhalten der Luftspeichergasturbine Huntorf bei einem Lastabwurf mit Schnellabschaltung,” Brown Boveri, Technical Report No. TA-58. 1982.

[13] Schobeiri, T. and Haselbacher, H. “Transient Analysis of Gas Turbine Power Plants, Using the Huntorf Compressed Air Storage Plant as an Example.” *Proceedings of ASME 1985 International Gas Turbine Conference and Exhibit*. pp. V003T10A015-V003T10A015. March 1985.

[14] Schobeiri, T. “A general Computational method for simulation and prediction of transient behavior of gas Turbines.” *Proceedings of ASME 1986 International Gas Turbine Conference and Exhibit*. pp. V001T01A070-V001T01A070. June 1986.

[15] Schobeiri, Meinhard T. and Ghoreyshi, Seyed M. "The Ultrahigh Efficiency Gas Turbine Engine with Stator Internal Combustion." *ASME Journal of Engineering for Gas Turbines and Power* Vol. 138, no. 2 (2016): pp. 021506. DOI 10.1115/1.4031273.

[16] Schobeiri, Meinhard T. and Ghoreyshi, Seyed M. “UHEGT, the Ultra-High Efficiency Gas Turbine Engine with Stator Internal Combustion.” *Proceedings of the ASME Turbo Expo 2015: Turbine Technical Conference and Exposition*. pp. V003T06A019-V003T06A019. Montreal, Quebec, Canada, June 15–19, 2015. DOI 10.1115/GT2015-43447.

[17] Ghoreyshi, Seyed M. and Schobeiri, Meinhard T. “Numerical Simulation of the Multistage Ultra-High Efficiency Gas Turbine Engine, UHEGT.” *Proceedings of ASME Turbo Expo 2017: Turbomachinery Technical Conference and Exposition*. pp. V003T06A034-V003T06A034. Charlotte, North Carolina, USA, June 26–30, 2017. DOI 10.1115/GT2017-65029.

[18] Ghoreyshi, Seyed M. and Schobeiri, Meinhard T. “A Numerical Study on Reducing the Stator Blade Surface Temperature in the Ultra-High Efficiency Gas Turbine Engine by Indexing Fuel Injectors and Using Film Cooling.” *Proceedings of ASME Turbo Expo 2018: Turbomachinery Technical Conference and Exposition*. Oslo, Norway, June 11–15, 2018.

[19] EPRIGEN. “Thermal Performance of the ABB GT24 Gas Turbine in Peaking Service at the Gilbert Station of GPU Energy.” EPRIGEN, Palo Alto, CA. 1998.

[20] Savic, S., Lindvall, K., Papadopoulos, T., and Ladwig, M. “The Next Generation KA24/GT24 from Alstom, the Pioneer in Operational Flexibility.” *Alstom Power Industry Seminar*. Newport, RI, USA, 2011.

[21] Güthe, Felix, Hellat, Jaan and Flohr, Peter. "The reheat concept: the proven pathway to ultralow emissions and high efficiency and flexibility." *ASME Journal of Engineering for Gas Turbines and Power* Vol. 131, no. 2 (2009): pp. 021503. DOI 10.1115/1.2836613.

[22] Eroglu, Adnan, Flohr, Peter, Brunner, Philipp and Hellat, Jaan. “Combustor design for low emissions and long lifetime requirements.” *Proceedings of ASME Turbo*

Expo 2009: Power for Land, Sea, and Air. Paper No. GT2009-59540, pp. 435-444. Orlando, Florida, USA, June 8–12, 2009. DOI 10.1115/GT2009-59540.

[23] Cottle, Andrew E. and Polanka, Marc D. "Numerical and Experimental Results from a Common-Source High-G Ultra-Compact Combustor." *Proceedings of the ASME Turbo Expo 2016: Turbomachinery Technical Conference and Exposition*. pp. V04AT04A013-V04AT04A013. Seoul, South Korea, June 13-17, 2016. DOI 10.1115/GT2016-56215.

[24] Zelina, Joseph, Sturgess, Geoff and Shouse, Dale. "The Behavior of an Ultra-Compact Combustor (UCC) Based on Centrifugally-Enhanced Turbulent Burning Rates." *Proceedings of 40th AIAA/ASME/SAE/ASEE Joint Propulsion Conference and Exhibit*. AIAA 2004-3541. Fort Lauderdale, FL, 2004. URL https://doi.org/10.2514/ 6.2004-3541.

[25] Sirignano, W. A. and Liu, F. "Performance Increases for Gas-Turbine Engines Through Combustion Inside the Turbine." *Journal of Propulsion and Power* Vol. 15, no. 1 (1999): pp. 111-118. URL https://doi.org/10.2514/2.5398.

[26] Sirignano, W. A., Dunn-Rankin, D., Liu, F., Colcord, B. and Puranam, S. "Turbine Burners: Performance Improvement and Challenges of Flameholding." *AIAA Journal* Vol. 50, no. 8 (2012): pp. 1645-1669. DOI 10.2514/1.J051562.

[27] Zajadatz, M., Lachner, R., Bernero, S., Motz, C., & Flohr, P. "Development and design of ALSTOM'S staged fuel gas injection EV burner for NOx reduction." *Proceedings of ASME Turbo Expo January 2007: Power for Land, Sea, and Air*. pp. 559-567. January 2007.

[28] Bobusch, B. C., Berndt, P., Paschereit, C. O., & Klein, R. “Shockless explosion combustion: An innovative way of efficient constant volume combustion in gas turbines.” *Combustion Science and Technology* Vol. 186, no. 10-11 (2014): pp. 1680-1689.

[29] Reichel, T. G., Schäpel, J. S., Bobusch, B. C., Klein, R., King, R., & Paschereit, C. O. “Shockless Explosion Combustion: Experimental Investigation of a New Approximate Constant Volume Combustion Process.” *Journal of Engineering for Gas Turbines and Power* Vol. 139, no. 2 (2017): pp. 021504.

[30] Schobeiri, M. T. “Final Report on GETRAN: The GEneric, Modularly Structured Computer Code for Simulation of the Transient Behavior of Single- and Multi-spool Aero and Power Generation Gas Turbine Engines.” Volume I: Technical Report, submitted to NASA Lewis Research Center. December, 1995.

[31] Schobeiri, M. T. “Final Report on GETRAN: The GEneric, Modularly Structured Computer Code for Simulation of the Transient Behavior of Single- and Multi-spool Aero and Power Generation Gas Turbine Engines.” Volume II: Technical Report, submitted to NASA Lewis Research Center. December, 1995.

[32] Schobeiri, M. T. “Final Report on GETRAN: The GEneric, Modularly Structured Computer Code for Simulation of the Transient Behavior of Single- and Multi-spool Aero and Power Generation Gas Turbine Engines.” Volume III: Technical Report, submitted to NASA Lewis Research Center. December, 1995.

[33] Lefebvre, A. H. and Ballal, D. R. *Gas Turbine Combustion: Alternative Fuels and Emissions*. Third Edition. CRC press, Taylor and Francis. 2010.

[34] Thornburg, H., Sekar, B., Zelina, J., Lin, C., and Holder, R. “Prediction of Inter-Turbine Burner (ITB) Performance with Curved Radial Vane Cavity at Various Equivalence Ratios.” *ASME* Paper No. GT2008-50192. 2008.

[35] Schobeiri, M. T. “On the Stability Behavior of Vortex Flows in Turbomachinery.” *Z. Flugwiss. Weltraumforsch*. Vol. 13 (1989): pp. 233–239 (in German).

[36] Schobeiri, M. T., and Ozturk, B. “Experimental Study of the Effect of the Periodic Unsteady Wake Flow on Boundary Layer Development, Separation, and Re-Attachment Along the Surface of a Low Pressure Turbine Blade.” *ASME J. Turbomach.* Vol. 126, no. 4 (2004): pp. 663–676.

[37] Schobeiri, M. T., and Chakka, P. “Prediction of Turbine Blade Heat Transfer and Aerodynamics Using Unsteady Boundary Layer Transition Model.” *Int. J. Heat Mass Transfer* Vol. 45, no. 4 (2002): pp. 815–829.

[38] Schobeiri, M. T., Read, K., and Lewalle, J. “Effect of Unsteady Wake Passing Frequency on Boundary Layer Transition, Experimental Investigation and Wavelet Analysis.” *ASME J. Fluids Eng.* Vol. 125, no. 2 (2003): pp. 251–266.

[39] Wright, L., and Schobeiri, M. T. “The Effect of Periodic Unsteady Flow on Boundary Layer and Heat Transfer on a Curved Surface.” *ASME J. Heat Transfer* Vol. 121, no. 1 (1999): pp. 22–33.

[40] Claypole, T. “Coherent Structures in Swirl Generators and Combustors.” *Proceedings of the ASME Symposium Vortex Flows*. Winter Annual Meeting, Chicago, IL, Nov. 16–21, 1980.

[41] Lilley, D. “Swirl Flows in Combustion: A Review.” *AIAA Journal* Vol. 15, no. 8 (1977): pp. 1063–1078.

[42] Claypole, T., and Syred, N. “The Effect of Swirl Burner Aerodynamics on NOx Formation.” *Symp. (Int.) Combust.* 18(1) (1981): pp. 81–89.

[43] Farber, J., Koch, R., Bauer, H., Hase, M., and Krebs, W. “Effects of Pilot Fuel and Liner Cooling on the Flame Structure in a Full Scale Swirl-Stabilized Combustion Setup.” *ASME J. Eng. Gas Turbines Power* Vol. 132, no. 9 (2010): p. 091501.

[44] Lucca-Negro, O., and O’Doherty, T. “Vortex Breakdown: A Review.” *Prog. Energy Combust. Sci.* Vol. 27, no. 4 (2001): pp. 431–481.

[45] Keller, J., Egli, W., and Althaus, R. “Vortex Breakdown as a Fundamental Element of Vortex Dynamics.” *Z. Angew. Math. Phys.* Vol. 39, no. 3 (1988): pp. 404–440.

[46] Keller, J. J., Sattelmayer, T., and Thueringer, F. “Double-Cone Burners for Gas Turbine Type 9 Retrofit Application.” *19th International Congress on Combustion Engines*. CIMAC, Florence. 1991.

[47] Kazemi, A. and Curet, O. "PIV measurements and flow characteristics downstream of mangrove root models." *In APS Division of Fluid Dynamics Meeting Abstracts*. 2016.

[48] Kazemi, A., Van de Riet, K. and Curet, O. M. "Hydrodynamics of mangrove-type root models: the effect of porosity, spacing ratio and flexibility." *Bioinspiration & biomimetics* Vol. 12, no. 5 (2017): 056003.

[49] Gupta, A. K., Lilley, D. G., and Syred, N. *Swirl Flows*. Abacus, Tunbridge Wells, Kent, England (1984).

[50] Anacleto, P. M., Fernandes, E. C., Heitor, M. V., and Shtork, S. I. “Swirl Flow Structure and Flame Characteristics in a Model Lean Premixed Combustor.” *Combust. Sci. Technol.* Vol. 175, no. 8 (2003): pp. 1369–1388.

[51] Beer, J. M., and Chigier, N. A. *Combustion Aerodynamics*, Wiley, Halstead Press Division, New York (1972).

[52] Duwig, C., Ducruix, S., and Veynante, D. “Studying the Stabilization Dynamics of Swirling Partially Premixed Flames by Proper Orthogonal Decomposition.” *ASME J. Eng. Gas Turbines Power* Vol. 134, no. 10 (2012): p. 101501.

[53] Galley, D., Ducruix, S., Lacas, F., and Veynante, D. “Mixing and Stabilization Study of a Partially Premixed Swirling Flame Using Laser Induced Fluorescence.” *Combust. Flame* Vol. 158, no. 1 (2011): pp. 155–171.

[54] Wurm, B., Schulz, A., Bauer, H., and Gerendas, M. “Impact of Swirl Flow on the Cooling Performance of an Effusion Cooled Combustor Liner.” *ASME J. Eng. Gas Turbines Power* Vol. 134, no. 12 (2012): p. 121503.

[55] Wurm, B., Schulz, A., & Bauer, H. J. “A new test facility for investigating the interaction between swirl flow and wall cooling films in combustors.” *Proceedings of ASME Turbo Expo 2009: Power for Land, Sea, and Air*. pp. 1397-1408. January 2009.

[56] Beard, P., Smith, A., and Povey, T. “Effect of Combustor Swirl on Transonic High Pressure Turbine Efficiency.” *ASME J. Turbomach*. Vol. 136, no. 1 (2014): p. 011002.

[57] Shanbhogue, S. J., Husain, S., and Lieuwen, T. “Lean blowoff of bluff body stabilized flames: Scaling and dynamics.” *Progress in Energy and Combustion Science* Vol. 35, no. 1 (2009): pp. 98-120.

[58] Rao, K. V. L., & Lefebvre, A. H. “Flame blowoff studies using large-scale flameholders.” *Journal of Engineering for Power* Vol. 104, no. 4 (1982): pp. 853-857.

[59] Rizk, N. K., & Lefebvre, A. H. “The relationship between flame stability and drag of bluff-body flameholders.” *Journal of Propulsion and Power* Vol. 2, no. 4 (1986): pp. 361-365.

[60] Ballal, D. R., & Lefebvre, A. H. “Weak extinction limits of turbulent flowing mixtures.” *Journal of Engineering for Power* Vol. 101, no. 3 (1979): pp. 343-348.

[61] Ballal, D. R., & Lefebvre, A. H. “Weak Extinction Limits of Turbulent Heterogeneous Fuel/Air Mixtures.” *Journal of Engineering for Power* Vol. 102, no. 2 (1980): pp. 416-421.

[62] Baxter, M. R., & Lefebvre, A. H. “Weak extinction limits of large-scale flameholders.” *Journal of engineering for gas turbines and power* Vol. 114, no. 4 (1992): pp. 776-782.

[63] Jenny, P., Lenherr, C., Abhari, R. S., and Kalfas, A. “Effect of Hot Streak Migration on Unsteady Blade Row Interaction in an Axial Turbine.” *ASME J. Turbomach.* Vol. 134, no. 5 (2012): pp. 051020.

[64] Mathison, R., Haldeman, C., and Dunn, M. “Aerodynamics and Heat Transfer for a Cooled One and One-Half Stage High-Pressure Turbine–Part I: Vane Inlet

Temperature Profile Generation and Migration." *Proceedings of ASME Turbo Expo 2010: Power for Land, Sea and Air*. Jun. 14–18, 2010, Glasgow.

[65] Mathison, R. M., Haldeman, C. W., & Dunn, M. G. "Aerodynamics and Heat Transfer for a Cooled One and One-Half Stage High-Pressure Turbine–Part II: Influence of Inlet Temperature Profile on Blade Row and Shroud." *Journal of Turbomachinery* Vol. 134, no. 1 (2012): pp. 011007.

[66] Simone, S., Montomoli, F., Martelli, F., Chana, K., Qureshi, I., and Povey, T. "Analysis on the Effect of a Nonuniform Inlet Profile on Heat Transfer and Fluid Flow in Turbine Stages." *ASME J. Turbomach*. Vol. 134, no. 1 (2012): p. 011012.

[67] Barringer, M., Thole, K., and Polanka, M. "Effects of Combustor Exit Profiles on Vane Aerodynamic Loading and Heat Transfer in a High Pressure Turbine." *ASME J. Turbomach*. Vol. 131, no. 2 (2009): p. 021008.

[68] Khanal, B., He, L., Northall, J., and Adami, P. "Analysis of Radial Migration of Hot-Streak in Swirling Flow Through High-Pressure Turbine Stage." *ASME J. Turbomach*. Vol. 135, no. 4 (2013): p. 041005.

[69] Shang, Tonghuo and Epstein, Alan H. "Analysis of Hot Streak Effects on Turbine Rotor Heat Load." *ASME J. Turbomach* Vol. 119, no. 3 (1997): pp. 544–553. DOI 10.1115/1.2841156.

[70] Qureshi, I., Beretta, A., and Povey, T. "Effect of Simulated Combustor Temperature Nonuniformity on HP Vane and End Wall Heat Transfer: An Experimental and Computational Investigation." *ASME J. Eng. Gas Turbines Power* Vol. 133, no. 3 (2011): p. 031901.

[71] Wang, J., Ge, N., & Sheng, C. “Analysis of swirling flow effects on the characteristics of unsteady hot-streak migration.” *Chinese Journal of Aeronautics* (2016).

[72] Błachnio, J., & Pawlak, W. I. “Non-uniformity of the combustor exit flow temperature in front of the gas turbine.” *acta mechanica et automatica* Vol. 8, no 4 (2014): pp. 209-213.

[73] Barzegarian, R., Aloueyan, A., and Yousefi, T. "Thermal performance augmentation using water based Al2O3-gamma nanofluid in a horizontal shell and tube heat exchanger under forced circulation." *International Communications in Heat and Mass Transfer* Vol. 86 (2017): 52-59.

[74] Jafari, M. M., Atefi, G. A. and Khalesi, J. “Advances in nonlinear stress analysis of a steam cooled gas turbine blade.” Latin American Applied Research Vol. 42, no. 2 (2012): pp. 167-175.

[75] Atefi, G. A., Jafari, M. M., Khalesi, J., & Soleymani, A. “The thermoelastic stress analysis of a gas turbine blade with cooling.” *In 13th Annual & 2nd Int. Fluid Dyn. Conf*. 2010.

[76] Chibli, H. A., Abdelfattah, S. A., Schobeiri, M. T., & Kang, C. “An experimental and numerical study of the effects of flow incidence angles on the performance of a stator blade cascade of a high pressure steam turbine.” *Proceedings of ASME Turbo Expo 2009: Power for Land, Sea, and Air*. pp. 821-830. January 2009.

[77] Schobeiri, M. T., & Nikparto, A. “A comparative numerical study of aerodynamics and heat transfer on transitional flow around a highly loaded turbine blade with

flow separation using rans, urans and les." *Proceedings of ASME Turbo Expo 2014: Turbine Technical Conference and Exposition*. pp. V05CT17A001-V05CT17A001. June 2014.

[78] Rezasoltani, M., Lu, K., Schobeiri, M., and Han, J. C. "A Combined Experimental and Numerical Study of the Turbine Blade Tip Film Cooling Effectiveness Under Rotation Condition." *ASME J. Turbomach*. Vol. 137, no. 5 (2015): p. 051009.

[79] Nikparto, A., & Schobeiri, M. T. "Numerical and Experimental Investigation of Aerodynamics on Flow Around a Highly Loaded Low-Pressure Turbine Blade with Flow Separation Under Steady and Periodic Unsteady Inlet Flow Condition." *Proceedings of ASME Turbo Expo 2016: Turbomachinery Technical Conference and Exposition*. pp. V05AT13A010-V05AT13A010. June 2016.

[80] Nikparto, A., & Schobeiri, M. T. "Investigation of Aerodynamics and Heat Transfer of a Highly Loaded Turbine Blade Using the Universal Intermittency Function." *Proceedings of ASME Turbo Expo 2017: Turbomachinery Technical Conference and Exposition.* pp. V02DT46A030-V02DT46A030). June 2017.

[81] Nikparto, Ali and Schobeiri, Meinhard T. "Combined numerical and experimental investigations of heat transfer of a highly loaded low-pressure turbine blade under periodic inlet flow condition." *Proceedings of IMechE, Part A: Journal of Power and Energy* (2018). DOI https://doi.org/10.1177/0957650918758158.

[82] Mortazavi, Farzam and Palazzolo, Alan. "Prediction of Rotordynamic Performance of Smooth Stator-Grooved Rotor Liquid Annular Seals Utilizing

Computational Fluid Dynamics.” *ASME Journal of Vibration and Acoustics* Vol. 140, no. 3 (2017): pp. 031002-031002-031009. DOI 10.1115/1.4038437.

[83] Mortazavi, Farzam, Riasi, Alireza and Nourbakhsh, Ahmad. “Numerical Investigation of Back Vane Design and Its Impact on Pump Performance.” *ASME Journal of Fluids Engineering* Vol. 139, no. 12 (2017): pp. 121104-121104-121109. DOI 10.1115/1.4037281.

[84] Ghoreyshi, Mostafa, Saidi, Mohamad S., Navabi, Mohamad A., Firoozabadi, Bahar D. and Shabanian, Reza. “Numerical investigation of antegrade flow effects on flow pulsations in Fontan operation.” *International Journal of Biomedical Engineering and Technology* Vol. 10, no. 3 (2012): pp. 221-238. URL https://doi.org/10.1504/IJBET. 2012.050291.

[85] Jafari, M., Afshin, H., Farhanieh, B. and Bozorgasareh, H. "Numerical aerodynamic evaluation and noise investigation of a bladeless fan." *Journal of Applied Fluid Mechanics* Vol. 8, no. 1 (2015): 133-142.

[86] Jafari, M., Afshin, H., Farhanieh, B. and Bozorgasareh, H. "Experimental and Numerical Investigation of a 60cm Diameter Bladeless Fan." *Journal of Applied Fluid Mechanics* Vol. 9, no. 2 (2016).

[87] Jafari, Mohammad, Afshin, Hossein, Farhanieh, Bijan and Sojoudi, Atta. "Numerical investigation of geometric parameter effects on the aerodynamic performance of a Bladeless fan." *Alexandria Engineering Journal* Vol. 55, no. 1 (2016): 223-233.

[88] ANSYS. “ANSYS CFX-Solver Modeling Guide.” Release 15.0. Nov. 2013.

[89] Magnussen, B. F., and Hjertager, B. H. “On mathematical modeling of turbulent combustion with special emphasis on soot formation and combustion.” *In Symposium (International) on Combustion* Vol. 16, No. 1 (1977): pp. 719-729, Elsevier.

[90] Menter, F. R. “Two-equation eddy-viscosity turbulence models for engineering applications.” *AIAA journal* Vol. 32, no. 8 (1994): pp. 1598-1605.

[91] Mansouri, Z., Aouissi, M., & Boushaki, T. “A Numerical Study of Swirl Effects on the Flow and Flame Dynamics in a Lean Premixed Combustor.” *International Journal of Heat and Technology* Vol. 34, No. 2 (2016): pp. 227-235.

[92] Lefebvre, A.H. “The Role of Fuel Preparation in Low-Emission Combustion.” *Journal of Engineering for Gas Turbines and Power* Vol. 117 (1995): pp 617-654.

[93] Mitsubishi. “MHPS Gas Turbine M501G/M701G.” Mitsubishi Hitachi Power Systems, LTD. Technical Report.

[94] König, S., Stoffel, B., & Schobeiri, M. T. “Experimental investigation of the clocking effect in a 1.5-stage axial turbine—part i: Time-averaged results.” *Journal of Turbomachinery* Vol. 131, no. 2 (2009): pp. 021003.

[95] Huber, F. W., Johnson, P. D., Sharma, O. P., Staubach, J. B., and Gaddis, S. W. “Performance Improvement Through Indexing of Turbine Airfoils: Part 1—Experimental Investigation.” *ASME J. Turbomach*. Vol. 118 (1996): pp. 630–635.

[96] Griffin, L. W., Huber, F. M., and Sharma, O. P. “Performance Improvement Through Indexing Turbine Airfoils: Part 2—Numerical Simulation.” *ASME J. Turbomach.* Vol. 118 (1996): pp. 636–642.

[97] Padture, N. P., Gell, M., & Jordan, E. H. “Thermal barrier coatings for gas-turbine engine applications.” *Science* Vol. 296, no. 5566 (2002): pp. 280-284.

[98] Clarke, D. R., Oechsner, M., & Padture, N. P. “Thermal-barrier coatings for more efficient gas-turbine engines.” *MRS bulletin* Vol. 37, no. 10 (2012): pp. 891-898.

[99] Kroniger, D., Wirsum, M., Horikawa, A., Okada, K., & Kazari, M. “NOx Correlation for an Industrial 10 MW Non-Premixed Gas Turbine Combustor for High Hydrogen Fuels.” *In ASME Turbo Expo June 2016: Turbomachinery Technical Conference and Exposition.* pp. V04AT04A012-V04AT04A012. June 2016.

[100] Nikparto, Ali and Schobeiri, Meinhard T. “Experimental Investigation of Film-Cooling Effectiveness of a Highly Loaded Turbine Blade Under Steady and Periodic Unsteady Flow Conditions.” *ASME Journal of Heat Transfer* Vol. 139, no. 7 (2017): pp. 072201. DOI 10.1115/1.4035651.

[101] Nikparto, Ali, Rice, Tyler and Schobeiri, Meinhard T. "Experimental and Numerical Investigation of Heat Transfer and Film Cooling Effectiveness of A Highly Loaded Turbine Blade Under Steady And Unsteady Wake Flow Condition." *Proceedings of ASME Turbo Expo 2017: Turbomachinery Technical Conference and Exposition*. pp. V05CT19A029-V05CT19A029. Charlotte, North Carolina, USA, June 26–30, 2017. DOI 10.1115/GT2017-65012.

[102] Nirmalan, N. V. and Hylton, L. D. " An Experimental Study of Turbine Vane Heat Transfer with Leading Edge and Downstream Film Cooling." *ASME Journal of Turbomachinery* Vol. 112, no. 3 (1990): pp. 477-487. DOI 10.1115/1.2927683.

[103] El-Gabry, Lamyaa A., Thurman, Douglas R., Poinsatte, Philip E. and Heidmann, James D. "Turbulence and Heat Transfer Measurements in an Inclined Large Scale Film Cooling Array: Part I— Velocity and Turbulence Measurements." *Proceedings of ASME 2011 Turbo Expo: Turbine Technical Conference and Exposition*. pp. 541-550. Vancouver, British Columbia, Canada, June 6–10, 2011. DOI 10.1115/GT2011-46491.

[104] Thurman, Douglas R., El-Gabry, Lamyaa A., Poinsatte, Philip E. and Heidmann, James D. "Turbulence and Heat Transfer Measurements in an Inclined Large Scale Film Cooling Array: Part II—Temperature and Heat Transfer Measurements." *Proceedings of ASME 2011 Turbo Expo: Turbine Technical Conference and Exposition*. pp. 551-558. Vancouver, British Columbia, Canada, June 6–10, 2011. DOI 10.1115/GT2011-46498.

[105] Abuaf, N., Bunker, R. and Lee, C. P. "Heat transfer and film cooling effectiveness in a linear airfoil cascade." *ASME Journal of Turbomachinery* Vol. 119, no. 2 (1997): pp. 302-309. DOI 10.1115/1.2841113.

[106] Jafari, M. M., Atefi, G., Khalesi, J. and Soleymani, A. “A new conjugate heat transfer method to analyse a 3D steam cooled gas turbine blade with temperature-dependent material properties.” *Proceedings of the IMechE, Part C: Journal of Mechanical Engineering Science* Vol. 226, no. 5 (2012): pp.1309-1320. DOI:10.1177/0954406211418734.

[107] Khodabandeh, Erfan, Ghaderi, Mohsen, Afzalabadi, Abolfazl, Rouboa, Abel and Salarifard, Amir. “Parametric Study of Heat Transfer in an Electric Arc Furnace

and Cooling System." *Applied Thermal Engineering* Vol. 123 (2017): pp. 1190-1200.

[108] Womack, K. M., Volino, R. J., and Schultz, M. P. "Measurements in Film Cooling Flows With Periodic Wakes." *ASME J. Turbomach*. Vol. 130, no. 4 (2008): p. 041008.

[109] Coulthard, S. M., Volino, R. J., and Flack, K. A. "Effect of Jet Pulsing on Film Cooling—Part I: Effectiveness and Flow-Field Temperature Results." *ASME J. Turbomach.* Vol. 129, no. 2 (2007): pp. 232–246.

[110] Womack, K. M., Volino, R. J., and Schultz, M. P. "Combined Effects of Wakes and Jet Pulsing on Film Cooling." *ASME J. Turbomach*. Vol. 130, no. 4 (2008): p. 041010.

[111] Soong, C. Y. "Thermal buoyancy effects in rotating non-isothermal flows." *International Journal of Rotating Machinery* Vol. 7, no. 6 (2001): pp. 435-446. DOI http://dx.doi.org/10.1155/S1023621X01000380.

[112] Ghasemi, Arman, Dardel, Morteza and Ghasemi, Mohammad Hassan. "Collective Effect of Fluid's Colioris Force and Nano-Scale's Parameter on Instability Pattern and Vibration Characteristic of Fluid-Conveying Carbon Nanotubes." *Journal of Pressure Vessel Technology* Vol. 137, no. 3 (2015): pp. 031301. DOI 10.1115/1.4029522.

[113] Ghasemi, Arman, Dardel, Morteza and Ghasemi, Mohamad Hassan. "Control of the non-linear static deflection experienced by a fluid-carrying double-walled carbon nanotube using an external distributed load." Proceedings of the Institution

of Mechanical Engineers, Part N: Journal of Nanoengineering and Nanosystems 226, no. 4 (2012): 181-190.

[114] Schobeiri, M. T., Attia, M, Lippke, C. "Nonlinear Dynamic Simulation of Single and Multi-spool Core Engines, Part I: Theoretical Method." *AIAA, Journal of Propulsion and Power* Vol. 10, No. 6 (1994): pp. 855- 862.

[115] Schobeiri, M. T., Attia, M, Lippke, C. "Nonlinear Dynamic Simulation of Single and Multi-spool Core Engines, Part II: Modeling and Simulation Cases." *AIAA Journal of Propulsion and Power* Vol. 10, No. 6 (1994): pp. 863-867.

[116] Widyanto, Erie. "Design of Multi-Stage Compressor Using Streamline Curvature Method." Thesis for Degree of Master of Science. Texas A&M University (2015).

APPENDIX A

SAMPLE DESIGN CODES

A.1. Turbine Stage Flow Path Design (FORTRAN)

```
C   ======================================
C   TURBINE STAGE DESIGN
C   ======================================
    REAL MAIR,MTOT,MFTOT,MF
    COMMON/GAS/ NG,NGC,NGE,NGS
    COMMON/VAR/ MAIR,MTOT,MFTOT,PRATIO_COMBUST,XW,HU,ETA_T,ETA_C
    COMMON/MATRIX/ P(20),T(20),H(20),S(20),RHO(20),MF(20),C_GAS(20)
    DIMENSION Z(13)

    REAL LM(10),W(10),RHO1(10),RHO3(10),PHI(10),R(10),H1(10),H3(10)
    REAL U3(10),V1(10),V3(10),MU(10),NU(10),BH1(10),BH3(10)
    REAL LAMBDA(10),ALPHA2(10),ALPHA3(10),BETA2(10),BETA3(10)
    REAL DM1(10),DM2(10),DM3(10),MDOT(10),C_GAS3(10),MACH3(10)
    REAL R_A(10),ALPHA3_A(10),BETA2_A(10),BETA3_A(10)
    REAL PRATIO_TURB(10),A_TURB(10),LAMBDA_SUM
    REAL R_HUB(10),R_HUB_A(10),PHI_HUB(10),LAMBDA_HUB(10),NU_HUB(10)
    COMMON PI
    PI=3.14159

    NOUT1=1
    NOUT2=2
    NOUT3=3
        NOUT4=4
        NOUT5=5
    OPEN(UNIT=NOUT1,FILE='CYCLE.DAT')
    OPEN(UNIT=NOUT2,FILE='STAGE_PARAM.DAT')
    OPEN(UNIT=NOUT3,FILE='GEOMETRY.DAT')
        OPEN(UNIT=NOUT4,FILE='STATOR_DATA.DAT')
        OPEN(UNIT=NOUT5,FILE='ROTOR_DATA.DAT')

    NG  = -1        !INPUT: XB AND XW, OUTPUT: R
    NGC = 1             !INPUT: TEPMERATURE, OUTPUT: CP
    NGE = 3             !INPUT: TEMPERATURE AND PRESSURE, OUTPUT: ENTROPY
    NGS = 5             !INPUT: ENTROPY AND PRESSURE, OUTPUT: TEMPERATURE

    MAIR=150.0
    MF(1)=2.301
    MF(2)=1.32
```

```
      MF(3)=1.32
      HU=42.0E6/1000.0
      ETA_C=0.90
            ETA_T=0.88
      XW=0.0
      MTOT=MAIR
      MFTOT=0.0
      PRATIO_COMP=40.0
            PRATIO_COMBUST=.98
      PRATIO_TURB_ALL=PRATIO_COMP*(PRATIO_COMBUST**3)

      MDOT(1)=MAIR+MF(1)
      MDOT(2)=MAIR+MF(1)+MF(2)
      DO 10 I=3,6
      MDOT(I)=MAIR+MF(1)+MF(2)+MF(3)
10    CONTINUE

      P(1)=.9861            !COMP INLET
      T(1)=288.21
      CALL PROPERTIES(1)

      CALL COMPRESSOR(1,PRATIO_COMP)

      DHUB=1.0
      OMEGA_N=6000.0
      OMEGA=OMEGA_N*2*PI/60
      BH1(1)=.05
      DM1(1)=DHUB+BH1(1)

      DO 20  I=1,6
      DRATIO=0.99-(I-1)*.015
      DM3(I)=DM1(I)/DRATIO
      DM3(1)=1.06
            DM3(5)=1.31
            DM3(6)=1.45
      BH3(I)=DM3(I)-DHUB
      U3(I)=0.5*DM3(I)*OMEGA
      BH1(I+1)=BH3(I)
      DM1(I+1)=DM3(I)
20    CONTINUE

      DO 30  I=1,6
      A_TURB(I)=1.0/6
      PRATIO_TURB(I)=PRATIO_TURB_ALL**(A_TURB(I))
30    CONTINUE

      DO 40  ITR=1,100
      MTOT=MAIR
      MFTOT=0.0

      CALL COMBUSTOR_MF(2,MF(1))
      CALL TURBINE(3,PRATIO_TURB(1))
      CALL COMBUSTOR_MF(4,MF(2))
```

```
      CALL TURBINE(5,PRATIO_TURB(2))
      CALL COMBUSTOR_MF(6,MF(3))
      CALL TURBINE(7,PRATIO_TURB(3))
      CALL TURBINE(8,PRATIO_TURB(4))
      CALL TURBINE(9,PRATIO_TURB(5))
      CALL TURBINE(10,PRATIO_TURB(6))

      LM(1)=1000.*(H(3)-H(4))
      LM(2)=1000.*(H(5)-H(6))
      LM(3)=1000.*(H(7)-H(8))
      LM(4)=1000.*(H(8)-H(9))
      LM(5)=1000.*(H(9)-H(10))
      LM(6)=1000.*(H(10)-H(11))

      LAMBDA_SUM=0.0
      DO 50  I=1,6
      LAMBDA(I)=LM(I)/U3(I)**2
      LAMBDA_SUM=LAMBDA_SUM+LAMBDA(I)
50    CONTINUE

      IF (ITR.EQ.100) GOTO 40
      A_TURB_SUM=0.0
      DO 60  I=1,6
      D_LAMBDA=LAMBDA(I)-LAMBDA_SUM/6.0
      A_TURB(I)=A_TURB(I)-D_LAMBDA*.01
      A_TURB_SUM=A_TURB_SUM+A_TURB(I)
60    CONTINUE

      DO 70  I=1,6
      A_TURB(I)=A_TURB(I)/A_TURB_SUM
      PRATIO_TURB(I)=PRATIO_TURB_ALL**(A_TURB(I))
70    CONTINUE
40    CONTINUE

C     WRITE(*,*) A_TURB(1),A_TURB(2),A_TURB(3)
C          1                ,A_TURB(4),A_TURB(5),A_TURB(6)

      PRATIO_TURB(1)=PRATIO_TURB_ALL**(0.12)
            PRATIO_TURB(2)=PRATIO_TURB_ALL**(0.12)
            PRATIO_TURB(3)=PRATIO_TURB_ALL**(0.14)
            PRATIO_TURB(4)=PRATIO_TURB_ALL**(0.16)
            PRATIO_TURB(5)=PRATIO_TURB_ALL**(0.195)
            PRATIO_TURB(6)=PRATIO_TURB_ALL**(0.265)

      MTOT=MAIR
      MFTOT=0.0

      CALL COMBUSTOR_MF(2,MF(1))
      CALL TURBINE(3,PRATIO_TURB(1))
      CALL COMBUSTOR_MF(4,MF(2))
      CALL TURBINE(5,PRATIO_TURB(2))
      CALL COMBUSTOR_MF(6,MF(3))
      CALL TURBINE(7,PRATIO_TURB(3))
```

```
CALL TURBINE(8,PRATIO_TURB(4))
CALL TURBINE(9,PRATIO_TURB(5))
CALL TURBINE(10,PRATIO_TURB(6))

LM(1)=1000.*(H(3)-H(4))
LM(2)=1000.*(H(5)-H(6))
LM(3)=1000.*(H(7)-H(8))
LM(4)=1000.*(H(8)-H(9))
LM(5)=1000.*(H(9)-H(10))
LM(6)=1000.*(H(10)-H(11))

RHO1(1)=RHO(3)
RHO3(1)=RHO(4)
RHO1(2)=RHO(5)
RHO3(2)=RHO(6)
RHO1(3)=RHO(7)
RHO3(3)=RHO(8)
RHO1(4)=RHO(8)
RHO3(4)=RHO(9)
RHO1(5)=RHO(9)
RHO3(5)=RHO(10)
RHO1(6)=RHO(10)
RHO3(6)=RHO(11)

      C_GAS3(1)=C_GAS(4)
      C_GAS3(2)=C_GAS(6)
      C_GAS3(3)=C_GAS(8)
      C_GAS3(4)=C_GAS(9)
      C_GAS3(5)=C_GAS(10)
      C_GAS3(6)=C_GAS(11)

DO 80  I=1,6
LAMBDA(I)=LM(I)/U3(I)**2
V1(I)=MDOT(I)/(RHO1(I)*PI*DM1(I)*BH1(I))
V3(I)=MDOT(I)/(RHO3(I)*PI*DM3(I)*BH3(I))
      PHI(I)=V3(I)/U3(I)
MU(I)=.5*(V1(I)+V3(I))/V3(I)
NU(I)=.5*(DM1(I)+DM3(I))/DM3(I)
W(I)=MDOT(I)*LM(I)

ALPHA2(I)=16.0*PI/180
ALPHA2(1)=15.0*PI/180

R(I)=.5/LAMBDA(I)*
      1     ( MU(I)**2*PHI(I)**2/TAN(ALPHA2(I))**2*(NU(I)**2-1)
      2           -2*MU(I)*NU(I)*PHI(I)*LAMBDA(I)/TAN(ALPHA2(I))
      3           +LAMBDA(I)**2+2*LAMBDA(I)-PHI(I)**2*(MU(I)**2-1) )
BETA2(I)=ACOT( 1/TAN(ALPHA2(I))-NU(I)/(MU(I)*PHI(I)) )
BETA3(I)=ACOT( MU(I)*NU(I)/TAN(ALPHA2(I))-(LAMBDA(I)+1)/PHI(I) )
ALPHA3(I)=ACOT(1/PHI(I)+1/TAN(BETA3(I)))

MACH3(I)=V3(I)/SIN(ALPHA3(I))/C_GAS3(I)
```

```
 80   CONTINUE

      PWC=(H(2)-H(1))*MAIR/1.0E3
           PWT=(W(1)+W(2)+W(3)+W(4)+W(5)+W(6))/1.0E6
      PCM=HU*(MF(1)+MF(2)+MF(3))/1.0E3
      ETA_TH=(PWT-PWC)/PCM*100
      WRITE(*,*) PWC,PWT,PCM,ETA_TH

C     ======================================
C     OUTPUT
      P(12)=P(1)
           DO 90  N=1,11
      WRITE(NOUT1,200) P(N),T(N),H(N),S(N),RHO(N),P(N)/P(N+1)
 90   CONTINUE

      DO 100  I=1,6
      WRITE(NOUT2,*) "STAGE: ",I
      WRITE(NOUT2,*) "INLET VELOCITY (m/s): ",V1(I)
      WRITE(NOUT2,*) "OUTLET VELOCITY (m/s): ",V3(I),MACH3(I)
      WRITE(NOUT2,*) "LAMBDA: ",LAMBDA(I)
      WRITE(NOUT2,*) "R: ",R(I)
      WRITE(NOUT2,*) "MU: ",MU(I)
      WRITE(NOUT2,*) "NU: ",NU(I)
      WRITE(NOUT2,*) "PHI: ",PHI(I)
      WRITE(NOUT2,*) "POWER (MW): ",W(I)/1.0E6
      WRITE(NOUT2,*) "ALPHA2 (deg): ",ALPHA2(I)*180/PI
      WRITE(NOUT2,*) "ALPHA3 (deg): ",ALPHA3(I)*180/PI
      WRITE(NOUT2,*) "BETA2 (deg): ",BETA2(I)*180/PI
      WRITE(NOUT2,*) "BETA3 (deg): ",BETA3(I)*180/PI
      WRITE(NOUT2,*)
      WRITE(NOUT3,*) I,DHUB/2,DM1(I)/2,(DM1(I)+BH1(I))/2,BH1(I)
           IF (I.EQ.1) WRITE(NOUT4,*) 90.0,ALPHA2(I)*180/PI
           1                     ,BH1(I)*1000,BH3(I)*1000
           IF (I.GT.1) WRITE(NOUT4,*) ALPHA3(I-1)*180/PI,ALPHA2(I)*180/PI
           1                     ,BH1(I)*1000,BH3(I)*1000
           WRITE(NOUT5,*) BETA2(I)*180/PI,BETA3(I)*180/PI
           1               ,BH1(I)*1000,BH3(I)*1000
 100  CONTINUE
      WRITE(NOUT3,*) 7,DHUB/2,DM3(6)/2,(DM3(6)+BH3(6))/2,BH3(6)

 200  FORMAT(8(1X,E12.5))

      STOP
      END


C     ======================================
C     SUBROUTINES
C     ======================================
      FUNCTION ACOT(XNUM)
      COMMON PI
      ACOT=ATAN(1/XNUM)
      IF (ACOT.LT.0) ACOT=ACOT+PI
```

```
      RETURN
      END

C     ======================================
      SUBROUTINE COMPRESSOR(I,PRATIO)
      REAL MAIR,MTOT,MFTOT,MF
      COMMON/GAS/ NG,NGC,NGE,NGS
      COMMON/VAR/ MAIR,MTOT,MFTOT,PRATIO_COMBUST,XW,HU,ETA_T,ETA_C
      COMMON/MATRIX/ P(20),T(20),H(20),S(20),RHO(20),MF(20),C_GAS(20)
      DIMENSION Z(13)

      P(I+1)=P(I)*PRATIO
      XB=MFTOT/MAIR
      CALL GASPRO(NG,XB,XW,RG,Z)
      CALL GASPRO(NGS,S(I),P(I+1),TSO,Z)
      CALL GASPRO(NGC,TSO,0.0,CPO,Z)
      HSO=TSO*CPO
      H(I+1)=H(I)+(HSO-H(I))/ETA_C
      T(I+1)=H(I+1)/CPO
      CALL GASPRO(NGE,T(I+1),P(I+1),S(I+1),Z)
      RHO(I+1)=P(I+1)*1E5/(T(I+1)*RG)
      RETURN
      END

C     ======================================
      SUBROUTINE COMBUSTOR(I,TOUT)
      REAL MAIR,MTOT,MFTOT,MF
      COMMON/GAS/ NG,NGC,NGE,NGS
      COMMON/VAR/ MAIR,MTOT,MFTOT,PRATIO_COMBUST,XW,HU,ETA_T,ETA_C
      COMMON/MATRIX/ P(20),T(20),H(20),S(20),RHO(20),MF(20),C_GAS(20)
      DIMENSION Z(13)

      P(I+1)=P(I)*PRATIO_COMBUST
      T(I+1)=TOUT

      XB=MFTOT/MAIR
      DO 10  ITR=1,50
      CALL GASPRO(NG,XB,XW,RG,Z)
      CALL GASPRO(NGC,T(I+1),0.0,CPO,Z)
      H(I+1)=T(I+1)*CPO
      MF(I)=MTOT*(H(I+1)-H(I))/(HU-H(I+1))
      XB=(MFTOT+MF(I))/MAIR
 10   CONTINUE

      MTOT=MTOT+MF(I)
      MFTOT=MFTOT+MF(I)
      CALL GASPRO(NGE,T(I+1),P(I+1),S(I+1),Z)
      RHO(I+1)=P(I+1)*1E5/(T(I+1)*RG)
      RETURN
      END

C     ======================================
      SUBROUTINE COMBUSTOR_MF(I,MF_VAL)
```

```
      REAL MAIR,MTOT,MFTOT,MF,MF_VAL
      COMMON/GAS/ NG,NGC,NGE,NGS
      COMMON/VAR/ MAIR,MTOT,MFTOT,PRATIO_COMBUST,XW,HU,ETA_T,ETA_C
      COMMON/MATRIX/ P(20),T(20),H(20),S(20),RHO(20),MF(20),C_GAS(20)
      DIMENSION Z(13)

      P(I+1)=P(I)*PRATIO_COMBUST
      MFTOT=MFTOT+MF_VAL
      XB=MFTOT/MAIR
      H(I+1)=(MTOT*H(I)+MF_VAL*HU)/(MTOT+MF_VAL)

      CPO=1.0
      DO 10  ITR=1,50
      T(I+1)=H(I+1)/CPO
      CALL GASPRO(NG,XB,XW,RG,Z)
      CALL GASPRO(NGC,T(I+1),0.0,CPO,Z)
   10 CONTINUE

      MTOT=MTOT+MF_VAL
      CALL GASPRO(NGE,T(I+1),P(I+1),S(I+1),Z)
      RHO(I+1)=P(I+1)*1E5/(T(I+1)*RG)
      RETURN
      END

C     ======================================
      SUBROUTINE TURBINE(I,PRATIO)
      REAL MAIR,MTOT,MFTOT,MF
      COMMON/GAS/ NG,NGC,NGE,NGS
      COMMON/VAR/ MAIR,MTOT,MFTOT,PRATIO_COMBUST,XW,HU,ETA_T,ETA_C
      COMMON/MATRIX/ P(20),T(20),H(20),S(20),RHO(20),MF(20),C_GAS(20)
      DIMENSION Z(13)

      P(I+1)=P(I)/PRATIO
      XB=MFTOT/MAIR
      CALL GASPRO(NG,XB,XW,RG,Z)
      CALL GASPRO(NGS,S(I),P(I+1),TSO,Z)
      CALL GASPRO(NGC,TSO,0.0,CPO,Z)
      HSO=TSO*CPO
      H(I+1)=H(I)+(HSO-H(I))*ETA_T
      T(I+1)=H(I+1)/CPO
      CALL GASPRO(NGE,T(I+1),P(I+1),S(I+1),Z)
      RHO(I+1)=P(I+1)*1E5/(T(I+1)*RG)
      C_GAS(I+1)=( CPO*1000/(CPO*1000-RG)*RG*T(I+1) )**0.5
      RETURN
      END

C     ======================================
      SUBROUTINE PROPERTIES(I)
      REAL MAIR,MTOT,MFTOT,MF
      COMMON/GAS/ NG,NGC,NGE,NGS
      COMMON/VAR/ MAIR,MTOT,MFTOT,PRATIO_COMBUST,XW,HU,ETA_T,ETA_C
      COMMON/MATRIX/ P(20),T(20),H(20),S(20),RHO(20),MF(20),C_GAS(20)
      DIMENSION Z(13)
```

```
      XB=MFTOT/MAIR
      CALL GASPRO(NG,XB,XW,RG,Z)
      CALL GASPRO(NGC,T(I),0.0,CPO,Z)
      H(I)=T(I)*CPO
      CALL GASPRO(NGE,T(I),P(I),S(I),Z)
      RHO(I)=P(I)*1E5/(T(I)*RG)
      RETURN
      END

C     ======================================
      SUBROUTINE PROPERTIES1(I)
      REAL MAIR,MTOT,MFTOT,MF
      COMMON/GAS/ NG,NGC,NGE,NGS
      COMMON/VAR/ MAIR,MTOT,MFTOT,PRATIO_COMBUST,XW,HU,ETA_T,ETA_C
      COMMON/MATRIX/ P(20),T(20),H(20),S(20),RHO(20),MF(20),C_GAS(20)
      DIMENSION Z(13)

      XB=MFTOT/MAIR

      CPO=1.0
      DO 10  ITR=1,50
      T(I)=H(I)/CPO
      CALL GASPRO(NG,XB,XW,RG,Z)
      CALL GASPRO(NGC,T(I),0.0,CPO,Z)
 10   CONTINUE

      P(I)=RHO(I)*RG*T(I)/1E5
      CALL GASPRO(NGE,T(I),P(I),S(I),Z)

      CALL GASPRO(NGS,S(I-1),P(I),TSO,Z)
      CALL GASPRO(NGC,TSO,0.0,CPO,Z)
      HSO=TSO*CPO
      ETA_T=(H(I)-H(I-1))/(HSO-H(I-1))

      RETURN
      END
```

A.2. Blade Profiling (FORTRAN)

```
C     ======================================
C     STATOR BEZIER BLADE PROFILING
C     ======================================
      REAL P0(2),P1(2),P2(2),GAMMA(6),CHORD(6),XLE(6),BH1(6),BH3(6)
      REAL XS(1001),YS(1001),XP(1001),YP(1001)
      REAL XS1(1001),YS1(1001),XP1(1001),YP1(1001),XC1(1001),YC1(1001)
      COMMON /CURVES/ T(1001),XC(1001),YC(1001)
            COMMON /PI_NUM/ PI
      PI=3.14159

      NOUT1=1
```

```
      OPEN(UNIT=NOUT1,FILE='CAMBER.TXT')
      NOUT2=2
      OPEN(UNIT=NOUT2,FILE='SUCTION.TXT')
      NOUT3=3
      OPEN(UNIT=NOUT3,FILE='PRESSURE.TXT')
      NIN20=20

      OPEN(UNIT=111,FILE='SPH1.TXT')
      OPEN(UNIT=112,FILE='SPH2.TXT')
      OPEN(UNIT=113,FILE='SPH3.TXT')
      OPEN(UNIT=114,FILE='SPH4.TXT')
      OPEN(UNIT=115,FILE='SPH5.TXT')
      OPEN(UNIT=116,FILE='SPH6.TXT')
      OPEN(UNIT=121,FILE='SPM1.TXT')
      OPEN(UNIT=122,FILE='SPM2.TXT')
      OPEN(UNIT=123,FILE='SPM3.TXT')
      OPEN(UNIT=124,FILE='SPM4.TXT')
      OPEN(UNIT=125,FILE='SPM5.TXT')
      OPEN(UNIT=126,FILE='SPM6.TXT')
      OPEN(UNIT=131,FILE='SPT1.TXT')
      OPEN(UNIT=132,FILE='SPT2.TXT')
      OPEN(UNIT=133,FILE='SPT3.TXT')
      OPEN(UNIT=134,FILE='SPT4.TXT')
      OPEN(UNIT=135,FILE='SPT5.TXT')
      OPEN(UNIT=136,FILE='SPT6.TXT')
      OPEN(UNIT=211,FILE='SSH1.TXT')
      OPEN(UNIT=212,FILE='SSH2.TXT')
      OPEN(UNIT=213,FILE='SSH3.TXT')
      OPEN(UNIT=214,FILE='SSH4.TXT')
      OPEN(UNIT=215,FILE='SSH5.TXT')
      OPEN(UNIT=216,FILE='SSH6.TXT')
      OPEN(UNIT=221,FILE='SSM1.TXT')
      OPEN(UNIT=222,FILE='SSM2.TXT')
      OPEN(UNIT=223,FILE='SSM3.TXT')
      OPEN(UNIT=224,FILE='SSM4.TXT')
      OPEN(UNIT=225,FILE='SSM5.TXT')
      OPEN(UNIT=226,FILE='SSM6.TXT')
      OPEN(UNIT=231,FILE='SST1.TXT')
      OPEN(UNIT=232,FILE='SST2.TXT')
      OPEN(UNIT=233,FILE='SST3.TXT')
      OPEN(UNIT=234,FILE='SST4.TXT')
      OPEN(UNIT=235,FILE='SST5.TXT')
      OPEN(UNIT=236,FILE='SST6.TXT')

C     STAGE PARAMETERS
            DHUB=1000.0
      DO 5  ISECT=1,3
            OPEN(UNIT=NIN20,FILE='STATOR_DATA.DAT')
            WRITE(NOUT1,*) 'ZONE'
      WRITE(NOUT2,*) 'ZONE'
      WRITE(NOUT3,*) 'ZONE'

      DO 10  ISTG=1,6
```

```
      READ(NIN20,*) ALPHA1,ALPHA2,BH1(ISTG),BH3(ISTG)
   ALPHA1=ALPHA1*PI/180
      ALPHA2=ALPHA2*PI/180
   IF (ISECT.EQ.1) THEN
      ALPHA1=ACOT( (DHUB+BH1(ISTG))*COT(ALPHA1)/DHUB )
      ALPHA2=ACOT( (DHUB+.5*(BH1(ISTG)+BH3(ISTG)))*COT(ALPHA2)/DHUB )
      END IF
   IF (ISECT.EQ.3) THEN
      ALPHA1=ACOT( (DHUB+BH1(ISTG))*COT(ALPHA1)/(DHUB+2*BH1(ISTG)) )
      ALPHA2=ACOT( (DHUB+.5*(BH1(ISTG)+BH3(ISTG)))*COT(ALPHA2)
     1          /(DHUB+2*.5*(BH1(ISTG)+BH3(ISTG))) )
      END IF
      GAMMA(1)=45.0*PI/180
      GAMMA(2)=65.0*PI/180
      IF (ISTG.GT.2) GAMMA(ISTG)=60.0*PI/180
      CHORD(ISTG)=80.0+(ISTG-1)*20.0
   XLE(1)=0.0
   IF (ISTG.GT.1 .AND. ISTG.LT.4) XLE(ISTG)=XLE(ISTG-1)+
     1          2*CHORD(ISTG-1)*SIN(GAMMA(ISTG-1))+120.0
      IF (ISTG.GT.3) XLE(ISTG)=XLE(ISTG-1)+
     1          2*CHORD(ISTG-1)*SIN(GAMMA(ISTG-1))+80.0

C    CAMBERLINE
   PHI1=PI/2+GAMMA(ISTG)-ALPHA1
   PHI2=PI/2-GAMMA(ISTG)+ALPHA2
   WRITE(*,*) ALPHA1*180/PI,ALPHA2*180/PI,PHI1*180/PI,PHI2*180/PI
   P0(1)=0.0
   P0(2)=0.0
   P1(1)=1.0/(1+COT(PHI1)/COT(PHI2))
   P1(2)=COT(PHI1)/(1+COT(PHI1)/COT(PHI2))
   P2(1)=1.0
   P2(2)=0.0
   DO 20  I=1,1001
   ZETA=(I-1)*.001
   XC(I)=(1-ZETA)**2*P0(1)+2*(1-ZETA)*ZETA*P1(1)+ZETA**2*P2(1)
   YC(I)=(1-ZETA)**2*P0(2)+2*(1-ZETA)*ZETA*P1(2)+ZETA**2*P2(2)
20   CONTINUE

C    SUPERIMPOSITION
   CALL BASE_PRF_INT
   DO 30  I=2,1001
   THETA=ATAN((YC(I)-YC(I-1))/(XC(I)-XC(I-1)))
   TFACTOR=1.2*(1+(3-ISECT)*.1)
      XS(I)=XC(I)-.5*TFACTOR*T(I)*SIN(THETA)
   YS(I)=YC(I)+.5*TFACTOR*T(I)*COS(THETA)
   XP(I)=XC(I)+.5*TFACTOR*T(I)*SIN(THETA)
   YP(I)=YC(I)-.5*TFACTOR*T(I)*COS(THETA)
30   CONTINUE

C    FLIP, ROTATION, SCALING, MOVE
   YCSUM=0.0
   DO 40  I=1,1001
      YC(I)=-YC(I)
```

```
      YS(I)=-YS(I)
      YP(I)=-YP(I)
   XC1(I)=CHORD(ISTG)*(COS(PI/2-GAMMA(ISTG))*XC(I)
     1          -SIN(PI/2-GAMMA(ISTG))*YC(I))+XLE(ISTG)
      YC1(I)=CHORD(ISTG)*(SIN(PI/2-GAMMA(ISTG))*XC(I)
     1          +COS(PI/2-GAMMA(ISTG))*YC(I))
   XS1(I)=CHORD(ISTG)*(COS(PI/2-GAMMA(ISTG))*XS(I)
     1          -SIN(PI/2-GAMMA(ISTG))*YS(I))+XLE(ISTG)
      YS1(I)=CHORD(ISTG)*(SIN(PI/2-GAMMA(ISTG))*XS(I)
     1          +COS(PI/2-GAMMA(ISTG))*YS(I))
      XP1(I)=CHORD(ISTG)*(COS(PI/2-GAMMA(ISTG))*XP(I)
     1          -SIN(PI/2-GAMMA(ISTG))*YP(I))+XLE(ISTG)
      YP1(I)=CHORD(ISTG)*(SIN(PI/2-GAMMA(ISTG))*XP(I)
     1          +COS(PI/2-GAMMA(ISTG))*YP(I))
   YCSUM=YCSUM+YC1(I)
40 CONTINUE
   YCAVE=YCSUM/1001

      NCOUNTER_P=100+10*ISECT+ISTG
      NCOUNTER_S=200+10*ISECT+ISTG
   DO 50 I=1,1001
   WRITE(NOUT1,*) XC1(I),YC1(I)-YCAVE,DHUB/2+BH1(ISTG)*.5*(ISECT-1)
     1          +(XC1(I)-XLE(ISTG))/(CHORD(ISTG)*SIN(GAMMA(ISTG)))
   2          *(BH3(ISTG)-BH1(ISTG))*.5*.5*(ISECT-1)
   WRITE(NOUT2,*) XS1(I),YS1(I)-YCAVE,DHUB/2+BH1(ISTG)*.5*(ISECT-1)
     1          +(XS1(I)-XLE(ISTG))/(CHORD(ISTG)*SIN(GAMMA(ISTG)))
   2          *(BH3(ISTG)-BH1(ISTG))*.5*.5*(ISECT-1)
   WRITE(NOUT3,*) XP1(I),YP1(I)-YCAVE,DHUB/2+BH1(ISTG)*.5*(ISECT-1)
     1          +(XP1(I)-XLE(ISTG))/(CHORD(ISTG)*SIN(GAMMA(ISTG)))
   2          *(BH3(ISTG)-BH1(ISTG))*.5*.5*(ISECT-1)

   WRITE(NCOUNTER_P,*) XP1(I),YP1(I)-YCAVE,DHUB/2+BH1(ISTG)*.5*
     1          (ISECT-1)+(XP1(I)-XLE(ISTG))/(CHORD(ISTG)*SIN(
   2          GAMMA(ISTG)))*(BH3(ISTG)-BH1(ISTG))*.5*.5*(ISECT-1)
   WRITE(NCOUNTER_S,*) XS1(I),YS1(I)-YCAVE,DHUB/2+BH1(ISTG)*.5*
     1          (ISECT-1)+(XS1(I)-XLE(ISTG))/(CHORD(ISTG)*SIN(
   2          GAMMA(ISTG)))*(BH3(ISTG)-BH1(ISTG))*.5*.5*(ISECT-1)

50 CONTINUE
10 CONTINUE
      CLOSE(NIN20)
5  CONTINUE

   STOP
   END


C  =======================================
C  SUBROUTINES
C  =======================================
   FUNCTION COT(ANGLE)
   COT=1.0/TAN(ANGLE)
   RETURN
```

```
      END
C     ========================================
      FUNCTION ACOT(XNUM)
            COMMON /PI_NUM/ PI
      ACOT=ATAN(1/XNUM)
      IF (ACOT.LT.0) ACOT=ACOT+PI
      RETURN
      END
C     ========================================
      SUBROUTINE BASE_PRF_INT       !THIS SUBROUTINE INTERPOLATES THE
           1                        !BASE PROFILE FOR CAMBERLINE POINTS
      COMMON /CURVES/ T(1001),XC(1001),YC(1001)
      NIN21=21
      OPEN(UNIT=NIN21,FILE='2_2.txt')

      T(1)=0.0
      XF=0.0
      DO 10  I=2,1001
   20 IF (XF.LT.XC(I)) THEN
      XF0=XF
      TF0=TF
      READ(NIN21,*) XF,TF
      GO TO 20
      END IF
      T(I)=TF0+(XC(I)-XF0)/(XF-XF0)*(TF-TF0)
   10 CONTINUE
      CLOSE(NIN21)
      RETURN
      END


C     ========================================
C     ROTOR BEZIER BLADE PROFILING
C     ========================================
      REAL P0(2),P1(2),P2(2),GAMMA(6),CHORD(6),XLE(6),BH1(6),BH3(6)
      REAL XS(1001),YS(1001),XP(1001),YP(1001)
      REAL XS1(1001),YS1(1001),XP1(1001),YP1(1001),XC1(1001),YC1(1001)
      COMMON /CURVES/ T(1001),XC(1001),YC(1001)
            COMMON /PI_NUM/ PI
      PI=3.14159

      NOUT1=1
      OPEN(UNIT=NOUT1,FILE='CAMBER.TXT')
      NOUT2=2
      OPEN(UNIT=NOUT2,FILE='SUCTION.TXT')
      NOUT3=3
      OPEN(UNIT=NOUT3,FILE='PRESSURE.TXT')
      NIN20=20

      OPEN(UNIT=111,FILE='RPH1.TXT')
      OPEN(UNIT=112,FILE='RPH2.TXT')
      OPEN(UNIT=113,FILE='RPH3.TXT')
      OPEN(UNIT=114,FILE='RPH4.TXT')
```

```
      OPEN(UNIT=115,FILE='RPH5.TXT')
      OPEN(UNIT=116,FILE='RPH6.TXT')
      OPEN(UNIT=121,FILE='RPM1.TXT')
      OPEN(UNIT=122,FILE='RPM2.TXT')
      OPEN(UNIT=123,FILE='RPM3.TXT')
      OPEN(UNIT=124,FILE='RPM4.TXT')
      OPEN(UNIT=125,FILE='RPM5.TXT')
      OPEN(UNIT=126,FILE='RPM6.TXT')
      OPEN(UNIT=131,FILE='RPT1.TXT')
      OPEN(UNIT=132,FILE='RPT2.TXT')
      OPEN(UNIT=133,FILE='RPT3.TXT')
      OPEN(UNIT=134,FILE='RPT4.TXT')
      OPEN(UNIT=135,FILE='RPT5.TXT')
      OPEN(UNIT=136,FILE='RPT6.TXT')
      OPEN(UNIT=211,FILE='RSH1.TXT')
      OPEN(UNIT=212,FILE='RSH2.TXT')
      OPEN(UNIT=213,FILE='RSH3.TXT')
      OPEN(UNIT=214,FILE='RSH4.TXT')
      OPEN(UNIT=215,FILE='RSH5.TXT')
      OPEN(UNIT=216,FILE='RSH6.TXT')
      OPEN(UNIT=221,FILE='RSM1.TXT')
      OPEN(UNIT=222,FILE='RSM2.TXT')
      OPEN(UNIT=223,FILE='RSM3.TXT')
      OPEN(UNIT=224,FILE='RSM4.TXT')
      OPEN(UNIT=225,FILE='RSM5.TXT')
      OPEN(UNIT=226,FILE='RSM6.TXT')
      OPEN(UNIT=231,FILE='RST1.TXT')
      OPEN(UNIT=232,FILE='RST2.TXT')
      OPEN(UNIT=233,FILE='RST3.TXT')
      OPEN(UNIT=234,FILE='RST4.TXT')
      OPEN(UNIT=235,FILE='RST5.TXT')
      OPEN(UNIT=236,FILE='RST6.TXT')

C     STAGE PARAMETERS
            DHUB=1000.0
      DO 5  ISECT=1,3
            OPEN(UNIT=NIN20,FILE='ROTOR_DATA.DAT')
            WRITE(NOUT1,*) 'ZONE'
      WRITE(NOUT2,*) 'ZONE'
      WRITE(NOUT3,*) 'ZONE'

      DO 10  ISTG=1,6
            READ(NIN20,*) BETA2,BETA3,BH1(ISTG),BH3(ISTG)
      BETA2=BETA2*PI/180
            BETA3=BETA3*PI/180
      IF (ISECT.EQ.1) THEN
            BETA2=ACOT( (DHUB+.5*(BH1(ISTG)+BH3(ISTG)))*COT(BETA2)/DHUB )
            BETA3=ACOT( (DHUB+BH3(ISTG))*COT(BETA3)/DHUB )
            END IF
      IF (ISECT.EQ.3) THEN
            BETA2=ACOT( (DHUB+.5*(BH1(ISTG)+BH3(ISTG)))*COT(BETA2)
            1              /(DHUB+2*.5*(BH1(ISTG)+BH3(ISTG))) )
            BETA3=ACOT( (DHUB+BH3(ISTG))*COT(BETA3)/(DHUB+2*BH3(ISTG)) )
```

```
      END IF
      BETA2=PI-BETA2
      BETA3=PI-BETA3
      GAMMA(1)=45.0*PI/180
      GAMMA(2)=65.0*PI/180
      IF (ISTG.GT.2) GAMMA(ISTG)=60.0*PI/180
   CHORD(ISTG)=80.0+(ISTG-1)*20.0
      XLE(1)=CHORD(1)*SIN(GAMMA(1))+40.0
   IF (ISTG.GT.1 .AND. ISTG.LT.4) XLE(ISTG)=XLE(ISTG-1)+CHORD(ISTG-1)
     1      *SIN(GAMMA(ISTG-1))+CHORD(ISTG)*SIN(GAMMA(ISTG))+120.0
      IF (ISTG.GT.3) XLE(ISTG)=XLE(ISTG-1)+CHORD(ISTG-1)
     1      *SIN(GAMMA(ISTG-1))+CHORD(ISTG)*SIN(GAMMA(ISTG))+80.0

C    CAMBERLINE
   PHI1=PI/2+GAMMA(ISTG)-BETA2
   PHI2=PI/2-GAMMA(ISTG)+BETA3
   WRITE(*,*) BETA2*180/PI,BETA3*180/PI,PHI1*180/PI,PHI2*180/PI
   P0(1)=0.0
   P0(2)=0.0
   P1(1)=1.0/(1+COT(PHI1)/COT(PHI2))
   P1(2)=COT(PHI1)/(1+COT(PHI1)/COT(PHI2))
   P2(1)=1.0
   P2(2)=0.0
   DO 20  I=1,1001
   ZETA=(I-1)*.001
   XC(I)=(1-ZETA)**2*P0(1)+2*(1-ZETA)*ZETA*P1(1)+ZETA**2*P2(1)
   YC(I)=(1-ZETA)**2*P0(2)+2*(1-ZETA)*ZETA*P1(2)+ZETA**2*P2(2)
20   CONTINUE

C    SUPERIMPOSITION
   CALL BASE_PRF_INT
   DO 30  I=2,1001
   THETA=ATAN((YC(I)-YC(I-1))/(XC(I)-XC(I-1)))
   TFACTOR=1.2*(1+(3-ISECT)*.1)
      XS(I)=XC(I)-.5*TFACTOR*T(I)*SIN(THETA)
   YS(I)=YC(I)+.5*TFACTOR*T(I)*COS(THETA)
   XP(I)=XC(I)+.5*TFACTOR*T(I)*SIN(THETA)
   YP(I)=YC(I)-.5*TFACTOR*T(I)*COS(THETA)
30   CONTINUE

C    ROTATION, SCALING, MOVE
   YCSUM=0.0
   DO 40  I=1,1001
      XC1(I)=CHORD(ISTG)*(COS(GAMMA(ISTG)-PI/2)*XC(I)
     1          -SIN(GAMMA(ISTG)-PI/2)*YC(I))+XLE(ISTG)
      YC1(I)=CHORD(ISTG)*(SIN(GAMMA(ISTG)-PI/2)*XC(I)
     1          +COS(GAMMA(ISTG)-PI/2)*YC(I))
   XS1(I)=CHORD(ISTG)*(COS(GAMMA(ISTG)-PI/2)*XS(I)
     1          -SIN(GAMMA(ISTG)-PI/2)*YS(I))+XLE(ISTG)
      YS1(I)=CHORD(ISTG)*(SIN(GAMMA(ISTG)-PI/2)*XS(I)
     1          +COS(GAMMA(ISTG)-PI/2)*YS(I))
      XP1(I)=CHORD(ISTG)*(COS(GAMMA(ISTG)-PI/2)*XP(I)
     1          -SIN(GAMMA(ISTG)-PI/2)*YP(I))+XLE(ISTG)
```

```
          YP1(I)=CHORD(ISTG)*(SIN(GAMMA(ISTG)-PI/2)*XP(I)
         1                +COS(GAMMA(ISTG)-PI/2)*YP(I))
      YCSUM=YCSUM+YC1(I)
 40   CONTINUE
      YCAVE=YCSUM/1001

          NCOUNTER_P=100+10*ISECT+ISTG
          NCOUNTER_S=200+10*ISECT+ISTG
      DO 50  I=1,1001
      WRITE(NOUT1,*) XC1(I),YC1(I)-YCAVE,
         1            DHUB/2+.5*(BH1(ISTG)+BH3(ISTG))*.5*(ISECT-1)
         2            +(XC1(I)-XLE(ISTG))/(CHORD(ISTG)*SIN(GAMMA(ISTG)))
     3           *(BH3(ISTG)-BH1(ISTG))*.5*.5*(ISECT-1)
      WRITE(NOUT2,*) XS1(I),YS1(I)-YCAVE,
         1            DHUB/2+.5*(BH1(ISTG)+BH3(ISTG))*.5*(ISECT-1)
         2            +(XS1(I)-XLE(ISTG))/(CHORD(ISTG)*SIN(GAMMA(ISTG)))
     3           *(BH3(ISTG)-BH1(ISTG))*.5*.5*(ISECT-1)
      WRITE(NOUT3,*) XP1(I),YP1(I)-YCAVE,
         1            DHUB/2+.5*(BH1(ISTG)+BH3(ISTG))*.5*(ISECT-1)
         2            +(XP1(I)-XLE(ISTG))/(CHORD(ISTG)*SIN(GAMMA(ISTG)))
     3           *(BH3(ISTG)-BH1(ISTG))*.5*.5*(ISECT-1)

      WRITE(NCOUNTER_P,*) XP1(I),YP1(I)-YCAVE,
         1            DHUB/2+.5*(BH1(ISTG)+BH3(ISTG))*.5*(ISECT-1)
         2            +(XP1(I)-XLE(ISTG))/(CHORD(ISTG)*SIN(GAMMA(ISTG)))
     3           *(BH3(ISTG)-BH1(ISTG))*.5*.5*(ISECT-1)
      WRITE(NCOUNTER_S,*) XS1(I),YS1(I)-YCAVE,
         1            DHUB/2+.5*(BH1(ISTG)+BH3(ISTG))*.5*(ISECT-1)
         2            +(XS1(I)-XLE(ISTG))/(CHORD(ISTG)*SIN(GAMMA(ISTG)))
     3           *(BH3(ISTG)-BH1(ISTG))*.5*.5*(ISECT-1)

 50   CONTINUE
 10   CONTINUE
          CLOSE(NIN20)
 5    CONTINUE

      STOP
      END


C     ========================================
C     SUBROUTINES
C     ========================================
      FUNCTION COT(ANGLE)
      COT=1.0/TAN(ANGLE)
      RETURN
      END
C     ========================================
      FUNCTION ACOT(XNUM)
      COMMON /PI_NUM/ PI
      ACOT=ATAN(1/XNUM)
      IF (ACOT.LT.0) ACOT=ACOT+PI
      RETURN
```

```
      END
C     ========================================
      SUBROUTINE BASE_PRF_INT       !THIS SUBROUTINE INTERPOLATES THE
     1                              !BASE PROFILE FOR CAMBERLINE POINTS
      COMMON /CURVES/ T(1001),XC(1001),YC(1001)
      NIN21=21
      OPEN(UNIT=NIN21,FILE='2_2.txt')

      T(1)=0.0
      XF=0.0
      DO 10  I=2,1001
   20   IF (XF.LT.XC(I)) THEN
      XF0=XF
      TF0=TF
      READ(NIN21,*) XF,TF
      GO TO 20
      END IF
      T(I)=TF0+(XC(I)-XF0)/(XF-XF0)*(TF-TF0)
   10   CONTINUE
      CLOSE(NIN21)
      RETURN
      END
```